Femtosecond spectroscopy of the electronic distribution function in Copper

Dissertation

for the degree of

"Doktor der Naturwissenschaften"

Faculty 08:

Physics, Mathematics and Computer Science

Johannes Gutenberg-Universität

in Mainz

submitted by

Manuel Obergfell

born in Villingen-Schwenningen

Mainz, September 2017

Abstract

Ultrafast spectroscopy is the method of choice to study carrier dynamics and coupling strengths between electrons and other degrees of freedom (e.g. phonons, magnons, ...) in solids. Many materials are investigated with time-resolved spectroscopy, ranging from well understood systems, such as metals and semiconductors, to advanced materials with complex low temperature orders, like high temperature superconductors, ferromagnets or multiferroics. Although the physics of simple metals like Cu and Au is well understood and many theoretical and experimental studies of the electronic band structure, optical- and transport-properties and their temperature dependencies are reported, some important parameters are still difficult to determine with adequate precision. One such parameter is the electron-phonon coupling strength, which is a key parameter in describing the phonon-mediated interaction between two electrons forming a Cooper pair in a superconductor.

In this thesis, a broadband ultrafast spectroscopy setup is designed to record the dynamics of optical constants in thin Cu films upon excitation with a femtosecond optical pulse. The analysis of experimental data is performed with a particularly developed model, which relates the optical conductivity of thin Cu films to the electronic distribution function around the Fermi level. Moreover, this model allows to determine the time-evolution of the electronic distribution function from the time-resolved data and provides access to quantitatively follow the electronic thermalization and lattice heating processes. Important parameters such as the electron thermalization time and the electron-phonon coupling constant are determined. Further, a method is developed, which allows to read out the electron-phonon coupling constant directly from the unprocessed data by using simple analytical modeling. With the experimental data on the time evolution of the changes in the electronic distribution function at hand we are able to test the existing models of ultrafast carrier relaxation in metals, and provide clues for the description of dynamics at times where the electronic distribution is highly athermal.

Importantly, the presented approach could also be extended to advanced solids, like high temperature superconductors, where the consensus on the coupling strengths between the different subsystems and - correspondingly - on the nature of coupling bosons is still missing.

Zusammenfassung

Die ultraschnelle optische Spektroskopie ist das Verfahren der Wahl um die Ladungsträgerdynamik und die Kopplungstärke zwischen den Elektronen und anderen Freiheitsgraden in Festkörpern (z.B. Phononen oder Magnonen) zu untersuchen. Viele Materialien unterschiedlicher Klassen, von Metallen und Halbleitern bis zu modernen Materialien mit komplexen Ordnungsparametern, z.B. Hochtemperatursupraleiter, Ferromagnete und Multiferroika, wurden mit der zeitaufgelösten Spektroskopie untersucht. Obwohl die physikalischen Eigenschaften einfacher Metalle wie Cu und Au gut verstanden sind und viele theoretische und experimentelle Untersuchungen zur Bandstruktur, den optischen- und den Transport-Eigenschaften und deren Temperaturabhängigkeit veröffentlicht wurden, ist es immer noch eine Herausforderung, bestimmte aussagekräftige Parameter mit genügender Genauigkeit zu bestimmen. Einer dieser Parameter ist die Elektron-Phonon-Kopplungsstärke, die einen Schlüsselparameter darstellt in der Beschreibung der phononen-vermittelten Wechselwirkungsstärke zwischen zwei Elektronen, welche ein Cooper-Paar in einem Supraleiter bilden.

Im Rahmen dieser Doktorarbeit wurde ein breitbandiger ultraschneller Spektroskopieaufbau entwickelt, um die Dynamik der optischen Eigenschaften dünner Cu-Filme bei unterschiedlichen Anregedichten zu messen. Die Analyse der experimentellen Daten wurde mit einem speziell entwickelten Modell durchgeführt, welches die optischen Eigenschaften dünner Kupferfilme mit der elektronischen Verteilungsfunktion am Fermi-Niveau in Beziehung setzt. Auf kurzen Zeitskalen erlaubt das Modell die Bestimmung der zeitlichen Entwicklung der elektronischen Verteilungsfunktion aus zeitaufgelösten Daten und ermöglicht die quantitative Beschreibung der Elektronen-Thermalisierungs- und Gitter-Aufheiz-Prozesse. Wichtige Parameter wie die Elektronen-Thermalisierung-Zeit und die Elektron-Phonon-Kopplungskonstante werden bestimmt. In dieser Arbeit wird auch eine Methode entwickelt, die es uns erlaubt, die Elektron-Phonon-Kopplungskonstante direkt aus den unbehandelten Daten mit einfachen analytischen Beschreibungen zu bestimmen. Mit den experimentellen Daten über die Zeitentwicklung der Änderungen der elektronischen Verteilungsfunktion können wir sowohl die vorhandenen Modelle zur Beschreibung der Ladungsträger-Relaxation testen, als auch Möglichkeiten erörtern, wie die Dynamik einer sehr athermalen elektronischen Verteilung beschreiben werden kann. Bedeutend ist, dass das aufgezeigte Vorgehen auf komplexere Festkörper wie Hochtemperatursupraleiter angepasst werden kann, für welche immer noch keine Einigkeit über die Kopplungsstärke zwischen den verschiedenen Untersystemen besteht und auch nicht über die Natur der Austauschteilchen.

Contents

1 Introduction

Time-resolved spectroscopy is a novel method, that allows to study scattering dynamics directly as a function of the time delay after excitation. Today, in the ultrafast spectroscopy it is technically possible to achieve time resolutions in the attoseconds range to study the dynamics of particles with very short lifetimes or scattering times (e.g. lifetime of atomic inner-shell vacancies [Dre+02]). In a metal, the electronic lifetime of an excited electron is in the range of a few femtoseconds up to several hundred femtoseconds [BMA15]. The electronic lifetime is related to the scattering rate at other electrons and at phonons. The latter, also known as the electron-phonon scattering time is a subject of research for more than hundred years [Dru00]. The first studies, up to the mid-eighties, usually investigated the electron momentum-relaxation rates from carrier conductivity measurements. These rates are linked to the transport electron-phonon coupling strength, which is an approximate measure of the electron-phonon coupling strength λ [All+86; BAP82].

Ultrafast time-resolved spectroscopy is based on ultrashort optical pulses, which are generated by laser systems [Kel10], in synchrotrons [Sch+00] or in free-electron lasers [Ack+07]. To study the ultrafast relaxation phenomena, the generated pulses are used to excite the sample (pump pulse) and to successively probe the resultant changes in the sample's properties. E.g., the electronic lifetime as a function of the energy above the Fermi level are experimentally determined with the time-resolved two photon photoemission [PO97]. These experiments were performed on simple metals (e.g. Cu and Au) quite extensively [BMA15]. Beyond that, a similar technique of time-resolved photoemission has access to the time evolution of the electronic distribution function [Fan+92; Lis+04; Per+07] in out of equilibrium. However, up to now, these experiments performed on metals are quite scarce.

In experiments on metals, femtosecond optical pulses are used to excite a small fraction of conduction electrons. The excited electrons scatter at other electrons redistributing energy to all electrons of the conduction band. During and after this electron thermalization process, the electrons scatter on the lattice to heat it up until the entire system reaches a common temperature (which is higher than before excitation). These processes, which take place on the femtosecond and picosecond timescale, are followed by heat diffusion, so by the next excitation pulse the system has cooled down to the initial temperature.

The first theoretical description of the fs-ps thermalization in a metal is based on the two temperature model introduced by Kaganov et al. [KLT57] and applied to pump-probe experiments [EA+87; All87;

BFI87; Bro+90] to determine electron-phonon coupling constants λ in various metals. These type of pump-probe experiments are performed with ultrashort optical pulses to excite and subsequently probe the changed optical properties (e.g. the change in reflectivity of the sample) of the metal as a function of time delay between the pump and the probe [Hil11]. The different temporal characteristics of the electronic and the lattice responses allow to disassemble the relative changes of the optical properties into components which are related to the electronic and to the lattice subsystems [Bro+90; Che+91; Per+07]. The problem herein is, that the model contains parameters which are not directly measured. There are proportionality constants between the temperatures of the subsystems and the measured change in optical constants. The relaxation times are simulated with the two temperature model to determine the electron-phonon coupling constant.

However, it has been demonstrated that the two temperature model does not work in some metals [Fan+92; Lis+04; Gad+10], especially at low temperatures [GSL95]. In these metals the two temperature model cannot reproduce the experimental data because the electrons do not thermalize instantaneously (see Figure 1), which is one of the main assumptions of the two temperature model [All87].

An alternative approach, which is not based on the assumption of the rapid electron thermalization,

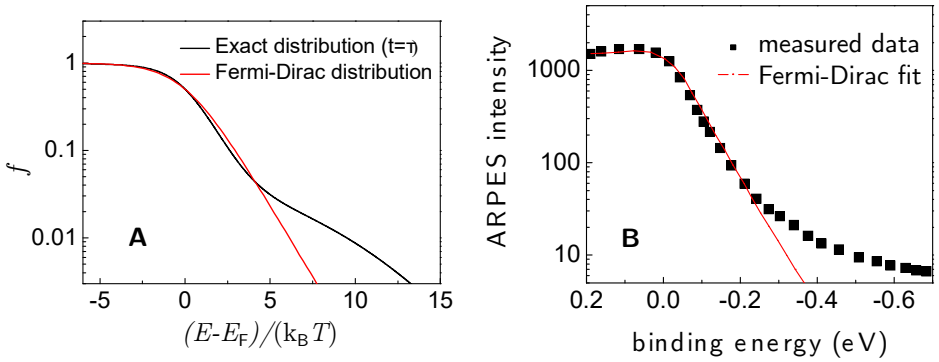

Figure 1: **The electronic distribution function in a metal after optical excitation. A** The electronic distribution function is derived from numerical calculations [KA08] after the characteristic electron-phonon relaxation time. Note the deviation between the result of the numerical calculations and the description of the result with Fermi-Dirac distribution functions. **B** ARPES spectra show a similar deviation between the electronic distribution function (assumed to be proportional to the ARPES intensity) in $Bi_2Sr_2CaCu_2O_8$ after 50 fs and the Fermi-Dirac distribution function. The graphs are taken from the supplementary of [Gad+10].

has been recently proposed. The model, which utilizes the linearized Boltzmann equations, was introduced by Kabanov et al. [KA08; BK14], and applied to the time-resolved quasiparticle response

to short laser pulses in cuprates [Gad+10]. Here the decay times are found which do not depend on the excitation density, while the two temperature model predicts an increase of the decay time with increasing excitation density.

Numerous groups go even beyond the two temperature model, introducing multi temperature models. E.g. Dal Conte et al. [DC+12] proposed an extension of the two temperature model to describe the time evolution of the quasiparticle response in cuprates based on four coupled subsystems with different temperatures[1](see Figure 2). Although this multi temperature analysis is fundamentally different to the application of the linearized Boltzmann equations [Gad+10], both studies result in similar values for the electron-phonon coupling constant λ in cuprates. The reason for this is, that both studies use similar equations (comparable at low excitation densities) to connect the experimental time signal decay time of about 1 ps to λ. We should note, however, that the important sample

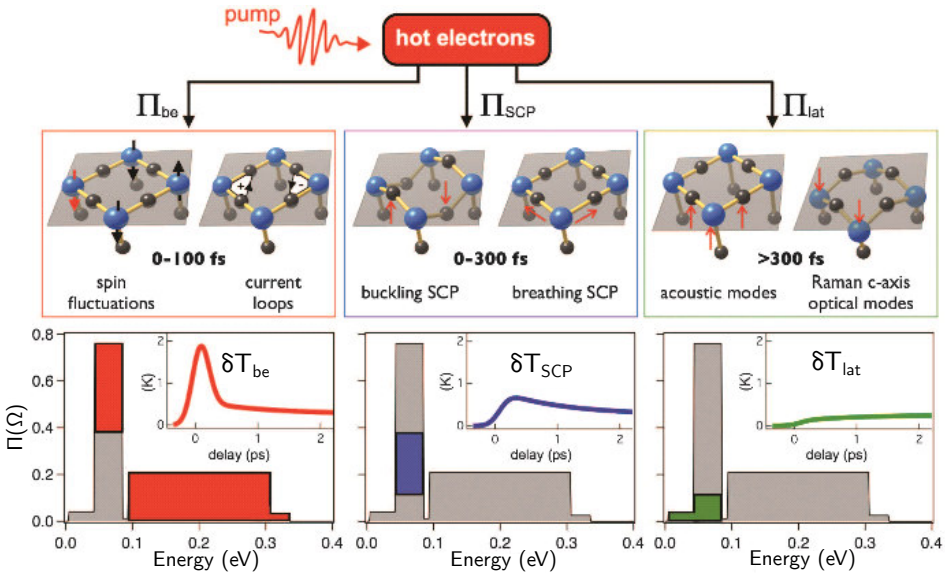

Figure 2: **Multi temperature model applied to the time-resolved data on $Bi_2Sr_2Ca_{0.92}Y_{0.08}Cu_2O_{8+\delta}$.** The application of the four temperature model allows to disentangle the contributions to the quasiparticle response in cuprates. Π_{be} covers the electronic contribution to the total bosonic function (red), Π_{SCP} the contribution which is related to the strongly coupled phonons (blue) and Π_{lat} the contribution of all the other phonons (green). Each component contributes to the quasiparticle response and its time-dependent strength is reproduced in the appropriate inset. The upper panels show the microscopic mechanisms related to the different components. The graph is taken from [DC+12].

dependent parameters, e.g. the critical temperature in superconductors, strongly depend on λ, be-

[1]Note that the electronic distribution function is found to be athermal in the analysis of Gadermaier et al. [Gad+10], whereas it is assumed to be thermal in the analysis done by Dal Conte et al. [DC+12]. Both views are irreconcilable.

cause λ appears in the exponent, i.e. $T_c \propto \exp(-1/\lambda)$ [McM68; AM83; AD75]. Superconductors are classified as the weak-coupling superconductors (e.g. Al, with $\lambda = 0.44$) and the strong-coupling superconductors (e.g. Pb, with $\lambda = 1.55$) [AD75]. Thus, knowing λ with a precision better than $\approx 10\,\%$ is required. Systematic experimental studies of the relation between the critical temperature and λ are reported by Bergmann [BR73; Ber76] on disordered metals and by Gadermaier et al. [Gad+14] on cuprate superconductors.

Beside superconductors, the scattering dynamics in the metallic state of a large amount of other materials can be studied as well. In a broad definition, all materials which show a reasonably good electrical conductivity can be considered to be metals. They are very heterogeneous considering the complexity of the unit cell (from single atom up to several tens of atoms in e.g. organic metals and superconductors [Sai+82; Yag+84]) and covers the range from perfect crystals to disordered systems [Gra+77; SHC94], glasses [SI11; LL04] and chemically- and photo-doped semiconductors [NKG02; Joy+13]; even liquids (e.g. Hg) can show metallic behavior. However, the characteristic electrical (DC) and optical conductivity in equilibrium is basically described by the same classical theory, the Drude model [Dru00]. The microscopic processes which are associated to the model parameters are the electron-electron and the electron-phonon scattering [PN66; BP91; Gri81]. As already discussed above, the time-resolved optical spectroscopy is sensitive to the electron scattering processes, but needs input from theory to determine the electron-phonon coupling strength. The lack of knowledge exists because of the unknown connection between the electronic distribution function and the optical properties of the metal. Although it is known, that the redistribution of the electrons are responsible for the observed dynamics in optical properties, the connection between both physical entities is usually made in a heuristic way with lots of free parameters. The theoretical understanding of the optical properties can be helpful to fix the models' parameters and to link the experimental result to the electronic distribution function of the metal. This function is the basis of all the models which describe the electron relaxation process in a metal [All87; Sun+94; Lis+04; Car06; BK14]. The theoretical models can be tested, if the experimental data allows one to determine the time evolution of the electronic distribution function. And, it is of some advantage to start the analysis on a simple metal with well known electronic structure and with one atom per unit cell to keep the relaxation path simple (e.g. only acoustic phonons are present).

This work shows, how to experimentally access the electronic distribution function and its time evolution in the simple metal Cu. The optical properties of thin Cu-films are probed in the range of the

d-band to Fermi level transitions, both in equilibrium and as a function of time after optical excitation at various excitation densities. To consistently describe the large data basis, a model is developed to account for the optical properties at the upmost d-band to Fermi level transitions. The sensitivity of these optical transitions to the changes of the electronic distribution function (see [RL72], Figure 3) allows to quantitatively extract the electronic distribution function.

The two temperature model and various other models [Sun+94; Car06; Lis+04; BK14] are tested

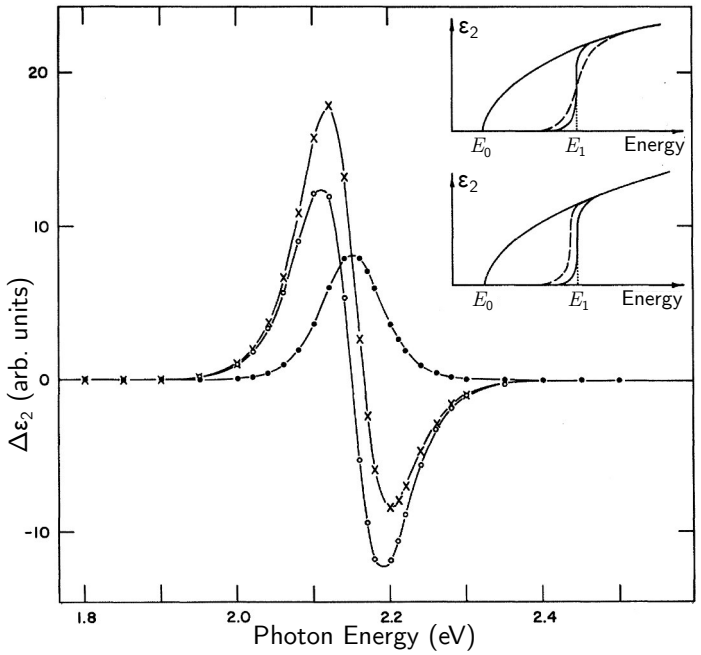

Figure 3: **The upmost d-band to Fermi level transitions in Cu.** The optical properties of Cu at 2.1 eV arise from transitions from the top of the d-bands to the empty states at the Fermi level. Changes in the transition probability are related to the thermal broadening of the electronic distribution function around the Fermi level (open circles, schematically shown in the upper inset) and to the shift of the Fermi level (closed circles and lower inset). The insets schematically show the conduction band and the electronic distribution function. Note the changes in the electronic distribution function at the Fermi level which directly affect the probability of the optically driven transitions between the d-bands and the Fermi level. The optical properties of Cu are discussed in Chapter 4. The figure is taken from [RL72].

using the experimental findings. The analysis provides access to the electron-electron thermalization time and the electron-phonon coupling constant. It is confirmed that the two temperature model well describes the relaxation process at times, when the electrons are already thermalized, while the model of linearized Boltzmann equations can be applied at very low excitation densities. Further, we modified the model of Lisowski et al. [Lis+04] to improve the agreement between the theory and

the experiment at short time delays, where the electrons are strongly athermal. The modified model shows good agreement with the experimental findings.

Chapter 2 introduces the electron scattering mechanisms, the electronic lifetime and the electron relaxation-, multiplication- and recombination-rates. This presents the basis to understand the approximate solutions of Boltzmann equations which is the topic of Chapter 3. These solutions answer the question of how the electrons thermalize after optical excitation and on which timescale the energy of the electrons is transferred to the lattice. The electronic structure and the related optical properties of Cu are elaborated in Chapter 4. The developed model is applied to the temperature dependent optical properties which are known from the literature. This model further allows to access the electronic distribution function from the experimental time-resolved broadband optical data. This step is made in Chapter 5. Here, the electron thermalization time and the electron-phonon coupling constant λ are determined. The way, this is done, is very elaborate and there are methods introduced, to determine λ directly from the unprocessed experimental data. Chapter 5 further shows that the electrons are strongly athermal up to several hundred femtoseconds. This non-thermal distribution function during the first few hundred femtoseconds is the topic of Chapter 6. Here, different extensions of the two temperature model, the model of the linearized Boltzmann equations and our own approach are tested.

2 Electron dynamics, scattering and lifetimes

This chapter introduces into the different concepts and views to describe the thermalization in metals following excitations. Thermalization processes take place after pushing the metal out of equilibrium and the metal turns back into locally established thermal equilibrium on a typically timescale of picoseconds[2]. A sufficient time resolution is achieved with femtosecond optical pulses. The sketch in Figure 4 describes the excitation-relaxation loop within the so called two temperature model (TTM) applied to a simple metal after the excitation with an ultrashort optical laser pulse (see also Section 3.1). The parameters are taken to sketch the situation in a "typical metal", to exemplify a typical relaxation process. First, the metal is in a thermal equilibrium, the electrons and the lattice are both at the same temperature (e.g. room temperature of 300 K)

$$T_{\mathsf{el}} = T_{\mathsf{la}} = T_0 = 300\,\mathsf{K}\,.$$

The electronic distribution in the metal is described by the Fermi-Dirac distribution function (state (1) in Figure 4)

$$f(E,T) = \frac{1}{1+\exp\left((E-E_{\mathsf{F}})/(\mathrm{k_B}\,T_{\mathsf{el}})\right)}\,.$$

The ultrashort laser pulse (∼50 fs) excites predominantly the electrons[3], the lattice remains cold. In the single-particle- and photon-electron-interaction picture, the energy of each absorbed photon is directly transferred to one electron in the conduction band. The electronic distribution function has a step-like shape after the excitation (see for example [DV+12]). This is shown in the graph at state (2) in the loop. The fraction of excited electrons compared to the number of electrons within the same range (with $E > E_{\mathsf{F}} - \mathrm{h}\nu$) is typically in the region of one-tenth of a percent up to a few percent. In this example it is

$$\frac{N_{\mathsf{exc}}}{N_0} = \frac{\bar{U}_{\mathsf{abs}}}{(\mathrm{h}\nu)^2\;\bar{D}} = 3\,\%\,.$$

corresponding to the absorbed energy density $\bar{U}_{\mathsf{abs}} = 500\,\mathrm{J/cm^3}$ and the average photon energy of $\mathrm{h}\nu = 1.5\,\mathrm{eV}$. $\bar{D}$ is the average density of states (in the range $-\mathrm{h}\nu < E < E_{\mathsf{F}}$) which is almost constant in the considered range and reads (free electron model, [AM11])

$$\bar{D} \approx D(E_{\mathsf{F}}) = \frac{(2\,m)^{3/2}}{2\,\pi^2\,\hbar^3}\,\sqrt{E_{\mathsf{F}}} = 3\cdot 10^{41}\frac{1}{\mathrm{J\,cm^3}}\,.$$

[2] A non-homogeneously excited large volume of the metal requires the transport of heat to equilibrate. This relaxation process evolve on timescales which depend on the size (distance s) of the volume and metal's speed of sound (c_{s}), it is $\tau_{\mathsf{ht}} \simeq s/c_{\mathsf{s}}$.

[3] Here, photon energies in the visible range are used with energies far above all phonon branches.

Typical Fermi energies are about $E_F = 6\,\text{eV}$, m is the mass of the free electron. The non-thermal

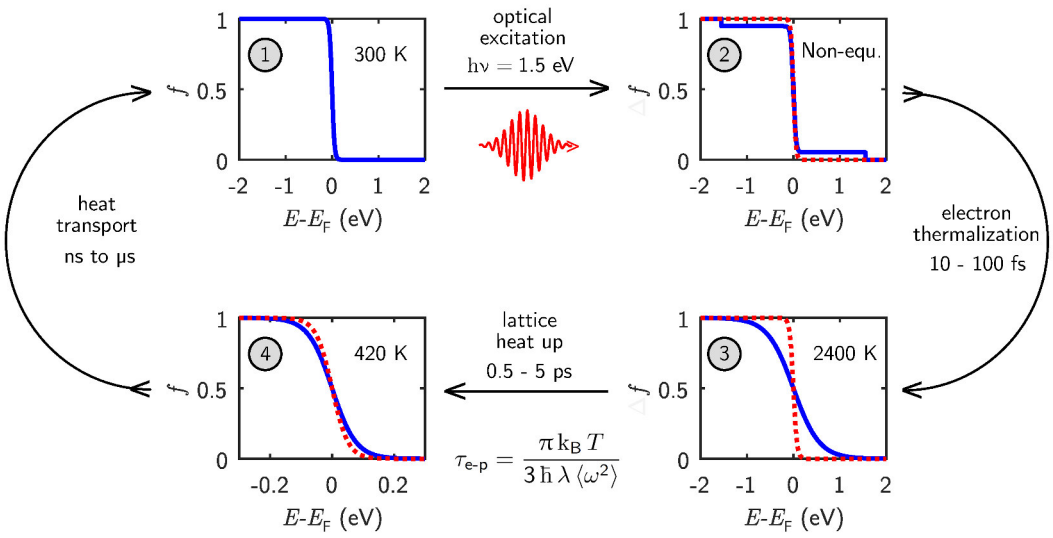

Figure 4: **Thermal relaxation of electrons in metals described by the two temperature model [All87; KLT57; AT02]. State 1**: The electrons are in thermal equilibrium at room temperature. **State 2**: The electrons are excited with a short laser pulse (∼50 fs). **State 3**: The electrons thermalize very quickly to temperatures of several thousand Kelvin (depending on the excitation density). **State 4**: On a longer timescale the energy is transferred from the electronic subsystem into the lattice subsystem. This process typically takes several hundred femtoseconds up to a few picoseconds. The lattice heats up to temperatures of tenths to hundreds of Kelvin above T_0. Because of the large heat capacity of the lattice compared to the electronic heat capacity, the lattice temperatures are lower than the electronic temperatures at short time delays. **Back to State 1**: The heat is transferred from the sample into the coupled heat bath. It takes typically several nanoseconds up to microseconds to cool the sample down to T_0 (in proper thermal contact to the heat bath).

electronic distribution is unstable and the excited electrons lose their energy which is transferred to other electrons and to the lattice. The TTM assumes the electrons to thermalize almost instantaneously, faster than the duration of the optical pulse ($< 50\,\text{fs}$). The electron's scattering rate at other electrons is expected to be much higher compared to the scattering rate with phonons because of the differences in the band widths ($\hbar\omega_D \ll E_F$) and heat capacities ($c_{el} \ll c_{la}$). The energy transfer to the lattice during this fast thermalization process is negligible. The electrons thermalize to the electronic temperature of

$$T_{el} = \sqrt{T_0^2 + 2\,\bar{U}_{abs}/\gamma} = 2400\,\text{K}\,. \tag{1}$$

This equation is based on the energy conservation law with the electronic heat capacity coefficient of (here Cu is used as the prototype material)

$$\gamma = \frac{(2\,m)^{3/2}}{6\,\hbar^3}\,\mathrm{k_B^2}\,\sqrt{E_\mathrm{F}} = 2\cdot 10^{-4}\,\frac{\mathrm{J}}{\mathrm{cm^3\,K^2}}\,.$$

The Fermi-Dirac distribution function at the highest temperature (blue solid line) is compared to the distribution function in thermal equilibrium (red dotted line) in the graph at state (3).

At later times the electrons lose their energy which is transferred to the lattice. This happens on a picosecond timescale. The lattice finally heats up to

$$T_\mathrm{la} = T_0 + \frac{\bar{U}_\mathrm{abs}}{c_\mathrm{V}} = T_0 + \frac{\bar{U}_\mathrm{abs}}{3\,\mathrm{k_B}\,\rho} = 420\,\mathrm{K}\,.$$

This is the case at temperature above the Debye temperature, where the heat capacity c_V is independent of the temperature (if there are no optical phonon branches). The ion density is $\rho = 0.09\cdot 1/\mathrm{Å}^3$.

The typical rise time of the lattice temperature is

$$\tau_\mathrm{e\text{-}p} = \frac{\pi\,\mathrm{k_B}\,T_\mathrm{el}}{3\,\hbar\,\lambda\,\langle\omega^2\rangle} = 3\,\mathrm{ps}$$

with an electron-phonon coupling constant (see Section 2.2) of

$$\lambda\left\langle\omega^2\right\rangle = 50\,\mathrm{meV^2}\,.$$

In the graph at state (4) the electronic distribution function at the new sample temperature (blue solid line) is compared to the distribution function in the beginning (red dotted line). The absorbed energy heats up the sample and this heat is transferred on a comparably long timescale to the surrounding heat bath to cool down the sample to its previous temperature T_0 (back to state (1)).

The described relaxation process is microscopically based on scattering events between the particles in the metal. In order to understand what is happen during the relaxation loop, the first things to focus on are the scattering mechanisms. In a metal the scattering between quasiparticles is always present. Electrons exchange energy and momentum with other electrons and with the lattice. These processes in combination with the motion of the electrons and the phonons lead to an overall thermalization of the metal. Out of equilibrium, the particles exchange energy and momentum to thermalize. The interaction between the electrons and the lattice is described in Section 2.1. The electron-electron interaction follows in Section 2.4.

The theoretical description of the particle dynamics is based on Boltzmann equations and the band structure calculation. These statistical methods can consider the large number of electrons which

is on the order of 10^{23}. The band structure calculations solve the many-body problem and they provide information about the electronic states screening the fixed ion positions. The ions can oscillate around their equilibrium positions. The quantized excitation states are characterized by the phonon dispersion relation. The only unknown parameters of the metal to fully characterize its current state are the electron and phonon distribution functions. Their time dependencies are determined with Boltzmann equations. These equations consider the movement and the scattering of the quasiparticles. One electron can scatter at another electron, at the surface, at a phonon, at a grain boundary or at an impurity. The (non-thermal) electrons lose their energy or momentum which is transferred to other electrons until the electronic subsystem is thermalized and they transfer energy to the phonons until the solid reaches its equilibrium state.

In the TTM model situation, the electron-electron-scattering is assumed to be much faster compared to electron-phonon related energy transfer and the phonons are always thermally distributed during the relaxation process (see Section 3.1). The Theory-sections 2.3, 2.5 and 2.2.1 help to prove these assumptions. The electron-phonon energy exchange is described in Section 2.2, it is the link between states (3) and (4) in Figure 4.

If the metal has a strong electron-phonon coupling, then the high energetic electrons have already lost a part of their energy which is transferred to the lattice according to the spontaneous phonon emission (Section 2.3) between states (2) and (3). In this case, equation (1) is inapplicable.

2.1 The electron-phonon scattering

The electron, scattering at the lattice, changes its state and creates or annihilates phonons. The scattering probability is characterized by Fermi's golden rule. In this first order perturbation theory one phonon, one electron and the empty final state (hole) are involved in the process. The electronic distribution function changes over time [All87; KA08] as

$$\begin{aligned}
\dot{f}_{\boldsymbol{k}} \;=\; & \frac{2\,\pi}{\hbar} \sum_{\boldsymbol{k}',\boldsymbol{q}} \Big[\left| M_{\boldsymbol{k},\boldsymbol{k}',\boldsymbol{q}} \right|^2 \delta(E_{\boldsymbol{k}} - E_{\boldsymbol{k}'} + \hbar\,\omega_{\boldsymbol{q}})\, f_{\boldsymbol{k}'}\,(n_{\boldsymbol{q}}+1)\,(1-f_{\boldsymbol{k}})\,\delta_{\boldsymbol{k}'-\boldsymbol{k},\boldsymbol{q}} \\
& + \left| M_{\boldsymbol{k},\boldsymbol{k}',\boldsymbol{q}} \right|^2 \delta(E_{\boldsymbol{k}} - E_{\boldsymbol{k}'} - \hbar\,\omega_{\boldsymbol{q}})\, f_{\boldsymbol{k}'}\, n_{\boldsymbol{q}}\,(1-f_{\boldsymbol{k}})\,\delta_{\boldsymbol{k}'-\boldsymbol{k},-\boldsymbol{q}} \\
& - \left| M_{\boldsymbol{k}',\boldsymbol{k},\boldsymbol{q}} \right|^2 \delta(-E_{\boldsymbol{k}} + E_{\boldsymbol{k}'} + \hbar\,\omega_{\boldsymbol{q}})\, f_{\boldsymbol{k}}\,(n_{\boldsymbol{q}}+1)\,(1-f_{\boldsymbol{k}'})\,\delta_{\boldsymbol{k}-\boldsymbol{k}',\boldsymbol{q}} \\
& - \left| M_{\boldsymbol{k}',\boldsymbol{k},\boldsymbol{q}} \right|^2 \delta(-E_{\boldsymbol{k}} + E_{\boldsymbol{k}'} - \hbar\,\omega_{\boldsymbol{q}})\, f_{\boldsymbol{k}}\, n_{\boldsymbol{q}}\,(1-f_{\boldsymbol{k}'})\,\delta_{\boldsymbol{k}-\boldsymbol{k}',-\boldsymbol{q}} \Big]
\end{aligned}$$

$$= \frac{2\pi}{\hbar} \sum_{\boldsymbol{q}} |M_{\boldsymbol{q}}|^2 \left[\delta(E_{\boldsymbol{k}} - E_{\boldsymbol{k}+\boldsymbol{q}} + \hbar\,\omega_{\boldsymbol{q}}) \; (f_{\boldsymbol{k}+\boldsymbol{q}}\,(n_{\boldsymbol{q}}+1)\,(1-f_{\boldsymbol{k}}) - f_{\boldsymbol{k}}\,n_{\boldsymbol{q}}\,(1-f_{\boldsymbol{k}+\boldsymbol{q}})) \right.$$
$$\left. + \delta(E_{\boldsymbol{k}} - E_{\boldsymbol{k}+\boldsymbol{q}} - \hbar\,\omega_{\boldsymbol{q}}) \; (f_{\boldsymbol{k}+\boldsymbol{q}}\,n_{\boldsymbol{q}}\,(1-f_{\boldsymbol{k}}) - f_{\boldsymbol{k}}\,(n_{\boldsymbol{q}}+1)\,(1-f_{\boldsymbol{k}+\boldsymbol{q}})) \right]. \tag{2}$$

This is the electron-phonon Boltzmann scattering term. The last equality holds if the scattering matrix element is symmetric with respect to the generation and absorption of a phonon, has spherical symmetry and does not depend on $\boldsymbol{k}$ and the direction of the spin, i.e. $M_{\boldsymbol{q}} \equiv M_{\boldsymbol{k},\boldsymbol{k}',\boldsymbol{q}}$. The phonon dispersion and the phonon distribution function have to be inversion symmetric ($\omega_{\boldsymbol{q}} = \omega_{-\boldsymbol{q}}$ and $n_{\boldsymbol{q}} = n_{-\boldsymbol{q}}$). To keep the notation simple, the different spin directions are included in $\boldsymbol{k}$ ($\boldsymbol{k} \leftrightarrow \boldsymbol{k}, \sigma$). The spin conservation is not considered explicitely. If all $f_{\boldsymbol{k}}$ at the same energy $E_{\boldsymbol{k}}$ are equal, then equation (2) simplifies to

$$\dot{f}(E) = 2\pi \int_{-\infty}^{\infty} \int_{-\infty}^{\infty} Q(\omega, E, E') \left[\delta(E - E' + \hbar\omega) \, (N(\omega)\,(f(E') - f(E)) + f(E')\,(1 - f(E))) \right.$$
$$\left. + \delta(E - E' - \hbar\omega) \, (N(\omega)\,(f(E') - f(E)) - f(E)\,(1 - f(E'))) \right] \mathrm{d}E' \, \mathrm{d}\omega \tag{3}$$

with the matrix elements

$$Q(\omega, E, E') = \frac{1}{D(E)\,\hbar} \sum_{\boldsymbol{k},\boldsymbol{q}} |M_{\boldsymbol{q}}|^2 \; \delta(E_{\boldsymbol{k}} - E) \, \delta(E_{\boldsymbol{k}+\boldsymbol{q}} - E') \, \delta(\omega_{\boldsymbol{q}} - \omega) \, . \tag{4}$$

The energy of the initial and the final state of the electron cannot be further apart than the energy of the highest energetic phonon $\hbar\omega_{\mathsf{max}}$. Electrons with energies below the threshold, $E - E_{\mathsf{F}} \leq \hbar\omega_{\mathsf{max}}$, can recombine with an empty state (hole) below E_{F}. Above the threshold the number of excited quasiparticles is conserved.

2.2 Eliashberg function and phonon decay in Cu

The Eliashberg function is related to matrix elements of the electron-phonon coupling (equation (4)). If the conduction band has a large bandwidth compared to the energy of phonons, and the density of states varies slowly near E_{F}, then the relation

$$Q(\omega, E, E') \approx Q(\omega, E_{\mathsf{F}}, E_{\mathsf{F}}) \equiv \alpha^2 F(\omega) \tag{5}$$

holds (see [KA08] and [JZ16]), where $\alpha^2 F(\omega)$ is the Eliashberg electron-phonon coupling function ($F(\omega)$ is the phonon density of states).

If one is not interested in the coupling of the electrons to each specific phonon state (or if this is

too difficult to determine) but to the whole bunch of phonons as such, then it is useful to take the integrated electron-phonon coupling strength (see also [All87; BK14])

$$\lambda \langle \omega^n \rangle = 2 \int_0^\infty \omega^{n-1} \alpha^2 F(\omega) \, \mathrm{d}\omega \,, \tag{6}$$

which is temperature independent. In transport experiments the resistivity (momentum relaxation) and in superconductors the critical temperature [McM68] are related to λ and the energy relaxation dynamics in metals is linked to a taylor expansion where the first order is proportional to $\lambda \langle \omega^2 \rangle$ [All87].

In Cu the Eliashberg function has been determined theoretically by different authors and techniques [JZ16; SS96; BAP82] and experimentally by Jansen et al. [JMW77; JMW78] based on electronic tunneling experiments through metallic point contacts. The results are presented in Figure 5**C**. The most striking differences in the spectra are the coupling strenghes between the electrons and the different phonon branches. The experimental finding of Jansen et al. [JMW77; JMW78] and the theoretical result of Ji and Zhang [JZ16] (they use the density functional theory implementation ABINIT of Gonze et al. [Gon+09]) is, that the electrons are stronger coupled to the transversal acoustical phonons than to the longitudinal acoustical phonons. Other authors, Savrasov & Savrasov [SS96] and Beaulac et al. [BAP82] (ab initio calculations and linear response at zero temperature) found similar coupling strengths to each of the phonon branches. If the coupling to all branches at all frequencies is equal (flat coupling), one expect the Eliashberg function to have the same shape as the phonon spectral function (green line, Figure 5**C**). The phonon density of states was measured by Nilsson and Rolandson [NR73] at 80 K with neutron scattering and is shown in Figure 5**B**. According to experimental results of Nicklow et al. [Nic+67], the phonon density of states does not change much with temperature between 49 K and 300 K. The relation between the Eliashberg function and the phonon density of states is in the case of a flat coupling

$$\alpha^2 F(\omega) = \frac{\lambda \cdot F(\omega)}{2 \int_0^\infty F(\omega) / \omega \, \mathrm{d}\omega} \,. \tag{7}$$

The electron-phonon coupling constants are given in the Table 1. The more the electron-phonon interaction is enhanced at higher frequencies (non-flat coupling), the more the phonon subsystem departs from equilibrium during the process of relaxation. The phonon decay processes, however, work towards the thermalization of the lattice subsystem. The phonon decay processes are described in Subsection 2.2.1.

Interestingly, the situation in aluminum seems to be somewhat different from the situation in Cu

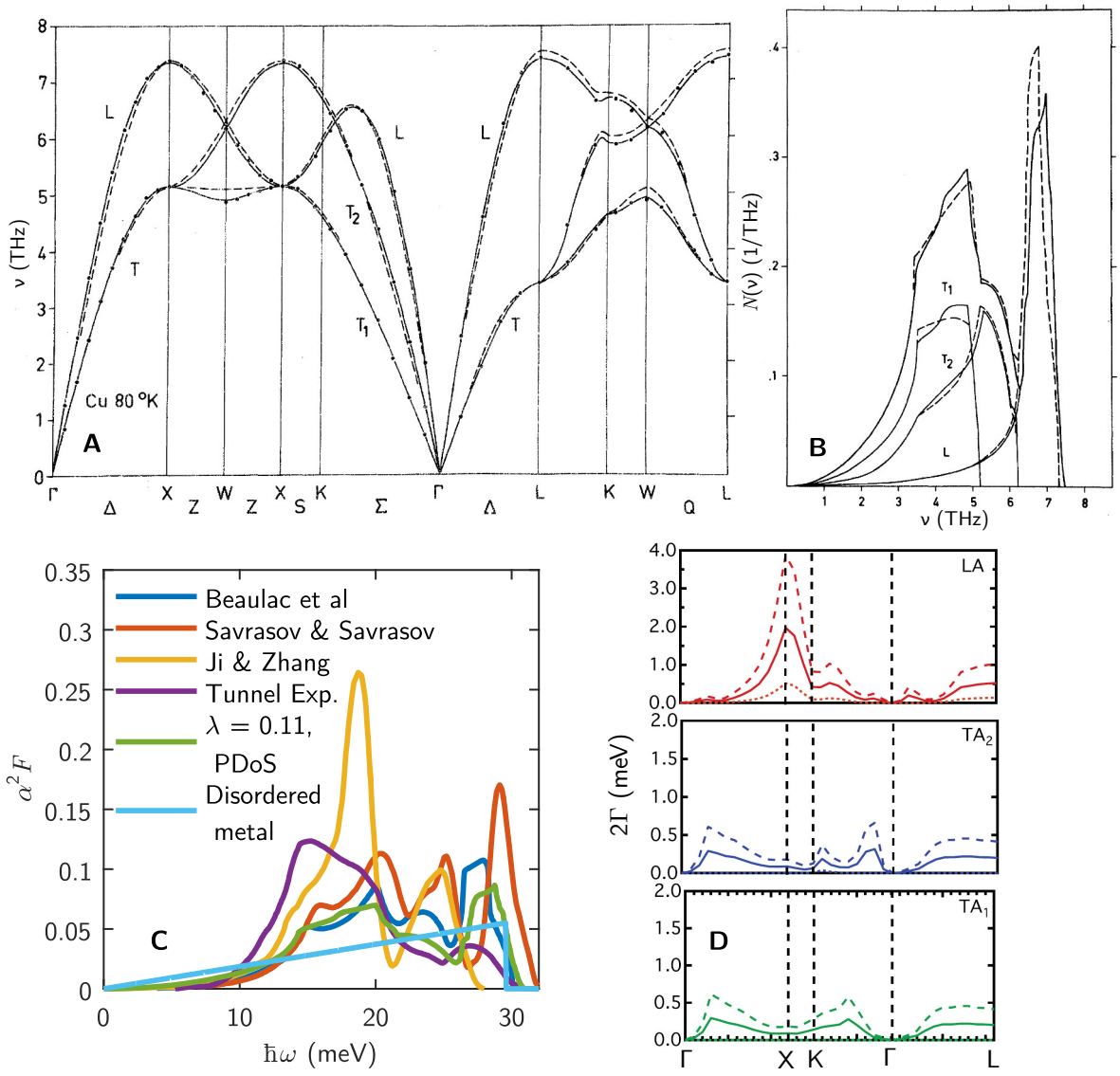

Figure 5: **Phonon dispersion, Eliashberg function and phonon damping in copper. A** Phonon dispersions of copper measured by Nilsson and Rolandson [NR73] at 80 K with neutron scattering. The data points are fitted with first-nearest-neighbor (dashed line) and eighth-nearest-neighbor Born-von Kármán model (solid line). **B** Phonon density of states based on data of **A** and compared to calculations with the force-constant model of Nicklow et al. [Nic+67; NR73]. The phonon density of states is plotted separately for each phonon branch together with the sum of all branches (30 meV ≡ 7.25 THz). **C** Eliashberg function in copper theoretically investigated by Ji & Zhang [JZ16], Savrasov & Savrasov [SS96] and Beaulac et al. [BAP82]. The results are compared to the experimental result of Jansen et al. [JMW77] and to the frequency independent electron-phonon coupling based on the phonon density of states (PDoS; green line; measured by Nilsson & Rolandson [NR73]). In a disordered metal the coupling strength between electrons and low energy phonons is enhanced. **D** Phonon line widths in copper due to phonon-phonon decay processes calculated by Tang & Fultz [TF11]. The dotted line is at 0 K, the solid line at 300 K and the dashed line at 600 K.

	Beaulac et al. [BAP82]	Savrasov & Savrasov [SS96]	Ji & Zhang [JZ16]	Jansen et al. [JMW77; JMW78]	Flat coupling
λ	0.110	0.138	0.162	0.146	0.11 (assumed)
$\lambda \langle \omega^2 \rangle$	46.1 meV^2	65.1 meV^2	54.5 meV^2	44.0 meV^2	41.1 meV^2

Table 1: **Electron-phonon coupling constants in Cu.** The different values for the electron-phonon coupling constant are achieved by theory (columns 1 to 3) and experiment (column 4 and 5). The corresponding Eliashberg functions are presented in Figure 5.

(referring to the theoretical predictions presented in Figure 5**C** and the work of Waldecker et al. [Wal+16]), although it is also a face centered cubic crystal. Waldecker et al. [Wal+16] found a stronger coupling between the electrons and the longitudinal phonon modes compared to the coupling to transversal modes. The difference might be related to the differences in the electronic structures. If the metal is disordered, then the coupling to low energy phonons is pronounced compared to the coupling to high energy phonons. In this case the Eliashberg function is linear proportional to the phonon energy [BK14; Bel87], i.e.

$$\alpha^2 F(\omega) = \frac{\lambda\,\omega}{2\,\omega_{\mathrm{D}}}\,. \tag{8}$$

This is understood, if one takes into account, that the interacting electron and phonon can scatter on other electrons or on impurities. I.e. if the electron-phonon interaction time is longer than the electronic lifetime ($q_T\,l > 1$, l is the electron mean free path and q_T is the thermal phonon wavevector, see [BKB98]), then the average scattering event is effectively a three particles scattering process of a phonon, an electron and a third particle which can take over a part of the momentum to fulfill the law of momentum conservation. This simplified picture is corroborated by the fact, that in a disordered metal, "the electron-momentum is not any longer a well defined quantum number" and Brillouin zones do not occur [Ber76].

2.2.1 Phonon decay

The phonons can decay via several decay channels. They can scatter at impurities, at electrons or holes or they can decay via phonon-phonon interaction mechanisms. The most prominent phonon-phonon interaction mechanisms are the phonon collision with other phonons and the anharmonic decay of one phonon into two phonons. If the temperature is high enough, umklapp processes are allowed. The phonon decay rates are indirectly measured via phonon line width analysis. This was

done in neutron scattering experiments in Cu made by Larose & Brockhouse [Lar75; LB76]. The fastest phonon decay is shown to happen to the longitudinal phonons at the Brillouin zone boundaries. The lowest lifetime is 400 fs ($\Gamma = 1.65$ meV) at room temperature. The transversal phonons live about 3 to 4 times longer until they decay ($\Gamma \approx 0.5$ meV). In an ultrasonic experiment made by Chang & Himmel [CH66] a consistent lifetime of 400 fs was found from the analysis of the line width at 300 K [Loi77].

The phonon-phonon interactions are theoretically investigated by Tang & Fultz [TF11] (in Cu) with an ab initio calculated interatomic force. The line width as a function of the wave vector for all three phonon branches are presented in Figure 5**D** at three different temperatures. The lifetimes of the longitudinal phonons are lowest at the X point ($\sim$ 700 fs at 300 K). They predominantly decay (98.2 %) into two transversal acoustic phonons. The decay rate of the transversal phonons is low at the X point (lifetime is more than 10 ps at 300 K). The main anharomonic decay channel at X is TA $\rightarrow$ LA - TA (92 %). Closer to the Γ point, the predominant decay channel of transversal phonons is TA $\rightarrow$ TA - TA with lowest lifetimes of about 3 ps at 300 K. One has to take the electron-phonon scattering rate and the scattering at impurities into account to compare the simulation results to the line width analysis of Larose & Brockhouse. The contribution of impurities may be low at 300 K and the phonon decay contribution is low for transversal phonons which is known from the simulation. Therefore the measured line widths of transversal phonons provide an idea of how the phonons are affected by phonon-electron scattering. The measured lifetime of about 1 ps is the average time until the phonon is absorbed in a phonon-electron scattering event (at 300 K). During this time period the phonon already traveled through more than 12 unit cells ($\sim$ 15 nm). For comparison, the electron mean free path is 39 nm (2.6 times longer) at the same temperature [Zha+04].

In parts of the first Brillouin zone, the anharmonic phonon decay rate at room temperature is higher than the scattering rate at electrons. During the energy transfer between the phonon subsystem and the electronic subsystem (between states (3) and (4) in Figure 4), the anharmonic decay is able to redistribute the phonon subsystem towards the equilibrium. The efficient rethermalization is required for the application of the TTM. This is because the electron-phonon coupling matrix element is expected to slowly vary with the phonon energy (compare the blue line with the green line in Figure 5**C**) and the thermal distribution function of phonons approximately goes with $1/\exp E/(\mathrm{k_B}T)$. Without any phonon decay, the phonon distribution will broaden. If the ratio between the numbers of high and low energy phonons is remarkably higher compared to the equilibrium condition, then the

overall number of phonons is lower than in equilibrium (comparing situations with the same energy in the lattice subsystem). The electron-phonon scattering probability is related to number of phonons (see equation (3); the process of stimulated phonon emission) and it is reduced in the case of a high ratio between the numbers of high and low energy phonons.

2.3 Spontaneous phonon emission

The accessible final states of quasiparticles scattered at phonons are limited by the energy of the highest energetic phonons with $\hbar\omega_{\mathsf{max}}$. To determine the electron-phonon scattering rate in an excited state, one commonly uses the spontaneous phonon emission[4] which is equal to the implementation of the "empty final state approximation". The empty final state approximation assumes that all states in the (phonon energy) limited range around the initial energy of the electron are empty. This approximation is applicable in case of a low density of non-thermal quasiparticles which are widespread in their energy (quasiparticles with $|E - E_{\mathsf{F}}| > k_{\mathsf{B}}\,T$). This condition may arise in metals after off-resonant excitations (e.g. intraband excitations) with low excitation densities. Shortly after excitation the phonons are still thermally distributed and the distribution of the electrons is highly athermal (see Figure 4, state (2)). In the empty final state approximation, the rate of the energy transfer from the quasiparticles to the lattice is linearly dependent on the number of excited quasiparticles (holes lose their energy the same as electrons). It is

$$\frac{\partial U_{\mathsf{el}}}{\partial t} = -\alpha_{\mathsf{efs}} \cdot N_{\mathsf{qp}} = -\pi\,\hbar\,\lambda\left\langle\omega^2\right\rangle \cdot N_{\mathsf{qp}}\,. \tag{9}$$

This result is derived in Section 8.1.1 and by Gusev & Wright [GW98] and Baranov & Kabanov [BK14]. The result of Tas & Maris [TM94] is by a factor of $2\,\ln(2)$ different. The characteristic energy loss time of a single quasiparticle is

$$\tau_{\mathsf{el\text{-}ph}}(E - E_{\mathsf{F}}) = \frac{|E - E_{\mathsf{F}}|}{\pi\,\hbar\,\lambda\,\langle\omega^2\rangle}\,. \tag{10}$$

From equations (9) and (10) it follows that

$$\frac{\partial U_{\mathsf{el}}}{\partial t} = -\frac{U_{\mathsf{el}}}{\tau_{\mathsf{el\text{-}ph}}(\langle E - E_{\mathsf{F}}\rangle)}\,,$$

which is related to the average energy loss time. The theoretical prediction for copper with [BAP82]

$$\lambda\left\langle\omega^2\right\rangle = 46\,\mathsf{meV}^2\,,$$

[4]The name spontaneous phonon emission is chosen in analogy to the spontaneous and field independent light emission, because the phonon emission is independent of the number of phonons $N(\omega)$.

results in

$$\alpha_{\mathrm{efs}} = 0.22\,\mathrm{eV/ps}\,.$$

If this process is considered only, the relaxation of an excited electron with $E - E_{\mathrm{F}} = 1.55\,\mathrm{eV}$ lasts about 7 ps.[5]

2.4 The electron-electron scattering

The Boltzmann term of the electron-electron scattering within a single electron band reads [KA08]

$$\begin{aligned} \dot{f}_{\boldsymbol{k}} &= \frac{2\pi}{\hbar} \sum_{\boldsymbol{p},\boldsymbol{q}} |V_{\boldsymbol{q}}|^2 \; \delta(E_{\boldsymbol{k}} + E_{\boldsymbol{q}} - E_{\boldsymbol{k}+\boldsymbol{q}} - E_{\boldsymbol{p}-\boldsymbol{q}}) \\ &\quad \cdot [f_{\boldsymbol{k}+\boldsymbol{q}}\, f_{\boldsymbol{p}-\boldsymbol{q}}(1-f_{\boldsymbol{k}})(1-f_{\boldsymbol{p}}) - f_{\boldsymbol{k}} f_{\boldsymbol{p}}(1-f_{\boldsymbol{k}+\boldsymbol{q}})(1-f_{\boldsymbol{p}-\boldsymbol{q}})] \; . \end{aligned} \tag{11}$$

It is based on Fermi's golden rule and relate the change in the electronic distribution function to the scattering matrix element $V_{\boldsymbol{q}}$. Further the energy and the momentum conservation laws are considered. The sums count all possible electronic transitions between filled initial and empty final states which contribute to the change in $f_{\boldsymbol{k}}$. The states are characterized by their wavevectors. The scattering matrix element is assumed to be spin independent and independent of the initial and final wavevectors $\boldsymbol{k}$ and $\boldsymbol{p}$. The electron-electron-related electronic lifetime is obviously given by the second term of equation (11)

$$\frac{1}{\tau_{\boldsymbol{k}}} = \frac{2\pi}{\hbar} \sum_{\boldsymbol{p},\boldsymbol{q}} |V_{\boldsymbol{q}}|^2 \; \delta(E_{\boldsymbol{k}} + E_{\boldsymbol{q}} - E_{\boldsymbol{k}+\boldsymbol{q}} - E_{\boldsymbol{p}-\boldsymbol{q}}) \; [f_{\boldsymbol{p}}(1-f_{\boldsymbol{k}+\boldsymbol{q}})(1-f_{\boldsymbol{p}-\boldsymbol{q}})] \; . \tag{12}$$

This presents the basis for the calculation of the electronic lifetime in the Fermi liquid theory [GV05].

2.5 The Fermi liquid theory and the electronic lifetime

The term "electronic lifetime" is ambiguous in the solid state physics. First of all, the electrons within a solid are interacting and therefore one deals with quasiparticles. The electronic lifetime is the average time one electronic quasiparticle stays wihin the same state. As already seen, the excited quasiparticle can undergo different possible scattering events. It can scatter with phonons, other quasiparticles or impurities. These scattering events can happen within the bulk or at the surface. In the same manner as the excited electrons are quasiparticles, the unoccupied states below E_{F} are

[5] Half the time is needed for an electron and a hole where both take half of the energy. The more quasiparticles share the same overall energy, the faster the energy is dumped into the lattice subsystem as long as the empty final states approximation holds (if the (competing) electron thermalization process and the Pauli blocking at the Fermi level are negligible).

hole-quasiparticles. In case of no specific asymmetry around the Fermi level, the excited holes have the same lifetimes as the electrons. Their energy is measured with respect to the Fermi energy $E_{\text{hole}} = |E_{\text{state}} - E_{\text{F}}|$.

The electronic lifetime differs from its relaxation time. The relaxation time is the characteristic time in which the quasiparticle has lost its energy (energy relaxation time) or initial momentum direction (momentum relaxation time). The lifetime just refers to the fact that the electron changed its state or the former empty state gets occupied. Every scattering event changes the state of the involved quasiparticles from the initial state into the final state. This definition corresponds to equation (12) if the lifetime is predominantly related to electron-electron scattering events.

The probability of electron-electron scattering increases with the energy of the quasiparticle. This is because of the monotonic increase in the number of possible empty final states. Fermi liquid theory predicts the electronic lifetime to follow [GV05; PN66]

$$\tau_{\boldsymbol{k},\sigma} \simeq \frac{8\,\hbar\,E_{\text{F}}}{\pi\,\xi_3(r_{\text{s}})} \cdot \frac{1 + \exp\left(-(E_{\boldsymbol{k},\sigma} - E_{\text{F}})/(\mathrm{k_B}\,T)\right)}{(E_{\boldsymbol{k},\sigma} - E_{\text{F}})^2 + (\pi\,\mathrm{k_B}\,T)^2}\,, \tag{13}$$

where E_{F} is the Fermi energy, σ is the spin direction, $\boldsymbol{k}$ is the wave vector, $E_{\boldsymbol{k},\sigma}$ the energy of the electron, ξ_3 is the geometrical factor in three dimensions

$$\xi_3(r_{\text{s}}) = \sqrt{\frac{\alpha_3\,r_{\text{s}}}{4\,\pi}}\,\arctan\left(\frac{\pi}{\alpha_3\,r_{\text{s}}}\right) + \frac{1}{2\,(1 + \pi/(\alpha_3\,r_{\text{s}}))} \tag{14}$$

with the Wigner-Seitz radius r_{s} in units of the Bohr radius and $\alpha_3 = \sqrt[3]{4/\,(9\,\pi)}$. For all that the electron-electron interaction processes are only considered.

The lifetime is defined such, that it corresponds to the differential equation:

$$\frac{\partial N_{\boldsymbol{k},\sigma}}{\partial t} = -\frac{N_{\boldsymbol{k},\sigma}}{\tau_{\boldsymbol{k},\sigma}}\,. \tag{15}$$

Figure 6 shows simulations of the electronic lifetimes according to the equation (13) at different electron energies and temperatures. The simulations are based on the parameters for Cu. In Cu the lifetimes are considered as isotropic (depend only on $|\boldsymbol{k}|$) and spin independent. The electronic lifetime is energy dependent because of the different density of accessible empty final states (and the density of possible scattering partners below the Fermi level which gain enough energy to scatter into an empty final state above the Fermi level). The change in temperature causes a change in the number of possible scattering partners for quasiparticles close to the Fermi level. Far from the Fermi level the electronic lifetime is not affected by temperature changes.

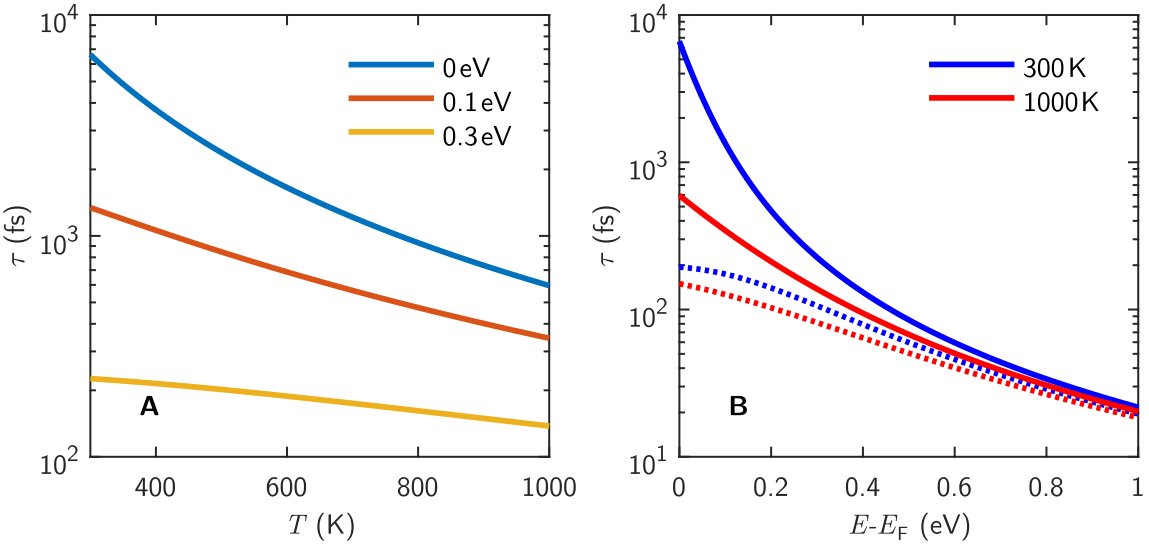

Figure 6: **Fermi liquid theory. Energy and temperature dependence of the electronic lifetime.** The simulation is based on the electronic lifetime (equation (13)) with the parameters for Cu [AM11]. **A** Temperature dependence of the electronic lifetime at different electron energies relative to the Fermi level. Electron-electron scattering processes are considered only. **B** Electronic lifetimes at two different temperatures with (dotted line) and without (solid line) adding a constant electron-phonon relaxation term ($\tau_{\text{e-p}} = 200\,\text{fs}$). The value of $\tau_{\text{e-p}}$ was chosen to describe the two photon photoemission result of Cao et al. [Cao+97] which is reproduced in Figure 7**C** (significant deviations from Fermi liquid theory appear below 0.4 eV and there are only two data points below 0.4 eV; $\tau_{\text{e-p}}$ is determined with a large error bar).

Other scattering mechanisms are included by adding the corresponding scattering rates. The electron-phonon scattering rate, the electron-impurity scattering rate and the electronic scattering rate (the inverse of the Fermi liquid lifetime, equation (13)) add up (Matthiessen's rule[6]). The lifetime of a quasiparticles is

$$\tau = \frac{1}{1/\tau_{\text{e-e}} + 1/\tau_{\text{e-p}} + 1/\tau_{\text{e-i}}}\,. \tag{16}$$

Usually the electron-impurity scattering rate is dominant at low temperatures and low electron energies. The lifetime related to the electron-phonon coupling $\tau_{\text{e-p}}$ may decrease linearly with temperature above the Debye temperature (the linear dependence on the temperature is characteristic for metals, see [All+86; AM11]). The energy dependence is considered to be weak for energies higher than the energy of the upmost phonons (which is the Debye energy $\hbar\omega_{\text{D}}$ or the most energetic optical phonon mode). In Figure 6**B** a constant lifetime ($\tau_{\text{e-p}} = 200\,\text{fs}$) is added to the electron-electron scattering

[6] The Matthiessen rule holds if there are no interdependencies between the scattering mechanisms, see for example Cao et al. [Cao+98] or text books [AM11].

to account for the electron-phonon contribution to the electronic lifetime. At low electron energies the electronic lifetime is reduced by the electron-phonon interaction (compare dotted and solid lines). This happens because of the suppression of the electron-electron scattering at the Fermi level (also known as Pauli blocking). The temperature dependence of $\tau_{\text{e-p}}$ is not considered in the simulation in Figure 6**B**.

It is useful to determine the prefactor of equation (13), i.e. [GV05; QF58]

$$\tau_0 = \frac{8\,\hbar}{\pi\,\xi_3(r_\text{s})\,E_\text{F}} \approx \frac{128}{\sqrt{3}\,\pi^2\,\omega_\text{p}}\,, \tag{17}$$

where ω_p is the plasma frequency of the conduction electrons. The relation to the plasma frequency is often used in publications, for example by Carpene [Car06]. The approximations made to derive this expression differ from those found in Giuliani [GV05]. In Cu the value of the prefactor is $\tau_0 = 0.4456\,\text{fs}$.

2.6 The two photon photoemission experiments

The electronic lifetime is experimentally determined by two photon photoemission experiments (see Figure 7). The two photon photoemission experiments are pump-probe experiments performed at low excitation densities. A first short laser pulse (pump) excites a small amount of electrons in the solid to an intermediate state. The energy of the photons are lower than the work function to prevent the direct photoemission (the pulse intensities are low and high-harmonic effects are negligible). A second time-delayed laser pulse (probe) further excite the electrons from the intermediate states into vacuum levels to disengage them from the solid. The number of emitted electrons and their kinetic energy are measured. The overall energy of the pump and probe photons has to be higher than the work function

$$\text{h}\nu_\text{pump} + \text{h}\nu_\text{probe} > E_\text{work}\,. \tag{18}$$

Only a few electrons within the first surface layers are probed by this technique and the surface has to be very clean and smooth. The polarization of the second pulse is perpendicular to the polarization of the first pulse to suppress coherent artefacts and wave mixing processes. The energy of the intermediate state is determined from the measured kinetic energy of the emitted electrons [PO97]. The number of detected electrons decreases as a function of time delay between the pump and the probe. The characteristic relaxation time is thus connected to the electronic lifetime of the intermediate state. At very low excitation densities, for which the contribution of secondary electrons

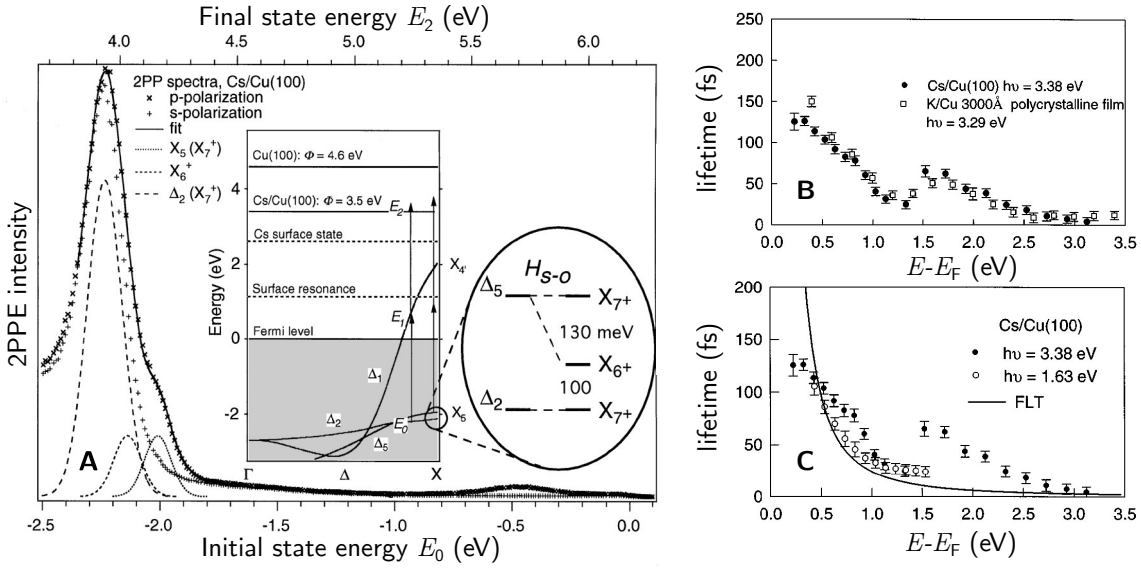

Figure 7: **Two photon photoemission in copper.** **A** presents the two photon photoemission intensities measured on cesiated copper (100) surface by Petek et al. [PO97]. The resonance attributed to the initial states located in the upmost d-band is modeled with three gaussians. Two of them are only present by excitation with p-polarized light (here the incident angle is 30°). The bubble shows the spin-orbit splitting at the X-point. **B** & **C** The electronic lifetime in copper as a function of energy measured with the two photon photoemission by Cao et al. [Cao+97]. **B** shows that the electronic lifetime is independent of the material of the cover layer which was used to lower the work function. **C** compares the lifetimes which are measured at two different photon energies. The local maximum at 1.5 eV is known as the d-band catastrophe [PO97]. **A** is taken from [PNO99], **B** and **C** are taken from [Cao+97].

is insignificant, the relaxation time of the photoelectron intensity represents the electronic lifetime. Secondary electrons are electrons changing their energy from the intermediate state after excitation, into an intermediate state at a different energy. At high excitation densities the picture of single excited electrons thus fails and the relaxation of the entire electronic distribution has to be considered in order to interpret the measured relaxation time correctly. The effect of secondary electron generation "prolongs" the relaxation process. Another effect which can cause errors is the ballistic motion of excited electrons from the surface region into the bulk (if present the measured lifetime is reduced [BFI87][7]). Other limitations of the technique are its energy and momentum resolution. The experiment cannot distinguish between states of almost same energy and similar momentum. Scattering events which change the state of the quasiparticle in energy or momentum by a smaller amount than what can be detected, do not contribute to the measured relaxation time.

[7] Cao et al. [Cao+98] argued that the loss of electrons out of the probed volume by the ballistic transport is low at low excitation densities, so the contribution of this effect to the measured relaxation time is rather small.

The lifetimes as a function over the intermediate state energy were measured in different Cu samples on the (100)-surface. The results taken from Cao et al. [Cao+97] are presented in Figure 7**B** and **C**. The Cu surface was covered with cesium or potassium atoms to reduce the work function. Pump and probe pulses have the same photon energies but different polarization. It is known from Cu band structure calculations, that the photon energies of 1.63 eV are not sufficient to excite electrons from the d-band states of copper. With higher photon energies ($\mathrm{h}\nu > 1.9\,\mathrm{eV}$) electrons from the d-bands are excited (compare inset on Figure 7**A**). The relaxation of the photoemission intensity shows an unexpected local maximum at 1.5 eV (see Figure 7**B**). This local maximum was connected to the surprisingly long (non-Fermi-liquid) lifetime of the d-band holes (see Section 4.3.1). The link to the upmost d-band states is clear, the energy of those states is at about 1.9 eV below the Fermi level and the photon energy is 3.38 eV, the maximum has to appear at 1.5 eV. Similar measurements using different photon energies confirm this correlation [KHW98]. From this point of view it is obvious, that the relaxation of the photoemission intensity is not related to the lifetime of the intermediate state only. There is a contribution of secondary electrons which is related to Auger processes or electron-electron scattering processes with nonhomogeneously excited intermediate states (discussions and details about the Auger decay are found in [KHW98; Pet+00; Kno+00; KBB01], the nonhomogeneous effect is explained in the following). The d-band density of states is more than one order of magnitude larger than the density of states of the conduction band. The onset of the upmost d-band at 1.9 eV below the Fermi level is very steep (see later on in Figure 21**A**). The populations of the intermediate states which are pumped by electrons from the conduction band only is far lower than the populations of states pumped with electrons from the d-band (by a factor of more than 10). The separation between the different populated intermediate states is small because of the steep d-band edge. The relaxation process is such, that most of the electrons lose their energy over time, but there is always a possibility that some of the electrons temporarily gain a little amount of energy. This results in a smearing of the steep edge between highly populated and the weakly populated intermediate states and causes an increase in the photoemission relaxation time on the site of the weakly populated states. This effect is a result of the secondary electrons and cannot be avoided with a lowering of the excitation density because the relative differences between the populations in the intermediate states remain the same.

Beside this "d-band catastrophe", the lifetimes of the electrons in lower energy states are also remarkable. According to the electron transport measurements, the electronic lifetime in Cu at room

temperature is much shorter than the lifetime which is determined at 0.5 eV and below. Yet, the resistivity is mostly related to electron-phonon scattering and umklapp processes. In order to understand the different results, one has to take a closer look into the technique. Although the electrons change the states many times by electron-phonon scattering, the two photon photoemission may not be sensitive to such events. Electron-phonon interactions mainly change the momentum of the quasiparticles but the change in energy is limited to the energy of the involved phonons (≤ 20 meV in Cu). The change in momentum may change the matrix element for the emission process (this effect can either speed up or slow down the relaxation of the photoemission intensity), but how much the measured electronic lifetime is affected by electron-phonon interaction mainly depends on the energy resolution of the experiment. At typical energy resolutions in the range of 15-200 meV [Sch+94; WF97; KHW98] and with a Debye energy of about 30 meV, each electron may need to scatter at least 1 time with the highest energy resolution and up to more than than 7 times with the lowest energy resolution at acoustical phonons for this to affect the observed population relaxation time. On the other hand, a single electron-electron scattering event is enough to change the energy of the quasiparticle by an amount that it counts to the depopulation of the state. Such events usually overcome the energy resolution of the experiment. In common experiments with low momentum resolution and no secondary electron contribution, the measured electronic lifetime follows the assumption of the Fermi liquid theory (equation (13)). The characteristic energy dependence of the electronic lifetime has been measured in Cu and it is plotted in the Figure 7**C** (open circles). At low electron energies the lifetime saturates because of the scattering of the excited electrons with high energetic acoustical phonons.

2.7 The quasiparticle multiplication rate

The interaction between the electron gas and the external field generates excited quasiparticles which are out of equilibrium. If the number of excited quasiparticles is not too large, then the interaction between the excited quasiparticles is negligible compared to the scattering at the thermally excited quasiparticles located around the Fermi level. The Fermi liquid theory expression of the electronic lifetime (equation (13)) is still valid in this situation. The assumption is that most of the quasiparticles are in thermal equilibrium around the Fermi level and there is only a small amount of quasiparticles which are out of equilibrium at higher energy levels (situations where the density of the excited electrons is in the range of $\ll 1\,\%$). The excited quasiparticles with high energy

($|E - E_\mathrm{F}| \gg 2 \cdot (\mathrm{k_B}\, T_\mathrm{th})$) contribute to the generation of new excited quasiparticles in almost every scattering event. Each such scattering event generates two newly excited quasiparticle, an electron and a hole. Here, the electronic subsystem is split into a part consisting of the non-thermally photo-excited quasiparticles and the remaining thermal quasiparticles. The situation is sketched in Figure 8**A**. Statistically, the quasiparticle multiplication or cascade processes are described by averaging

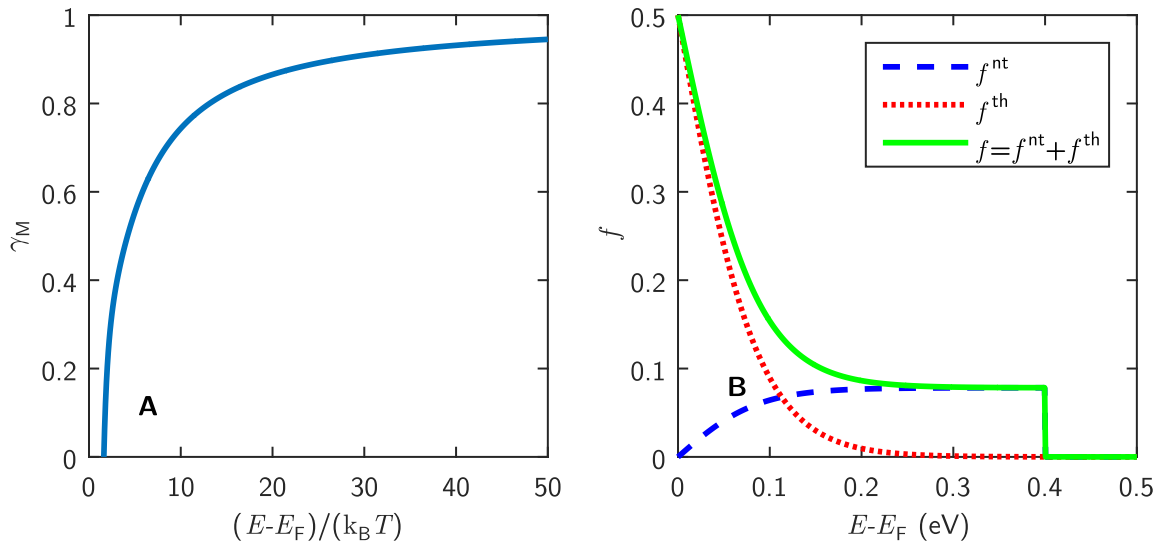

Figure 8: **Splitting of the electronic distribution function in thermal and non-thermal parts and the probability factor γ_M. A** Shortly after photo-excitation, the electronic distribution function, f, can be (mathematically) split into thermal and non-thermal parts, f^th and f^nt. **B** The probability to create new electron-hole pairs is described by the factor γ_M, which is determined by performing the integrals in equation (19). This calculation additionally includes a few approximations to end up with an analytic expression.

over the quasiparticle lifetime multiplied with the probability to create an electron-hole pair. A small number of (non-thermally) excited quasiparticles give rise to new excitations of formerly thermal

quasiparticles with the quasiparticle multiplication rate of

$$\begin{aligned}\frac{\partial N_{\mathsf{qp}}}{\partial t} \;\approx\; & 2\cdot 2\cdot \int_{\mathrm{k_B}\,T}^{\infty} \mathrm{d}E\, D(E)\, \frac{f^{\mathsf{nt}}(E)\,(1-f^{\mathsf{nt}}(E))}{\tau^{\mathsf{FLT}}\,(E-E_{\mathsf{F}})} \cdot \frac{\int_{E_{\mathsf{F}}-E}^{E-E_{\mathsf{F}}} \mathrm{d}E' \int_{-\infty}^{\infty} \mathrm{d}E_x \left(1-f^{\mathsf{th}}(E-E_x)\right)}{\int_{E_{\mathsf{F}}-E}^{E-E_{\mathsf{F}}} \mathrm{d}E' \int_{-\infty}^{\infty} \mathrm{d}E_x \,(1-f^{\mathsf{th}}(E-E_x))} \\ & \frac{\cdot f^{\mathsf{th}}(E')\,\left(1-f^{\mathsf{th}}(E'+E_x)\right)\Big[\Theta(-(E'-E_{\mathsf{F}}))\,\Theta(E'+E_x-E_{\mathsf{F}})\,\Theta(E-E_x-E_{\mathsf{F}})}{\cdot f^{\mathsf{th}}(E')\,(1-f^{\mathsf{th}}(E'+E_x))} \\ & \frac{-\Theta(E'-E_{\mathsf{F}})\,\Theta(-(E'+E_x-E_{\mathsf{F}}))\,\Theta(-(E-E_x-E_{\mathsf{F}}))\Big]}{} \\ = \;& 4\cdot \int_{\mathrm{k_B}\,T}^{\infty} \mathrm{d}E\, D(E)\, \frac{f^{\mathsf{nt}}(E)\,(1-f^{\mathsf{nt}}(E))}{\tau^{\mathsf{FLT}}\,(E-E_{\mathsf{F}})} \cdot \gamma_{\mathsf{M}}\left(\frac{E-E_{\mathsf{F}}}{\mathrm{k_B}\,T}\right)\end{aligned} \tag{19}$$

(in this approximation the momentum conservation is not considered). The nominator in equation (19) counts the scattering events of high energetic electrons (see Figure 9**C**) which generate electron-hole pairs, subtracting all scattering events doing the opposite (see Figure 9**D**). The denominator

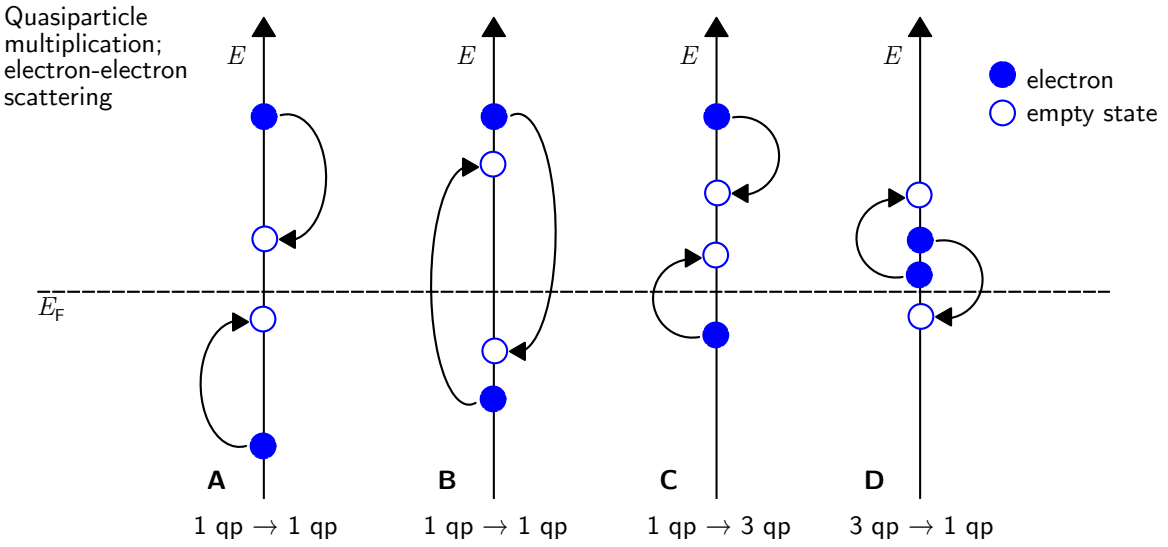

Figure 9: **Characterization of the electron-electron scattering events.** **A**-**D** are sketches to characterize the quasiparticle multiplication (or cascade) process. In **A** and **B** the number of excited quasiparticle remains the same. **C** A high energy electron creates an additional electron-hole pair and after scattering the energy of the scattered electron is partly transferred to the electron-hole pair. **D** A statistically unlikely case would be, that an excited electron gains energy via recombination of an electron-hole pair. In this case the number of excited quasiparticle would be reduced after scattering.

counts the total number of scattering events (sketched in Figure 9**A**-**D**). First prefactor of 2 is due to the same dynamics for high energetic holes. The second prefactor 2 takes into account that each

scattering event generates 2 excited quasiparticles. The probability to create a new electron-hole pair, γ_{M}, as a function of the scaled energy, $(E - E_{\mathsf{F}})/(\mathrm{k_B}\, T)$, is presented in Figure 8**B**. Here a few approximations are made in order to get an analytic expression for γ_{M}.

Quasiparticles with high energies ($|E - E_{\mathsf{F}}| \gg 2 \cdot (\mathrm{k_B}\, T_{\mathsf{th}})$) are likely to excite an additional electron-hole pair at every scattering event. In a situation with only high energy quasiparticles on the one hand and thermal quasiparticles on the other hand, the quasiparticle multiplication rate simplifies to

$$\frac{\partial N_{\mathsf{qp}}}{\partial t} \approx \frac{2}{\langle \tau \rangle}\, N_{\mathsf{qp}} \approx 2\, N_{\mathsf{qp}}\, \frac{\left\langle (E - E_{\mathsf{F}})^2 \right\rangle + (\pi\, \mathrm{k_B}\, T_{\mathsf{th}})^2}{\tau_0\, E_{\mathsf{F}}^2}\,. \tag{20}$$

The quasiparticle multiplication rate together with the description of their energy loss due to the spontaneous phonon emission (Section 2.3) provide the opportunity to describe the initial quasiparticle relaxation process prior to the quasiparticle thermalization. This opportunity will be used in Section 6.2 to investigate the nature of the fast lattice heat up in Cu, which is seen in the experiment, at short time delays.

3 Multi-temperature models - Characterization of the thermalization process

The Boltzmann equations describe the electron relaxation process. These equations are used to perform many particle simulations. This chapter introduces approximations to simplify the many particle problem which are sensitive to the excitation density. To begin with, in Section 3.1 the high excitation density limit is treated, where the two temperature model is assumed to be valid. In Section 3.3 is shown that the two temperature model is not applicable for Au at lower excitation densities. Extensions to the two temperature model which are able to take the non-thermal electronic distribution functions into consideration are presented in Section 3.4. These extensions split the electronic subsystem into two parts. Both parts, the thermalized quasiparticles and the non-thermal quasiparticles, are handled separately to focus directly on the different dynamics. The models which are discussed, are the model of Sun et al. (Section 3.4), Carpene (Section 3.4.1) and Lisowski et al. (Section 3.4.2). Finally, in the very low perturbation limit, the model of Baranov and Kabanov [BK14] is used to describe the thermalization in metals (see Section 3.5).

3.1 The Two-Temperature-Model (TTM)

The TTM, which was introduced in the beginning of Chapter 3, predicts the relaxation dynamics between a thermal electronic subsystem (at T_{el}) and a coupled (thermal) lattice subsystem at a different temperature T_{la} [KLT57; AKP74; All87]. The model is based on the energy conservation law and it is described by two coupled differential equations

$$\frac{\partial U_{\mathsf{el}}}{\partial t} = c_{\mathsf{el}} \frac{\partial T_{\mathsf{el}}}{\partial t} = g \cdot (T_{\mathsf{la}} - T_{\mathsf{el}}) \ , \tag{21}$$

$$\frac{\partial U_{\mathsf{la}}}{\partial t} = c_{\mathsf{la}} \frac{\partial T_{\mathsf{la}}}{\partial t} = -g \cdot (T_{\mathsf{la}} - T_{\mathsf{el}}) \ . \tag{22}$$

c_{el} and c_{la} are the electronic and lattice heat capacities. The factor g is a constant above the Debye temperature ($T_{\mathsf{el}}, T_{\mathsf{la}} \gg \Theta_{\mathsf{D}}$), given by [All87]

$$g = \pi \hbar \, D(E_{\mathsf{F}}) \, \lambda \left\langle \omega^2 \right\rangle \, \mathrm{k_B} \, .$$

The temperature dependence of g below Θ_D are found in the publications of Kaganov et al. [KLT57] and Allen [All87][8].

T_{el} and T_{la} as a function of time are plotted in Figure 10**A** in an example scenario (considering Cu). A lattice heat capacity is used which is about two orders of magnitude higher than the electronic heat capacity ($c_{el} \ll c_{la}$). The final state is described by a higher temperature, where the lattice

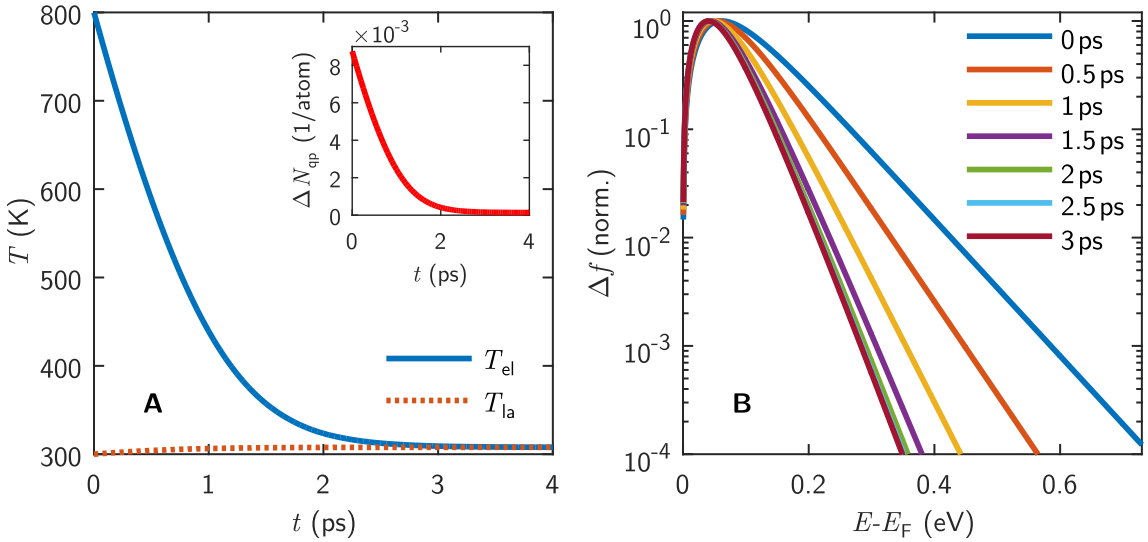

Figure 10: **The Two-Temperature-Model. A** The TTM predicts the time evolution of the electron and the lattice temperatures where the electrons are considered to be thermalized. The energy of the electronic subsystem is transferred to the lattice by the electron-phonon interaction. The inset shows the relaxation of the number of excited quasiparticles, where the reference is the number of quasiparticles at 300 K which is $5.3 \cdot 10^{-3}$ 1/atom. In **B** the change in the electronic distribution function (the reference is at 300 K) is plotted as a function of time. The high energy states depopulate over time due to the decreasing thermal energy in the electronic subsystem. The result shows that the exponent in the exponential tail of Δf changes over time and the position of the maximum shifts slightly to lower energies.

heats up by a few Kelvin. Initially, a temperature difference of several hundreds of Kelvin between both subsystems was induced by photo-excitation. The electronic distribution function is plotted as a function of energy at different time delays in Figure 10**B**. Besides the decreasing amplitude of Δf, Δf also shows a narrowing over time. Below E_F the holes show the same dynamics (not shown in the figure).

The electron-phonon scattering alone does not keep the electronic distribution function thermal. In order for the TTM to work, a very fast electron thermalization process is required. In Cu at

[8] Allen examines the deviation at low temperatures in a taylor expansion.

$T_{\mathrm{el}} = 1000\,\mathrm{K}$ and $T_{\mathrm{la}} = 300\,\mathrm{K}$ average electron-electron scattering times within $2\,k_B T_{\mathrm{el}}$ around E_F of less than 200 fs are required (see Section 8.1.2, value (131)). Prolonged lifetimes slow up the electron-phonon thermalization and increase the electron-phonon thermalization time. The quasiparticles around the Fermi level have lifetimes on the required order of magnitude (see Section 2.5). Therefore it is possible, that the rethermalization of the quasiparticles is fast enough to support the TTM-like relaxation characteristics.

In metals without optical phonon branches, the influence of a non-thermalized lattice to the dynamics of the electrons and holes may be low. In this case the lattice temperature reproduces the average lattice temperature of all phonon branches (see Waldecker et al. [Wal+16] for more detailed description) or the temperature of the best thermal fit to the non-thermal distributions.

The TTM is often extended to multi temperature models, if additional subsystems are considered, for example a spin subsystem or a subdivision of the phonon subsystem into the different phonon branches [Wal+16]. Every additional subsystem extends the system of coupled differential equations by one further equation.

3.1.1 The TTM in highly excited Gd(0001)

The TTM describes the thermalization process between the thermal electronic subsystem and a thermal lattice subsystem which are at different temperatures. Optical excitations create a non-thermal electronic subsystem, as pointed out in Figure 4. If the electron thermalization time is short compared to the electron-phonon thermalization time, the electrons do not transfer energy to the lattice up to the time at which the electrons are in thermal equilibrium. In this case the equation (1) is valid and it allows to calculate the maximum electronic temperature which is reached shortly after the excitation. In gadolinium (Gd) the electrons thermalize in less than 100 fs (at 1000 K) and the lattice heating takes more than 600 fs. The fast electron thermalization may has something to do with the high density of states at the Fermi level (factor 6 higher than in Cu), since s-, p-, d- and f-states contribute to the density of states at E_F [TS90]. Bovensiepen et al. & Lisowski et al. measured the electronic distribution function of Gd with time-resolved photoemission [Bov07; Lis05]. They excited the electrons with ultrashort light pulses at 1.5 eV. The probe pulses at 4.2 eV further excite the electrons into the vacuum where they are detected. The results are presented in Figure 11 and Figure 12. The photoelectron intensity is assumed to be proportional to the electronic distribution function f. The TTM seems to describe the relaxation dynamics of f after 100 fs with

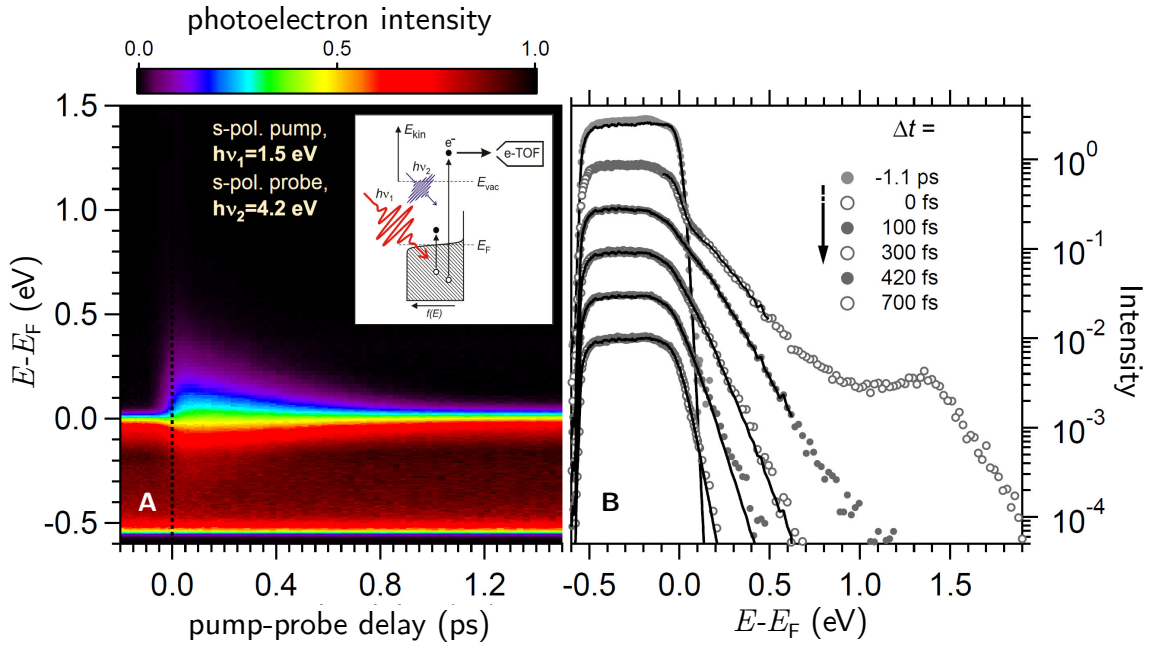

Figure 11: **Electron photoemission from the gadolinium surface. A** and **B** are showing photoemission spectra measured on a thin Gd(0001) film (thickness of 10 nm) with an absorbed fluence of $F_{\text{abs}} = 0.25\,\text{mJ/cm}^2$ by Bovensiepen & Lisowski [Bov07; Lis05]. Approximately 0.5 % of the conduction band electrons in the range between 1.5 eV below the Fermi level and E_{F} are excited. After 100 fs the electrons seem to be in thermal equilibrium. Note that the curves in **B** are plotted with offset. The graphs are taken from Bovensiepen [Bov07].

an electron-phonon coupling constant of ([Lis05; TS90])

$$\lambda \left\langle \omega^2 \right\rangle = 67\,\text{meV}^2\,. \tag{23}$$

The experimentally determined electronic temperature is about 50 % lower than the theoretically predicted maximum temperature of 1500 K, calculated with the equation (1) and based on the absorbed fluence of $0.25\,\text{mJ/cm}^2$ and the film thickness of 10 nm [Bov07; Hil+87]. However, in this experiment the hot electrons were able to enter the (metallic) tungsten substrate, the related energy transfer to the substrate was not considered in the calculation of the electronic temperature.

3.2 Electron- and electron-phonon-thermalization

The photo-excited out-of-equilibrium electronic distribution in a metal is unstable. Electron-electron scattering aims to thermalize the electronic subsystem and the electron-phonon interaction equilibrates the electronic subsystem with the phonons. The thermalization times are defined to be characteristic to the electronic subsystem thermalization process (electron-electron thermalization

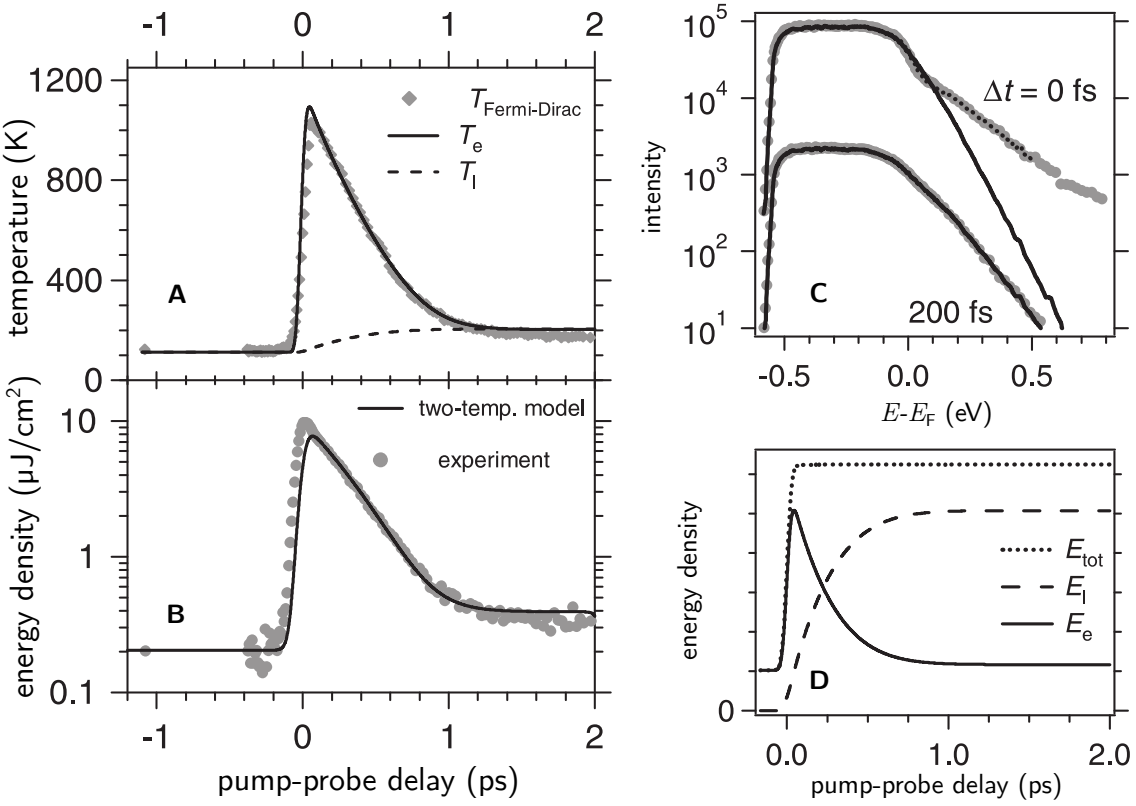

Figure 12: **Application of the TTM to Gd. A** The temperature of the electronic subsystem as function of time fitted with TTM on the basis of photoemission data presented in Figure 11. The temperatures are taken from Fermi-Dirac fits to the experimental Δf. **B** The energy in the electronic subsystem (here the non-thermal part of Δf is considered as well). **C** The electrons are non-thermally distributed at 0 fs. After 200 fs the electrons are in thermal equilibrium. **D** Sketch of the time evolution of the energy density. The y-axis is in arbitrary units. All graphs are taken from Bovensiepen [Bov07].

time $\tau_{e\text{-}e}$) or to the process of the electronic temperature relaxation (electron-phonon thermalization time $\tau_{e\text{-}ph}$). Contrary to the definitions of the lifetime and the scattering time (see Section 2.5), the thermalization time is not an average over all particles. In general, the thermalization time is the time delay after excitation, when a thermal distribution (e.g. electrons rearrange to Fermi-Dirac distribution functions) is reestablished within the excited volume of the sample or any well defined subsystem (electrons/ phonons/ spins). Thermalization times depend on material, temperature, the type of excitation and the excitation density (see Figure 13**B** and **C**, showing that the electron thermalization time in Au depends on the excitation density).

In a simple metal the electronic subsystem and the phonon subsystem are weakly coupled.[9] This

[9]These subsystems may be further separated into subsystems of different phonon branches, different spins, valleys or bands; this section deals with the most degenerate case only.

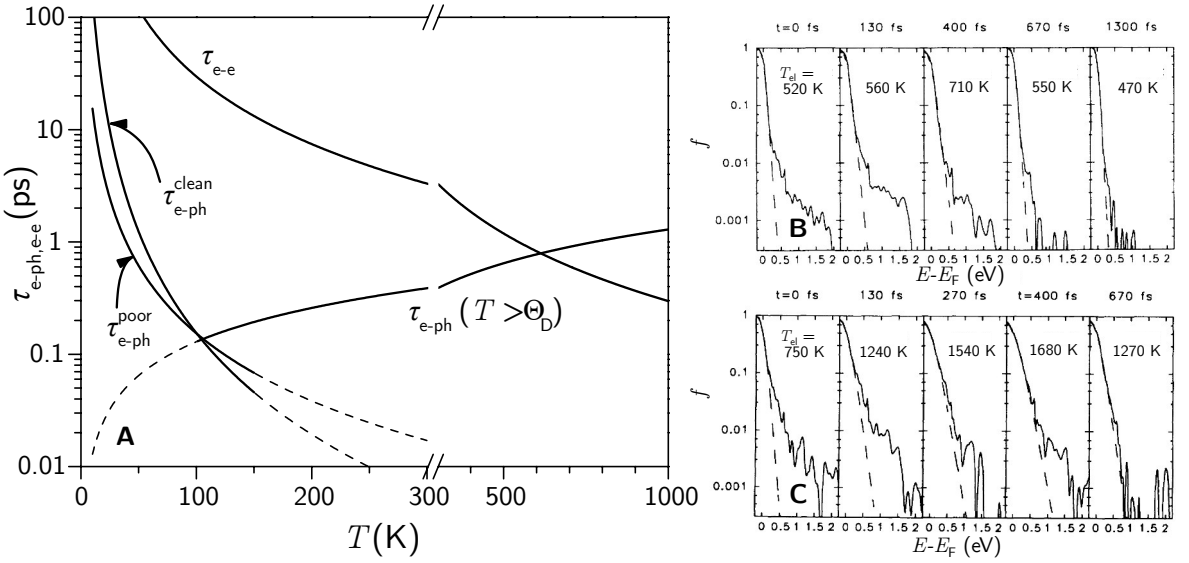

Figure 13: **Thermalization times in metals. A** Theoretical estimates of the quasiparticle thermalization times within the electronic subsystem $\tau_{\text{e-e}}$ at very low excitation densities ($T_{\text{el}} - T_{\text{la}} \ll T_{\text{la}}$) and estimates of the time $\tau_{\text{e-ph}}$ after which the electron- and the phonon-subsystems are in thermal equilibrium at the same temperature (see also [DD11]). The same parameters as for Cu are applied. **B** and **C** show the electronic distribution function in Au measured by Fann et al. [Fan+92] with time-resolved photoemission. The excitation densities were with 40 J/cm^3 in **B** and 100 J/cm^3 in **C** quite high. The electrons need more than 1.3 ps to thermalize at the lower excitation density and approximately 670 fs at the higher excitation density.

weak coupling between the electrons and phonons may allow the electronic subsystem to thermalize first (one may approximate the electron thermalization time at very low excitation densities with the electronic lifetime at $E = E_{\text{F}} + \text{k}_{\text{B}}\,T$ known from Fermi liquid theory, see equation (13) for a 3D metal and [GV05; DD11]). The approximate electron thermalization time $\tau_{\text{e-e}}$ in Cu is presented in Figure 13**A**.

After the electrons are in thermal equilibrium, the excited quasiparticles lose their energy which is transferred to the lattice and the excited electrons and holes at the Fermi level start to recombine. The corresponding time is the electron-phonon thermalization time. At low temperatures the electron-phonon thermalization time depends on the impurity concentrations in the metallic sample. The limits are referred to as "clean" or "poor" metals (see Figure 13**A**). If a metal is clean, the momentum conservation has to be considered during the electron-phonon scattering event. In a poor metal, the electron-phonon scattering process can be slower compared to the electron (momentum) lifetime ($1/\omega_{\text{D}} \gg \tau$). The second electron, which is involved, can take or provide the additional momentum to achieve momentum conservation. One can turn a clean metal into a poor metal by adding

impurities or by generation of vacancies. The disorder enhances the electron-electron scattering rate more than the electron-phonon scattering rate (see [BKB98]). In poor metal the phonon trapping is also enhanced (see [KA08; BW95]). Thus, the electron-phonon thermalization time may depend on the sample's impurity concentration, disorder and dimensionality. The thermalization times are estimated to follow (see [DD11])

$$\begin{aligned} \tau_{\text{e-ph}}^{\text{poor}}(T \ll \Theta_{\text{D}}) &= \frac{2\,\hbar^2\,\omega_{\text{D}}}{\pi^3\,\lambda\,(\mathrm{k_B}\,T)^2} \\ \tau_{\text{e-ph}}^{\text{clean}}(T \ll \Theta_{\text{D}}) &= \frac{1.76\,\hbar^3\,\omega_{\text{D}}^2}{3\,\pi^3\,\lambda\,(\mathrm{k_B}\,T)^3} \\ \tau_{\text{e-ph}}(T > \Theta_{\text{D}}) &= \frac{2\,\mathrm{k_B}\,T}{\pi\,\hbar\,\lambda\,\langle\omega^2\rangle}\,. \end{aligned} \tag{24}$$

These approximate thermalization times are plotted in Figure 13**A** as a function of the temperature with the parameters of Cu. The result shows that at very low excitation densities and up to about 600 K, the electron-electron thermalization process in Cu takes longer than the thermalization of the electrons with the lattice. For strong electron-phonon coupling the quasiparticles and the lattice may reach the thermal equilibrium distribution the same time. In this case the electron- and electron-phonon-thermalization time are indistinguishable. The coupling provides an additional channel for the thermalization of the slower subsystem and the energy transfer rate between the excited high energy quasiparticles and the "thermal" quasiparticles at the Fermi level can be lower than the energy transfer to the lattice. The coupling between the electrons and phonons may also result in polaronic ground states.

The different ω-dependencies of the Eliashberg functions for clean and poor metals (see Figure 5**C**) are the reason for the different T dependencies of $\tau_{\text{e-ph}}$ at low temperatures $T \ll \Theta_{\text{D}}$. One should note that also λ is different in a metal with a high amount of impurities than in the same material with no impurities (see [Mal+11]) and the electron-phonon coupling to low energy acoustical phonons is enhanced compared to the coupling to high energy acoustical phonons in poor metals (see Section 2.2).

If the metal is split into more than two subsystems, the picture gets even more complicated. The situation of splitting the phonon subsystems into its different branches is investigated e.g. by Waldecker et al. [Wal+16] on aluminum. They simulate the time evolution of the different temperatures of each acoustic phonon branch considering different coupling strengths to each branch. In graphene for example, optical phonons are involved in the thermalization process, the dynamics are measured and analyzed by Malic et al. [Mal+11]. In high-temperature cuprate superconductors (above T_{c}), the

absorbed optical energy is assumed to heat up the subsystem of the bosonic excitations of electronic origin which is strongly coupled to specific phonon modes which heat up as well. These subsystems decay on different timescales and the energy is transferred to the remaining (previously unexcited) phonon modes. The dynamics are described by an extended TTM [Per+07; DC+12; Cil+13].

As already seen on Gd (Section 3.1.1), the time-resolved photoemission is a suitable tool to determine the thermalization times of electrons. The thermalization processes in Au are experimentally measured by Fann et al. [Fan+92] with results shown in Figure 13**B** and **C**.[10] From Figure 13**C** one can conclude, that the electron-phonon thermalization time is longer than the electron thermalization time. This is because the temperature of the electrons after 670 fs is very high. For sure, at this small excitation density, the lattice cannot heat up that much. Therefore the electrons do thermalize first. The electron thermalization time depends on the excitation density (compare Figures 13**B** and **C**). After the electrons are in thermal equilibrium, T_{el} decreases until electrons and phonons finally reach the same temperature on a picosecond timescale. All-optical experiments [DV+12; Sch+87] found the electron-phonon thermalization time to depend on the excitation density, too. Importantly, however, the data of Fann et al. shows that the electrons in Au are still athermal after more than 300 fs. Because of that, the equation (1) fails and thus the TTM may not be valid.

3.2.1 Ultrafast electron diffraction results

To study structural dynamics in solids directly, time-resolved x-ray and ultrafast electron diffraction (UED) are used. In particular, the intensity of the diffraction peaks (Bragg peaks) is sensitive to the lattice temperature, i.e. disorder due to thermal motion. The Bragg peaks appear if the electrons, which are scattered at the lattice planes, interfere constructively (Bragg condition). The higher the lattice temperature, the more the Bragg peaks lose their intensity, which is transferred to the inelastic background instead. This effect allows to study the temperature evolution of the lattice in UED experiments after optical excitation.

Experiments on Cu are presented in Figure 14. The results of Klose et al. [Klo13; Eic+15] give timescales for the lattice heating of 2 ps which is almost double the value measured by Ligges et al. [Lig+09; Lig09]. The reason for this deviation is not clear. Note that the relative intensity decrease of the (111)-peak is more than a factor of 2 larger in Figure 14**A** (Klose et al.) compared to Figure

[10] The photoemission technique is sensitive to changes in the distribution function above the Fermi level. Below the Fermi level the electron density is high, thus the small changes are hard to detect. One expects, however, similar dynamics of the photo-excited holes below the Fermi level (an antisymmetric Δf in respect to the Fermi level).

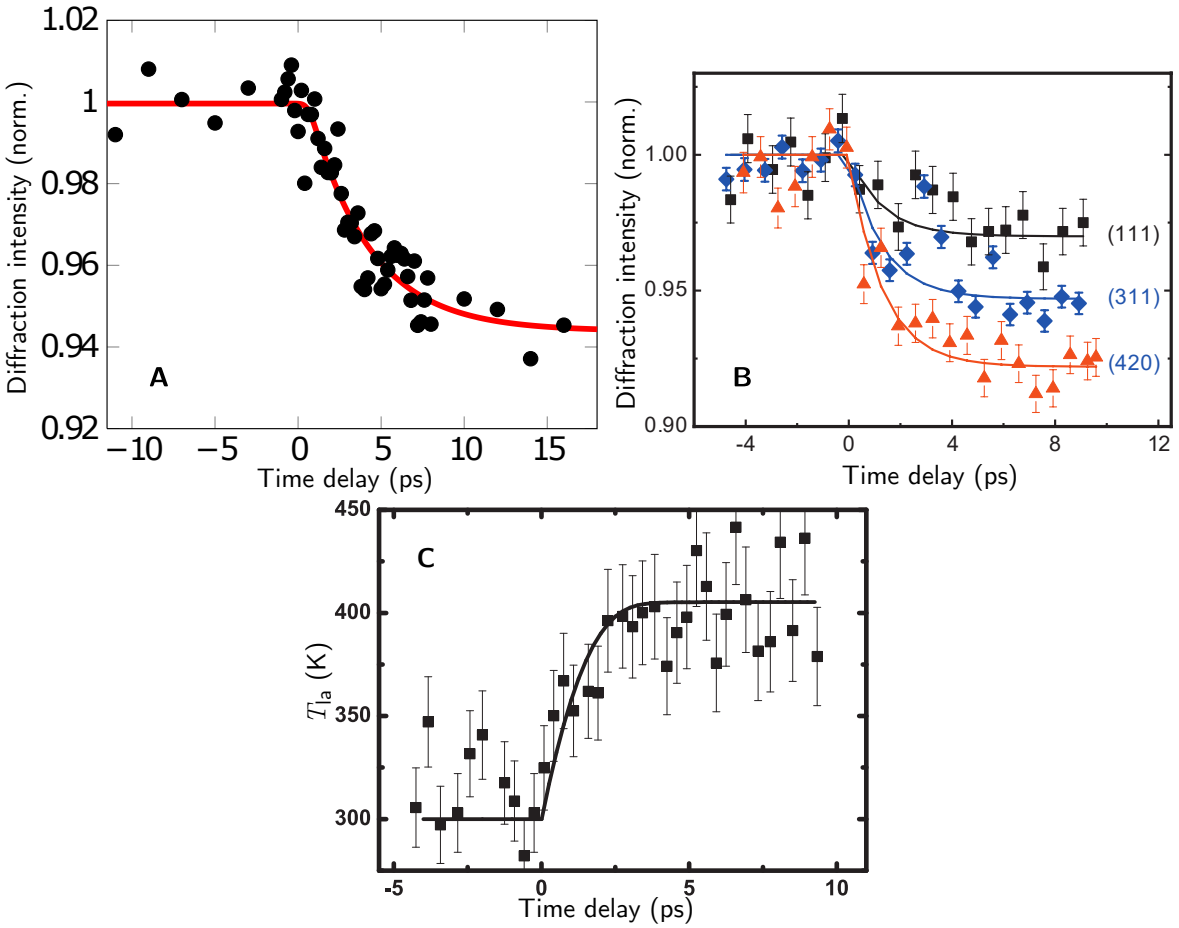

Figure 14: **Ultrafast electron diffraction in Cu.** The experiments are performed by Klose et al. [Klo13; Eic+15] and Ligges et al. [Lig+09; Lig09]. **A** Relative intensity of the Cu-(111) diffraction peak after excitation with a 50 fs optical pulse ($\mathrm{h}\nu = 1.55\,\mathrm{eV}$, $U_{\mathrm{abs}} = 123\,\mathrm{J/cm^3}$). **B** Relative intensity of different diffraction rings measured on polycrystalline Cu films, $U_{\mathrm{abs}} = 350\,\mathrm{J/cm^3}$. **C** Lattice temperature over time calculated from the measured relative intensity in **B** (see [Lig09]). The graphs are taken from [Eic+15] and [Lig+09; Lig09].

14**B** (Ligges et al.), whereas the excitation density used for the result in **A** is determined to be 1/3 of the excitation density used for **B**.

Ligges et al. determined a electron-phonon coupling constant of $\lambda \langle \omega^2 \rangle = 61\,\mathrm{meV}^2$ with the application of the TTM.

3.3 Failure of the TTM in the ultrafast thermalization approximation

Contrary to the situation in Gd, there are many metals (for example Au and Cu) which cannot be satisfactory described within the TTM picture. The electron thermalization is substantially slower in these metals and the ultrafast (instantaneous) electron thermalization approximation is not valid. In

this situation equation (1) fails because of the large amount of energy may already be transferred to the lattice during the electron thermalization process. Results on Au clearly show (see Figure 13**B** and **C**; [DV+12; Sun+94]) such a slow electron thermalization process. However many all-optical experiments consider the ultrafast electron thermalization approximation to hold (see for example [DC+12]) without proving it. At high excitation densities or at high temperatures, the ultrafast electron thermalization approximation is more likely to be applicable because the Pauli blocking is less effective, thereby reducing the electronic lifetimes $\tau_{\mathsf{FLT}} \propto T_{\mathsf{el}}^{-2}$ (see Figure 13**A**).

The higher the excitation density, the higher is the electronic temperature of the new quasi-equilibrium and the more scattering partners are available which reduces the electron thermalization time. In contrast, the electron-phonon relaxation process slows down with increasing excitation density. According to the equations (24) and (1), the thermalization time

$$\tau_{\mathsf{e\text{-}ph}} \propto \sqrt{U_{\mathsf{abs}}} \text{ at } (T_{\mathsf{el}} - T_0) \gg T_0\,, \tag{25}$$

grows sublinearly with U_{abs}.[11]

After the electrons are in thermal equilibrium, the further relaxation and the transfer of the energy from the electrons to the lattice could be described by the TTM (such a description is performed on experimental data of Cu and will be presented in Section 5.8). However, the temperature of the electronic subsystem is in principle unknown since the equation (1) does not hold. Photoemission experiments have access to the electronic temperature based on the measured electronic distribution function, in all-optical experiments it is typically not possible to determine the electronic temperature. Note, however, that time-resolved photoemission experiments are very scarce.

3.4 Extensions of the TTM

The TTM has several extensions to describe non-thermalized electrons. Models made by Sun et al. [Sun+94], Carpene [Car06] and Lisowski et al. [Lis+04] split the electronic subsystems into two subsystems. One subsystem describes the thermal part of the electronic quasiparticles and the second one the non-thermal part. This approach is completely phenomenological. In the beginning, the energy of the absorbed photons is fully transferred to the non-thermal quasiparticle subsystem. The energy of this non-thermal quasiparticles is transferred to the thermal quasiparticles via electron-electron scattering and to the lattice via electron-phonon scattering. The coupling between the

[11] The derivation is based on thermalized electrons, the proportionality can differ from this expression if the electrons are non-thermally distributed.

thermal quasiparticles and the lattice follows the TTM. These simplifications are such that e.g. the model of Sun et al. provide an incomplete description only, because it does not provide any information about the spectral shape of the non-thermal electronic distribution function and its time evolution. The model of Carpene does not include rearrangements of the non-thermal distribution function either, which is unphysical. The heat bath model of Lisowski et al. assumes the non-thermal quasiparticles to rearrange very quickly. They form a Fermi-Dirac distribution with a very high temperature far above the temperature of the thermal quasiparticles. This very quick initial rearrangement seems to be supported by their experiment [Lis+04].

The extension of the TTM by Sun et al. models the time evolution of the energy density in the different subsystems with three coupled differential equations

$$\frac{\partial U_{\mathsf{nt}}}{\partial t} = \frac{\partial U_{\mathsf{abs}}}{\partial t} - \alpha\, U_{\mathsf{nt}} - \beta\, U_{\mathsf{nt}}\,, \tag{26}$$

$$\frac{\partial U_{\mathsf{el}}}{\partial t} = c_{\mathsf{el}} \frac{\partial T_{\mathsf{el}}}{\partial t} = -g \cdot (T_{\mathsf{el}} - T_{\mathsf{la}}) + \alpha\, U_{\mathsf{nt}}\,, \tag{27}$$

$$\frac{\partial U_{\mathsf{la}}}{\partial t} = c_{\mathsf{la}} \frac{\partial T_{\mathsf{la}}}{\partial t} = g \cdot (T_{\mathsf{el}} - T_{\mathsf{la}}) + \beta\, U_{\mathsf{nt}}\,. \tag{28}$$

In the beginning, all of the absorbed energy is in the non-thermal electronic subsystem. This energy is transferred partially to the thermal quasiparticles and partially to the lattice. The shape of the distribution function of the non-thermal electronic subsystem is not specified in this model. The first application of this model was made within the same publication [Sun+94] and is presented in Figure 15. The dynamics of R and T are measured at different photon energies in Au. Although all transients rely on the same d-band to Fermi level resonance, they are all measured and fitted separately (note that both pump and probe are changed between each measurement). The transients are assumed to additively consist of a fast component related to the non-thermal quasiparticles and a slow component related to the thermal subsystem[12]. The Sun-model can describe each of the transients with such a two component fit. β is kept constant at 1/ps and the amplitudes of the two components are used as fit parameters. The change in the electronic distribution function and the contribution of intraband transitions to the measured signal are not considered in the fits. α is found to be 2/ps. The inverse of α is related to the electron thermalization time [Sun+94], giving

$$\tau_{\mathsf{th}} = 500\,\mathsf{fs}.$$

[12]The additivity of both components hold if the Fresnel equations and the sum over all multiple reflections in the sample, which are connecting the dielectric function with R and T, are in good approximation linear (in the considered range).

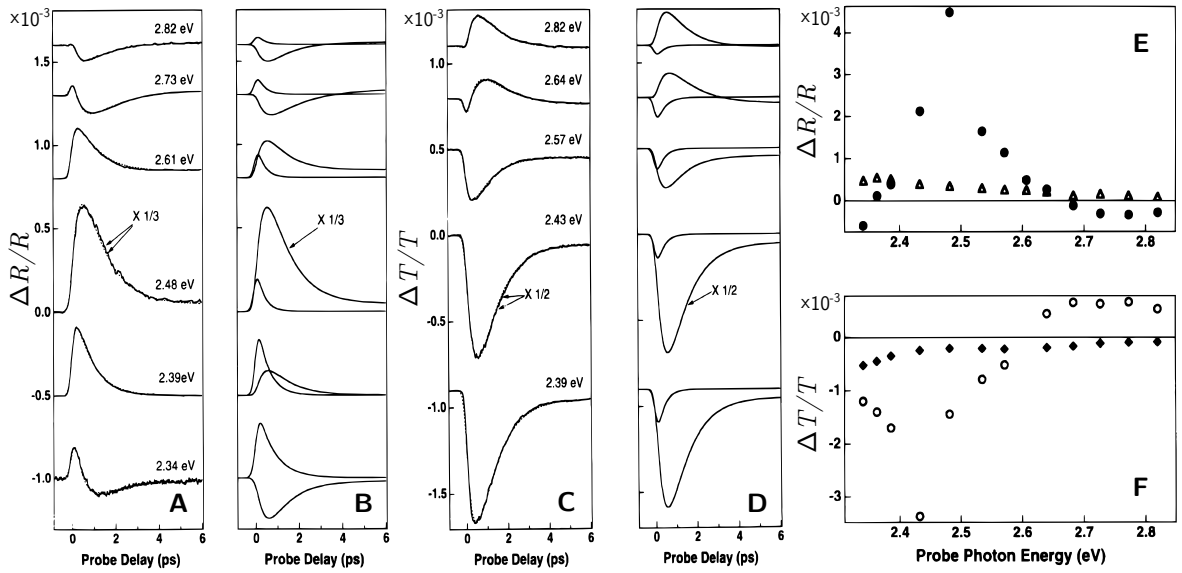

Figure 15: **Extension of the TTM by Sun et al. [Sun+94]. A** & **C** Relative changes in reflectivity and transmission measured on thin Au films with $U_{\text{abs}} \approx 0.75\,\text{J/cm}^3$. The different transients are measured as a function of time at different pump and probe photon energies (the probe photon energies are double the energy of the pump photons). These transients are plotted vertically displaced in steps of $0.5 \cdot 10^{-3}$. The transients are labeled by the probe photon energies. The (barely seen) dotted lines are best fits to the transients. They consist of two components which are shown in **B** and **D**. The component with lower amplitude and faster decay represents the response of the non-thermal quasiparticles, the other one represents the response of the thermal quasiparticles. The fits are individually made on all transients. The amplitudes of each component of the fit at each transient are presented in **E** and **F**. The solid and open circles give the contribution to the signal of the thermal quasiparticles, while triangles and diamonds present the amplitudes of the non-thermal quasiparticle components.

The spectral dependencies of the amplitudes are plotted in Figure 15**E** and **F**. These spectra reproduce the width of the characteristic upmost d-band to Fermi level transitions in Au (see Section 4.3 for further information) at 100 fs (the part of the non-thermal quasiparticles) and 350 fs (thermal quasiparticles). If the non-thermal electronic distribution and the thermal one do not change their spectral shape over time, then it is possible to decompose both components by performing the two component analysis. However, the simulation in Section 6.2 show that the spectrum of the non-thermal quasiparticles is spectrally broad at the beginning and narrows over time. The spectrum of the thermal electrons, however, broadens over time because of the increasing electronic temperature. Higher temperatures broadens the Fermi smearing around the Fermi level resulting in an increase in the spectral width of the d-band to Fermi level transitions. This two component spectral analysis of

Sun et al. is comparable to the result of the singular value decomposition (SVD of the data on Cu[13], presented in Section 5.5.2).

The physical meaning of α and β and their time dependence

The relaxation rate α is related to the electronic lifetime and β to the electron energy loss by spontaneous phonon emission. It is useful to rewrite the energy exchange rate to

$$\frac{\partial U_{\mathsf{nt}}}{\partial t} = N_{\mathsf{nt}} \frac{\partial \langle |E_{\mathsf{nt}} - E_{\mathsf{F}}| \rangle}{\partial t} + \langle |E_{\mathsf{nt}} - E_{\mathsf{F}}| \rangle \frac{\partial N_{\mathsf{nt}}}{\partial t}$$

with E_{nt} being the energy of a non-thermal quasiparticle and N_{nt} being the quasiparticle density of the non-thermal subsystem. The electron-electron relaxation parameter reads

$$\alpha \approx -\frac{\partial \langle |E_{\mathsf{nt}} - E_{\mathsf{F}}| \rangle}{\partial t} / \langle |E_{\mathsf{nt}} - E_{\mathsf{F}}| \rangle + 2 \frac{\left\langle (E_{\mathsf{nt}} - E_{\mathsf{F}})^2 \right\rangle + (\pi \, \mathrm{k_B} \, T_{\mathsf{el}})^2}{\tau_0 \, E_{\mathsf{F}}^2} \,. \tag{29}$$

Here equation (20) is used. The energy exchange with phonons is governed by

$$\beta \lessapprox \frac{\pi \, \hbar \, \lambda \, \langle \omega^2 \rangle}{\langle |E_{\mathsf{nt}} - E_{\mathsf{F}}| \rangle} \,. \tag{30}$$

This is the result of the empty final state approximation (equation (9); see Section 2.3). This approximation does not consider the electron-hole recombination at the Fermi level and is a good approximation if the number of non-thermal quasiparticles is low in the region around the Fermi level ($N_{\mathsf{nt}}(|E - E_{\mathsf{F}}| < \mathrm{k_B} \, T_{\mathsf{la}}) \ll N_{\mathsf{nt}}(|E - E_{\mathsf{F}}| > \mathrm{k_B} \, T_{\mathsf{la}})$).

3.4.1 The model of Carpene

The model of Carpene [Car06] describes the dynamics of the non-thermal electronic distribution function in metals. This model uses material parameters instead of the phenomenological α and β of Sun et al. This makes the dynamics "predictive". The suggested non-thermal electronic distribution function evolves like

$$\Delta f_{\mathsf{nt}}(E, t - t') = \Delta f_{\mathsf{exc}}(E, t') \, \exp\left(-\frac{t - t'}{\tau_0} \left(\frac{E - E_{\mathsf{F}}}{E_{\mathsf{F}}} \right)^2 - \frac{t - t'}{\tau_{\mathsf{p}}} \right) . \tag{31}$$

$\Delta f_{\mathsf{exc}}(E, t')$ is the laser driven "step like" distribution function (see Figure 4 (2)). This initial distribution function varies in time t' following the absorption of a fraction of the pump pulse.

[13] The feature in Cu at 2.1 eV is basically the same kind of resonance (related to the upmost d-band to Fermi level transitions) as the feature in Au at about 2.5 eV.

The first exponential term describes the scattering with thermal electrons and the second term the scattering with phonons. The energy loss based on the first process is added to the subsystem of thermal electrons, while for the second process, it is added to the phonon subsystem. The energy flow is similar to the model of Sun et al. (see Section 3.4).

Della Valle et al. [DV+12] provide the equation to calculate the non-thermal electronic distribution function. The assumed changes of the electronic distribution function in Au are shown in Figure 16**B** after different time delays. The change in the optical properties of Au is related to the change in the electronic distribution function Δf (compare Figure 16**A** (d)-(f) with **B**). The responses of the thermal and non-thermal quasiparticles add up to give the measured $\Delta T/T$ (see Figure 16**A** (a)-(c)). The simulation is based on the model of Rosei [Ros74] to describe the upmost d-band to Fermi level transitions in Ag.[14] The agreement between theory and experiment is quantitative. Heating effects of the lattice are not assumed to contribute to the measured response. In contrast to the original model of Carpene, the simulations on Au by Della Valle et al. [DV+12] are based on the experimentally estimated prefactor for the electronic lifetime $\tau_0 = 7\,\mathrm{fs}$ (Fann et al. [Fan+92]) which is about one order of magnitude larger than the theoretical prediction of

$$\tau_0 = \frac{128}{\sqrt{3}\,\pi^2\,\omega_\mathrm{p}} = 0.55\,\mathrm{fs}\,,$$

see equation (17). The electron-phonon relaxation time of

$$\tau_\mathrm{p} = 1.38\,\mathrm{ps}$$

is used.

The model of Carpene suggests that the shape of the non-thermal part of the electronic distribution function changes over time. The tails of the step-like distribution function decrease faster than the region around the Fermi level. However, the equation (31) is the solution of the differential equation which relates the changes in f_nt over time to f_nt times the scattering rate. This relation states that every scattering event of a non-thermal electron decreases f_nt at a certain electron energy and it does not affect f_nt at a lower energy. Thus, the possibility of a non-thermal electron to stay in the non-thermal subsystem at a different energy level after scattering is not included in this model. This could be the reason of the factor of 10 difference between the τ_0 used and the theoretically predicted

[14] The model of Rosei is based on the assumption that the electronic transitions at the L-point of Ag, Au and Cu are responsible for the measured upmost d-band to Fermi level response. The model includes several parameters to describe the band dispersions at the L-point.

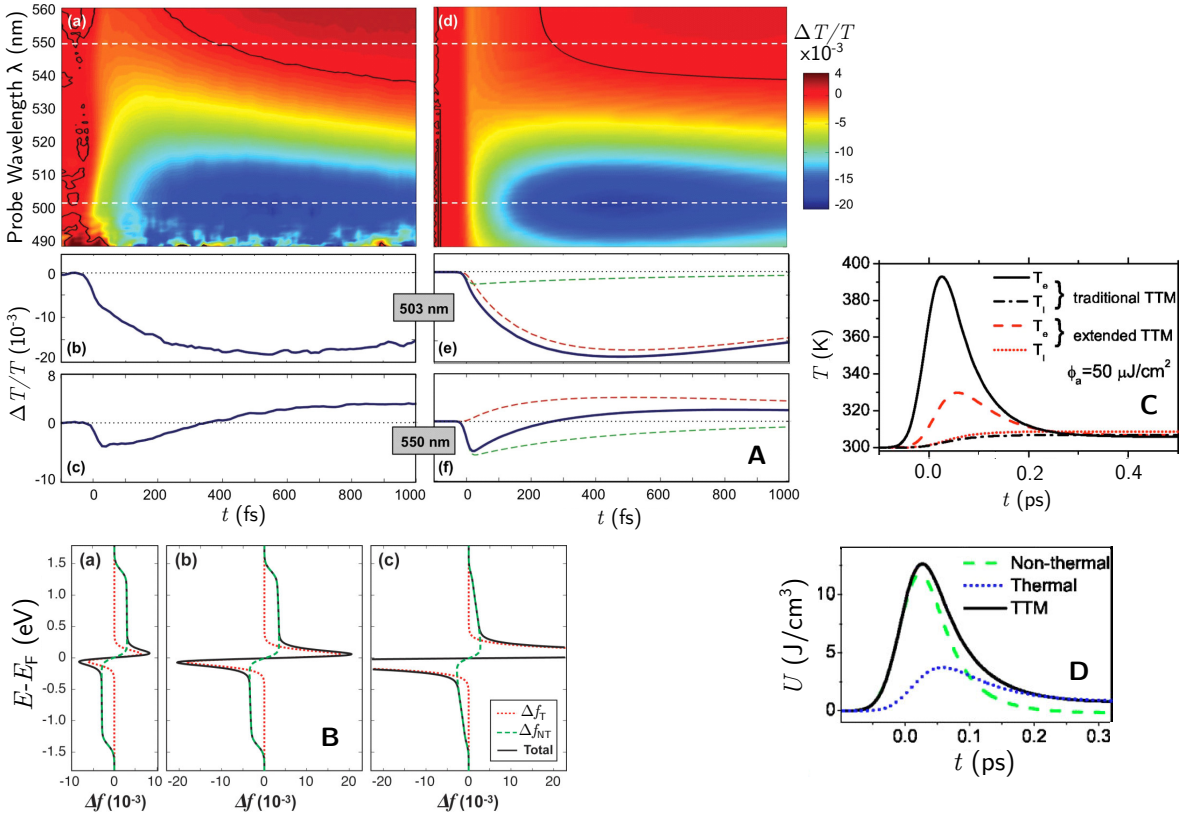

Figure 16: **Model of Carpene [Car06] and the findings of Della Valle et al. [DV+12] to describe the time evolution of the electronic distribution function in Au and Ru. A** Time-resolved changes in transmission measured on Au at different wavelengths ((a), (b) and (c)). The pump photon energy is 1.4 eV. (d), (e) and (f) show the simulated response based on the model of Carpene. The response consists of two components arising from distribution changes in the thermal and non-thermal electronic subsystems. **B** The electronic distribution function after (a) 10 fs, (b) 40 fs and (c) 300 fs is assumed by the model. **C** and **D** are the results of the model calculations on Ru, which are based on one order of magnitude lower fluences compared to **A** and **B**. The time evolution of both the electronic temperature and the electron energy density are shown. **A** and **B** are taken from [DV+12], **C** and **D** from [Car06].

one.

In Figure 16**C** and **D** the temperature and energy density evolution of the subsystems in Ru are presented and compared to the TTM predictions. The extracted electron-electron and the electron-phonon thermalization times are 60 fs and 70 fs [Car06]. τ_p and $\tau_{e\text{-}e}$ are too close, thus the TTM cannot describe the relaxation in such a metal and the simulations show this. The TTM predicts much higher electronic temperatures than the extended model of Carpene. The thermalization process in Ru is discussed in the following subsection in more detail.

3.4.2 The model of Lisowski et al.

The model of Lisowski et al. [Lis+04; Lis05] is developed to explain the experimental results on Ru(0001) (presented in Figure 17). The experimental technique is the time-resolved photoemission which gives access to the electronic distribution function above the Fermi level (see Figure 17**B**). For $E < E_F$ the experimental technique is not so sensitive because of the large number of electrons contributing to the signal.

The model of Lisowski et al. [Lis+04; Lis05] is based on a strict separation between the thermal-

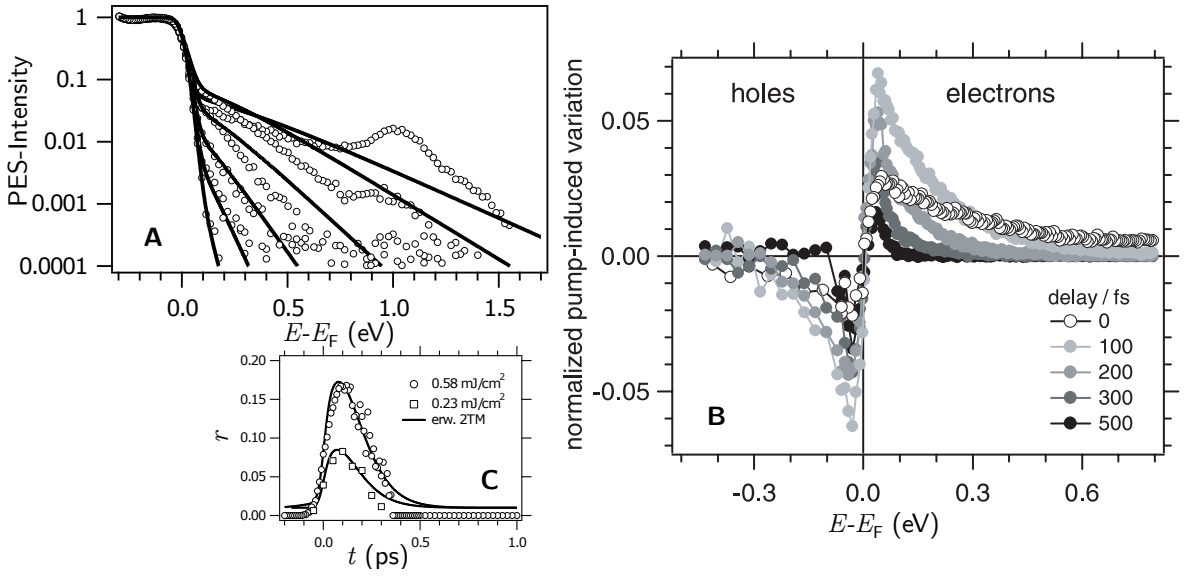

Figure 17: **Photoemission on Ru(0001) analyzed with the extended TTM of Lisowski et al. [Lis+04; Lis05].** **A** Photoemission intensity on Ru(0001) at different time delays after excitation (1.55 eV and an absorbed fluence of 580 µJ/cm^2). The experimental data is reproduced with simulated values of $r(t)$, plotted in **C**. **B** Change in the electronic distribution function near the Fermi level calculated from the experimental data of **A**. The model of Lisowski et al. is fitted to the experimental data with the fit parameter $r(t)$. The dots in **C** give the found values. The experimental $r(t)$ is compared to the theoretically assumed $r(t)$ (solid lines), which is the solution of the equation (38). The figures are taken from Lisowski et al. [Lis+04; Lis05].

and non-thermal quasiparticle subsystems. The excited non-thermal quasiparticles are split apart from the thermal quasiparticles with the time dependent variable r

$$D_{\mathsf{nt}}(E) = r \cdot D(E) \tag{32}$$

$$D_{\mathsf{el}}(E) = (1-r) \cdot D(E)\,, \tag{33}$$

where D is the electronic density of states. The non-thermal quasiparticles operate on D_{nt} and the thermal quasiparticles on D_{el}. This is not a rigid separation as both subsystems interact by

the exchange of energy, where $r = r(t)$. This phenomenological splitting allows to work with two separated electronic subsystems at different temperatures in the same metal. The non-thermal electrons are assumed to redistribute quickly to a Fermi-Dirac distribution function. This assumption is verified by the photoemission experiment performed by Lisowski et al. [Lis+04] and it is reasonable from a theoretical point of view by taking the Fermi liquid theory into consideration[15]. These assumptions change the problem to consist of two coupled quasi-thermal electronic subsystems at different temperatures acting on separate parts of the electronic density of states. The differential equations are[16]

$$\frac{\partial T_{\mathsf{nt}}}{\partial t} = \frac{1}{r\,\gamma\,T_{\mathsf{nt}}}\left[\frac{\partial U_{\mathsf{abs}}}{\partial t} - r\cdot g\cdot(T_{\mathsf{nt}} - T_{\mathsf{la}}) - \gamma\,(T_{\mathsf{nt}}^2 - T_{\mathsf{el}}^2)/\tau_{\mathsf{th}} + \frac{1}{2}\,\frac{\partial r}{\partial t}\,\gamma\,\left(T_{\mathsf{el}}^2 - T_{\mathsf{nt}}^2\right)\right] \quad (34)$$

$$\frac{\partial T_{\mathsf{el}}}{\partial t} = \frac{1}{(1-r)\,\gamma\,T_{\mathsf{el}}}\left[-(1-r)\cdot g\cdot(T_{\mathsf{el}} - T_{\mathsf{la}}) + \gamma\,(T_{\mathsf{nt}}^2 - T_{\mathsf{el}}^2)/\tau_{\mathsf{th}}\right] \quad (35)$$

$$\frac{\partial U_{\mathsf{la}}}{\partial t} = c_{\mathsf{la}}\frac{\partial T_{\mathsf{la}}}{\partial t} = (1-r)\cdot g\cdot(T_{\mathsf{el}} - T_{\mathsf{la}}) + r\cdot g\cdot(T_{\mathsf{nt}} - T_{\mathsf{la}})\ . \quad (36)$$

On one hand, the TTM term which describes the coupling between thermal electrons and the lattice can be used in both subsystems, thereby reducing the number of fit parameters. On the other hand, the dynamics get more complicated because the temperature relaxation rates are related to the relaxation rate of r (see the term which contains $\frac{\partial r}{\partial t}$ in the equation (34)).

The energy exchange between both electronic subsystems is supposed to be "proportional to the energy difference in the two electronic subsystems"[17] [Lis+04]

$$E_{\mathsf{therm}} = \gamma\,(T_{\mathsf{nt}}^2 - T_{\mathsf{el}}^2)/\tau_{\mathsf{th}}\,. \quad (37)$$

Here τ_{th} is the electron thermalization time between the different electronic subsystems.

Note that the photoemission is also a surface sensitive technique. Additional diffusion terms within the differential equations count for the loss of excited quasiparticles into the volume of the metal (these terms are not considered in the equations (34) and (35), but they are considered in the fits in Figure 17 and are found in [Lis+04]). The part of the relaxation which is not linked to diffusion

[15] The low values of the Sommerfeld constant (γ is split by r, typically $r \ll 1$) leads to high equilibrium temperatures, short electron lifetimes and thermalization times. The proportionality between the electronic lifetime and the electronic temperature is given in the equation (13) and Figure 13**A**.

[16] The energy exchange term between the thermal and non-thermal subsystems does not depend on r. An energy exchange is possible even in the case of $r = 0$, which is unphysical. A second noticeable problem is that the differential equations in [Lis+04] and [Lis05] are not consistent. The term related to $\frac{\partial r}{\partial t}$ is missing in [Lis05] and the energy conservation is not achieved.

[17] This statement is not true because of the splitting of γ into its thermal and non-thermal parts. In the original publications [Lis+04; Lis05] f is split instead of the density of states D (equations (32) and (33)), but in that case the energy in each subsystem is ill defined, it is $\gamma\cdot\left(T_{\mathsf{el}}^2 - T_0^2\right)/2 \neq \int_{-\infty}^{\infty} D(E)\ (E - E_{\mathsf{F}})\ (1-r)\ |f(E, T_{\mathsf{el}}) - f(E, T_0)|\ \mathrm{d}E$.

are related to the temporal changes of the electronic distribution functions of the non-thermal part Δf_{nl} and the thermal Δf_{el} part of the excited quasiparticles. The parameter r is used as a time dependent fit parameter. The rise time of r corresponds to the duration of the excitation pulse and the time which the excited electrons need to rearrange into a Fermi-Dirac distribution function. The amplitude of r depends linearly on the excitation density which can be seen in Figure 17**C**. An additional differential equation is used to describe the time evolution of r [Lis05]

$$\frac{\partial r}{\partial t} = \frac{1}{(\mathrm{h}\nu)^2\, D(E)} \frac{\partial U_{\mathsf{abs}}}{\partial t} - \frac{r}{\tau_{\mathsf{th}}} + \frac{T_{\mathsf{nt}} - T_0}{\tau_{\mathsf{sec}}}\,. \tag{38}$$

r increases due to the photo-excitation of electrons (first term) and the generation of secondary electrons (last term; time constant τ_{sec}) forming a Fermi-Dirac distribution and it decreases exponentially with the electron thermalization time of $\tau_{\mathsf{th}} = 65\,\mathrm{fs}$ [Lis05]. The photoemission intensity is reproduced by r as seen in Figure 17**C** (solid lines).

Although the TTM extensions of Carpene and Lisowski et al. are to some extent phenomenologic, application to experimental data show, that they can overcome the limitation of the TTM ($\tau_{\mathsf{e\text{-}e}}/\tau_{\mathsf{e\text{-}p}} \ll 1$) and determine the time evolution of the non-thermal electronic distribution function. Thus, they can describe the electron dynamics in metals with large electron-electron thermalization times.

3.5 Model of the linearized Boltzmann equations

The Boltzmann equations with included electron-phonon and electron-electron scattering terms is a system of a large number of coupled differential equations. It seems to be impossible to solve this problem analytically for every possible initial electron- and phonon-distribution functions. The TTM can solve the problem for thermal distributions. A different simplification of the problem is to expand the non-equilibrium part of the electronic distribution function. If Δf is small, higher orders can be neglected and the linearized Boltzmann equation can be transformed to a generalized Fokker-Planck differential equation (Baranov & Kabanov [BK14]):

$$\frac{\dot{\phi}(\xi,t)}{\gamma} = \frac{\partial}{\partial \xi}\left[\tanh\left(\frac{\xi}{2}\right)\phi(\xi,t) + \frac{\partial}{\partial \xi}\phi(\xi,t)\right] + \frac{p(t)\sinh\left(\xi/2\right)}{2\,\cosh^3\left(\xi/2\right)} + \frac{I_{\mathsf{e\text{-}e}}}{\gamma}\,. \tag{39}$$

Here, $\xi = (E - E_{\mathsf{F}}) \,/\, (\mathrm{k_B}\, T_0)$, ϕ is the non-equilibrium correction of the electronic distribution function according to

$$f(\xi) = \frac{1}{1 + \exp\left((E - E_{\mathsf{F}}) \,/\, (\mathrm{k_B}\, T_0)\right)} + \phi(\xi)\,,$$

$I_{\text{e-e}}$ is the electron-electron collision integral and p refers to the non-equilibrium part of the phonon distribution function. The parameter γ is proportional to the electron-phonon coupling constant λ as [BK14]

$$\gamma = \frac{\pi \hbar \lambda \langle \omega^2 \rangle}{k_B T_0} .$$

Solutions to the generalized Fokker-Planck equation are presented[18] in Figure 18.

For high temperatures T_0, the Fokker-Planck equation gives the energy relaxation rate [KA08;

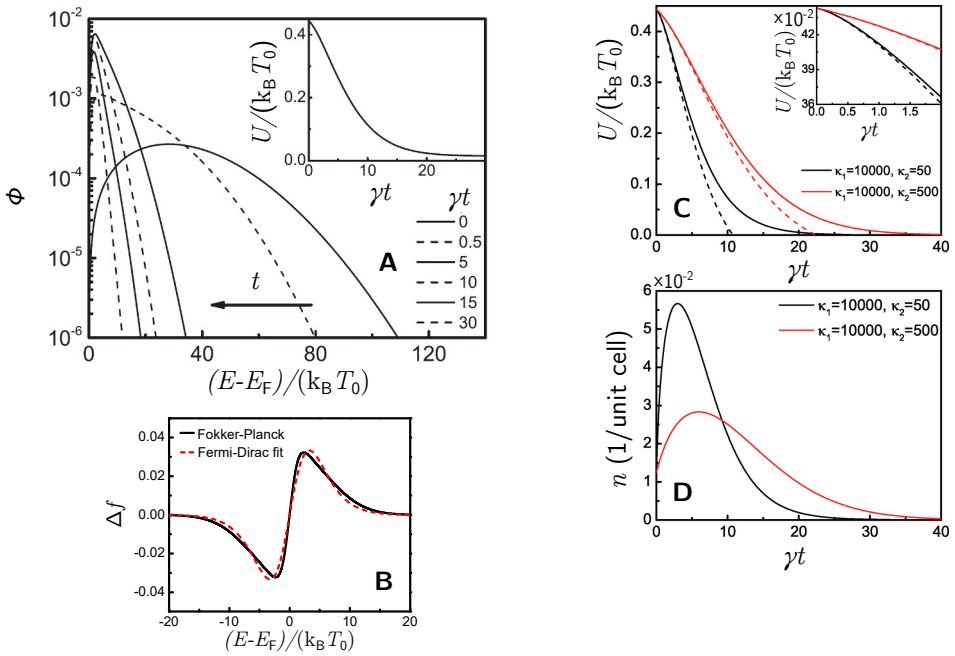

Figure 18: **Model of Kabanov et al. [KA08; BK14].** **A** Relaxation of the electronic distribution function ϕ (as a function of energy ξ) of a metal with $\kappa_1 = \kappa_2 = 100$.[18] The inset presents the energy relaxation of the electronic subsystem. After the electrons have transferred 90 % of their initial energy to the lattice, the electrons are thermalized [BK14]. **B** The electronic distribution function from the solution of the Fokker-Planck equation fitted with a Fermi-Dirac function. **C** & **D** Energy relaxation & non-equilibrium quasiparticle density relaxation in metals with large κ_1. The dashed lines correspond to the approximate analytical solution (equation (41)). Figures **A**, **C** and **D** are taken from [BK14], figure **B** from [Gad+10].

[18] The definitions

$$\kappa_1 = \frac{\hbar \lambda \langle \omega^2 \rangle}{\lambda \omega_D \beta k_B T_0} \approx \frac{\pi^2 C_{\text{la}}}{3 C_{\text{el}}} ,$$

$$\kappa_2 = \frac{4 \hbar^2 \lambda \langle \omega^2 \rangle E_F}{\pi^2 \mu_c^2 (k_B T_0)^3}$$

are used. κ_1 describes the average time a hot phonon survives until it is absorbed by the electronic subsystem and a new electron-hole pair is created. κ_2 describes the relative time the electrons need to thermalize. μ_c is the Coulomb pseudopotential.

BK14]

$$\frac{\partial U_{\mathsf{el}}}{\partial t} = -\gamma \int_{-\infty}^{\infty} \tanh\left(\xi/2\right) \phi(\xi, t)\, \mathrm{d}\xi \tag{40}$$

$$\approx -\pi\, \hbar\, \lambda \left\langle \omega^2 \right\rangle \cdot N_{\mathsf{qp}}\,. \tag{41}$$

The last approximation holds if ϕ is negligible for $|E - E_{\mathsf{F}}| < 2\,\mathrm{k_B} T_0$, then the $\tanh$ is approximated by a step function. In this situation the recombination rate of the quasiparticles is low and the result of Section 2.3 (spontaneous phonon emission) is reproduced. The equation (40) additionally includes the recombination of the quasiparticles at the Fermi level. In order to use this equation, it is necessary to know ξ as a function of time. The differential equation (39) allows to determine ξ numerically. Figure 18**A** present the solution of equation (39) for selected parameters. Simulations which implement the equations (40) and (41) are shown in **C** and **D**.

4 Electronic structure and optical properties of Cu

A short optical pulse can drive the electronic subsystem into non-equilibrium. An ultrafast technique which is sensitive to the changes in the electronic distribution function is the broadband optical probing of electronic interband transitions with final states in the conduction band at the Fermi level. The sharp fully filled d-band in Cu provides a source of electrons with well defined energy E_{d} and the electronic transition to the states at the Fermi level is optically allowed. To be more precise, the excitation of one d-band electron is only allowed if the final state at the Fermi level is empty because of the Pauli exclusion principle. Therefore the optical transitions from the d-band to the Fermi level are proportional to number of empty final states $1 - f(E,T)$ where the final state energy is

$$E = \mathrm{h}\nu + E_{\mathsf{d}}\,. \tag{42}$$

$\mathrm{h}\nu$ is the photon energy. The situation is sketched in Figure 19 (left side). The number and the distribution of the empty final states change with temperature. This affects the absorption coefficient which is a function of $\mathrm{h}\nu$, as shown in Figure 19 (right side). The increase of the temperature reduces the number of empty final states above the Fermi level and the absorption coefficient for light with $\mathrm{h}\nu > E_{\mathsf{F}} - E_{\mathsf{d}}$ as well. Photons with lower energy can only excite electrons from the d-band into empty states below the Fermi level. The number of empty final states below the Fermi level increases with increasing temperature resulting in an increase of the absorption coefficient for the light consisting of lower energetic photons $\mathrm{h}\nu < E_{\mathsf{F}} - E_{\mathsf{d}}$.

The sketch in Figure 19 is a simplification of the real conditions in Cu. A general rule is that the absorption of light is only possible if there is a dephasing between the electrons in the solid and the electromagnetic wave (otherwise the electrons reemit the incoming light and the dielectric constant is real). Dephasing is related to scattering events. The energy of the absorbed photon is not just transferred to a single quasiparticle but to at least two quasiparticles. These processes are usually taken into account by a damping constant (see Section 4.3.1). Another simplification in Figure 19 is the energetically sharp density of states of the d-band. In Cu there are five d-bands and they all have dispersions. The more elaborate optical properties related to the d-band to Fermi level transitions are found in Section 4.3.

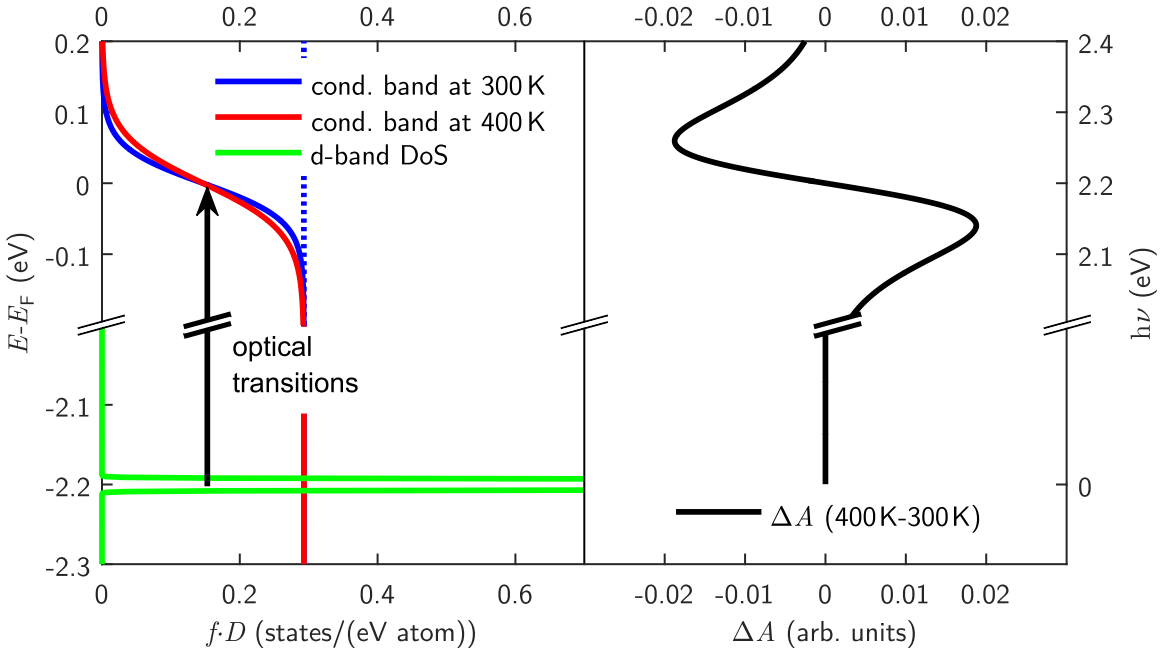

Figure 19: **Cu d-band to Fermi level transitions.** An energetically sharp d-band provides an ideal configuration to study the changes in the electronic distribution function at the Fermi level. The graph on the left side shows the idealized density of states multiplied to the electronic distribution function as function of energy relative to the Fermi level at 300 K and 400 K. The dotted line indicates only the density of states. The right side shows the temperature dependent change in the absorption coefficient. The increase in the number of excited electrons above the Fermi level reduces the absorption coefficient for photons with sufficient energy to drive those transitions. Photons with lower energy are more likely absorbed at higher temperatures because of the additional holes below the Fermi level.

4.1 The electromagnetic response of a solid

The electromagnetic response of solids is related to their electronic structure[19]. The first electronic interband transitions occur at photon energies in the infrared, visible or ultraviolett range. If the transition is optically allowed, then electrons are excited from the initial into the final band and photons are absorbed. The upmost d-band to Fermi level transition in Cu is an example for such a transition (see Section 4.3). Each excited electron leaves a positively charged hole in the initial band. At high photon energies the tightly bound electrons close to the ions can contribute to the optical properties. In metals, semi-metals or excited semiconductors there is an additional contribution due

[19]Additionally, optical phonons can be excited with infrared electromagnetic radiation (if these phonons are infrared active).

to intraband transitions between the filled initial and the empty final states of the conduction band. The electrons collective response to the electromagnetic field is approximated with the Drude model (see Section 4.4).

The contributions of all optically allowed transitions to the dielectric function are additive because all the corresponding polarization fields add up [DG02]

$$\epsilon = 1 + \sum_{i=1}^{N} \epsilon^{(i)} \,. \tag{43}$$

1 is the vacuum contribution and N is the number of allowed optical transitions within the solid. The first step to identify the allowed interband transitions is to analyze the electronic structure of the solid, which in a second step allows to determine the optical properties. If the link between the electronic structure and the optical properties is made, then it is possible to determine the non-equilibrium electronic distribution function Δf using ultrafast optical pump-probe methods.

The electronic structure of Cu is known from numeric band structure calculations presented and discussed in Section 4.2. Although Janak et al. [JWM75] already determined the dielectric function of Cu, taking the band structure calculations into account, it is required to reproduce this result with a simplified and adjustable model. Unfortunately, the computed dielectric function often show major deviations from the measured experimental dielectric functions and even those differ substantially between the various publications (e.g. compare [JC75] with [PS69]). The reasons for the deviations are the approximations in the calculations (often temperature effects are not included), the quality of the sample[20] and so on. As a matter of fact, even recent temperature dependent band structure calculations do not properly include all the temperature-related effects (see for example in Ag: Sundari et al. [SCT13] - although the theory is done carefully, the temperature dependencies of the experimentally determined optical properties are not reproduced with a sufficient accuracy).

As discussed above, it can be useful to get a simplified and analytic expression for the dielectric function with a few adjustable parameters, which are able to tune the expression that reproduces the experimental dielectric function quantitatively at different temperatures. This analytic expression for the optical properties is prepared by band structure approximations in Section 4.2. In Section 4.3 the analytic equation to describe the contribution of the upmost d-band to Fermi level transitions to ϵ of Cu follows. In addition to the Drude component, this expression allows to reproduce the experimental dielectric function and its temperature dependence up to photon energies of 3 eV. The

[20] Thin films for example can sustain stress and may be composed of several small grains rather than forming a single crystal. Band structure calculations are performed for perfect single crystals at zero temperature (see Section 4.2).

model parameters to reproduce the experimental data of the various publications are given in Section 4.6.

4.2 The electronic band structure

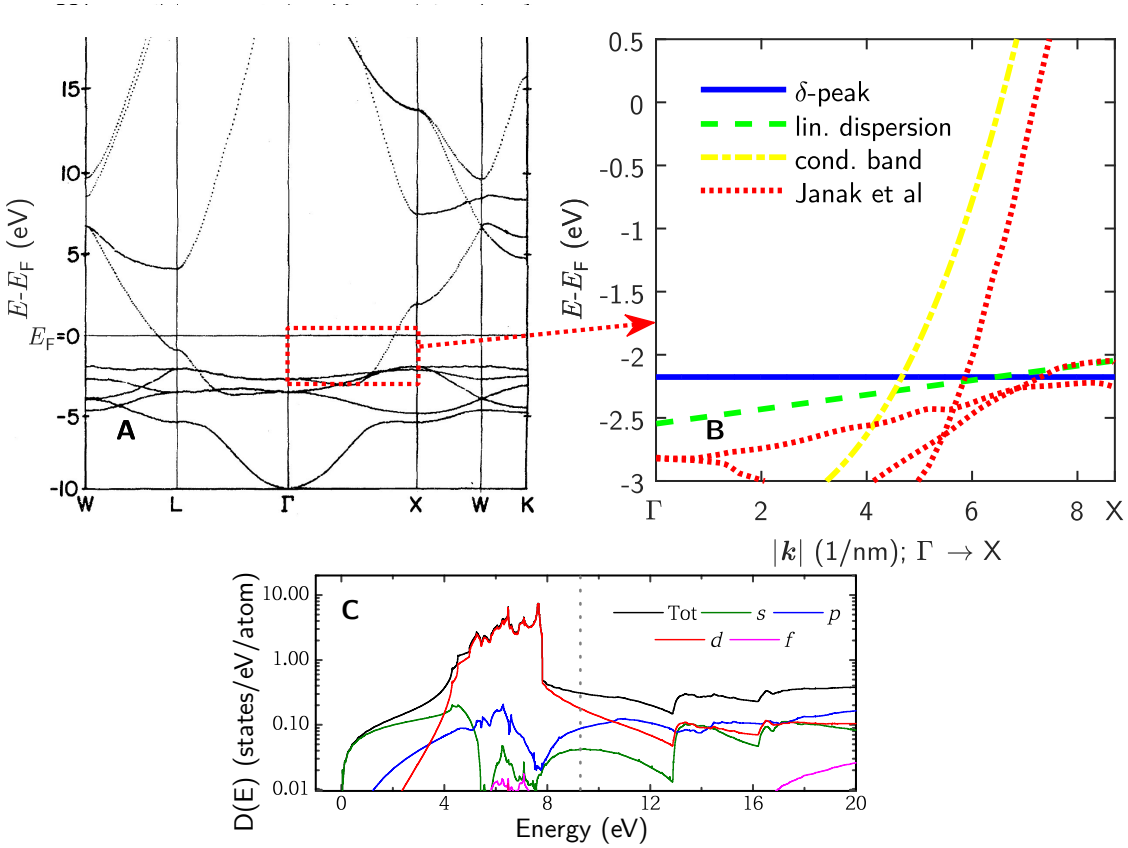

Figure 20: **Band structure of Cu. A** The band structure of Cu computed by Janak et al. [JWM75]. **B** The simplified band structure is shown which is used to describe the optically driven upmost d-band to Fermi level transitions. The upmost d-band is described by a flat band (solid blue line) or with linear dispersion (dashed green line). The conduction band is described with cubic dispersion (yellow dash-dotted line). The computed band dispersion between Γ and X is given as reference (dotted red lines, reproduced from **A** - area sketched by a red square). **C** Density of states calculated by Bévillon et al. [Bév+14]. The states are projected to the atomic wave functions in a sphere around the ions [Tor+08]. The dotted line refers to the Fermi level.

Cu is a transition metal and has 29 electrons per atom. In a single atom the first 3 shells are fully filled by 28 electrons. The last electron is in the 4th shell. It fills an orbital which is mostly a linear combination of the 4s- and 4p-orbitals, influenced by 3d-orbitals (band structure calculations based on linear combination of atomic orbitals are computed by Eschrig & Bergert [EB78]). Cu is often used to test band structure calculation techniques. There are plenty of different band structure

calculations on Cu with comparable results [JWM75; EB78; Bur63; DFJ68; MODS01; Wak65; Mij73; EFN84; FC70; Bag+80; FWC75; Sno68; LSB81; Seg62; JGM81]. Differences in the calculated band structures are mostly caused by the use of different screened potentials (the potential of the ions screened by the first two shells). Comparing several band structure calculations, the band dispersions differ slightly and the position of the Fermi level varies by about 0.5 eV. Some authors use experimental results to find a reliable screened potential (see for example [JWM75]). Photoelectron spectroscopy, studies of the optical properties and de Haas-van Alphen measurements provide further information about the band structure. The results can be compared to the computed band structure. In order to minimize the deviation between the computed band structure and the measured one, it is suitable to adjust the shape of the screened potential. The experimental results are well reproduced with the self-consistent $X\,\alpha$ potential [Sla72] which is based on two adjustable parameters. The corresponding band structure is shown in Figure 20**A**. But besides the good agreement, the calculation is done at zero temperature and it does not account for the temperature related changes in the optical properties.

The band structure shows that eleven electrons per atom are in the bands below the Fermi level with energies down to $E - E_\mathrm{F} =$ -10 eV. Most bands below the Fermi level are flat (they have low band dispersion) corresponding to 3d band dispersions. In an atom the 4s states are preferentially filled compared to 3d states. E.g. K and Ca have electrons in the 4s shells and empty 3d-orbitals. In analogy to this, one band starts with a 4s symmetry at $E - E_\mathrm{F} =$ -10 eV. Another band which is half-filled has 4p symmetry and crosses the Fermi level. The unfilled bands above the Fermi level have spectrally broad 4s and 4p character (see [EB78; SE85] and Figure 20**C**). Most of the d-band states are localized and filled (located below the Fermi level). The s-, p- and a small amount of d-like quasiparticles are delocalized and mobile. Bévillon et al. [Bév+14] calculated a number of 1.9 free electrons per atom at room temperature.

The optical properties with photon energies up to 3 eV are mostly affected by the conduction band electrons and the upmost d-band electrons (the lower lying d-bands contribute to ϵ_1 but do not cause much absorption; see for example [JWM75]). In order to simulate the optical properties, it is useful to approximate the d-band and conduction band dispersions. In a simplified model of the band dispersions an analytic expression for ϵ is obtained. The model of the upmost d-band is either done with a delta function (blue solid line in Figure 20**B** and paragraph **b**) or with linear dispersion (green dashed line and paragraph **c**). The models are intentionally simple in order to keep the amount of

free parameters to a minimum. These parameters are then adjusted to reproduce the experimental (see for example Section 4.6) or computed (Figure 21) dielectric function.

The conduction band is modeled with a cubic dispersion (see paragraph **a**). The choice of this "unphysical" approximation is based on the fact, that the corresponding density of states is constant. A nearly constant density of states around the Fermi level is also the result of many band structure calculations (e.g. the calculation of Janak et al. [JWM75]) and the derivation of the optical properties is greatly simplified by this fact. All the simplified bands are considered to be spherically symmetric. A comparison of the corresponding density of states to the result of band structure calculations is presented in Figure 21**A**.

a) Simplified conduction band

The conduction band is simplified in that way, that the resultant density of states is constant at the Fermi level

$$D_{\mathrm{c}}(E) = D_{\mathrm{c}}\,. \tag{44}$$

This corresponds to a cubic band dispersion

$$E(\boldsymbol{k}) = E_{\mathrm{c0}} + r\,k^3\,. \tag{45}$$

The dispersion between Γ and X is plotted in Figure 20**B**. The density of states at the Fermi level is experimentally determined by the electronic heat capacity of

$$c_{\mathrm{V}}(T) = \gamma \cdot T = D_{\mathrm{c}}\,\mathrm{k_B^2}\,\pi^2/3 \cdot T = 0.69\,\frac{\mathrm{mJ}}{\mathrm{K^2\,mole}} \cdot T\,. \tag{46}$$

measured at low temperatures [Phi71]. This gives a value of

$$D_{\mathrm{c}} = 0.293\,\frac{\mathrm{states}}{\mathrm{eV\,atom}} \tag{47}$$

(the value considers both spin directions). Whereas the simplified conduction band fails to describe the whole band from the bottom at Γ to the top at X, it is a good approximation around the Fermi level.

It turns out, that the momentum conservation is not important in the description of the upmost d-band to Fermi level transition (Section 4.3). Thus, the simplified band structure needs to replicate the density of states, the deviation in $\boldsymbol{k}_{\mathrm{F}}$ is unimportant because it does not affect the optical properties.

b) Upmost d-band described with a δ-peak

In this simple model the upmost d-band has zero dispersion

$$E_{\mathrm{d}}(\boldsymbol{k}) = E_{\mathrm{d0}}\,. \tag{48}$$

The density of states of the upmost d-band reads

$$D_{\mathrm{d}}(E) = 2\,\delta(E - E_{\mathrm{d0}})\,. \tag{49}$$

The only independent parameter E_{d0} is related to the onset of the absorption around 2 eV. It is adjusted to reproduce the dielectric function in this spectral range (see Figure 20, Section 4.3).

c) Upmost d-band with linear dispersion

One needs only two free parameters to describe a spherically symmetric band with linear dispersion. Of course this is an unphysical approximation, because at the Brillouin zone boundary the band needs to have zero dispersion and this is not the case in this approximation. However the sharp edge in the density of states is rendered (see Figure 21**A**) and electronic band structure calculations show that the dispersion of the upmost d-band between Γ and the X-point is almost linear. The linear dispersion reads

$$E_{\mathrm{d}}(\boldsymbol{k}) = E_{\mathrm{d0}} + a\,\sqrt{k_{\mathrm{x}}^2 + k_{\mathrm{y}}^2 + k_{\mathrm{z}}^2}\,.$$

The density of states of the upmost d-band is

$$D_{\mathrm{d}}(E) = \frac{(E - E_{\mathrm{d0}})^2\,V}{\pi^2\,a^3}\,.$$

The parameters E_{d0} and a are determined to reproduce the optical properties (Figure 21**B**), V is the volume of the unit cell. Two electrons per atom are in the band, this gives the maximum energy for states in the band

$$E_{\mathrm{d,max}} = E_{\mathrm{d0}} + a\,\sqrt[3]{6\,\pi^2/V}\,.$$

$E_{\mathrm{d,max}}$ is used to characterize the energetic separation between the d-bands and the Fermi level. This separation is temperature dependent. There are two reasons for a temperature dependent separation between the d-band and the Fermi level. First of all, the changes in the temperature cause the lattice to expand and this expansion modifies the bandstructure. The effect is also known from alloys of Cu and Au (rose gold). The color and the energy separation of the d-bands and the Fermi level change with the concentration of Au atoms. The Au atoms are larger than the Cu atoms, so the lattice

expands with Au concentration compared to pure Cu.

Secondly, a non-constant density of states at the Fermi level is the reason for a shift of the chemical potential (the Fermi level and chemical potential are used as synonyms) with temperature (since D_c is nearly constant around E_F, this contribution is small). The temperature dependence of the separation of the d-bands in respect to the Fermi level is characterized by[21]

$$E_G(T) = E_F(T) - E_{d,max}(T) = E_{G,0} + \partial E_G/\partial T \cdot T\,. \tag{50}$$

The dependence of E_G on the electronic temperature T_{el} is theoretically investigated by Bévillon et al. [Bév+14] at 0 K and with a fixed lattice constant. According to their result the Fermi level shifts because of the different density of states below the Fermi level compared to the density of states above the Fermi level. In addition the change in the electronic temperature triggers changes of the bandstructure (e.g. bond hardening (in Au) or softening (in Bi) near the photo-induced melting transition [Ern+09; Fri+07]). Due to the increased electronic pressure, stress is introduced into the metal. The local electronic densities change and related to this, the electronic band structure changes as well. With electronic temperatures in the range of 300 K up to 2000 K they surprisingly found a quite large coefficient [Bév+14]

$$\partial E_G/\partial T_{el} \approx 400\,\mu eV/K\,. \tag{51}$$

If the electrons and the lattice heat up, then the lattice expansion reduces the electronic pressure and the stress. Experimental results and lattice spacing dependent bandstructure calculations found a negative change with temperature of the upmost d-band to Fermi level separation (see Table 2). The approximate value is

$$\partial E_G/\partial T \approx \text{-}60\,\mu eV/K\,.$$

Note that the sign is different compared to the value (51).

4.3 Upmost d-band to Fermi level transitions

In the photon energy range up to several eV, the optical properties of group 11 metals (Cu, Ag and Au) are characterized by two different kind of electronic transitions. Light is absorbed by driving intraband transitions in the conduction band (Drude response) or transitions between different bands. In Cu the onset of the interband transitions is around 2.1 eV, in Au it is 2.6 eV and in Ag 4 eV. The

[21] The reference $E_{G,0}$ is taken at $T = 0$ (instead of room temperature) to consider the published experimental optical properties below room temperature.

Data from	Winsemius et al.	Pells & Shiga	Zallen	Gerhardt	Davis et al.
Method	optical prop.	optical prop.	piezo-reflectance	piezo-reflectance	bandstructure calculation
Analysed by	Winsemius et al.	Colavita et al.	Antonangeli et al.	Antonangeli et al.	Antonangeli et al.
$\partial E_G/\partial T$ (μeV/K)	-100	-70	$>$ -60 & $<$ 60	-50	-40

Table 2: Temperature dependence of the energy separation between the top of the upmost d-band and the Fermi level. The piezo-reflectance measurements by Zallen [Zal66] and Gerhardt [Ger68] allow to determine the change in the energy separation with change of the size of the unit cell. The value of Davis et al. [DFJ68] results from lattice constant dependent bandstructure calculations. The link between the temperature and the lattice expansion allows to determine $\partial E_G/\partial T$. This is done by Antonangeli et al. [Ant+74]. The temperature dependent lattice expansion is measured by Hahn [Hah70]. The energy shift of the d-band edge in ϵ_2 is measured and analyzed by Winsemius et al. [Win+76] and in addition the data of Pells and Shiga [PS69] is analyzed by Colavita et al. [CMR75].

interband transitions together with the Drude related metallic reflection at lower photon energies cause the redish color of Cu and the yellowish color of Au. Beside the differences in the positions of the d-bands, the band structure of Ag and Au is similar to the one of Cu (Figure 20**A**).

The metallic state provides a good reflectivity in the spectral range of near-infrared to dc based on the intraband transitions (metallic reflectivity; see [DG02]). This range of good reflectivity abruptly ends at photon energies higher than the energy which is needed to excite electrons from the filled d-bands into empty states of the half-filled conduction band around and above the Fermi level. The reason for the steep rise of ϵ_2 (see Figure 21**B**) is the following. The d-bands have large density of states compared to the conduction band (Figure 21**A**), so if the photon energy increases by little into the energy range where the d-band to Fermi level transitions are possible, then the number of possible initial states increases dramatically. The higher the photon energy, the more d-electrons contribute to the response and the more optical transitions become possible. According to these transitions, the energy of an absorbed photon is transferred to the electronic subsystem of the metal via excitation.

There are several models to analytically describe the d-band to Fermi level transitions. Firstly, the most general models to describe interband transitions, the Lorentz model (gives the response of a harmonic oscillator) or the Brendel-Bormann model [BB92] (this model assigns a "Gaussian line

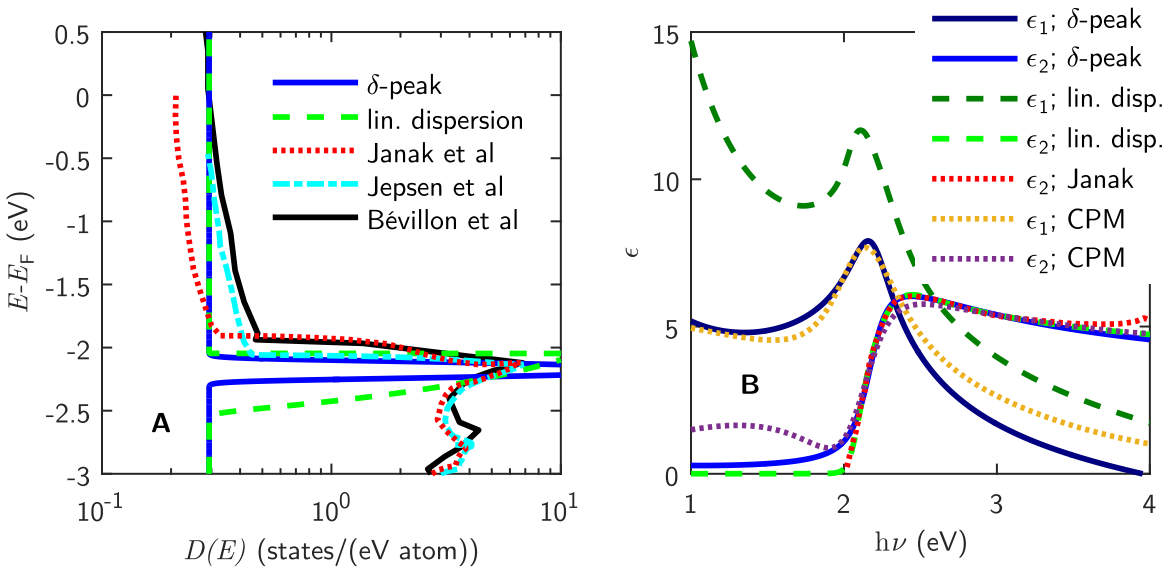

Figure 21: **Density of states and dielectric function of Cu.** Comparison between the band structure calculations and the simplified model description of the band structure. **A** Density of states below the Fermi level. The red dotted line, the cyan dash-dotted lines and the black line are computed densities ([JWM75], [JGM81] and [Bév+14]). The Fermi levels in the data of Jepsen et al. and Bévillon et al. are shifted by about 0.5 eV. The solid blue line and the green dashed line are the density of states of the simplified bands. The dielectric function with all optical interband transitions up to 4 eV are plotted in **B** (Drude is not included). The real and the imaginary part of the dielectric function are calculated with different models (at 0 K; details in the text) and compared to the band structure result of Janak et al. [JWM75] (red dotted line).

shape to every single mode") are not very accurate or they need plenty of parameters to describe all possible transitions (see for example Rakić et al. [Rak+98]). More convincing is the so called critical point model (see paragraph **a**) which generalizes the Lorentz model to "include the effects of *k*-space integration on both lineshape and broadening parameters by changing the orders of the poles and including phase factors" [Len+98]. The model was developed to represent the optical properties of crystalline and amorphous Si (see Leng et al. [Len+98]). Moreover, it is able to describe the upmost d-band to Fermi level transitions in Cu at room temperature ([RCZ11], the result is reproduced in Figure 21**B**). The temperature dependence of the dielectric function is mentioned in [RCZ11] but not described in detail. The problem is, that the electronic distribution function at the Fermi level and its temperature dependence are not included in the critical point model. The model may reproduce the temperature dependent shape of ϵ with the temperature dependent damping parameters, but if the electronic distribution function is athermal, there is no rule how to modify the model to describe the modified d-band to Fermi resonance (modified because of the different final state contribution).

Parameter	**a**) Critical point model [RCZ11]	**b**) δ-peak	**c**) linear dispersion
M	yes	yes	yes
$\partial M/\partial T$	yes	yes	yes
E_G	yes	yes	yes
$\partial E_\mathsf{G}/\partial T$	yes	yes	yes
γ	yes	yes	yes
$\partial\gamma/\partial T$	yes	no	no
Δf	no	yes	yes
free parameters at single specific T	8	4	5
T-dependent parameters	≥ 3	2	2

Table 3: **Overview over the most important model parameters of the upmost d-band to Fermi level transitions.** The table show which model includes which parameters. The critical point model does not consider the modification of the final state distributions with temperature according to Δf. In order to describe the flattening of the edge in ϵ_2 at 2.1 eV with increasing temperature (see Figure 25**B**), the parameter γ is temperature dependent in this model. The critical point model has 8 parameters (two extended Lorentz-oscillators). At least 3 of them are necessarily temperature dependent to describe the published optical properties of Cu. Unfortunately Ren et al. [RCZ11] do not describe the temperature dependence of their model parameters to compare the model predictions to the temperature dependent optical data.

The model to describe the optical properties of the d-band to Fermi level transitions needs to include a few physically important parameters which are listed in Table 3. The parameters which depend on the changes in the band structure are E_G (see Section 4.2) and the transition matrix element M. At temperatures around and above the Debye temperature, the lattice spacing, the band structure and all the mentioned parameters so far are expected to change linearly with temperature. The most important input for the model is the change in the electronic distribution function Δf at the Fermi level. The change of the occupation at the Fermi level, the increased Fermi level smearing, causes the edge in ϵ_2 to flatten. Another important parameter is the damping constant γ which is related to the dephasing process between the electron's initial and final states and the electromagnetic field.

This work presents an analytical description of the d-band to Fermi level transitions which includes all important parameters. The basis of this approach is the time dependent perturbation theory (see Appendix 8.2.1) and the interaction of light and matter (Appendix 8.2.3). The model includes the electronic distribution of the initial and the final states of the transitions. To keep the model simple and the dielectric function analytic, the band structure is simplified according to Section

4.2. The conduction band is given by a band with a constant density of states around the Fermi level. The upmost d-band is represented with either a dispersionless band or a band with linear dispersion. The electronic transitions between both bands are optically allowed. Figure 21**B** presents model optical properties which reproduce the results of the electronic band structure calculation [JWM75]. The equations to calculate the interaction of light with the electronic transitions between the upmost d-band and the conduction band are based on the results of Section 8.2.6. Equation (151) takes the density of states of the involved bands into account. The momentum conservation is not considered within this model because the dephasing time is short (governed by interactions, where a third particle (electron, phonon or impurity) takes the momentum to fulfill the momentum conservation). At the Fermi level electron-electron interactions are suppressed compared to electron-phonon interactions (see Section 2.6). The d-band holes are expected to have short lifetimes because of the high scattering probability with electrons below the Fermi level (< 10 fs). However, Knorren et al. [KBB01] found quite long d-band hole lifetimes of about 35 fs based on results from two photon photoemission experiments (the hole lifetimes are discussed in Section 4.3.1).

a) Critical point model

The critical point model (see reference [Len+98]) generalizes the Lorentz model (see for example [DG02]). A single critical point results in the dielectric function of

$$\epsilon = C_0 \cdot [\exp(\mathrm{i}\,\phi) \cdot (E_0 - \mathrm{h}\nu - \mathrm{i}\Gamma)^{\mu} + \exp(-\mathrm{i}\,\phi) \cdot (E_0 + \mathrm{h}\nu + \mathrm{i}\Gamma)^{\mu}] \ . \tag{52}$$

The equilibrium dielectric functions of Ag, Au and Cu are reproduced with a sum over a few single critical points in addition to the Drude response. This model gives a better description of the optical properties than the sum over Lorentz oscillators or the use of the Brendel Bormann model (compare Rakić et al. [Rak+98]). The upmost d-band to Fermi level transition in Au is modeled by Etchegoin et al. [ELRM06; ELRM07] with two critical points based on 6 free parameters (amplitudes C_0, relative positions E_0 and damping constants Γ), the phase of $\phi = -\pi/2$ and the orders of the poles are $\mu = -1$. In a similar manner Vial and Laroche [VL08] reproduce the optical properties of Au, Ag, chromium and aluminum. The orange and violett dotted lines in Figure 21**B** are the result of Ren et al. [RCZ11]. They adjusted the model parameters of three oscillators to the dielectric function of Cu at room temperature measured by Johnson and Christy [JC72]. The upmost d-band to Fermi level transitions in Cu are modeled with two critical points, one at 2.11 eV and a strongly damped one at 2.26 eV (see Ren et al. [RCZ11], 8 fit parameters, which are the two phases, the relative positions,

the damping constants and the amplitudes; $\mu = -1$ for both). The parameters are optimized to the dielectric function at room temperature and the result is compared to calculations made at zero temperature. The model parameter are not modified here to optimize the agreement between the band structure ϵ and the model but with small changes a better agreement is certainly achievable.

b) Model with a δ-peak description of the d-band

The description is based on the simplified band structure which is described in Section 4.2. The dielectric function is based on equation (151). The integration over the d-band can be performed analytically. The upmost d-band to Fermi level transitions contribute to the dielectric function according to

$$\begin{aligned}
\epsilon_1(\nu) &= -\frac{2\,\mathrm{e}^2\,D_\mathsf{c}}{V\,\epsilon_0}\int_0^\infty \left(\frac{\left|\langle k',\mathsf{c}|\,\hat{\mathrm{r}}\,|k,\mathsf{d}\rangle\right|^2}{(2\pi\nu)^2} + \left|\langle k',\mathsf{c}|\,\hat{\mathrm{r}}\,|k,\mathsf{d}\rangle\right|^2\right)(1-f(E)) \\
&\quad \cdot\left(\frac{E_{\mathsf{d}0}-E+\mathrm{h}\nu}{(E_{\mathsf{d}0}-E+\mathrm{h}\nu)^2+(\gamma_\mathsf{d}+\gamma_\mathsf{c})^2} + \frac{E_{\mathsf{d}0}-E-\mathrm{h}\nu}{(E_{\mathsf{d}0}-E-\mathrm{h}\nu)^2+(\gamma_\mathsf{d}+\gamma_\mathsf{c})^2}\right)\mathrm{d}E \\
\epsilon_2(\nu) &= \frac{2\,\mathrm{e}^2\,D_\mathsf{c}}{V\,\epsilon_0}\int_0^\infty \left(\frac{\left|\langle k',\mathsf{c}|\,\hat{\mathrm{r}}\,|k,\mathsf{d}\rangle\right|^2}{(2\pi\nu)^2} + \left|\langle k',\mathsf{c}|\,\hat{\mathrm{r}}\,|k,\mathsf{d}\rangle\right|^2\right)(1-f(E)) \\
&\quad \cdot\left(\frac{\gamma_\mathsf{d}+\gamma_\mathsf{c}}{(E_{\mathsf{d}0}-E+\mathrm{h}\nu)^2+(\gamma_\mathsf{d}+\gamma_\mathsf{c})^2} - \frac{\gamma_\mathsf{d}+\gamma_\mathsf{c}}{(E_{\mathsf{d}0}-E-\mathrm{h}\nu)^2+(\gamma_\mathsf{d}+\gamma_\mathsf{c})^2}\right)\mathrm{d}E
\end{aligned}$$

with the Fermi-Dirac distribution function

$$f(E) = \frac{1}{1+\exp\left((E-E_\mathsf{F})/(\mathrm{k_B}\,T)\right)}\,.$$

The damping $\gamma = \gamma_\mathsf{d} + \gamma_\mathsf{c}$ is described by a Lorentz function (equation (152)). ϵ_1 is a symmetric function of $\mathrm{h}\nu$ and ϵ_2 is an antisymmetric function of $\mathrm{h}\nu$.

The parameters γ, $E_{\mathsf{d}0}$, $M_\mathsf{cu} = \left|\langle k',\mathsf{c}|\,\hat{\mathrm{r}}\,|k,\mathsf{d}\rangle\right|$ and $M_\mathsf{di} = |\langle k',\mathsf{c}|\,\hat{\mathrm{r}}\,|k,\mathsf{d}\rangle|$ are adjusted to fit the band structure result (see Figure 21**B**). The values are $\gamma = 0.9\,\mathrm{meV}$,[22] $M_\mathsf{cu} = 1.26\cdot 10^5\,\mathrm{m/s}$, $M_\mathsf{di} = 3.5\cdot 10^{-11}\,\mathrm{m}$ and $E_{\mathsf{d}0} = -2.18\,\mathrm{eV}$.

[22]The fact that the electrons in the metal have finite lifetimes goes beyond the electronic structure description of Janak et al. [JWM75]. Because of many-body effects like scattering, the particle's self energy is complex (see e.g. [MB15]). The damping parameter γ refers to the imaginary part of the self energy and at $\gamma = 0$ (correspond to a purely real self energy), there is no absorption of light ($\epsilon_2 \equiv 0$), because the incident light is fully reemitted (for short pulses, parts of the emitted light show up delayed and in the limit of continuous light, a detailed balance is established). The Kubo-Greenwood equation (see [DG02]) used by Janak et al. provides a way to circumvent the problem of the purely real self energy by considering the absorption of light only and neglecting the spontaneous and stimulated emissions. Therefore, this value of γ is the result of an incomplete theory and does not have to reflect the experimental value. With the exception of the damping parameter, ϵ_2 derived by Janak et al., with its values for the joint density of states and the matrix elements, is applicable.

c) Model with linear dispersion of the d-band (LD→F model)

The approximation of the upmost d-band with linear band dispersion is made in Section 4.2. The resultant density of states provide a way to find an analytic expression for the upmost d-band to Fermi level transition in Cu. Equations (151) and (152) give

$$\begin{aligned}
\epsilon_1(\nu) &= -D_{\mathsf{c}}\,\frac{\mathrm{e}^2}{\epsilon_0}\int\limits_{E_{\mathsf{d,max}}}^{E_{\mathsf{c,max}}}(1-f(E))\int\limits_{E_{\mathsf{d0}}}^{E_{\mathsf{d,max}}}\frac{(E_{\mathsf{d}}-E_{\mathsf{d0}})^2}{\pi^2\,a^3}\left(\frac{\left|\langle k',\mathsf{c}|\,\hat{\mathrm{r}}\,|k,\mathsf{d}\rangle\right|^2}{(2\pi\nu)^2}+\left|\langle k',\mathsf{c}|\,\hat{\mathrm{r}}\,|k,\mathsf{d}\rangle\right|^2\right)\\
&\quad\cdot\left(\frac{E_{\mathsf{d}}-E+\mathrm{h}\nu}{(E_{\mathsf{d}}-E+\mathrm{h}\nu)^2+(\gamma_{\mathsf{d}}+\gamma_{\mathsf{c}})^2}+\frac{E_{\mathsf{d}}-E-\mathrm{h}\nu}{(E_{\mathsf{d}}-E-\mathrm{h}\nu)^2+(\gamma_{\mathsf{d}}+\gamma_{\mathsf{c}})^2}\right)\mathrm{d}E_{\mathsf{d}}\,\mathrm{d}E\\
&= A\,(M_{\mathsf{cu}}^2/\,(2\pi\nu)^2+M_{\mathsf{di}}^2)\int\limits_{E_{\mathsf{d,max}}}^{E_{\mathsf{c,max}}}(1-f(E))\,\Big(L^{(1)}(E,\mathrm{h}\nu)+L^{(1)}(E,-\mathrm{h}\nu)\Big)\,\mathrm{d}E \qquad (53)\\
\epsilon_2(\nu) &= D_{\mathsf{c}}\,\frac{\mathrm{e}^2}{\epsilon_0}\int\limits_{E_{\mathsf{d,max}}}^{E_{\mathsf{c,max}}}(1-f(E))\int\limits_{E_{\mathsf{d0}}}^{E_{\mathsf{d,max}}}\frac{(E_{\mathsf{d}}-E_{\mathsf{d0}})^2}{\pi^2\,a^3}\left(\frac{\left|\langle k',\mathsf{c}|\,\hat{\mathrm{r}}\,|k,\mathsf{d}\rangle\right|^2}{(2\pi\nu)^2}+\left|\langle k',\mathsf{c}|\,\hat{\mathrm{r}}\,|k,\mathsf{d}\rangle\right|^2\right)\\
&\quad\cdot\left(\frac{\gamma_{\mathsf{d}}+\gamma_{\mathsf{c}}}{(E_{\mathsf{d}}-E+\mathrm{h}\nu)^2+(\gamma_{\mathsf{d}}+\gamma_{\mathsf{c}})^2}-\frac{\gamma_{\mathsf{d}}+\gamma_{\mathsf{c}}}{(E_{\mathsf{d}}-E-\mathrm{h}\nu)^2+(\gamma_{\mathsf{d}}+\gamma_{\mathsf{c}})^2}\right)\mathrm{d}E_{\mathsf{d}}\,\mathrm{d}E\\
&= A\,(M_{\mathsf{cu}}^2/\,(2\pi\nu)^2+M_{\mathsf{di}}^2)\int\limits_{E_{\mathsf{d,max}}}^{E_{\mathsf{c,max}}}(1-f(E))\,\Big(L^{(2)}(E,\mathrm{h}\nu)-L^{(2)}(E,-\mathrm{h}\nu)\Big)\,\mathrm{d}E \qquad (54)
\end{aligned}$$

with

$$\begin{aligned}
A &= D_{\mathsf{c}}\,\frac{\mathrm{e}^2}{\epsilon_0\,\pi^2\,a^3}=D_{\mathsf{c}}\,\frac{6\,\mathrm{e}^2}{\epsilon_0\,V}\,\frac{1}{(E_{\mathsf{d,max}}-E_{\mathsf{d0}})^3}\\
\gamma &= \gamma_{\mathsf{d}}+\gamma_{\mathsf{c}}\\
M_{\mathsf{cu}}^2 &= \left|\langle k',\mathsf{c}|\,\hat{\mathrm{r}}\,|k,\mathsf{d}\rangle\right|^2\\
M_{\mathsf{di}}^2 &= \left|\langle k',\mathsf{c}|\,\hat{\mathrm{r}}\,|k,\mathsf{d}\rangle\right|^2\\
L^{(1)}(E,\mathrm{h}\nu) &= \frac{E_{\mathsf{d0}}^2-E_{\mathsf{d,max}}^2}{2}+2\,E_{\mathsf{d0}}\,E_{\mathsf{d,max}}-2\,E_{\mathsf{d0}}^2+(\mathrm{h}\nu-E)\,(E_{\mathsf{d,max}}-E_{\mathsf{d0}})\\
&\quad+\Big(E_{\mathsf{d0}}\,E-E_{\mathsf{d0}}\,\mathrm{h}\nu-E_{\mathsf{d0}}^2/2+\gamma^2/2-(E-\mathrm{h}\nu)^2/2\Big)\\
&\quad\cdot\ln\left(\frac{(E-E_{\mathsf{d,max}}-\mathrm{h}\nu)^2+\gamma^2}{(E-E_{\mathsf{d0}}-\mathrm{h}\nu)^2+\gamma^2}\right)+2\,(E-\mathrm{h}\nu-E_{\mathsf{d0}})\,\gamma\\
&\quad\cdot\left(\arctan\left(\frac{E_{\mathsf{d,max}}+\mathrm{h}\nu-E}{\gamma}\right)-\arctan\left(\frac{E_{\mathsf{d0}}+\mathrm{h}\nu-E}{\gamma}\right)\right) \qquad (55)\\
L^{(2)}(E,\mathrm{h}\nu) &= \gamma\,(E_{\mathsf{d,max}}-E_{\mathsf{d0}})+(E-\mathrm{h}\nu-E_{\mathsf{d0}})\,\gamma\,\ln\left(\frac{(E-E_{\mathsf{d,max}}-\mathrm{h}\nu)^2+\gamma^2}{(E-E_{\mathsf{d0}}-\mathrm{h}\nu)^2+\gamma^2}\right)\\
&\quad+\Big((E-\mathrm{h}\nu-E_{\mathsf{d0}})^2-\gamma^2\Big)\\
&\quad\cdot\left(\arctan\left(\frac{E_{\mathsf{d,max}}+\mathrm{h}\nu-E}{\gamma}\right)-\arctan\left(\frac{E_{\mathsf{d0}}+\mathrm{h}\nu-E}{\gamma}\right)\right) \qquad (56)
\end{aligned}$$

The parameters are adjusted to reproduce the dielectric function given by Janak et al. [JWM75]. They are found to be $\gamma = 0.9\,\mathrm{meV}$,[22] $M_{\mathrm{cu}} = 1.07 \cdot 10^5\,\mathrm{m/s}$ (less than 10 % of the Fermi velocity), $M_{\mathrm{di}} = 3.70 \cdot 10^{-11}\,\mathrm{m}$ (10 % of the lattice constant), $E_{\mathrm{d,max}} = -2.05\,\mathrm{eV}$ and $E_{\mathrm{d0}} = -2.55\,\mathrm{eV}$. The result is plotted in Figure 21**B** (green dashed lines).

4.3.1 Dephasing of the d-band to Fermi level transitions

This subsection discusses the damping constant of the d-band to Fermi level transitions to reduce the number of unknown parameters in the model describtion of the transitions. The damping constant depends on the scattering rate of the electrons at the Fermi level and the scattering rate (the inverse of the lifetime) of the d-band holes

$$\gamma = \gamma_{\mathrm{d}} + \gamma_{\mathrm{F}}\,.$$

These scattering rates include every scattering event or process which causes dephasing. At room temperature the scattering rate at the Fermi level is determined by the electron-phonon interaction. The dc-conductivity in the scattering time approximation reads

$$\begin{aligned} \sigma_{\mathrm{DC}} &= \epsilon_0\,\omega_{\mathrm{p}}^2\,\tau(E_{\mathrm{F}})\,, \\ \gamma_{\mathrm{F}} &= \hbar/\tau(E_{\mathrm{F}})\,. \end{aligned}$$

The measured mean free path of 39 nm [Zha+04] corresponds to $\gamma_{\mathrm{F}} = 26.5\,\mathrm{meV}$.
The transport electron-phonon coupling constant λ_{tr} is related to the conductivity above the Debye temperature [Gri76; All+86]

$$\sigma_{\mathrm{DC}} = \frac{\epsilon_0\,\omega_{\mathrm{p}}^2}{2\,\pi\,\mathrm{k_B}\,T\,\lambda_{\mathrm{tr}}}\,.$$

In copper λ_{tr} is close to the coupling constant λ [BAP82]. Theoretical values for λ are in the range of 0.11 to 0.15 [BAP82; Gri76; All+86; Mat98]. This gives

$$\gamma_{\mathrm{F}} \approx 2\,\pi\,\mathrm{k_B}\,T\,\lambda_{\mathrm{tr}} = 18\text{-}24\,\mathrm{meV}$$

at room temperature (this approximation is valid in the high temperature limit).
According to the Fermi liquid theory, the d-band holes should have short lifetimes because of the high scattering probability with other quasiparticles ($\tau_{\mathrm{h}} < 10\,\mathrm{fs} \rightarrow \gamma_{\mathrm{d}} > 66\,\mathrm{meV}$). Line width analysis from Knapp et al. [KHE79] of angle-resolved photoemission data yielded $\gamma_{\mathrm{d}} \simeq 100\,\mathrm{meV}$ at the top of the upmost d-band and at room temperature. This result is in agreement to the short lifetime scenario (note that the definition of γ in the paper differs to the definition used here by a factor of

2).

On the other side Knoesel et al. [KHW98; KBB01] found a d-band hole lifetime of about 35 fs (γ_d = 19 meV) based on results from two photon photoemission experiments. Matzdorf et al. [Mat+94] measured with high-resolution angle-resolved photoemission upper limits for the d-hole widths at 35 K. They found $\gamma_d \leq 26$ meV at the top of the upmost d-band. With a similar technique, Thiry et al. [Thi+79] found upper limits of 25 meV and 50 meV at the top of the d-band at two different points of the Brillouin zone (W and X). These measurements were performed at room temperature. Gerlach et al. [Ger+01] report 29 meV around the X point at room temperature. A systematic test series to determine the temperature dependence of the d-hole decoherence time is made by Petek et al. [PNO99] also around the X point. The result is a decreasing decoherence time with increasing temperature below the room temperature. At room temperature the damping constant is γ_d = 33 meV (similar measurements on Cu(111) and Cu(110) result in much lower lifetimes corresponding to bigger damping constants [Pet+00]). Possible reasons why the d-band holes may scatter less at other holes or phonons are because of their large mass, their localization, the low spatial overlap and/or the small scattering matrix elements. Simulations are made to determine the hole lifetimes (a few of them are tabled in [ZCE03]). The results ([Cam+00; Zhu+01; ZCE03; Mar+02; Ger+01]) span a broad range from 18 fs up to 99 fs (γ_d = 7-37 meV) for the d-band hole lifetime. The lifetime's wave vector and energy dependence based on the calculations of Zhukov et al. [Zhu+01] is reproduced in the Figure 22.

To sum it up, the line width of the upmost d-band to Fermi level transition is in the range of

$$\gamma \approx \text{30-60 meV}$$

at room temperature.

4.4 Drude model

The collective response of conduction electrons to electromagnetic waves is described by the Drude-Sommerfeld model [DG02]. The dielectric function depend on the photon energy, it is

$$\epsilon_1(\nu, T) = -\frac{(\hbar\omega_p)^2}{(h\nu)^2 + \gamma_D(T)^2} \quad (57)$$

$$\epsilon_2(\nu, T) = \frac{(\hbar\omega_p)^2 \cdot \gamma_D(T)}{(h\nu)^3 + h\nu \cdot \gamma_D(T)^2}\,, \quad (58)$$

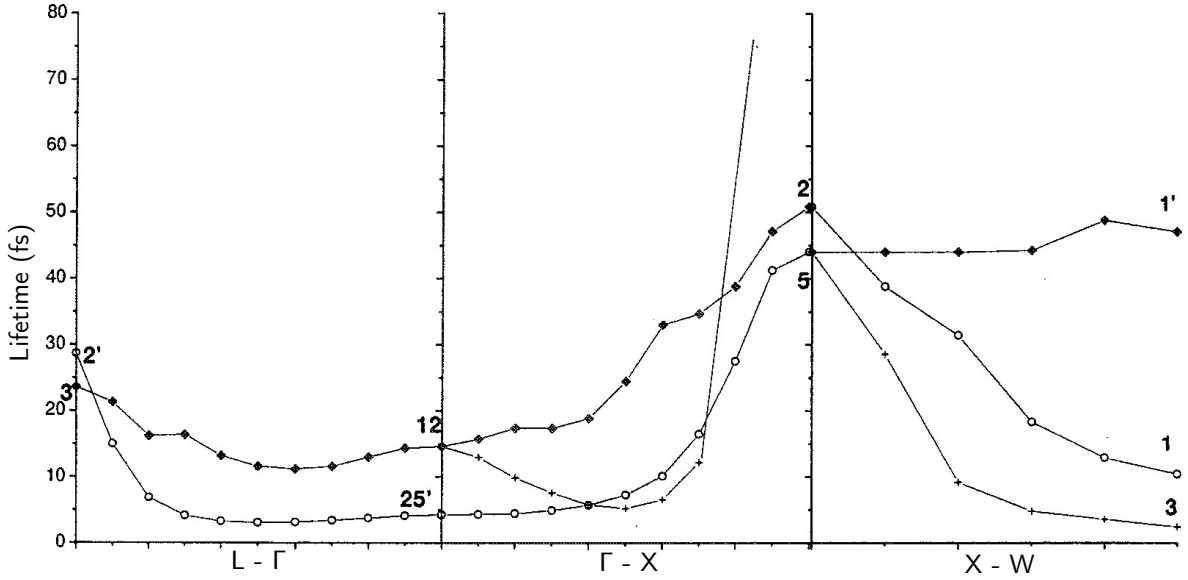

Figure 22: **Lifetimes of the holes in the upmost d-bands in Cu.** The d-band hole lifetimes are simulated by Zhukov et al. [Zhu+01]. The $\boldsymbol{k}$-dependence of the hole lifetimes shows that the longest lifetimes appear in the upmost d-band states at the X-point. The graph is taken from [Zhu+01].

ω_p is the plasma frequency which is the resonance frequency of the collective electron oscillation and depends on the electron density. γ_D is the dephasing rate[23] of the quasiparticles in the metal and it is linear dependent on the temperature (Ohm's law) around and above the Debye temperature ($T \gtrsim \Theta_\mathrm{D}$)

$$\gamma_\mathrm{D}(T) = \gamma_{\mathrm{D},0} + \partial\gamma_\mathrm{D}/\partial T \cdot T\,. \tag{59}$$

The higher the temperature, the more phonons are available to scatter on. The temperature dependence of ϵ is sketched in Figure 23**B**. The dephasing can also occur from electron-electron scattering and electron-impurity scattering events.

4.5 Electronic transitions at $\mathrm{h}\nu > 3\,\mathrm{eV}$

The dielectric function of Cu above $\mathrm{h}\nu = 3\,\mathrm{eV}$ and below 6 eV is characterized by two prominent features. At room temperature those features are at about 4.5 eV and 5 eV which is clearly seen in the experimental data measured by Pells and Shiga [PS69; Pel67] (Figure 24**A**). It is seen in the figure that the peak position, the width and the strength of the features change with temperature. Janak et al. [JWM75] related the peak at 4.5 eV to transitions in the vicinity of the L-point and the feature

[23] γ_D is not exactly the sum of the scattering rates of the excited quasiparticles (electron & hole), because not every scattering event induces a dephasing with the electromagnetic wave. Especially electron-electron scattering events do not fully contribute to the dephasing.

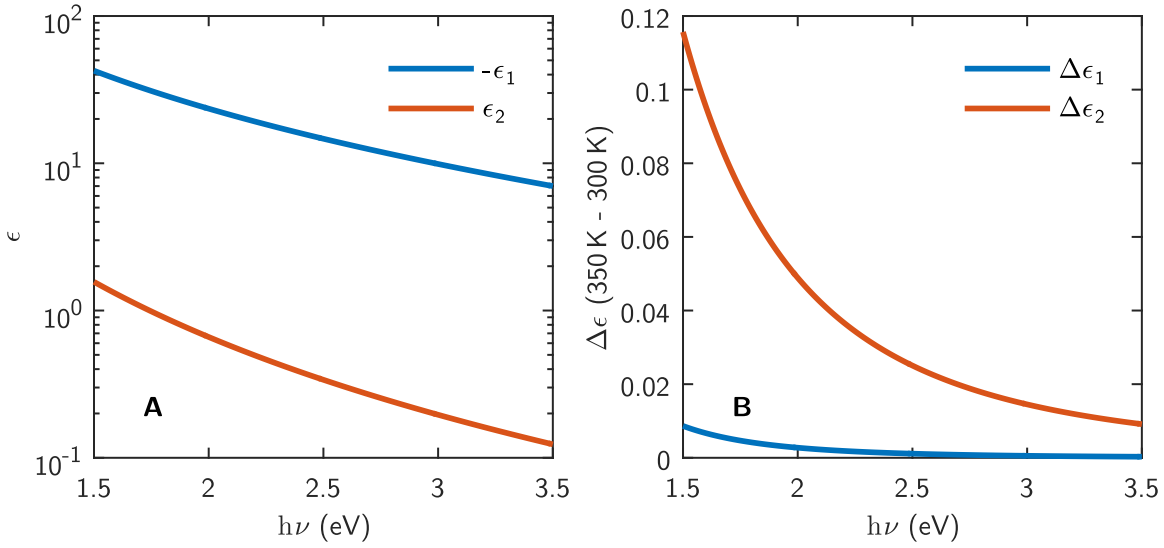

Figure 23: **Optical properties of the conduction electrons - Drude model. A** The metallic conductivity gives a large negative ϵ_1 at low frequencies. The absolute values of ϵ_1 and ϵ_2 decrease with increasing photon energy. The width is related to the temperature dependent scattering rate $\gamma(T)$, γ increases with temperature. In **B** the temperature dependence of the dielectric function is shown. The temperature change has a higher impact on the imaginary part of the dielectric function in comparison to the real part.

at 5 eV is known to be related to "temperature-sensitive transitions between nearly-free-electron-like bands". The peaks are affected by changes in the electronic band structure. These changes are triggered by the linear expansion of the lattice with increasing temperature. It is reasonable to assume that the parameters depend on temperature linearly.

The optically allowed transitions between a filled state or band and an empty state or band are often described with a Lorentz oscillator [DG02]. The optical properties of a Lorentz oscillator are

$$\epsilon_1(\nu) = \frac{E_{\text{os}}^2 \left(E_{\text{res}}^2 - (\text{h}\nu)^2\right)}{\left(E_{\text{res}}^2 - (\text{h}\nu)^2\right)^2 + (\text{h}\nu)^2 \cdot \gamma_{\text{o}}^2}\,, \tag{60}$$

$$\epsilon_2(\nu) = \frac{E_{\text{os}}^2 \cdot \text{h}\nu \cdot \gamma_{\text{o}}}{\left(E_{\text{res}}^2 - (\text{h}\nu)^2\right)^2 + (\text{h}\nu)^2 \cdot \gamma_{\text{o}}^2}\,. \tag{61}$$

The parameters are the plasma frequency or oscillator strength

$$E_{\text{os}}(T) = E_{\text{os},0} + \partial E_{\text{os}}/\partial T \cdot T\,, \tag{62}$$

the resonance frequency

$$E_{\text{res}}(T) = E_{\text{res},0} + \partial E_{\text{res}}/\partial T \cdot T \tag{63}$$

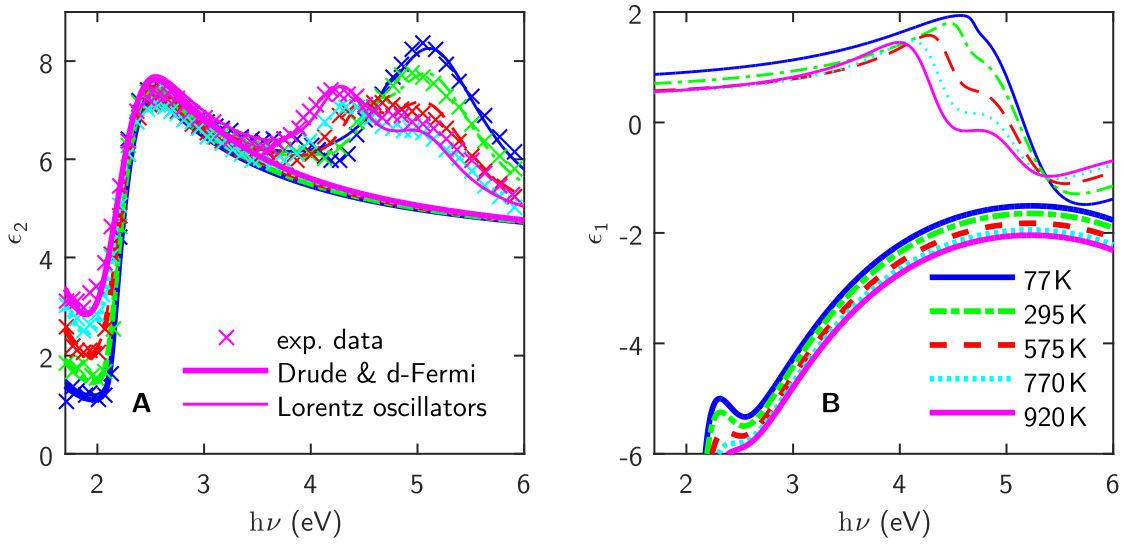

Figure 24: **Temperature dependence of the high frequency dielectric function of Cu.** The reflectivity of bulk Cu (5 mm grain size) is measured at different input angles and polarizations according to the method of Beattie and Conn [Bea55; BC55] which allows the reconstruction of the dielectric function (dots in **A**, measured by Pells and Shiga [PS69]). The d-band to Fermi level transitions and the Drude responses are reproduced with the LD→F and the Drude models (thick lines; the models are described in Section 4.3 and 4.4, parameters listed in Table 5). The transitions at higher photon energies are modeled with two temperature dependent Lorentz oscillators (thin lines). The corresponding real part of the dielectric function is plotted in figure **B**, the parameters are presented in Table 4.

and the damping constant

$$\gamma_o(T) = \gamma_{o,0} + \partial\gamma_o/\partial T \cdot T\,. \tag{64}$$

Two temperature dependent oscillators can describe the features at 4.5 eV and 5 eV in Cu (thin lines in Figure 24**A**). The parameters are used in a global fit which considers all data at every temperature and minimizes the absolute deviations. Contributions from the d-band to Fermi level transitions and intraband transitions of the conduction band are subtracted. The resultant parameters are listed in Table 4.

The fits allow one to deduce the contribution of the transitions at 4.5 eV and 5 eV to the optical properties at lower photon energies (e.g. $h\nu < 3$ eV). The contribution to ϵ_2 below 3 eV is negligible. However, ϵ_1 is affected by these additional oscillators (their contribution to $\epsilon_1(h\nu < 3\,\text{eV})$ is about 1). This contribution decreases with increasing temperature. The relation is

$$\epsilon_1^\infty(T) = \epsilon_{1,0}^\infty + \partial\epsilon_1^\infty/\partial T \cdot T = 0.94 - 6.06 \cdot 10^{-4} \cdot T\,.$$

Oscillator	$E_{os,0}$ (eV)	$\partial E_{os}/\partial T$ (meV/K)	$E_{res,0}$ (eV)	$\partial E_{res}/\partial T$ (μeV/K)	$\gamma_{o,0}$ (eV)	$\partial \gamma_o/\partial T$ (μeV/K)
1	0.1791	2.24	4.738	-474	0.1083	595
2	4.751	-2.64	5.172	-109	1.247	-413

Table 4: **Parameters of the Lorentz oscillators and their temperature dependence.** The dielectric function of Cu in the range between 3 eV and 6 eV is reproduced with two Lorentz oscillators. The parameters change linearly with temperature.

This holds well between 77 K and 575 K.

4.6 Application of the model to the published optical data on Cu

All contributions to the optical properties of Cu up to about 3.5 eV are discussed in the previous sections. These contributions are all additive, summing up to

$$\epsilon_1 = 1 + \epsilon_1^{\text{Drude}} + \epsilon_1^{\text{LD}\to\text{F}} + \epsilon_1^{\infty}\,, \tag{65}$$

$$\epsilon_2 = \epsilon_2^{\text{Drude}} + \epsilon_2^{\text{LD}\to\text{F}}\,. \tag{66}$$

These equations are tested on the published temperature dependent dielectric function data. The parameters of the best fits are listed in Table 5. The first test of the data of Pells and Shiga is already presented in Section 4.5 Figure 24. The temperature dependence of the Drude component and the temperature dependence of the upmost d-band to Fermi level transitions are assumed to be linear in this large T-range in question.

The second test is the application of the model to the data of Hanekamp et al. [HLB82]. They used a similar technique compared to Pells and Shiga (ellipsometry) to determine the dielectric function of Cu. The dielectric function is presented in Figure 25 together with the best-fit curve based on equations (65) and (66). They further tested the effective error of several systematic error sources, for example the effect of oxygen monolayers on the Cu surface. The result is an almost constant relative error within the test range. The fits are performed in this respect by weighting the data with its reciprocal absolute values. The measured optical properties of a single sample at different temperatures is considered together in one global fit to minimize the deviations between the experiment and the model.

Further tests are on the data of Roberts [Rob60] and Johnson & Christy [JC75]. Roberts measured two different bulk samples with different grain sizes (0.1 mm and 1 mm) in an ellipsometry-setup. The energy resolution was rather low compared to the other experiments. Johnson & Christy [JC75]

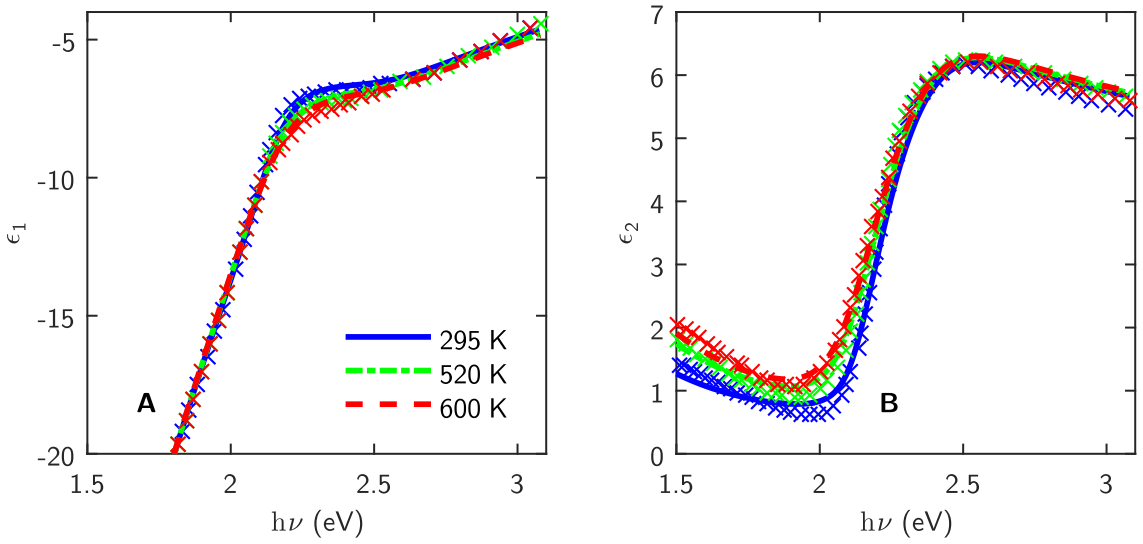

Figure 25: **Dielectric function of the Cu-surface (110).** The optical properties are measured with ellipsometry by Hanekamp et al. [HLB82] at three different temperatures. The measured amplitude component Ψ and the phase difference Δ allow to calculate the real (**A**) and imaginary part (**B**) of the dielectric function (dots). The dielectric function at all temperatures is fitted in a global fit procedure with the equations (65) and (66) (lines). The found parameters are listed in Table 5.

measured the reflectivity of optically thick films and the transmission through a thin semitransparent film (see Figure 26). Different films might have slightly different optical properties as showed by Savaloni et al. [SK05] and similar on Au [Thè70] and Ag [DT71] thin films. Stress in the film because of the different thermal expansion coefficients of the substrate and the film can influence the result, especially the temperature dependence of the parameters (the lattice expansion may be triggered by the substrate).

4.7 Thermomodulation spectroscopy

Even more challenging than describing the equilibrium dielectric function is the fit of thermomodulation data. In thermomodulation experiments the temperature is periodically modulated. The temperature related changes of the reflectivity and transmission through thin films is detected. The main advantage of the modulation technique is the higher sensitivity to temperature changes, which gives higher accuracy. The disadvantage of this technique is, although the changes in R and T are of high precision, equilibrium ϵ_1 and ϵ_2 are needed to obtain $\Delta\epsilon_1$ and $\Delta\epsilon_2$.

Thermomodulation experiments were performed by Rosei and Lynch [RL72] on Cu. The thin semi-

authors	Hanekamp et al.	Roberts	Johnson & Christy*	Pells & Shiga	Rosei & Lynch	Rosei & Lynch
published (year)	1982	1960	1975	1969	1972	1972
sample	bulk (110)-surface	bulk	films, diff. thick-nesses	bulk	thin film	thin film
technique	ellipso-metry	ellipso-metry	R & T of thin films	ellipso-metry	thermo-modulation	thermo-modulation
range of T (K)	295 - 600	90 - 500	78 - 423	77 - 920	120 - 128	350 - 374
$\hbar\omega_\mathsf{p}$ (eV)	9.99	9.49	9.27	[10]	9.61	9.90
$\gamma_{\mathsf{D},0}$ (meV)	18.8	25.8	62.3	51.2	[80]	[-10]
$\partial\gamma_\mathsf{D}/\partial T$ (μeV/K)	70.5	60.0	133.3*	113.2	33.3	33.3
M_cu (10^5 m/s)	1.04	0.77	0.94	1.26	1.14	0.77
$E_{\mathsf{G},0}$ (eV)	2.143	2.127	2.026*	2.128	2.1496	2.1065
$\partial E_\mathsf{G}/\partial T$ (μeV/K)	-70.1	-70.4	47.0*	-36.0	-0.2	-10.2
$\epsilon^\infty_{1,0}$	[1]	[1]	[1]	(0.94)	[1]	[1]
$\partial\epsilon^\infty_1/\partial T$ (10^{-4}/K)	-9.53	14.6	5.98*	(-6.06)	[-1.06]	[-0.201]

Table 5: **Fit parameters of the fits to the published temperature dependent optical properties of Cu.** For the fits the equations (65) and (66) are used to reproduce the experimental data measured by Hanekamp et al. [HLB82], Roberts [Rob60], Johnson & Christy [JC75], Pells & Shiga [PS69] and Rosei & Lynch [RL72]. In all fits the matrix element $M_\mathsf{di} = 3.85 \cdot 10^{-11}$, the d-band bandwidth of $E_\mathsf{BW} = E_{\mathsf{d,max}} - E_{\mathsf{d0}} = 0.5\,\mathrm{eV}$ and the damping constant $\gamma = 30\,\mathrm{meV}$ are kept constant. The values in round brackets are taken from the data analysis in Section 4.5. The square brackets indicate values which are less reliable because the fits are not sensitive to those values. A very sensitive technique to determine the changes of the optical properties with increasing temperature is the thermomodulation which is described in Section 4.7. *) The optical properties taken from Johnson & Christy are determined from reflectivity and transmission measurements on different films in air. The strain in those annealed films may be responsible to the different onset of the upmost d-band to Fermi level transition and that this value decreases with increase of the temperature (all other measurements have shown an increase with increasing temperature). All temperature dependencies determined in the fit on this dataset are less reliable compared to the parameters of the other films.

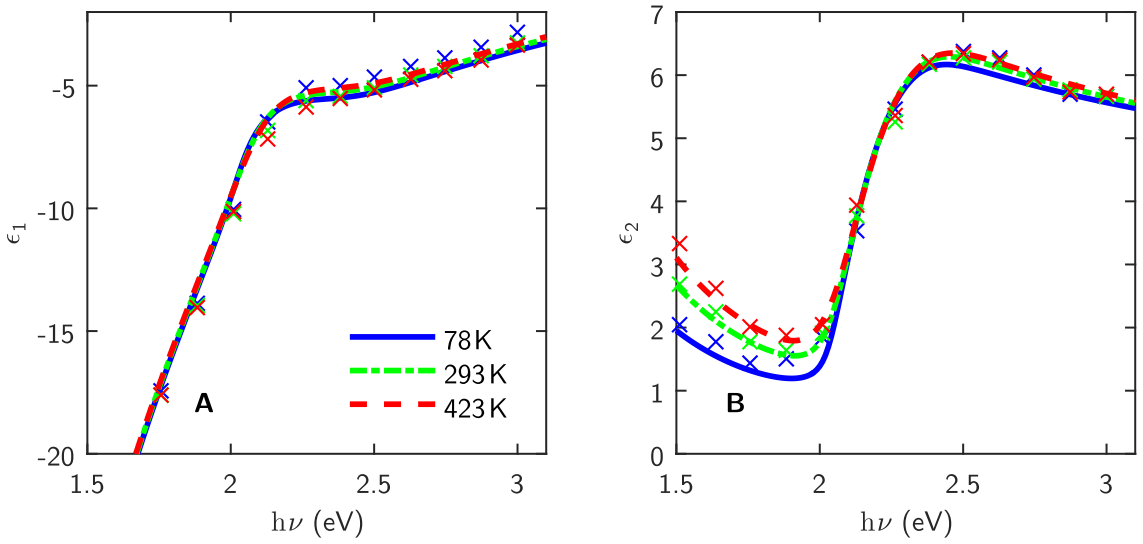

Figure 26: **Optical properties of Cu films.** Johnson and Christy [JC75] measured the reflectivity of opaque films and the transmission through thinner semitransparent films at different temperatures. The data of different samples are taken to determine the dielectric function, the result is shown as dots in **A** and **B**. The experimental dielectric function is modeled with equations (65) and (66) (lines). The parameters are listed in Table 5.

transparent films were "evaporated with an electron gun or a hot filament in a vacuum" [RL72]. They measured two different films, one at 120 K and the other at 350 K. The dissipation of a periodically applied current (120 kHz) in combination with a coupled heat bath modulates the temperature of the sample in the experiment. The measured changes in R and T are presented in Figure 27**A** and **B**. The graphs in Figure 28**A** and **B** compare two ways to determine $\Delta\epsilon$ from the measured $\Delta R/R = (\delta R - R)/R$ and $\Delta T/T$. The first way is to use the published dielectric function of Pells and Shiga [PS69] to calculate R and T (use of the Fresnel equations [DAP94a; DAP94b], they give $R(\epsilon)$ and $T(\epsilon)$). The modulated δR and δT give the modulated $\delta\epsilon$ in a second step (blue crosses in the figure).

The second way is to fit $\Delta R/R$ and $\Delta T/T$ with a model which is known to reproduce ϵ_1 and ϵ_2 and their temperature dependence for differently prepared and processed samples (e.g. the model needs parameters to consider the strain of thin films on substrate, different grain size and surface

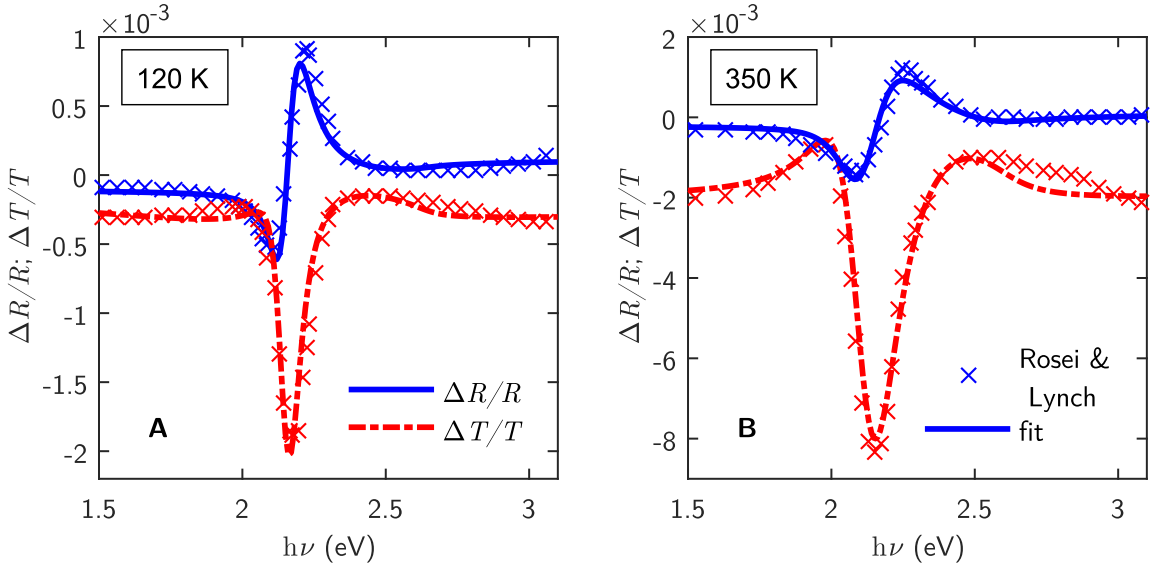

Figure 27: **Thermomodulation of R and T and the related change in ϵ of Cu. A** and **B** show $\Delta R/R$ and $\Delta T/T$ at two different temperatures measured by Rosei and Lynch [RL72] (crosses). $\Delta R/R$ and $\Delta T/T$ are most pronounced in the region of the d-band to Fermi level transitions at 2.1 eV. The width of this feature is related to the width of the Fermi smearing ($\propto \mathrm{k_B}\, T$). The thermomodulation data is reproduced based on the optical properties determined by the equations (67) and (68) (lines), the parameters are listed in Table 5.

roughness). It is

$$\Delta R/R = \frac{R(\delta\epsilon) - R(\epsilon)}{R(\epsilon)}\,, \tag{67}$$

$$\Delta T/T = \frac{T(\delta\epsilon) - T(\epsilon)}{T(\epsilon)}\,, \tag{68}$$

$$\Delta\epsilon = \delta\epsilon - \epsilon\,.$$

$\delta\epsilon$ and ϵ are determined with the equations (65) and (66). The model parameters are adjusted to reproduce the experimental data which is presented in Figure 27 (solid lines). The temperature increase caused by the applied current is a fit parameter, the results are a temperature increase of 8.2 K in the film measured at the low temperatures and 24.4 K in the other film at high temperature. The thickness of the films are modulated

$$d(T) = 45.5\,\mathrm{nm}\cdot\left(1 + 2.58\cdot 10^{-6}/\mathrm{K}\cdot T\right)\,,\ \text{film at } 120\,\mathrm{K}$$

$$d(T) = 31\,\mathrm{nm}\cdot\left(1 + 2.34\cdot 10^{-5}/\mathrm{K}\cdot T\right)\,,\ \text{film at } 350\,\mathrm{K}\,.$$

The used lattice expansion coefficients are close to the ones measured at a bulk sample by Hahn [Hah70]. At 120 K the relative bulk lattice expansion is about $1.2\cdot 10^{-5}/\mathrm{K}$ and at 350 K it is

$1.7 \cdot 10^{-5}$/K.

The corresponding $\Delta\epsilon$ are the black lines in Figure 28**A**-**D**. The fit model allows to decompose the

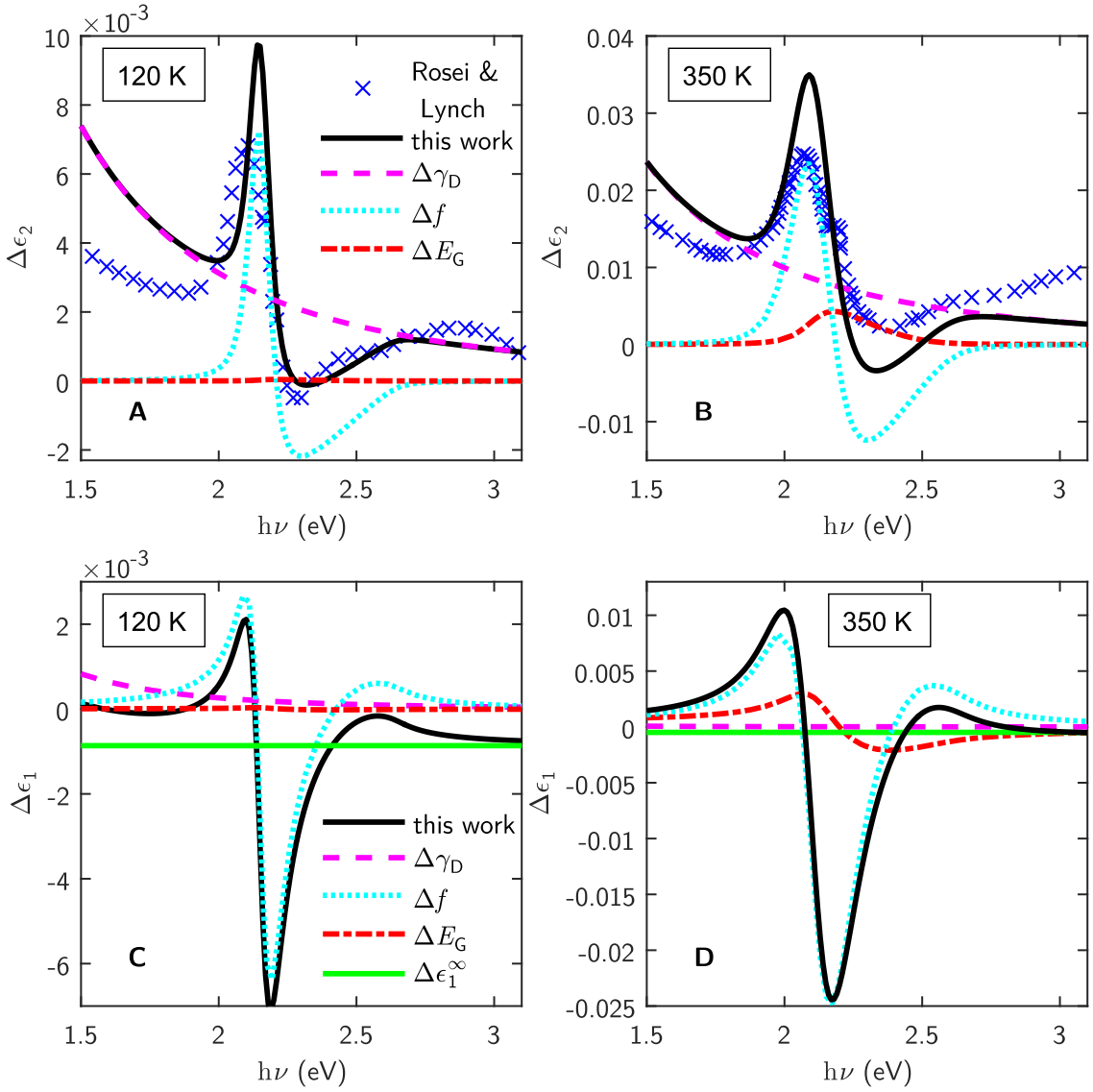

Figure 28: **Thermomodulation of ϵ in Cu.** The changes in R and T (Figure 27) allow to reconstruct the change in the dielectric function $\Delta\epsilon$. Rosei & Lynch did this based on equilibrium values of ϵ from Pells & Shiga [PS69]. $\Delta\epsilon_2$ (presented in **A** and **B**) is determined at each measured photon energy (blue dots). In addition the graphs **A** to **D** show $\Delta\epsilon$ from the fits to $\Delta R/R$ and $\Delta T/T$ (black lines). They partly consist of four different components which are described in the text.

response into its components. The result show that the change in E_G (red dash-dotted line) is not important at low temperatures but at higher temperatures. Δf at the Fermi level affects the signal around 2.1 eV (blue dotted line). Temperature induced excess electrons above the Fermi level lower the transition probability at photon energies above the energy of the separation between the upmost

d-band and the Fermi level ($\mathrm{h}\nu > 2.1\,\mathrm{eV}$, where $\Delta\epsilon_2$ is negative) and excess holes below the Fermi level increase the transition probability at $\mathrm{h}\nu < 2.1\,\mathrm{eV}$ (positive values of $\Delta\epsilon_2$). The temperature dependence of the Drude component ($\Delta\gamma_\mathrm{D}$, magenta dashed line) is already known from Figure 23. $\Delta\epsilon_1^\infty$ represent the changes in higher energetic transitions (green solid line, see Section 4.5).

5 Time-resolved broadband spectroscopy of Cu thin films

The pump-probe technique is an experimental technique to measure the dynamical properties of single atoms, few- or many-particle systems. The idea behind is to excite the system with the so called pump pulse and to record the resulting changes of the sample by using the probe pulse. Possible observations of certain processes are limited by the pulse duration of the pump pulse. If the duration of the pump pulse is longer than the rise and relaxation time of a process, it is not possible to investigate the process. The time resolution which was used for measuring the response of the sample is limited by the pulse durations of the pump and the probe pulses. The pump pulse excites the system into a non-equilibrium state and therby deposits the energy into the system. At the beginning, the energy is usually located in the electronic subsystem followed by the thermalization with other degrees of freedom (e.g. phonons or spins). These relaxation processes are recorded by the probe pulse, which is delayed with respect to the pump pulse. Different kinds of probe pulses are possible (e.g. light, x-rays, electrons) to gain information about the non-equilibrium state. These pulses can be reflected, diffracted, scattered, absorbed and/or move through the excited sample. This can result in a change of the amplitude, the phase, the beam divergence and direction, the polarization, the pulse length and shape, the frequency, etc. In addition the probe pulses can be used to emit electrons (in time-resolved photoemission experiments) or to break molecular bonds. All the information about the non-equilibrium state is recorded as a function of time delay between the pump- and the probe-pulses.

5.1 Setup of the NIR-pump and broadband-optical-probe setup

In an all-optical pump-probe setup the sample is pumped and probed with optical pulses. A broadband probe continuum allows to measure the time-resolved response of the sample by recording the optical properties of the non-equilibrium state after excitation. In solids visible light probes mostly the charged quasiparticles which undergo interband transitions. Such electronic interband transitions are probed to gain information about changes in the population of the electronic states, the electronic distribution function, the lifetimes of the electronic states, etc. In Subsection 5.1.1 the generation of ultrashort optical near-infrared (NIR) pulses is described. Subsection 5.1.2 gives information about

the energy- and time-resolution of the experimental system. The experimental setup, which was used to perform NIR-pump and broadband-probe laser spectroscopy in solids, is presented in the Subsections 5.1.3 and 5.1.4. In such experiments it is important that the amount of energy is known which is deposited in the solid by the absorption of the pump pulse. The excitation density is used for the estimation of the maximum heating of the sample, cw-heating effects, the maximum number of excited quasiparticles and the amount of energy which is necessary to drive phase transitions, etc. The equations to determine the excitation density are given in Subsection 5.1.5.

5.1.1 The laser system

Ultrashort laser pulses are generated by a commercial temperature-stabilized mode-locked titanium-sapphire (ti:sa) laser system. The laser system is manufactured by Coherent Inc. (Santa Clara, USA) and it consists of a diode-pumped continuous wave (cw) laser for pumping the ti:sa crystal of an oscillator system (the product name is "Micra"). The pump laser (named "Verdi") is a diode-pumped Nd:Vanadate crystal (Nd:YVO_4) operating at 1064 nm. A lithium triborate crystal is temperature tuned to frequency double the 1064 nm laser light via type I phase matching condition. The doubled, 532 nm light leaves the Verdi cavity and enters the cavity of the oscillator. The output is 5 W with a noise level below 0.03 % [Coh10].

The oscillator is designed to passively stabilize the mode-locked operation. Therefore modes with different frequencies are phase locked to form ultrashort pulses with a repetition rate of 76 MHz given by the length of the cavity. The ti:sa crystal acts as a Kerr lens for high photon densities. The Kerr lens is a third order non-linear effect and is therefore proportional to the intensity of the electromagnetic wave. The short laser pulses are more strongly focussed because the photon densities are higher compared to the cw-laser mode. In the design of the laser cavity smaller foci gain more power from the population inversion than large foci. The mode-locked operation is therefore preferred and stable in this cavity. In addition, the ti:sa crystal self-phase modulates the short laser pulses and the laser bandwidth is increased by the third order non-linear effect (also proportional to the photon density) for the generation of shorter pulses. The pulses are kept short with a prism compressor being part of the cavity. It reduces the chirp on the pulses which has its origin in the dispersive optics inside the cavity. The laser light is not fully reflected by one cavity mirror and an output of approximately 500 mW is achieved. The prism compressor is adjusted to provide operations for pulses with a bandwidth of 40 nm centered at 800 nm [Coh07]. The Micra operates at 76 MHz and

produces output pulses of less than 10 nJ. The high repetition rate limits the application of the laser to spectroscopy on samples with a fast recovering time (good thermal contact to the heat bath) and to spectroscopy at low excitation densities.

A regenerative amplifier (Coherent "RegA" Model 9000) is applied to overcome the limitations of the oscillator. The amplifier consists of a cavity with a ti:sa crystal as active medium. The crystal is pumped with a 10 W Nd:YVO_4-Laser described above. A switchable Q-switch based on the acousto-optic effect prohibits the cw-lasing inside the cavity. The Q-switch stops operation periodically for hundreds of nanoseconds. These timings are electronically controlled, the repetition rate is usually tuned to 283 kHz. The cavity dumper, a second acousto-optical crystal, uses a short acoustic pulse to inject a single laser pulse from the oscillator in a double pass configuration. This happens during the time where the Q-switch is off. Each round trip the pulse gets amplified in the ti:sa crystal. After approximately 28 round trips the cavity dumper ejects the amplified pulses. To prevent non-linear effects in the laser crystal, the oscillator pulses are stretched using a grating before entering the amplifier [Coh97]. The pulses which have left the amplifier are compressed by a grating compressor to a pulse duration of approximately 50 fs. The pulse energy is 5 µJ, the central wavelength is 800 nm and the spectral width is 30 nm.

5.1.2 The energy- and time-resolution

The uncertainty principle states that the light pulses have to cover a set of different wavelengths (usually the wavelengths are close together in a continuous spectral range). The shorter the pulses are, the larger the minimum spectral range to cover. The pulses which have the highest compression in time and energy are gaussian distributed (see the inset on the Figure 29 and [DR06]). The uncertainty relation is

$$\Delta\nu \cdot \Delta t \geq 2 \cdot \ln(2)/\pi\,. \tag{69}$$

The region above the blue line in Figure 29 is physically possible. Phase delays between different spectral components of the pulse (chirp) are the reason for a lower time resolution compared to the theoretically possible time resolution of the given spectral shape and width.

5.1.3 The time-resolved broadband spectroscopy

This section introduces the time-resolved broadband spectroscopy which is used to measure the dielectric function of thin films time-resolved after excitation with an ultrashort laser pulse. The

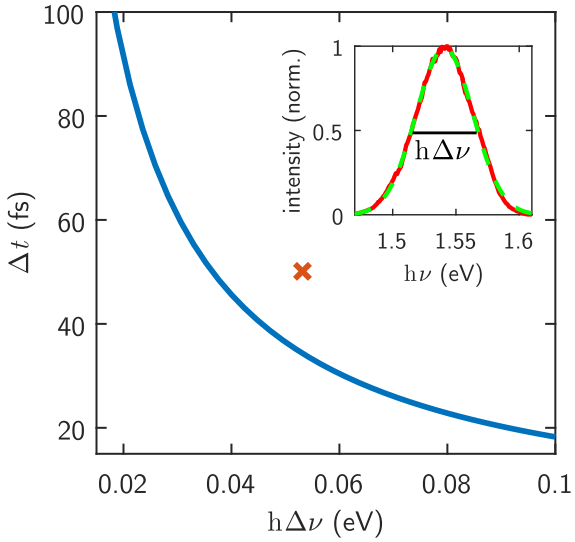

Figure 29: **Uncertainty principle and spectral width of gaussian pulses.** The uncertainty relation restrictes the maximum time resolution at a given energy resolution (minimum pulse duration-bandwidth product, blue line). The amplified laser system operates at the point of the red cross. The pulses are close to the minimum pulse duration-bandwidth product of gaussian pulses. The system is a compromise between energy- and time-resolution. The inset show the spectrum of the laser system (red solid line) which is described by a gaussian curve (green dashed line). The spectral width is defined as the full width at half of the maximum of the gaussian (black line).

NIR pump and white light probe setup is designed to operate with a pulsed laser of a few hundred kHz repetition rate, perfectly matching the laser system described above. The input pulses have a negative chirp to finally provide laser pulses of 50 fs duration in the white light generating sapphire crystal (probe) or in the sample (pump).

The setup is schematically presented in Figure 30. Most elements used are common in an all-optical pump-probe setup. The laser pulse is split by the first polarizing beamsplitter cube (PBSC1) into the pump and into the probe pulse with adjustable power ratio (angle of the $\lambda/2$).

Time delay and modulation unit A stage (Stage1) is used to control the time delay between the pump and the probe pulses. The repetition rate of the laser system is high enough to perform measurements in fast scan mode, which is realized with a periodically driven shaker. The shaker modulates the time delay between the pump and the probe pulses in the double pass configuration, which consists of the PBSC3, a $\lambda/4$, a retroreflector R2 and the endmirror M6. The shaker operates with a displacement amplitude of 1.2 mm which gives a range in time delay of 32 ps ($8/\mathrm{c} \cdot 1.2\,\mathrm{mm} = 32\,\mathrm{ps}$). The frequency of the modulation is about 20 Hz, corresponding to 14000 laser shots during

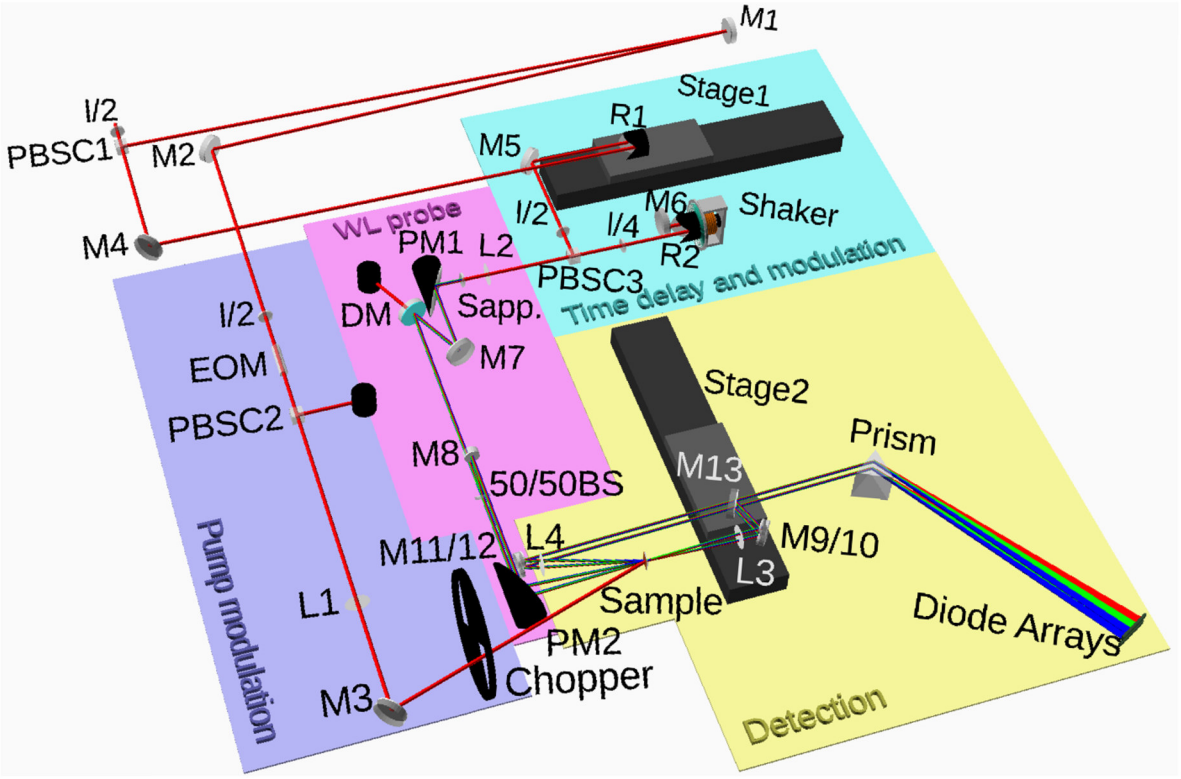

Figure 30: **Experimental setup.** The laser pulses are split by the polarizing beam splitter cube PBSC1 into pump and into probe pulses. The time delay between both is periodically modulated by the time-delay and modulation unit. The white light is generated, collimated, filtered, refocussed and splitted into probe and reference in the WL probe unit. The intensity of the excitation pulses is modulated in the pump modulation unit. The detection unit can switch between the reflection and transmission configuration and splits the white light into its spectral components to detect them separately.

one shaker period. Thus, in one minute 1200 transients are measured and averaged. A single transient has 7000 points which are separated by 5 fs on average[24] (this separation is short compared to the pulse duration).

White light (WL) probe unit The specialized parts of the setup which allow to cover a broad spectral range within a single experiment are in the WL probe unit and in the detection unit. The white light is generated by self-phase modulation in the sapphire crystal (Sapp.). It works optimally with 200 nJ pulses tightly focussed (with lens L2) onto the crystal. After the generation of the white light, the light diverges strongly. Contrary to the second order non-linear processes, the divergence does not depend on the beam divergence of the incoming light. The fundamental around 800 nm

[24] The temporal separation follow the characteristic of the shaker oscillation, typically a sinus curve, which provides a good stability.

is mostly filtered by a dielectric mirror (DM) and damped. The white light pulses are guided with reflective optics to keep the chirp as low as possible. The pulses are collimated and refocussed with off-axis parabolic mirrors (PM1 and PM2) (lenses introduce dispersion and chromatic aberation). The diameter of the foci on the sample is smaller than 50 µm for all spectral components of the white light. Despite the fact that no chromatic abberation is introduced to the white light pulses after the sapphire crystal, the foci are slightly separated on the sample (much less than 50 µm).
The generation of the white light is a third order non-linear process. The noise of the white light is at least cubic to the noise of the amplifier. The noise can be reduced via differential detection, where each white light pulse is split by a broadband beamsplitter (50/50BS) into two pulses with approximately the same intensity. The first pulse called "Reference" (lower beam) measures the sample's properties before the pump pulse arrives and the second one ("Probe", upper beam) probes the sample's properties under the influence of the pump pulse. Both pulses are detected on separate diode arrays. The signals from same photon energies are electronically subtracted and afterwards digitalized in the A/D converter of the data acquisition board.

Detection unit The detection unit is a homemade prism-spectrometer with a very fast read out. The beam is coupled into the prism at the Brewster angle. The prism splits the white light into it's spectral components. An array of 31 equivalent silicon diodes on reverse voltage linearly respond to the incoming light (Diode Arrays). Each diode detects the light in a different wavelength range. The response of the diode generates a current which gets amplified and finally digitalized in an A/D converter. Each diode has its own amplifier, the probe and the reference signals are subtracted electronically and the combined signal is the input of an A/D converter of a commercial multi-channel measure card. The measure card is triggered by the shaker and samples with the frequency of the regenerative amplifier. The wavelength range between 450 nm and 900 nm with a sub-100fs time-resolution is covered by this setup. The time resolution is basically given by the pulse duration of the output of the amplifier, it may slightly increase during the phase modulation in the sapphire crystal. The setup switches between reflection and transmission geometry by moving mirror M13 with Stage2. Both geometries are adjusted in a way, that the same spectral parts of the white light focus on the same diode. The mirrors M9-12 are used to steer the beams through the prism at the diode arrays. L3 and L4 are achromats which refocus on the detector to achieve the best possible wavelength resolution.

Pump modulation unit The basic optics of the pump modulation unit are L1 to focus the pump onto the sample (about 120 µm) and M3 which is used to optimize the spacial overlap between pump beam and probe beam in the sample. Special improvements to diminish the low frequency noise, which is mostly caused by the shaker, are made by performing additional reference measurements. An additional reference measurement is recorded using a lockin technique. The highest possible modulation frequency is half the frequency of the laser repetition rate, therefore the best possible modulation is the modulation with a frequency, where every second pump pulse is cut out. An electro-optic modulator (EOM) or Pockel's cell is tuned to change the polarization of every second pulse by 90°. An analyzer (PBSC2) is used to filter these pulses. The detector possess a high enough bandwidth to subtract the signal measured without excitation from the signal measured with excitation. In contrast, a mechanical chopper can only reduce the noise at very low frequencies or slow drifts of the laser beam, which arise from the shaker. In the special configuration of cutting the pump pulses with a mechanical chopper during every second shaker period, it is possible to reduce the noise arising from the mechanics of the shaker. The chopper can only be used, if the sample does not show significant steady state heating under influence of the train of many pump pulses. In the case of pronounced heating the chopper opens and the sample slowly heats up. After the chopper closes the sample cools down. In this case, the reference measurement is taken at a different temperature.

5.1.4 Setup calibration

The shaker, the detector and the spot sizes have to be calibrated in the setup.

Energy calibration The wavelength or photon energy of the light detected on each element of the diode array is determined in the energy calibration procedure. Different bandfilters are introduced into the white light to filter out small fractions of the spectrum. The filtered light arrives at one or two diodes of the detector. This procedure allows the direct calibration of a few channels. All other channels are calibrated by extrapolation. In a fit procedure the input angle of the light into the prism is varied under consideration of the refraction of the prism, the distance to the detector and the calibrated channels. The fit procedure results in the calibration of all channels.

Time calibration The shaker produces a periodical time delay (sinusoidal). This periodical time delay is calibrated with the mechanical delay-stage, which can be moved in calibrated steps. The transient of a sample with high signal to noise ratio is measured at different stage positions. The peak- or an edge-position of the transient give a good reference point. This position is related to the calibrated time steps of the stage. All the data points of a transient are assigned to the different time delays by extrapolation of the calibrated time steps with sinus functions.

Spot size calibration The foci of the pump and probe beams are measured at the sample's position with a CCD-camera. The known pixel size allows to reconstruct the gaussian beam profile and to determine the full width at half maximum of it. The white light pulses are measured with different bandpass filters. The spot sizes are below 50 µm at every measured wavelength.

5.1.5 Excitation density calculation

A rough estimate of the excitation power can be achieved by subtracting the power of reflected and transmitted light from the power of the incoming light. This method overestimates the absorbed power because the scattered light is not taken into account. If the material has high reflectivity and the surface is grainy (grain sizes in the range of the wavelength of the light or larger), then the absorbed power is lower compared to the estimated value. This method may thus fail on metals in the infrared range. In Cu the reflectivity below $\mathrm{h}\nu = 1.7\,\mathrm{eV}$ is above 95 %. If the optical properties of the material are known, then R and T are calculated with the Fresnel equations and the thin film equation [DAP94a; DAP94b]. The absorbed excitation density reads

$$\bar{U}_{\mathsf{abs}} = F \cdot (1 - R - T)\,/d\,, \tag{70}$$

d is the light penetration depth of the bulk sample or the thickness of the film. The fluence F is

$$F = \frac{P}{f \cdot \pi/4 \cdot \sigma_{\mathsf{FWHM}}^2}\,,$$

P denotes the averaged power, f is the repetition rate of the laser and σ_{FWHM} the full width at half maximum of the gaussian beam profile inside the sample. The energy density absorption rate follows the temporal profile of the pump pulse, it is

$$\frac{\partial U_{\mathsf{abs}}}{\partial t} = \bar{U}_{\mathsf{abs}} \cdot \frac{2\sqrt{2\,\ln(2)}}{\sigma_{\mathsf{FWHM}}\sqrt{2\,\pi}} \cdot \exp\left(-\frac{1}{2}\left(\frac{2\sqrt{2\,\ln(2)}}{\sigma_{\mathsf{FWHM}}} \cdot t\right)^2\right).$$

5.2 Dynamics of R and T

Thin copper films (24 nm thick) are measured with an ultrafast pump- and broadband-probe technique, which is described in the Section 5.1. The sample is excited with laser pulses centered at 1.55 eV and with a pulse duration of 50 fs. The pump pulses can excite electrons from the occupied states of the conduction into the empty states of the conduction band only. The full width at half maximum of the pump spot at the sample's position is 160 µm, which is more than two times the size of the probe spot. The excitation fluence is varied to span nearly two orders of magnitude in excitation density. These fluences between 530 µJ/cm^2 and 16.7 mJ/cm^2 are sufficient to transiently heat up the excited volume of the sample by 3 K at the lowest excitation density and up to 90 K at the highest excitation density.

The dielectric function consists of a real and an imaginary part. Although they are related via Kramers-Kronig (see for example [DG02]), it is advantageous to measure the optical properties in two different configurations, in the reflection and the transmission geometry. The Fresnel equations and the thin film equation connect ϵ with (R,T) [DAP94a; DAP94b]. This allows us to determine the dielectric function directly, where (ϵ_1,ϵ_2) are varied to reproduce (R,T) at each wavelength. The changes in reflectivity are measured subsequently to the changes in transmission at each fluence to ensure that both datasets are measured under the same pumping conditions. The probe pulses spanning one octave in frequency cover most of the dynamics around the upmost d-band to Fermi level transition. The chirp (the higher frequency components of the pulse are delayed compared to the lower frequency components because of lenses or windows in the beam path) of the white light pulses is corrected in the data analysis procedure. It is determined by the amount and the dispersion of the transparent media, where the probe beam has passed through. The recorded relative changes in R and T are presented in Figure 31. Although the pump pulses excite the electrons only within the conduction band, $\Delta R/R$ and $\Delta T/T$ are mostly related to changes of the interband transitions between the upmost d-band and the Fermi level. This is seen as the pronounced feature around the onset of the interband transitions at $\approx$ 2.1 eV. After excitation, the local minimum of R at 2.2 eV is reduced at all time delays (compare inset on Figure 31**A**). The local maximum at 2.6 eV is much less affected. In transmission the maximum at 2.15 eV and the kink at 2.35 eV are red shifted (inset on Figure 31**B**). The main reason for these signals are the changes in the electronic distribution near E_F, which affect the transition probability from the upmost d-band to the Fermi level, as already

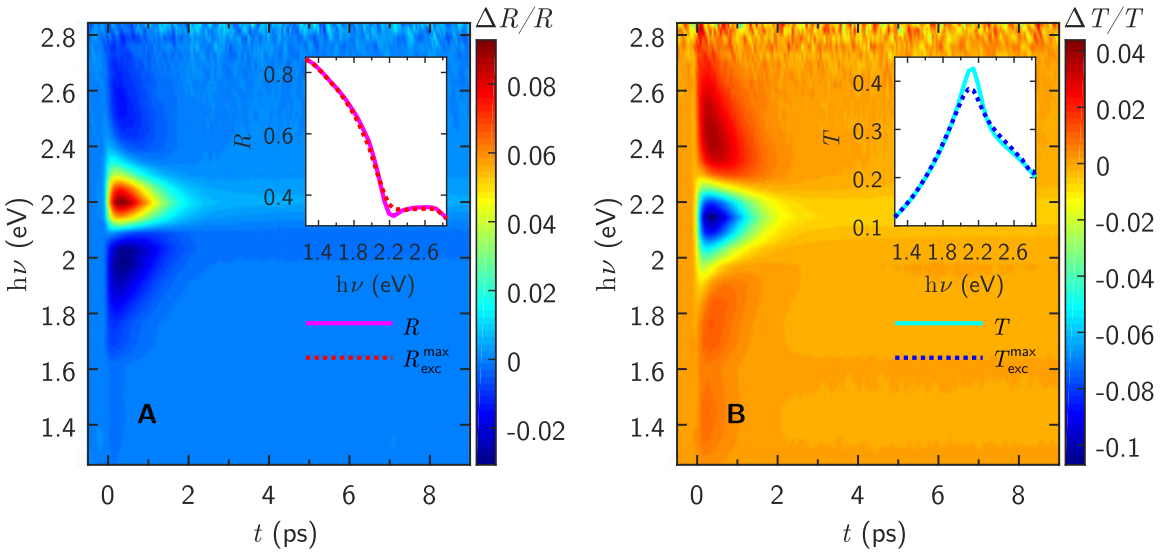

Figure 31: **Recorded relative changes in R and T of a thin copper film ($\bar{U}_{\text{abs}} = 99\,\text{J/cm}^3$).** The measured signal is pronounced around the interband transitions from the upmost d-band to the Fermi level. The signals increase during the first 350 fs and partially recover within the following 3 ps to an offset value. Note the different zero levels in both graphs. **A** presents the measured signal in the reflection geometry $\Delta R/R$. The separation between the upmost d-band and the Fermi level is close to the zero crossing of the bipolar response. **B** The minimum in $\Delta T/T$ corresponds to the separation between the upmost d-band to Fermi level.

discussed in Section 4.3. The structure in the optical properties which is related to these transitions smears out as a consequence of the changes in the electronic distribution function, Δf, at the Fermi level.

The time evolution of the spectral shape is analyzed first by normalization of the spectra to the maximum change at each time delay. A change of the spectral width over time allows to distinguish whether the signal is based on the change in the matrix element, on an energy shift or on a change in the characteristic width of the measured feature. The result is presented in Figure 32**A** and **B**. The relaxation of the spectral shape of $\Delta R/R$ and $\Delta T/T$ shows a characteristic narrowing in time. This spectral narrowing is related to the upmost d-band to Fermi level transitions (see Figure 32**C** and **D**) and has its origin in the spectral width of Δf at the Fermi level (Section 4.3). If the electrons are in thermal equilibrium, this the spectral width of Δf is expected to linearly decrease with a decreasing electronic temperature

$$\Delta w = w_0 + 2 \cdot \mathrm{k_B}\, \Delta T_{\mathrm{el}} \tag{71}$$

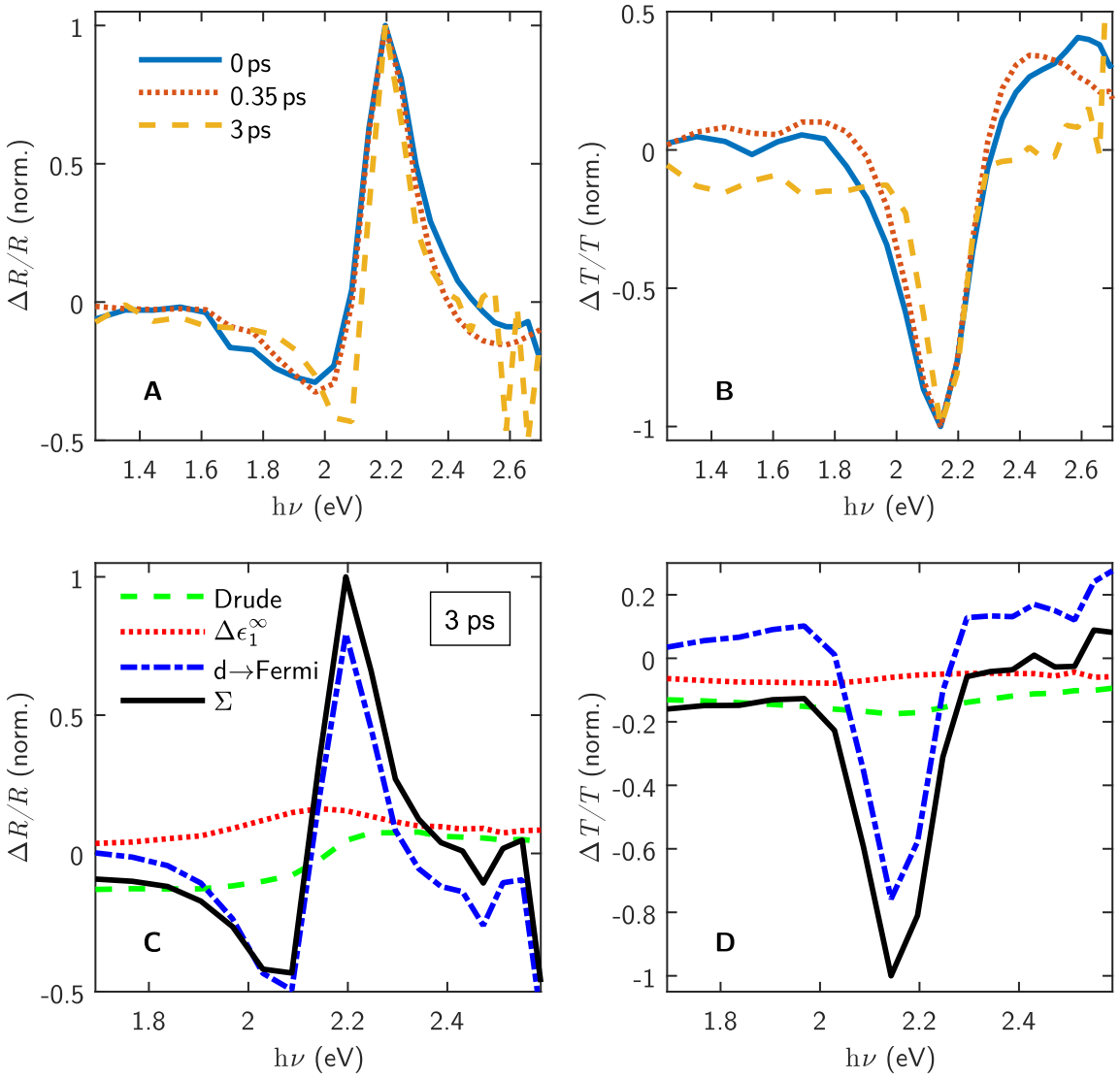

Figure 32: **Spectral shape of $\Delta R/R$ and $\Delta T/T$ over time and spectral analysis ($\bar{U}_{\text{abs}} = 99\,\text{J/cm}^3$).** The spectra are normalized to the extremal change. **A** and **B** The feature at 2.15 eV is seen in $\Delta R/R$ and $\Delta T/T$ and it narrows in time. The spectra are taken at the position of the pump pulse (0 ps), the position of the maximum change (0.35 ps) and at 3 ps, where electrons and phonons are almost thermalized. The response is decomposed into its components after 3 ps and it is presented in **C** and **D**. Most of the signal originates from the upmost d-band to Fermi level transitions. The additional components are more or less spectrally flat and they have less spectral weight in this spectral range. The component analysis is based on the thermomodulation fits of Section 5.3 and the linearized Fresnel equations (Section 5.4.1).

as further discussed in Subsection 5.2.1.[25] w_0 is a constant offset which is related to the damping constant γ of the upmost d-band to Fermi level transitions (see Section 4.3.1). The resonant

[25] In thermal equilibrium ΔT_{el} is proportional to the width of Δf; Δw is the convolution of Δf with an almost temperature-independent factor (essentially the Lorentz factors in the equations (53) and (54)). This results in the presented linear equation.

transition is at 2.14 eV, which corresponds to the transition between the initial states at the maximum of the density of states of the upmost d-band and the final states at the Fermi level. This photon energy is almost an isosbestic point in the data.

The flat spectral parts of the transmission (e.g. below 1.8 eV) rise on a longer timescale of about 1 ps. This timescale corresponds to the rise of the lattice temperature. This feature is hard to observe in the reflectivity data, it is visualized in Figure 32**C**. The intraband transitions (Drude) and $\Delta\epsilon_1^\infty$ are responsible for this spectrally flat feature with slow rise time. $\Delta\epsilon_1^\infty$ has no effect on the absorption, but changes in the Drude response lead to a reduction of the reflectivity and the transmission. This gives an increased effective absorption

$$\Delta A = 1 - \Delta R - \Delta T$$

(A is different from the absorbance which is related to the transmission data only). At 0 ps,[26] $\Delta R/R$ is almost equal to $\Delta T/T$, resulting in a small change of ΔA. Over time, $\Delta R/R$ evolves to get more bipolar (negative below 2.1 eV and positive above this point). $\Delta T/T$ is finally negative at all measured photon energies with its minimum value at 2.15 eV. It is clear from this rough analysis that the absorption ΔA rises over time at most photon energies.

The spectra at higher excitation densities are broader compared to the ones described in Figure 32, while the maximum changes in R and T rise approximately linearly with increasing excitation density.

5.2.1 Relaxation of the spectral response

The width of the d-band to Fermi level resonance around 2.14 eV is continuously decreasing over time to the final offset value of $w_0 + 2 \cdot \mathrm{k_B}\ (T_{\mathsf{new}} - T_0)$ according to equation (71). The temperature rise of the sample to the final temperature T_{new} is due to the absorbed energy density (discussed in Section 5.3; equation (72)). The characteristic width of the resonance can be defined using the contour lines at $\pm 1/\mathrm{e}$ of the normalized spectra. These lines are added to the normalized 2D-plots of $\Delta R/R$ and $\Delta T/T$ in Figure 33**A** and **B**. The relative width $\Delta w(t) = w(t) - w(5\,\mathrm{ps})$ is compared to $\Delta R/R(2.2\,\mathrm{eV})$ (it is shown below, in Section 5.8.1 and Figure 55, that $\Delta R/R(2.2\,\mathrm{eV})$ is proportional to ΔT_{el}) in Figure 33**C** and **D** at low and high excitation densities. As elaborated in Section 5.7,

[26] 0 ps is defined, that it corresponds to the time, where the measured quasiparticle response has grown to half of its maximum signal strength. This calibration is done at one excitation density in transmission and used for reflectivity as well and for the other datasets at all different excitation densities.

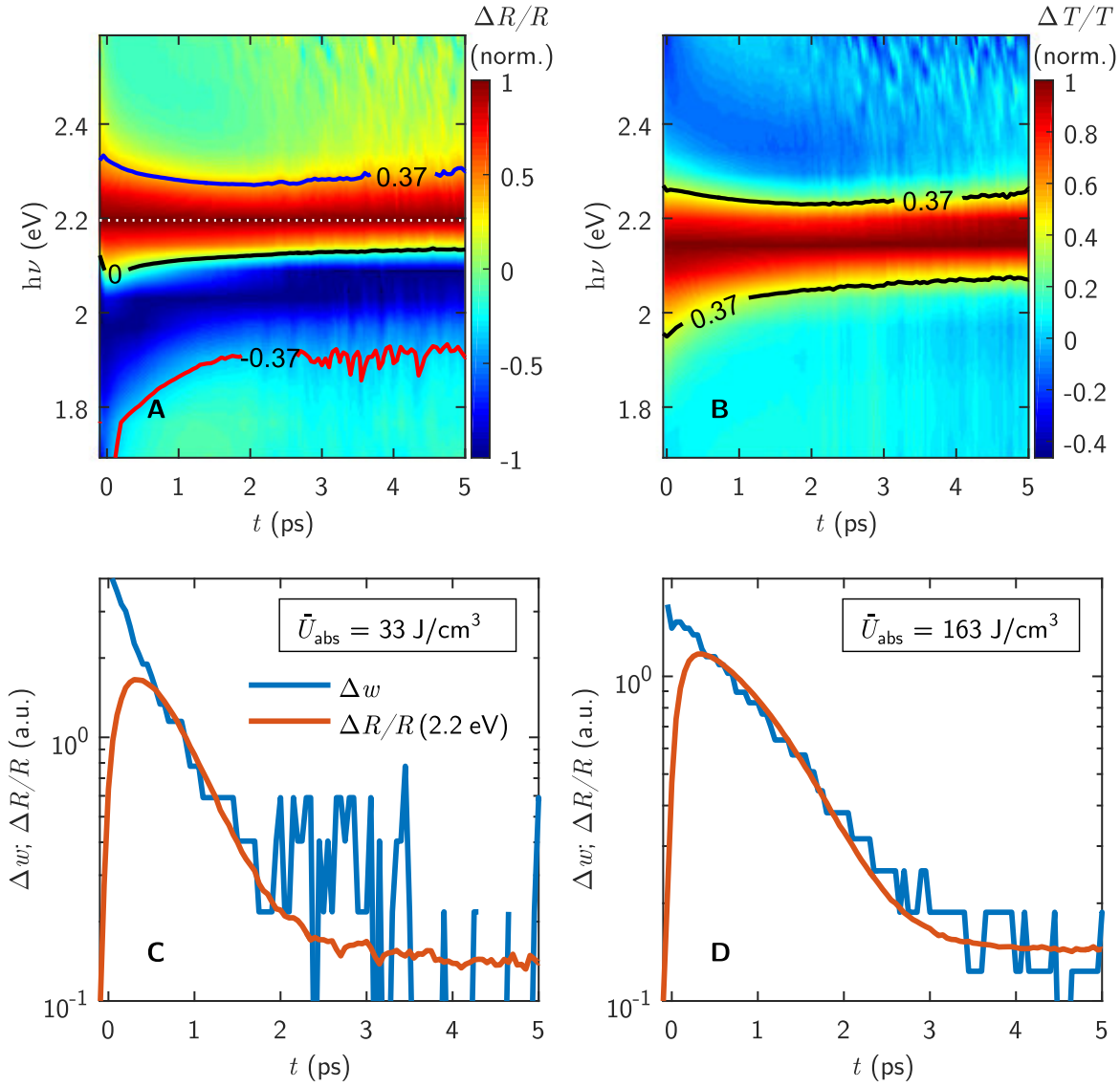

Figure 33: **The spectral dynamics of $\Delta R/R$ and $\Delta T/T$.** The spectra of $\Delta R/R$ (plotted in **A**) and $\Delta T/T$ (plotted in **B**) are obtained from data plotted in Figure 31, where at each time delay the data is normalized to the peak (in **A** the spectrum is separately normalized to 1 and -1 in the range above and below the 0 contourline to get a proper definition for the spectral width of a bipolar but asymmetric signal). The widths w are visualized with the contour lines at $\pm 1/e$ and demonstrate the spectral narrowing in time. In **C** and **D** Δw (from $\Delta T/T$) is plotted as a function of time at $\bar{U}_{abs} = 33\,\mathrm{J/cm^3}$ and $\bar{U}_{abs} = 163\,\mathrm{J/cm^3}$ (blue lines). The relaxation curve of $\Delta R/R$ at the resonance frequency (red curve) shows an initial increase followed by a relaxation, contrarily Δw starts at a high level (very broad spectrum) and decreases over time. The transients are normalized to the values at the electron thermalization time (the values are taken from Section 5.7). Note, the red and the green lines overlap before the electrons are thermalized.

ΔT_{el} is well defined only after a few hundred femtoseconds, and after the electrons are thermalized, equation (71) holds. The initial width of Δf, which is on the order of the photon energy of the

excitation ($\mathrm{h}\nu = 1.55\,\mathrm{eV}$), implies that Δw starts at the same large initial value regardless of the excitation density. Δw decreases continuously afterwards. The experiment shows that during the first few hundred femtoseconds the decay of Δw (and with it also Δf) at low excitation densities is faster compared to the decay at high excitation densities. Interestingly, Δw does not show any kink or discontinuity corresponding to the electron thermalization time. Further, the normalized Δw and $\Delta R/R(2.2\,\mathrm{eV})$ overlap already before the electrons are thermalized (referring to the electron thermalization time as determined in Section 5.7). The reason for this is, that the non-thermally distributed high energy quasiparticles contribute to the signal with very small signal strengths (small wings with $|\Delta T/T|_{\text{non-thermal}} < 1/\mathrm{e}$ and thus they are neglected in this analysis).

5.3 Thermomodulation fits

In Chapter 4 it is shown that the temperature dependent optical properties can be described using the previously introduced simple model, just containing a few parameters. Of particular interest in this work is the extraction of the photo-induced changes in the electronic distribution function. At first the conventional thermomodulation analysis was applied to the data (studying changes in optical constants upon heating the sample by ΔT), where we know that the electronic distribution is in thermal equilibrium. In this way the simple model of the optical properties can be parametrized and used in a second step to study changes in the distribution function in non-equilibrium.

The time-resolved data of $\Delta R/R$ and $\Delta T/T$ show the relaxation to some constant value, which is reached after about 5 ps. Thereby the metal reaches a new thermal equilibrium at a temperature higher temperature compared to the temperature before the excitation. The optical properties (and therefore $\Delta R/R$ and $\Delta T/T$) further evolve on a nanosecond timescale, on which the introduced heat is dissipated to the substrate. The temperature of the quasi-equilibrium state at 5 ps can be calculated from the absorbed energy (equation (70)). The energy conservation law gives

$$T_{\text{new}} = T_0 + \bar{U}_{\text{abs}}/c_{\text{V}}\,. \tag{72}$$

According to Section 4.7, the thermomodulation response is described by equations (65) and (66). To parametrize the model for the optical properties of Cu thin films, which is necessary to describe the thermomodulation, we have performed systematic studies. $\Delta R/R$ and $\Delta T/T$ are measured at 12 different excitation densities[27]. In addition the equilibrium R and T are measured in a

[27] The maximum values of $\Delta R/R$ and $\Delta T/T$ scale approximately linear with excitation density. However, a rescale of the response measured at one excitation density does not coincide with the response at a different excitation density because the relaxation in $\Delta R/R$ and $\Delta T/T$ takes longer the higher the excitation density.

$\hbar\omega_p$ (eV)	$\gamma_{D,0}$ (meV)	$\partial\gamma_D/\partial T$ (μeV/K)	M_{cu} (10^5 m/s)	$E_{G,0}$ (eV)	$\partial E_G/\partial T$ (μeV/K)	$\partial\epsilon_1^\infty/\partial T$ (10^{-4}/K)
9	56.8	48.4	1.05	2.143	-21.41	-2.39

Table 6: **Adjusted fit parameters to reproduce the thermomodulation and equilibrium optical responses.** The listed fit parameters are adjusted to give best agreement between the measured and simulated R, T, $\Delta R/R$ and $\Delta T/T$. The fit parameters agree (they are in the same range) with the parameters which are able to reproduce published temperature dependent and thermomodulation optical properties of Cu (see Table 5). The additional parameters used in the thermomodulation fits are given in Table 7. Those parameters are not varied in order to improve the consistency between model and experimental result.

M_{di} (10^{-11} m)	$\epsilon_{1,0}^\infty$	E_{BW} (eV)	γ (meV)	Θ_D (K)	$D(E_F)$ (1/(eV atom))
3.85	1	0.5	30	303	0.293

Table 7: **The sample independent model parameters.** The fitting of the published optical properties of Cu show that some parameters do not need to be adjusted in order to achieve good agreement between the model and the experimental optical properties.

FTIR-spectrometer (Bruker Corp., Billerica, USA) and $\Delta T/T$ is measured with a conventional thermomodulation technique (modulation of the temperature with Peltier-elements inside a commercial uv-vis spectrometer). The dielectric function is related to R and T with Fresnel equations and thin film formula taken from [DAP94a; DAP94b]. All the measurements are made on the same thin Cu film with a film thickness of 24 nm (the film thickness is known from the growing rate and growing time). All the data is reproduced with a single set of parameters given in the Tables 6 and 7. A few parameters are known to be sample independent and taken from the previous analysis on published optical properties (Section 4.6; Table 7). The more sensitive parameters, which are sample or experiment specific[28] (see Section 4.6), are varied to reproduce the experimental R and T, as well as the thermomodulation $\Delta R/R$ and $\Delta T/T$. The result of the fit procedure is presented in the Figure 34 and the related parameter values are given in Table 6. Figure 34**A** presents the equilibrium data and **B** the fitting of the thermomodulation response ($t = 5$ ps) at the excitation density of 99 J/cm^3.

[28]The parameters used for different samples may differ because of different grain sizes, strains, orientation of the grains, surface roughness, CuO overlayers, impurity concentrations or any systematic error in the data processing procedure.

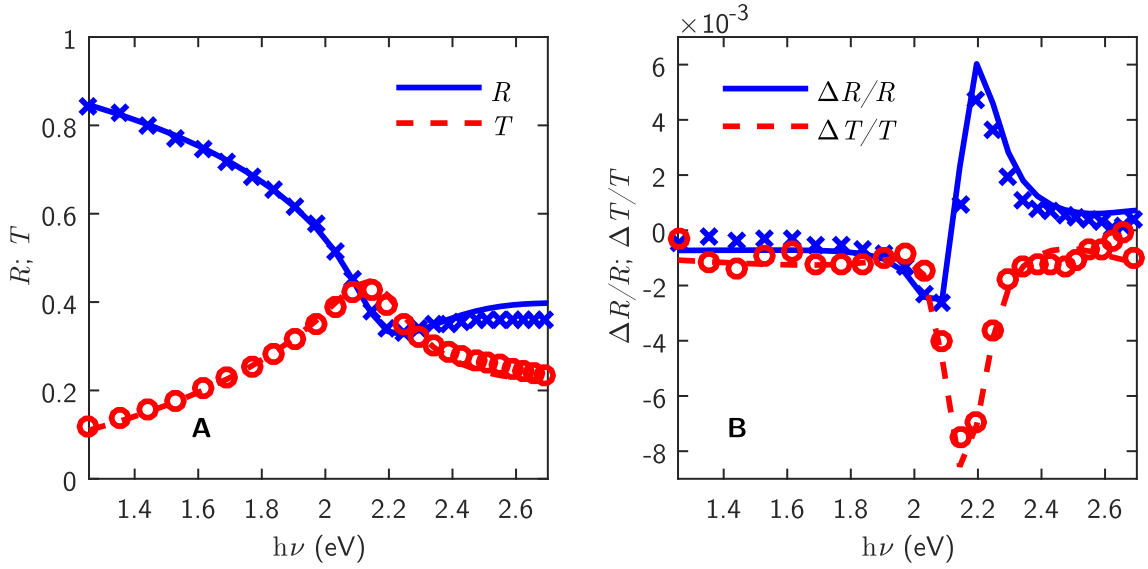

Figure 34: **Comparison between the measured and simulated equilibrium and thermomodulation spectra of R and T.** The model parameters are determined from the global fit of 12 thermomodulation measurements taken from ultrafast pump-probe experiments (Section 5.2), the equilibrium measurement of R and T at room temperature and a slow-scan thermomodulation spectrum measured with UV-Vis-spectrometer and Peltier elements. The fitted model is known from equations (65) and (66). **A** Reflectivity (blue) and transmission (red) of the thin copper film are measured at 300 K. The points are the result of the measurement and the curves are based on the global fit. **B** The thermomodulation of R and T. The data is taken from dynamic data averaged in the range between 5 ps and 9 ps measured at $\bar{U}_{\text{abs}} = 99\,\text{J/cm}^3$. The pump pulse heats up the sample by about 29 K.

5.4 Reconstruction of $\Delta\epsilon$ from experimental $\Delta R/R$ and $\Delta T/T$

The result of Section 5.3) allows to determine the sample dielectric function ϵ. ϵ consists of a real and an imaginary part and depends on the photon energy and the temperature. The photon energy dependence is shown in Figure 35. The shape of the depicted dielectric function is characteristic for Cu and close to the reported dielectric function [HLB82; JC72; PS69; Rob60; JK54]. Although comparable, ϵ varies for different samples which is known from the analysis of the published data described in Section 4.6. Thus, it is important to use ϵ which is characteristic for the sample in the reconstruction procedure of $\Delta\epsilon$. This keeps the systematic error minimal.

The result of the reconstruction of $\Delta\epsilon$ is presented in Figure 36**A**. The solid lines correspond to the simulation of $\Delta\epsilon$ based on the model (see equations (65) and (66)), whose parameters are adjusted to describe the thermomodulation response (see Section 5.3). The directly reconstructed $\Delta\epsilon$ (using Fresnel equations and R and T from the simulation) is illustrated by the crosses which are connected

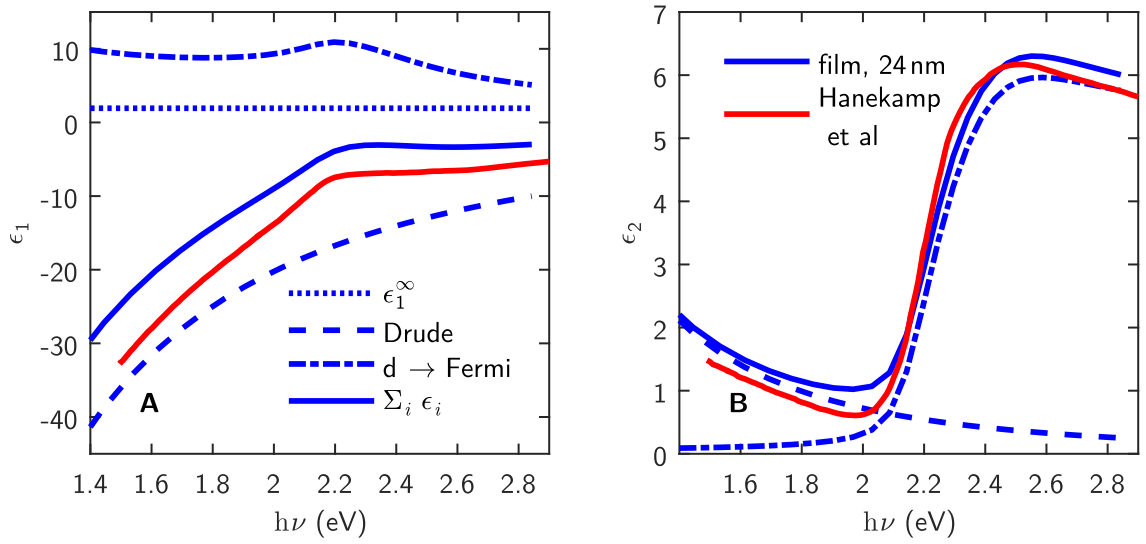

Figure 35: **Simulated ϵ_1 and ϵ_2 at 300 K.** The dielectric function (Σ) of the 24 nm thick film (blue solid lines) is compared to ellipsometric measurements of bulk Cu by Hanekamp et al. [HLB82] (red solid lines). The different additive contributions to the dielectric function are plotted with dotted, dashed dotted and dashed lines (contributions from higher energetic transitions, upmost d-band to Fermi level transitions and intra-conduction-band transitions). **A** Real part of the dielectric function. **B** Imaginary part of the dielectric function.

by dashed lines in Figure 36**A**. The reconstruction procedure is described in the following paragraph. First R and T are determined from the simulated ϵ of the sample at room temperature. This allows to calculate the changed reflectivity and transmission, $\mathrm{d}R = \Delta R/R \cdot R + R$ and $\mathrm{d}T = \Delta T/T \cdot T + T$. Afterwards the method of least squares was applied to find the corresponding $\mathrm{d}\epsilon$ (consisting of real and imaginary parts). The resulting $\Delta\epsilon$ corresponds to the measured $\Delta R/R$ and $\Delta T/T$ and is plotted using crosses in Figure 36**A**. The arising deviations between the simulated and the reconstructed $\Delta\epsilon$ are basically caused by the deviations between the experimental and the model based $\Delta R/R$ and $\Delta T/T$. The deviation between the experimental $\Delta\epsilon$ and the simulated $\Delta\epsilon$ shows a different spectral characteristic compared to the differences between experiment and simulation of $\Delta R/R$ and $\Delta T/T$ (compare Figure 36**A** with Figure 34**B**). In particular, the deviations between the differently determined $\Delta\epsilon$ are pronounced around 2.4 eV, although the deviations in the data of $\Delta R/R$ and $\Delta T/T$ are small in the same energy range. The deviation is seen at all excitation densities with similar relative amplitudes and is thus systematic and may be related to the influence of high energy interband transitions (effects which are beyond the assumed energy independent contribution ϵ_1^∞). More details about the deviation enhancement are given in Subsection 5.4.1.

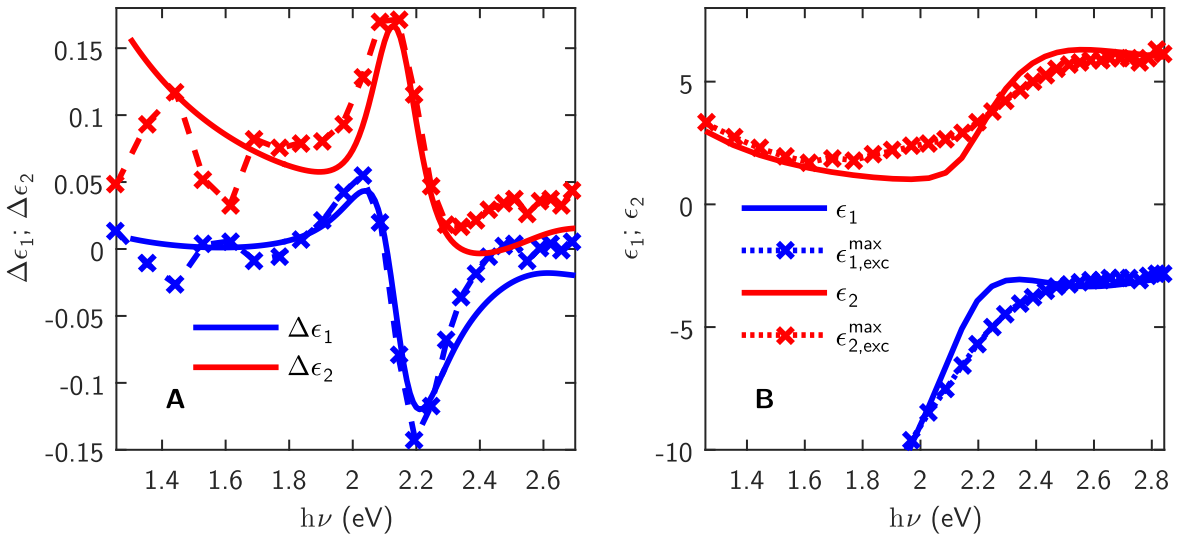

Figure 36: **Thermomodulation and maximum change in ϵ at $\bar{U}_{abs} = 308\,J/cm^3$. A** $\Delta\epsilon$ is simulated based on the model and parameters of Section 5.3 (solid lines). For comparison, $\Delta\epsilon$ is reconstructed from the measured $\Delta R/R$ and $\Delta T/T$ (dashed lines, details about the procedure are in the main text). **B** This graph shows the equilibrium ϵ in comparison to the maximally changed ϵ (ϵ_{exc}^{max}) taken at the highest highest excitation density which was used and at a delay time of 0.35 ps. The maximum in ϵ_1 at 2.2 eV is suppressed whereas the cutted part of ϵ_1 below 2 eV is not much affected from excitation. In ϵ_2 the edge at 2.2 eV flattens. Note that there is a difference in the x-axes of both graphs.

The same method of least squares is used to extract $\Delta\epsilon$ at short time delays from the experimental $\Delta R/R$ and $\Delta T/T$. The theoretic description of the upmost d-band to Fermi level transitions shows that $\Delta\epsilon$ depends on Δf. Therefore, $\Delta\epsilon$ contains the information about Δf. In a further step, the theory about the upmost d-band to Fermi level transitions can be used to reconstruct Δf from the experimental $\Delta\epsilon$ at short time delays. In Figure 36**B** the maximum change in ϵ is presented and it is shown that the characteristics of the previously mentioned d-band to Fermi level transitions flatten at short time delays. In ϵ_1 the maximum at 2.2 eV is reduced and in ϵ_2 the edge near 2.2 eV is smoothed out.

$\Delta\epsilon$ is extracted from the experimental $\Delta R/R$ and $\Delta T/T$ with the method of least squares described above. This procedure was applied successively on every experimentally gained data point (at different photon energies, time delays and excitation densities) to determine $\Delta\epsilon(\nu, t)$. The result at $\bar{U}_{abs} = 99\,J/cm^3$ is presented in Figure 37. Again, the photo-induced changes are mainly a broadening of the characteristic upmost d-band to Fermi level transitions. The change in ϵ_2 leads to a flattening of the edge at 2.1 eV and a lowering of the maximum at 2.4 eV. Between 2.1 eV and 2.4 eV

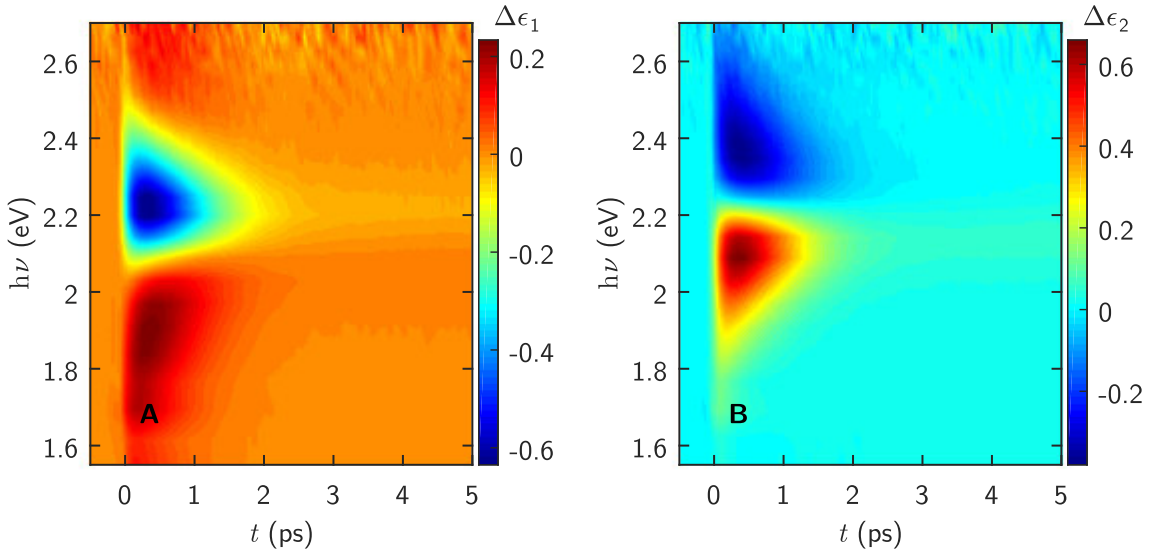

Figure 37: **Dynamics of the dielectric function ($\bar{U}_{\text{abs}} = 99\,\text{J/cm}^3$).** The changes are based on the experimental $\Delta R/R$ and $\Delta T/T$ and the samples ϵ at room temperature which is known from the thermomodulation fit procedure (Section 5.3). The main contribution to the signal is caused by the upmost d-band to Fermi level transition (compare Figure 39). **A** The time evolution of the change in the real part of the dielectric function is shown. The extremum of $\Delta\epsilon_1$ is at 2.2 eV. This change lowers the kink known from equilibrium data, see Figure 35**A**. **B** The time evolution of the change in the imaginary part of the dielectric function is shown. The maximum at 2.1 eV corresponds to a flattening of the edge which is known from equilibrium data ϵ_2 (Figure 35**B**).

there is a zero crossing acting as an isosbestic point. The change in ϵ_1 is mostly a lowering of the peak at 2.2 eV (referring to the equilibrium data, see Figure 35**A**) and an increase around the position of the minimum at 1.9 eV. In between there is no isosbestic point. The time evolution of $\Delta\epsilon$ is similar to the time evolution of $\Delta R/R$ and $\Delta T/T$. The relaxation times are the same and the spectra narrow over time (see Figure 39).

5.4.1 Fresnel equations and the thin film equation in the perturbative regime

The idea behind this subsection is to linearize the Fresnel equations in combination with the equation for thin films for small changes in R and T. The small changes in R and T linearly depend on $\Delta\epsilon$

$$\frac{\Delta R}{R} = \frac{\partial \ln(R)}{\partial \epsilon_1}\Delta\epsilon_1 + \frac{\partial \ln(R)}{\partial \epsilon_2}\Delta\epsilon_2\,, \tag{73}$$

$$\frac{\Delta T}{T} = \frac{\partial \ln(T)}{\partial \epsilon_1}\Delta\epsilon_1 + \frac{\partial \ln(T)}{\partial \epsilon_2}\Delta\epsilon_2\,, \tag{74}$$

with unknown partial derivatives. This approximation seems to be appropriate for Au using small input angles at optical frequencies [Sun+94; DV+12]. The coefficients can be determined using a set of thermomodulation data (at least two datasets). First of all, $\Delta\epsilon$ is determined by the procedure described in Section 5.4. In a second step, a fit procedure is performed to connect $\Delta R/R$ and $\Delta T/T$ to $\Delta\epsilon$ at different excitation densities using equation (73) and (74). The insets to Figure 38 show the results. Although the relations between $\Delta\epsilon$ and $\Delta R/R$ and $\Delta T/T$ include terms which are not linear, the linearized Thin-Film-Fresnel-Equations (73) and (74) can reproduce $\Delta\epsilon$ based on experimental $\Delta R/R$ and $\Delta T/T$ at every time delay. The comparison is presented in Figure 38. Here

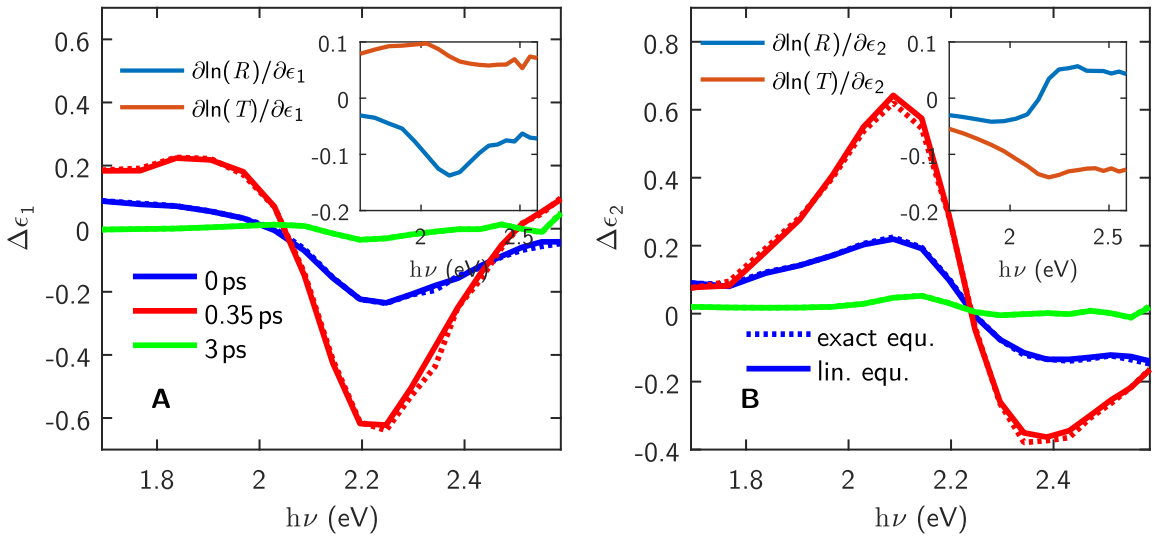

Figure 38: **The result of $\Delta\epsilon$ from the experimental $\Delta R/R$ and $\Delta T/T$ - exact vs. linearized approach.** $\Delta\epsilon$ (**A** shows $\Delta\epsilon_1$ and **B** shows $\Delta\epsilon_2$, both share the same legends) is determined in two different ways. The results on both ways are plotted at three different time delays. The dotted lines present $\Delta\epsilon$ from the experimental $\Delta R/R$ and $\Delta T/T$ based on the analytic expression with the Fresnel equations and the equation for multiple reflections in thin films [DAP94a; DAP94b]. The solid lines are based on the equations (75) and (76). The insets show the coefficients, which are determined from the experimental data ($\Delta R/R$ and $\Delta T/T$) at different excitation densities and the corresponding $\Delta\epsilon$ from Section 5.4.

the inverse functions are used:

$$\Delta\epsilon_1 = \frac{\frac{\partial \ln(T)}{\partial \epsilon_2}\frac{\Delta R}{R} + \frac{\partial \ln(R)}{\partial \epsilon_2}\frac{\Delta T}{T}}{\frac{\partial \ln(R)}{\partial \epsilon_1}\frac{\partial \ln(T)}{\partial \epsilon_2} - \frac{\partial \ln(R)}{\partial \epsilon_2}\frac{\partial \ln(T)}{\partial \epsilon_1}}, \tag{75}$$

$$\Delta\epsilon_2 = \frac{\frac{\partial \ln(T)}{\partial \epsilon_1}\frac{\Delta R}{R} + \frac{\partial \ln(R)}{\partial \epsilon_1}\frac{\Delta T}{T}}{\frac{\ln(R)}{\epsilon_2}\frac{\partial \ln(T)}{\partial \epsilon_1} - \frac{\partial \ln(R)}{\partial \epsilon_1}\frac{\partial \ln(T)}{\partial \epsilon_2}}. \tag{76}$$

5.5 Assignment of the parameters of the optical properties to Δf- or T_{la}-sensitive parameters

In order to study the measured spectra and their time dependence in more detail, it is helpful to decompose the spectra into its components: the intraband transitions, the upmost d-band to Fermi level transitions and the influence of high energy interband transitions on the dielectric function. Since the goal is to determine the time evolution of the electronic distribution function, it is also important to consider the effect that might be related to the lattice heating. For example, the changes in the Drude response are a result of changes in the Drude scattering rate, which is in turn linked to the changes in the lattice temperature, T_{la} (note that at room temperature the conductivity is determined by the electron-phonon scattering rate). Since the electrons and the lattice are thermalized on the picosecond-timescale (see Figure 31), and the absolute increase of the sample's temperature is known from the energy conservation law (the excitation density is determined with high accuracy), the next step is to consider the contributions to $\Delta\epsilon$ due to the lattice heating.

The lattice is assumed to heat up to its final temperature with a time constant of about 1 ps which depends on the excitation density. Indeed, for the further data analysis an exponential time dependence was used with the time constant equal to the relaxation time of the spectrally integrated $\Delta T/T$ and $\Delta R/R$. The Drude scattering rate γ_{D} and ϵ_1^∞ are assumed to linearly depend on the lattice temperature. The temperature dependencies of these parameters are known from the thermomodulation fits (see Section 5.3, Table 6, T is replaced by T_{la}). These two components are linked to the lattice temperature (as opposed to the link to the dynamics of the electronic subsystem). This link is supported by their spectral shapes and their slow rise times observed in the experimental $\Delta\epsilon$ (see Figure 39). The lattice temperature does not change much during the first 0.35 ps. Yet, after 3 ps the lattice temperature has almost reached its highest value. The sign of $\Delta\epsilon_1$ changes at about 1.8 eV after 3 ps which is linked to the contribution of $\Delta\epsilon_1^\infty$. Furthermore, Figure 39 shows the characteristic line shape of the upmost d-band to Fermi level transitions narrowing on the energy axis with increasing time delay.

The change in the Drude response affects the imaginary part of the dielectric function stronger than the real part, despite the fact that in equilibrium the contribution of the Drude component to ϵ_1 is much larger than to ϵ_2. To further investigate on the upmost d-band to Fermi level transitions, one can easily subtract the T_{la}-dependent changes of the Drude- and ϵ_1^∞-component from the experimen-

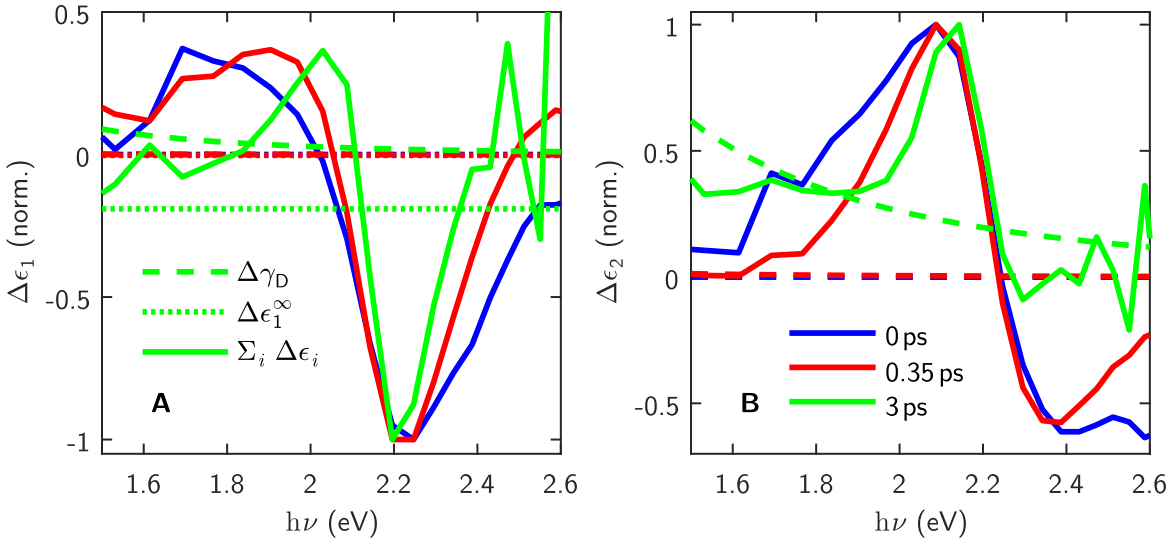

Figure 39: **Spectral relaxation characteristics of $\Delta\epsilon$.** The spectra are taken at different time delays (after 0 ps, 0.35 ps and 3 ps) and normalized to their extremal values. The excitation density is $\bar{U}_{\text{abs}} = 99\ \text{J/cm}^3$. **A** Time evolution of $\Delta\epsilon_1$. The spectral characteristic of the d-band to Fermi level transitions narrow over time. After 3 ps, $\Delta\epsilon_1^\infty$ has larger contribution to $\Delta\epsilon_1$ than the intraband Drude-type transitions. **B** The temporal evolution of $\Delta\epsilon_2$. The Drude component has a larger contribution to $\Delta\epsilon_2$ than to $\Delta\epsilon_1$. This component rises slowly and it is almost absent up to 350 fs, where $\Delta\epsilon$ has its maximum.

tal $\Delta\epsilon$. These components are weakly depending on E and t as compared to the component of the upmost d-band to Fermi level transitions.

5.5.1 Experimental approach to separate Δf- and T_{la}-sensitive components of the optical properties

The electron-electron scattering events transfer the photo-excited electronic subsystem into thermal equilibrium. The thermal quasiparticles lose their energy which is transferred to the lattice, e.g. as described by the TTM. In this limit, after the thermalization of the electrons, the system is characterized with only two variables, the electronic and the lattice temperature. The measurements performed at different excitation densities allow to compare different spectra taken at the same electronic temperature, T_{el}, but at different lattice temperatures, T_{la}. For example the monotonically decreasing $T_{\text{el}}(t)$ at high excitation densities reaches after a certain time delay the T_{el} which is reached after a shorter time delay at lower excitation densities. Comparing the data at selected excitation densities and selected time delays with matching T_{el}, the only difference is T_{la}. This allows us to

decouple the optical properties into electronic- and lattice-sensitive components. Such an analysis is presented in Figure 40. Here, T_{el} and T_{la} are taken from the data analysis in Section 5.7, where T_{la} is determined by the application of the energy conservation law. The spectral changes in $\Delta R/R$

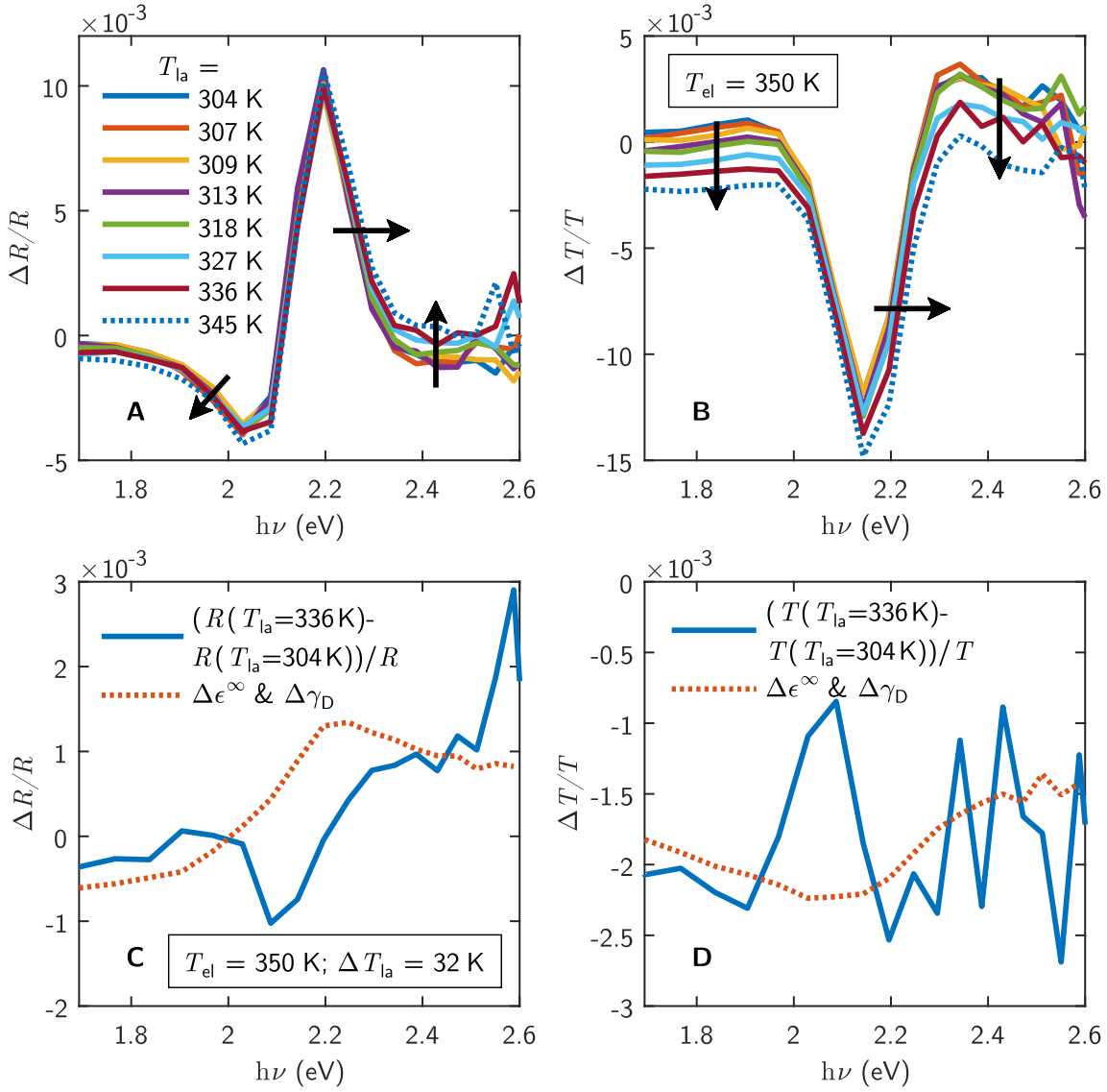

Figure 40: **Spectral shape of $\Delta R/R$ and $\Delta T/T$ at the same T_{el}, yet at different T_{la}.** The spectra are taken at different excitation densities and at different time delays to compare the spectra at the same $T_{\mathrm{el}} = 350\,\mathrm{K}$ (known from Section 5.7). **A** and **B** show the spectra of $\Delta R/R$ and $\Delta T/T$ (references are R and T at 300 K). The deviations between the curves illustrate the T_{la}-dependencies (both graphs share the same legend). **C** and **D** The blue curve subtracts out the T_{la}-dependence from the dark blue and dark red curves in **A** and **B**. The red dotted lines correspond to the T_{la}-dependent changes of the Drude scattering rate and of ϵ_1^∞ (computed with the linearized Thin-Film-Fresnel-Equations, see Section 5.4.1). The deviations between both curves indicate a T_{la}-dependent blue-shift of the upmost d-band to Fermi level resonance.

and $\Delta T/T$ which are related to an increase of T_{la} are marked by black arrows in Figure 40**A** and **B**. Around 2.14 eV the T_{la}-dependent changes of $\Delta\gamma_{\mathsf{D}}$ and $\Delta\epsilon^{\infty}$ are superimposed by the changes based on ΔE_{G}. In contrast to the result of the thermomodulation fits in Section 5.3 ΔE_{G} increases in this specific case with rising temperature and a rate of $\partial E_{\mathsf{G}}/\partial T \approx 300\,\mu\mathrm{eV/K}$. However, the changes in ΔE_{G} can hardly be resolved using the energy resolution of the experimental setup. The data analysis in this subsection considers only a few data points. On the contrary, in Section 5.3 (see Table 6) the analysis includes the entire dataset and an opposite result is reached (see also Section 5.6.2 for more detailed information).

5.5.2 Singular value decomposition (SVD)

The SVD is a mathematical method to factorize matrices (see for example [Gen07; Bey12]). The decomposition of each matrix M gives the three well defined matrices V, S and W with

$$M = V \cdot S \cdot W^{\mathsf{t}}\,.$$

V and W are unitary matrices and contain the information about each component of the factorization. Every line represents the information of one component. S is a diagonal matrix and the singular values are on the diagonal. The strength of each individual component is represented by a singular value. The component with the largest singular value makes the highest contribution to M (the smallest singular value component makes the highest contribution to the inverse of M).
Every time- and spectrally-resolved data set ($\Delta R/R$ or $\Delta T/T$) is represented by a single matrix

$$\begin{aligned}\Delta R/R &= V_R \cdot S_R \cdot W_R^{\mathsf{t}}\,,\\ \Delta T/T &= V_T \cdot S_T \cdot W_T^{\mathsf{t}}\,.\end{aligned}$$

Each column of the matrix contains a spectrum at a single time delay and each row contains the time evolution of the quasiparticle response at a single photon energy. In this specific application of the SVD the matrices V_R & V_T contain the spectral and the matrices W_R & W_T contain the temporal characteristics of each component.
First of all, the SVD can be applied to the experimental data to reduce the noise. The singular values of the noisy components are set to zero to reduce the noise in the experimental data. A second application of the SVD is to decouple spectral components with different temporal characteristics. The illustration of the dynamics of the surface plasmon resonance and the interband transitions

between the upmost d-band and the Fermi level in Au nanoparticle arrays gives a good example for the decomposition of different components in the measured response. The study of the time evolution of both spectral features in the plasmonic ferroelectric hybrid ITO/nano-Au/PZT (nano-Au arrays of approx. $270 \times 270 \times 60\,\mathrm{nm}^3$ on indium tin oxide glass, embedded in a PZT matrix) allows to identify the charge transfer between the nanoparticle Au array and PZT [Wan+16]. The SVD result of ITO/nano-Au is illustrated in Figure 41. Component 1 is linked to the upmost d-band to Fermi

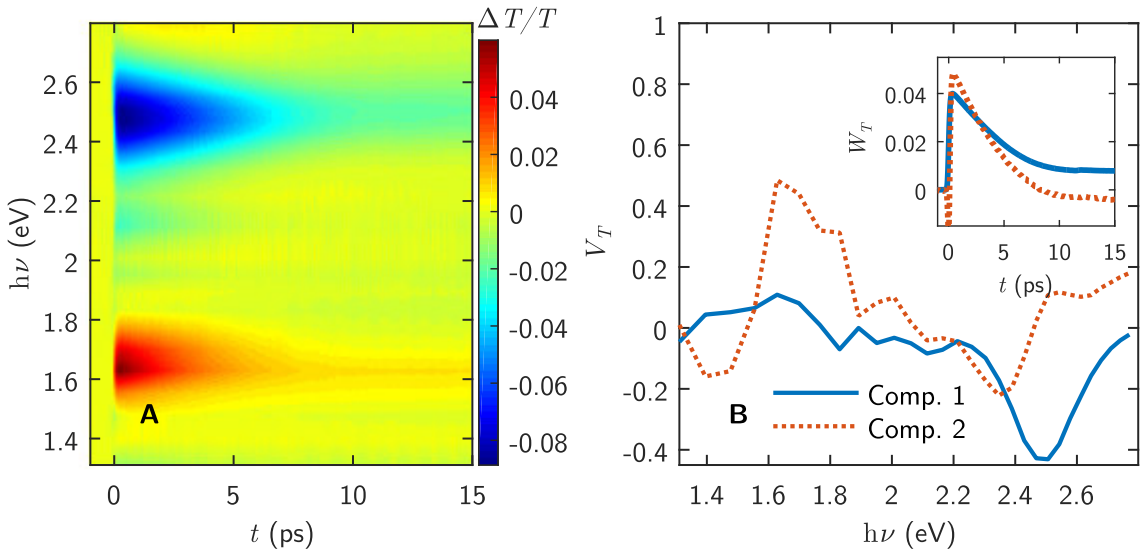

Figure 41: **SVD of $\Delta T/T$ recorded on a periodic array of Au nanoparticle on ITO substrate.** **A** $\Delta T/T$ taken after excitation in the near-UV at 400 nm. **B** and the inset to **B** show the spectral and temporal characteristics of the two most pronounced components. Component 1 is related to the upmost d-band to Fermi level transition with a relative strength of 70 % and component 2 mostly describes the photo-induced increase in transmission at the surface plasmon resonance at ≈ 1.7 eV with a relative strength of 15 %.

level transitions in Au at around 2.5 eV; the corresponding relative singular value is 0.7. The second component has a lower relative strength of 0.15. This component represents changes in the optical properties, which are related to the surface plasmon resonance. It has a lower relaxation time as the first component (see the inset to Figure 41**B**).

There is not always a distinct connection between a specific SVD component and a specific spectral feature. A single SVD component consists of a constant spectral characteristic, whose signal strength is changing over time. If the spectral shape of the optical feature changes over time, the dynamics are represented by more than one SVD component. A closer look to the upmost d-band to Fermi level transitions in Cu will show that these transitions are represented by more than one SVD

component.

The idea behind the application of the SVD on the experimental $\Delta R/R$ and $\Delta T/T$ (Section 5.2, Figure 31) is the attempt to separate the dynamics of the intraband Drude transitions from the d-band to Fermi level transitions. The separation of both components is systematically analyzed in Subsection 5.5.4.

The SVD is done numerically (using Matlab). It splits the experimental data (the 18 channels with the highest signal strength) into 18 different additive components. The first three components and their relative strenghs are plotted in Figure 42. Although the spectral shape of the components in $\Delta R/R$ and $\Delta T/T$ may differ fundamentally (the spectral shape $V_R(\nu)$ & $V_T(\nu)$ depend on the Fresnel equations and the thin film equation; $\Delta R/R$ and $\Delta T/T$ have different prefactors referring to equations (73) and (74)), the temporal characteristics of the corresponding components should be equal (the time evolutions of each component in $W_R(t)$ & $W_T(t)$ are the same as in $W_\epsilon(t)$, which is the result of the SVD of $\Delta\epsilon$). For the comparison of the components in $\Delta R/R$ and $\Delta T/T$ it is important to do not confuse the different components. The SVD components of $\Delta R/R$ are ordered by their relative strengths beginning with the highest value. The corresponding components of $\Delta T/T$ are arranged in the same order, where component 3 is found to have higher strength compared to component 2. The comparison of $W_R(t)$ and $W_T(t)$ (see Figure 42**B** and **D**) showed that the temporal characteristics of the corresponding components are equal, as expected. The components with lower relative strength were very noisy. At the highest excitation density of $\bar{U}_{\text{abs}} = 308\,\text{J/cm}^3$ the signal-to-noise ratio is larger than 1 for the first five components. At lower excitation densities the signal of the components 4 and 5 are below the noise level.

The experimental $\Delta R/R$ and $\Delta T/T$ can be reasonably well described by a single component (strength of about 70 %). This strongest component contains most of the dynamics induced by the transitions from the upmost d-band to the Fermi level (see Figure 42**B** and **D**) and its spectral characteristics (see Figure 42**A** and **C**). The spectral shape of the second and third components are influenced by the upmost d-band to Fermi level transitions as well. In conjunction with component 1 component 2 describes a very fast spectral broadening over time up to 100 fs followed by a spectral narrowing. Note, the components 1-3 simultaneously modify the optical properties before 2.5 ps. After 2.5 ps component 3 becomes the component with the highest contribution to $\Delta R/R$ and $\Delta T/T$, where component 2 is negligible. Under these considerations the first component describes the time evolution of the average spectral shape of $\Delta R/R$ and $\Delta T/T$. The changes over time in the width

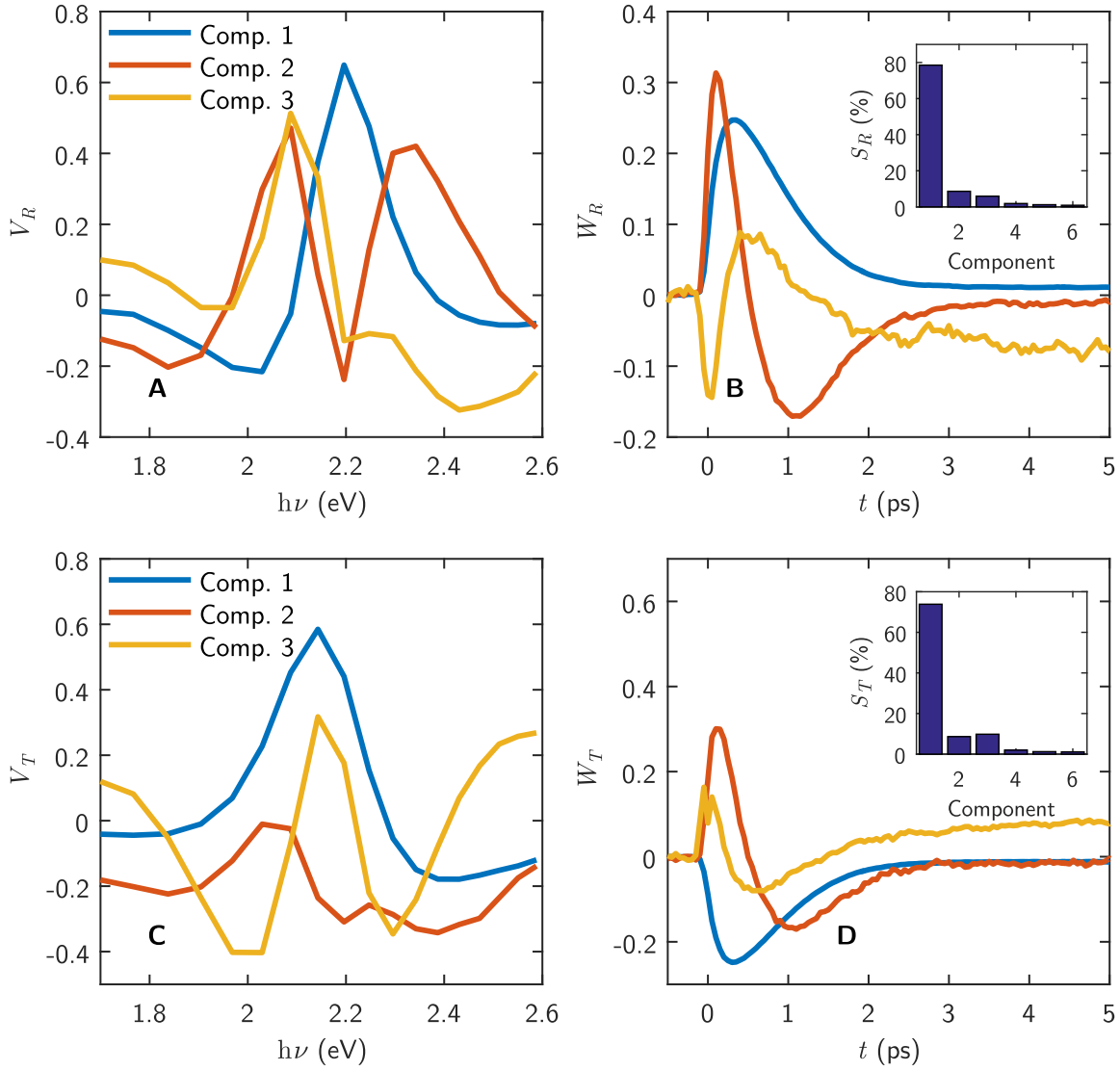

Figure 42: **SVD of $\Delta R/R$ and $\Delta T/T$ after excitation with $\bar{U}_{\text{abs}} = 99\,\text{J/cm}^3$.** In **A** and **C** the spectral characteristics of the three components with the highest signal strengths S are plotted. **B** and **D** show the temporal evolution of those components. The insets give the relative signal strength of the 6 components with the highest relative strengths. The components 4-6 (and all components with lower relative strengths) are noisy and their contribution to the signal is insignificant.

of the spectral feature is described by component 2. This spectral narrowing might be linked to the thermalization of the electrons, i.e. the high energy quasiparticles lose their energy which is transferred to the thermal electrons and to the lattice. The third component seems to describe a blue-shift of the upmost d-band to Fermi level resonance up to 300 fs followed by a red-shift. The spectral narrowing is also seen in the time evolution of Δf (the spectral width is proportional to the electronic temperature, verified in Section 5.2.1) and the spectral red-shift is found in Section 5.3.

The spectral width remains approximately the same after about 1 ps, where component 2 reaches its minimum and further evolves with the same temporal characteristics as the first component. A possible explanation could be, that the minima determine the electron thermalization time which is about 30 % larger compared to the result of the analysis in Section 5.8. To prove this interpretation the dynamics of the thermal quasiparticles are simulated in Subsection 5.5.3.

5.5.3 SVD on $\Delta R/R$ and $\Delta T/T$ in case of thermalized quasiparticles

Up to now it is not clear, whether the components 2 and 3 describe dynamics related to non-thermal quasiparticles or if these components are also present in case of thermalized quasiparticles and narrowing of Δf due to the cooling of the electrons. The answer is given in Figure 43. It shows

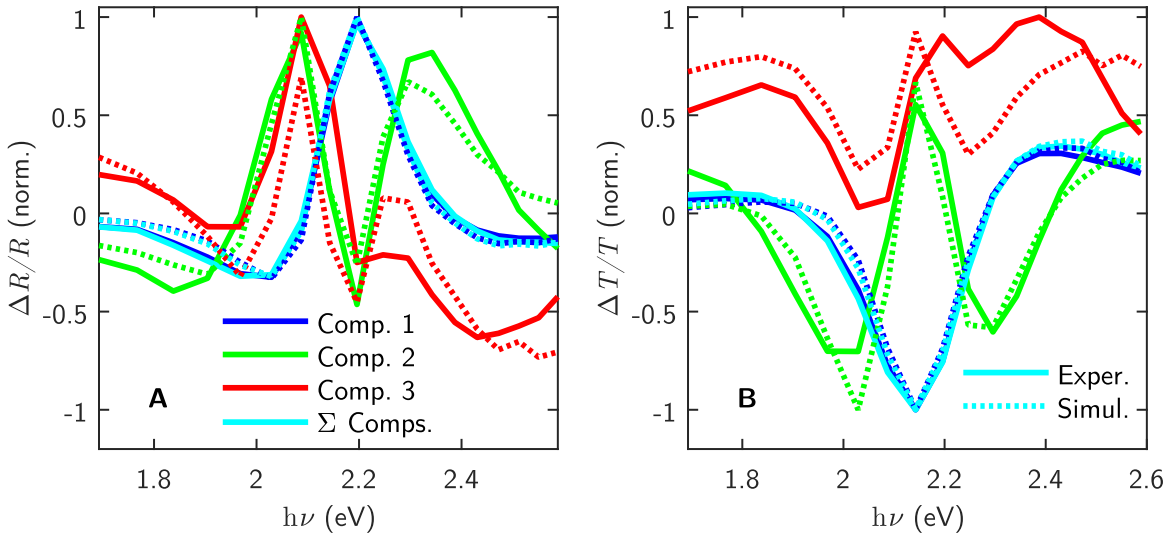

Figure 43: **The upmost d-band to Fermi level resonance analyzed with SVD after 400 fs.** Comparison between the response of purely thermal quasiparticles in the simulation (dotted lines) and the experimental data. The solid lines reproduce the result from the Figure 42**A** and **C**. The dotted lines are the result of the SVD on the simulated $\Delta R/R$ and $\Delta T/T$ of thermalized electrons with T_{el} taken from the Fermi-Dirac fits, Figure 51. Note, the legends are the same for **A** and **B**.

a simulation based on thermal quasiparticles assuming ΔT_{el} from Δf from Figure 51 in Section 5.7. These ΔT_{el} as a function of time are chosen to be the basis for the simulation because they best reproduce the experimental $\Delta R/R$ and $\Delta T/T$. This makes the simulation result (dotted lines) directly comparable to the experimental data (solid lines). The component 2 and 3 of the SVD (red and green dotted lines in Figure 43) are still present with comparable lineshapes (red and green solid lines). This implies that there is no specific component which purely describe non-thermal

quasiparticles (and none of the mentioned components is related to any systematic error in the experiment). In particular, the minimum of component 2 discussed in Section 5.5.2 is not linked to the electron thermalization time. Even if Δf is thermal during the entire relaxation process, the modifications to the upmost d-band to Fermi level transitions over time (the spectral width and the resonance position) are still parts of component 2 and component 3 of the SVD and there is still the minimum of component 2 in W_R and W_T at about 1 ps.

5.5.4 SVD components compared to responses of the inter- and intraband transitions

The Figure 44 shows the comparison between the SVD on $\Delta R/R$ and $\Delta T/T$ (dotted lines) and the separation of the quasiparticle response to the excitation pulse into the intraband (Drude) and interband components (solid lines).

Although the agreement is not perfect, the SVD components 1 and 2 cover most of the upmost

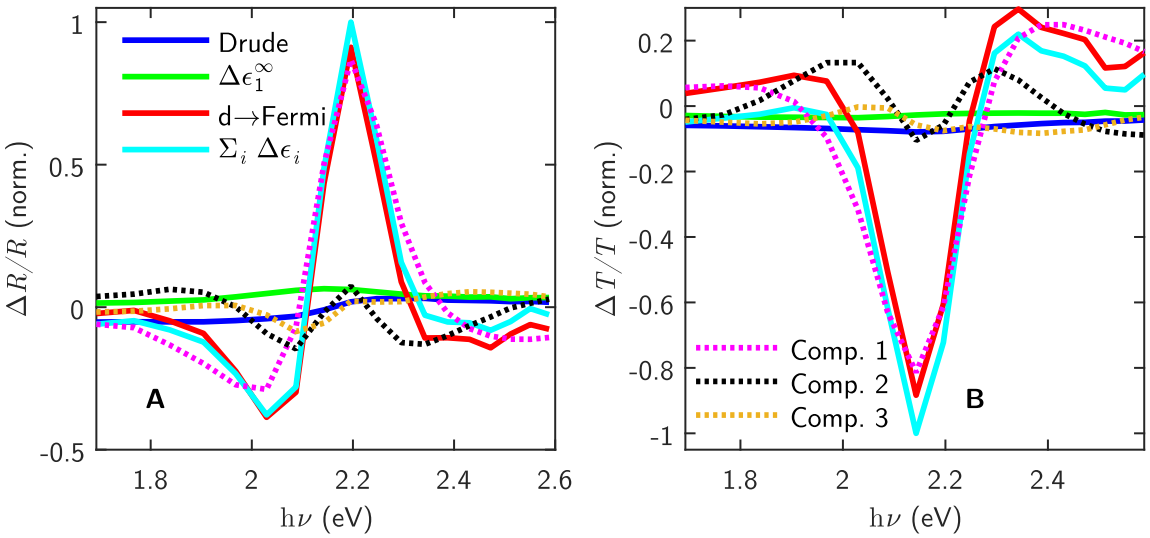

Figure 44: **The components of SVD compared to the components of the inter- and intraband responses after 2 ps ($\bar{U}_{\text{abs}} = 99\,\text{J/cm}^3$).** The quasiparticle response consists of intraband transitions within the conduction band (Drude response) and interband transitions (upmost d-band to Fermi level transitions and transitions between other bands ϵ_1^∞). **A** The spectral characteristics correspond to the different components of $\Delta R/R$. **B** The same components but related to $\Delta T/T$. **A** and **B** share the same legends.

d-band to Fermi level transitions. The Drude response and the dielectric offset ϵ_1^∞ are mostly part of the component 3. In order to motivate this link, component 3 is known to remain as an offset for longer time delays (Figure 42**B** and **D**). This offset indicates that this component is affected by

the rise of the lattice temperature. The spectral shape of component 3 is close to the one which is expected from the Drude response and the Drude response changes with the heating of the lattice. However the spectral shape of the component 3 shows that this component contains also information about the upmost d-band to Fermi level transitions (e.g. a shift of the resonance position). This implies that the SVD is not able to purely separate Drude from the remaining interband transitions of the quasiparticle response.

A systematic analysis of the strengths of the SVD component 3 is presented in Figure 45. If there

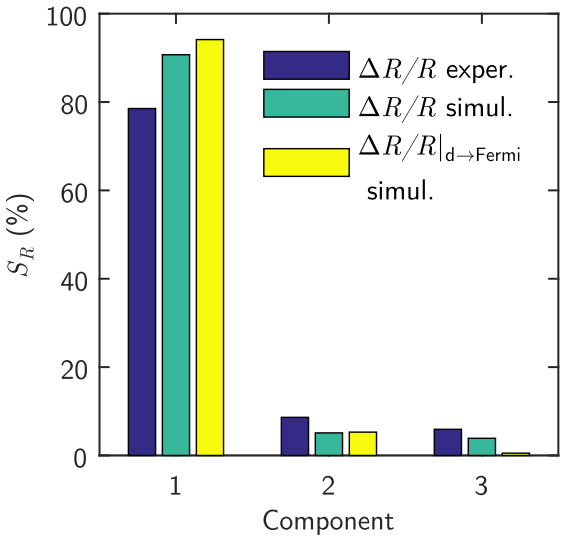

Figure 45: **The strengths of the first 3 components of the SVD on $\Delta R/R$ ($\bar{U}_{\mathrm{abs}} = 99\,\mathrm{J/cm^3}$).** The simulation is based on thermal electrons as described in Section 5.5.3. The component strengths of the experimental (dark blue bars) and the simulated $\Delta R/R$ (green bars) include intraband transitions within the conduction band (Drude response) and interband transitions (upmost d-band to Fermi level transitions and transitions between other bands, based on ϵ_1^∞). The simulation $\Delta R/R|_{\mathrm{d}\rightarrow\mathrm{Fermi}}$ takes the SVD of $\Delta R/R$ which includes only the upmost d-band to Fermi level transitions (yellow bars).

are no contributions to $\Delta R/R$ from Drude, ϵ_1^∞ and the time dependent spectral shift of the upmost d-band to Fermi level resonance, then the strength of component 3 is negligible (yellow bars) and the components 1 and 2 are only slightly modified (these modifications are not considered for the filtering procedure, which is applied to the experimental data to isolate the d-band to Fermi level resonance from the intraband and high energy interband transitions in the following).

To conclude, the SVD can be applied to the experimental $\Delta R/R$ and $\Delta T/T$ to eliminate the contributions from intraband and high energy interband transitions. The filtering of the experimental

data and the isolation of the upmost d-band to Fermi level transitions is performed with the selective use of the components 1 and 2 of the SVD. This filtered data can be used to determine the electronic temperature as a function of time and the electron-phonon coupling constant as discussed in Section 5.8.1. However, one should keep in mind that ignoring component 3 means to apply a coarse filter which also removes the small contributions to component 3 from the dynamics of the upmost d-band to Fermi level resonance.

5.6 Extracting the time evolution of the electronic distribution function

In this section the electronic distribution function Δf is determined as a function of time delay from the experimental $\Delta\epsilon$. This is possible because the part of the $\Delta\epsilon$ which is linked to the upmost d-band to Fermi level transitions depends on the electronic distribution function at the Fermi level. The task is to invert the equations (53) and (54). This is done numerically (see Subsection 5.6.1). In the following the definition of Δf is given.

The Fermi level is a particular point of the energy axis. The electronic distribution function, f, is often assigned in relation to the Fermi level because in thermal equilibrium, f is symmetrical identical around E_F. Thermomodulation gives rise to changes in the electronic distribution functions which are

$$f(E - E_\mathsf{F}(T_1), T_1) - f(E - E_\mathsf{F}(T_0), T_0)\,. \tag{77}$$

This difference contains two effects: the shift of the Fermi level with respect to the upmost d-band (see Section 4.2, equation (51) is found to be invalid for the investigated Cu thin film) and the change in the electronic distribution (e.g. due to an increase in the electronic temperature). Here, Δf is defined to the reference energy $E_\mathsf{F}(T_1)$:

$$\Delta f(E - E_\mathsf{F}(T_1), T_1, T_0) = f(E - E_\mathsf{F}(T_1), T_1) - f(E - E_\mathsf{F}(T_1), T_0)\,. \tag{78}$$

The temperature dependent Fermi level shift does not contribute to Δf in this definition (if Δf is plotted as a function of $E - E_\mathsf{F}$) to facilitate the mapping of the quasiparticle redistribution. Note, if both types of quasiparticles, the excited electrons and the excited holes, equally interact with other degrees of freedom, $\Delta f(E - E_\mathsf{F}(T_1), T_1, T_0)$ is antisymmetric about E.

In the non-thermal regime at short time delays ($t < 5\,\mathrm{ps}$), one deals with time dependent electronic distribution functions and Fermi levels. Equation (78) reads

$$\Delta f(E - E_\mathsf{F}(t), t, T_0) = f(E - E_\mathsf{F}(t), t) - f(E - E_\mathsf{F}(t), T_0)\,. \tag{79}$$

As it will be shown in Section 5.7, the electrons thermalize on a timescale in the range of 400-800 fs depending on the excitation density. After the thermalization, f depends on the electronic temperature

$$f(E - E_{\mathsf{F}}(t), t) \equiv f(E - E_{\mathsf{F}}(t), T_{\mathsf{el}}) \,.$$

In Subsection 5.6.2 it is shown that the shift of E_{G}, which includes a possible shift of E_{F} due to the variation of the density of states near E_{F} (see equation (50)), is proportional to the lattice temperature T_{la}. T_{la} is assumed to be well defined during the relaxation process and the lattice heats up exponentially

$$T_{\mathsf{la}}(t) \approx T_0 + \frac{U_{\mathsf{abs}}}{c_{\mathsf{V}}} \left(1 - \exp\left(-t/\tau_{\mathsf{la}}\right)\right) \,. \tag{80}$$

The characteristic timescale for τ_{la} is on the order of the relaxation time of $\Delta\epsilon$, $\tau_{\mathsf{la}} \gtrsim 1\,\mathrm{ps}$ (Section 5.4).

Δf is determined from $\Delta\epsilon$ in the following Subsection 5.6.1.

5.6.1 Reconstruction of Δf

The probability for the electronic transitions between the upmost d-band and the Fermi level depend on $f(E)$ at the Fermi level. The related ϵ (equations (53) and (54)) is basically given by two integrations. The first integration over the d-band density of states is performed analytically, using the model parameters for the studied thin film sample (see Tables 6 and 7). The second integration over the energy range of the conduction band is an integration over an analytical term, including a Lorentzian line broadening (lifetime effects), multiplied by $(1 - f)$. The first step to reproduce Δf from the measured $\Delta\epsilon$ is to discretize equations (53) and (54). The second integration is also discretized using the trapezoidal rule. The real and imaginary parts of the dielectric function read

$$\epsilon_{1,i}(T) = \sum_{j=1}^{n} K_{1,ij} \cdot F_j(T) \,, \tag{81}$$

$$\epsilon_{2,i}(T) = \sum_{j=2}^{n} K_{2,ij} \cdot F_j(T) \,, \tag{82}$$

$$\Delta\epsilon_{1,i}(T_1, T_0) = \sum_{j=1}^{n} K_{1,ij} \cdot \Delta F_j(T_1, T_0) \,, \tag{83}$$

$$\Delta\epsilon_{2,i}(T_1, T_0) = \sum_{j=1}^{n} K_{2,ij} \cdot \Delta F_j(T_1, T_0) \tag{84}$$

with

$$
\begin{aligned}
K_{x,ij} &= A\, M_i\, L^{(x)}_{j,i} \cdot \begin{cases} (E_2 - E_1) & \text{if } j = 1 \ , \\ (E_n - E_{n-1}) & \text{if } j = n \ \text{ or} \\ 0.5 \cdot (E_{j+1} - E_{j-1}) & \text{otherwise,} \end{cases} \\
M_i &= M^2_{\mathsf{cu}} / \left(2\pi\nu_i\right)^2 + M^2_{\mathsf{di}} \,, \\
F_j(T) &= f(E_j - E_{\mathsf{G}}(T), T) - 1 \,, \\
\Delta F_j(T_1, T_0) &= f(E_j - E_{\mathsf{G}}(T_1), T_1) - f(E_j - E_{\mathsf{G}}(T_0), T_0) \,, \qquad (85) \\
f(E,T) &= \frac{1}{1 + \exp\left(E/(\mathrm{k_B}\, T)\right)} \\
L^{(x)}_{j,i} &= L^{(x)}(E_j, \mathrm{h}\nu_i) \,. \\
L^{(1)}(E, \mathrm{h}\nu) &= -E_{\mathsf{BW}} \cdot \left(E - \mathrm{h}\nu + \frac{3}{2}\, E_{\mathsf{BW}} \right) \qquad (86) \\
&\quad + \frac{1}{2} \left((E - \mathrm{h}\nu + E_{\mathsf{BW}})^2 - \gamma^2 \right) \ln \left(\frac{(E - \mathrm{h}\nu + E_{\mathsf{BW}})^2 + \gamma^2}{(E - \mathrm{h}\nu)^2 + \gamma^2} \right) \qquad (87) \\
&\quad + 2\,\gamma\,(E - \mathrm{h}\nu + E_{\mathsf{BW}}) \left(\arctan\left(\frac{E - \mathrm{h}\nu + E_{\mathsf{BW}}}{\gamma} \right) - \arctan\left(\frac{E - \mathrm{h}\nu}{\gamma} \right) \right) \qquad (88) \\
L^{(2)}(E, \mathrm{h}\nu) &= \left((E - \mathrm{h}\nu + E_{\mathsf{BW}})^2 - \gamma^2 \right) \\
&\quad \cdot \left(\arctan\left(\frac{E - \mathrm{h}\nu + E_{\mathsf{BW}}}{\gamma} \right) - \arctan\left(\frac{E - \mathrm{h}\nu}{\gamma} \right) \right) \qquad (89) \\
&\quad + \gamma\, E_{\mathsf{BW}} + (E - \mathrm{h}\nu + E_{\mathsf{BW}})\ \gamma\ \ln \left(\frac{(E - \mathrm{h}\nu)^2 + \gamma^2}{(E - \mathrm{h}\nu + E_{\mathsf{BW}})^2 + \gamma^2} \right) \qquad (90)
\end{aligned}
$$

Note a different range of E (compared to equations (53) and (54)):

$$E \to E + E_{\mathsf{d,max}} \,.$$

In fact, the equations (81) to (84) are matrix multiplications of the matrices K_1 and K_2 with the vectors F and ΔF. The real and imaginary parts of those matrices are shown in Figure 47**A** and **C**. They relate specific points (values of F or ΔF at specific E) of the electronic distribution function to specific points of the dielectric function (at specific $\mathrm{h}\nu$). The matrices are numerically inverted (see Figure 47**B** and **D**). The inverted matrices are used to reconstruct the Δf from the experimental $\Delta\epsilon$. The matrix and the inverse matrix relations are

$$\epsilon_x = K_x \cdot F \quad \longleftrightarrow \quad F = K_x^{-1} \cdot \epsilon_x \qquad (91)$$

$$\Delta\epsilon_x = K_x \cdot \Delta F \quad \longleftrightarrow \quad \Delta F = K_x^{-1} \cdot \Delta\epsilon_x \qquad (92)$$

All the matrix elements are considered to be temperature independent. Because of this temperature independence, the equations (91) and (92) hold even in the case of a non-thermal F or ΔF. ΔF

Matrix	rel. amplitude, terms (86) & (87) or (90)	rel. amplitude, terms (88) or (89)	Width	Width of inverse
K_1	$\propto E_{\mathrm{BW}}^2$, $\sim 80\,\%$	$\propto E_{\mathrm{BW}} \cdot \gamma$, $\sim 20\,\%$	$\propto \lvert\ln(E_{\mathrm{BW}})\rvert$, $\sim 0.7\,\mathrm{eV}$	$2 \cdot \gamma$, $\sim 0.06\,\mathrm{eV}$
K_2	$\propto E_{\mathrm{BW}} \cdot \gamma$, $\sim 10\,\%$	$\propto E_{\mathrm{BW}}^2$, $\sim 90\,\%$	$\propto E_{\mathrm{BW}}^2$, $\sim 0.25\,\mathrm{eV}$	$2 \cdot \gamma$, $\sim 0.06\,\mathrm{eV}$

Table 8: **Matrix characteristics of K_1 and K_2.** Values are taken at the resonance of $\mathrm{h}\nu = 2.15\,\mathrm{eV}$, the given dependencies hold if $E_{\mathrm{BW}} \gg \gamma$.

can be obtained from the experimental $\Delta\epsilon$ if the energy resolution is better than $2\,\gamma = 60\,\mathrm{meV}$ (γ is the dephasing rate, Section 4.3.1). This is because the widths of the peaks along the diagonals of the inverse matrix elements are about $2 \cdot \gamma$ (see Table 8 and compare with insets on Figure 47**B** and **D**).

The procedure to determine ΔF is illustrated in Figure 46. The row of matrix K_2^{-1} at $E_j = 2\,\mathrm{eV}$

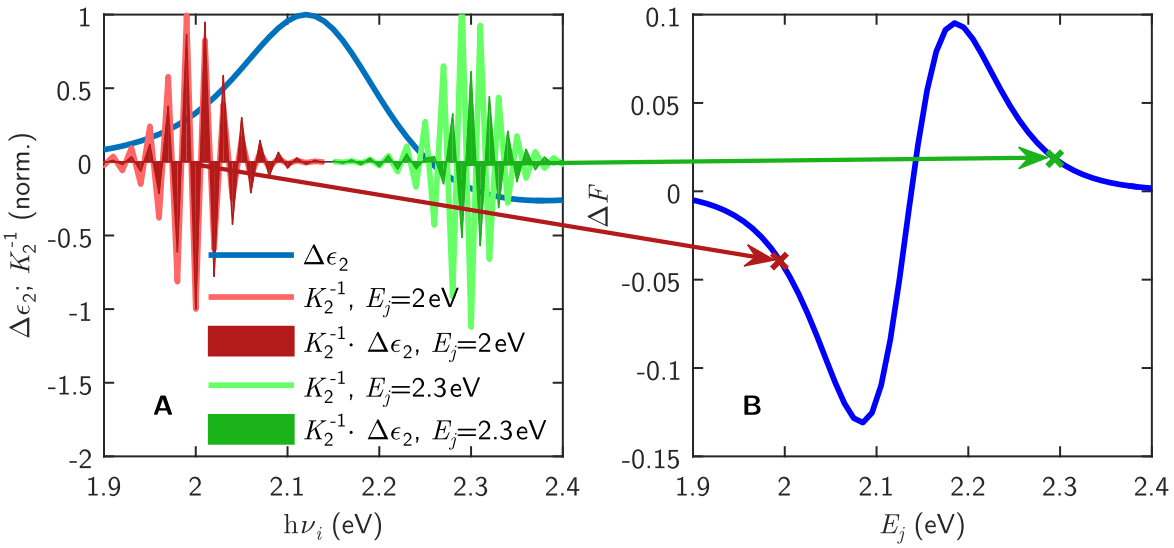

Figure 46: **Procedure to reconstruct Δf as function of E_j. A** The light green and light red lines are horizontal cuts through the matrix of Figure 47**D**. The cuts are oscillatory functions of $\mathrm{h}\nu$ with the width of $2 \cdot \gamma$. The blue line is $\Delta\epsilon_2$. The value of ΔF at a given E_j is the area under the curve $K_2^{-1} \cdot \Delta\epsilon_2$ (red and green areas). **B** These areas under the curve give ΔF at specific energy levels E_j (red and green crosses). The successive perfomance on each row of K_2^{-1} results in the blue line.

(light green or light red curve) is multiplied to $\Delta\epsilon_2$ (red or green curve). The area below the curve gives the value of ΔF at 2 eV (red dot in **B**) or at 2.3 eV (green dot). This procedure is done successively for every discrete energy E_j, where E_j are chosen such, that the condition number of

K_1 and K_2 are minimized. Here, different energy levels, $E_{1,j}$ and $E_{2,j}$, are found to minimize the condition numbers of K_1 and K_2. For every j, $E_{1,j}$ and $E_{2,j}$ differ by an average energy of about 20 meV. The condition number is a measure of the sensitivity of Δf on any error in $\Delta\epsilon$. A large condition number refers to high sensitivity. Matrices with the low condition numbers provide high accuracies for the solution of related linear equations. The matrices presented in Figure 47**A** and **C** are the result of the condition number minimization procedure[29] to find optimized energy levels $E_{1,j}$ and $E_{2,j}$. The insets show the diagonal cuts from the lower left corner to the upper right corner. Note that the x-axis of the cuts differ by about 20 meV because of the deviations in E_j. In fact, these deviations double the resolution of the computed Δf compared to the resolution of $\Delta\epsilon$. By the way, a higher resolution of the experimental $\Delta\epsilon$ could further improve the resolution of the extracted Δf. The insets to Figure 47 give the basic information about the mathematical relationship between the physical quantaties. E.g. a gaussian input function is broadened by a lineshape with a single peak (e.g. Figure 47**C**) and it is narrowed by an oscillatory lineshape (e.g. Figure 47**D**).

The next step to determine Δf is to relate it to ΔF. The equations (79) and (85) provide this relation:

$$\begin{aligned}\Delta f(E-E_{\mathsf{F}}(t),t,T_0) &= \Delta F_j(t,T_0)+f(E_j-E_{\mathsf{G}}(T_0),T_0)-f(E_j-E_{\mathsf{G}}(t),T_0)\\ &= f(E_j-E_{\mathsf{G}}(t),t)-f(E_j-E_{\mathsf{G}}(t),T_0) \qquad (93)\end{aligned}$$

with

$$E(j)=E_j+E_{\mathsf{d,max}}(T_1)\,.$$

E_{G} depends on the lattice temperature as shown in Section 5.6.2. The equations (50) and (80) give

$$E_{\mathsf{G}}(t)=E_{\mathsf{F}}(t)-E_{\mathsf{d,max}}(t)=E_{\mathsf{G},0}+\partial E_{\mathsf{G}}/\partial T\cdot\left(T_0+\frac{U_{\mathsf{abs}}}{c_{\mathsf{V}}}\left(1-\exp\left(-t/\tau_{\mathsf{la}}\right)\right)\right)\,. \qquad (94)$$

The analysis, which is described so far, allows to determine $\Delta f(t)$ from the experimental time-resolved optical data. The result is presented in Figure 48. $\Delta f(E-E_{\mathsf{F}})$ is found to be almost antisymmetric. This is what is expected if the electrons and holes belong to the same band and if they follow similar scattering characteristics. The small differences are seen after 1 ps, where the deviation between the thermal distribution function and the experimental Δf is lower above E_{F} than below. I.e., after 0.6 ps there seems to be some excess holes at $E<E_{\mathsf{F}}-0.3$ eV which are not expected from the

[29] The condition numbers are 60 in case of K_1 and 80 in case of K_2 (the inverse matrices have the same condition numbers).

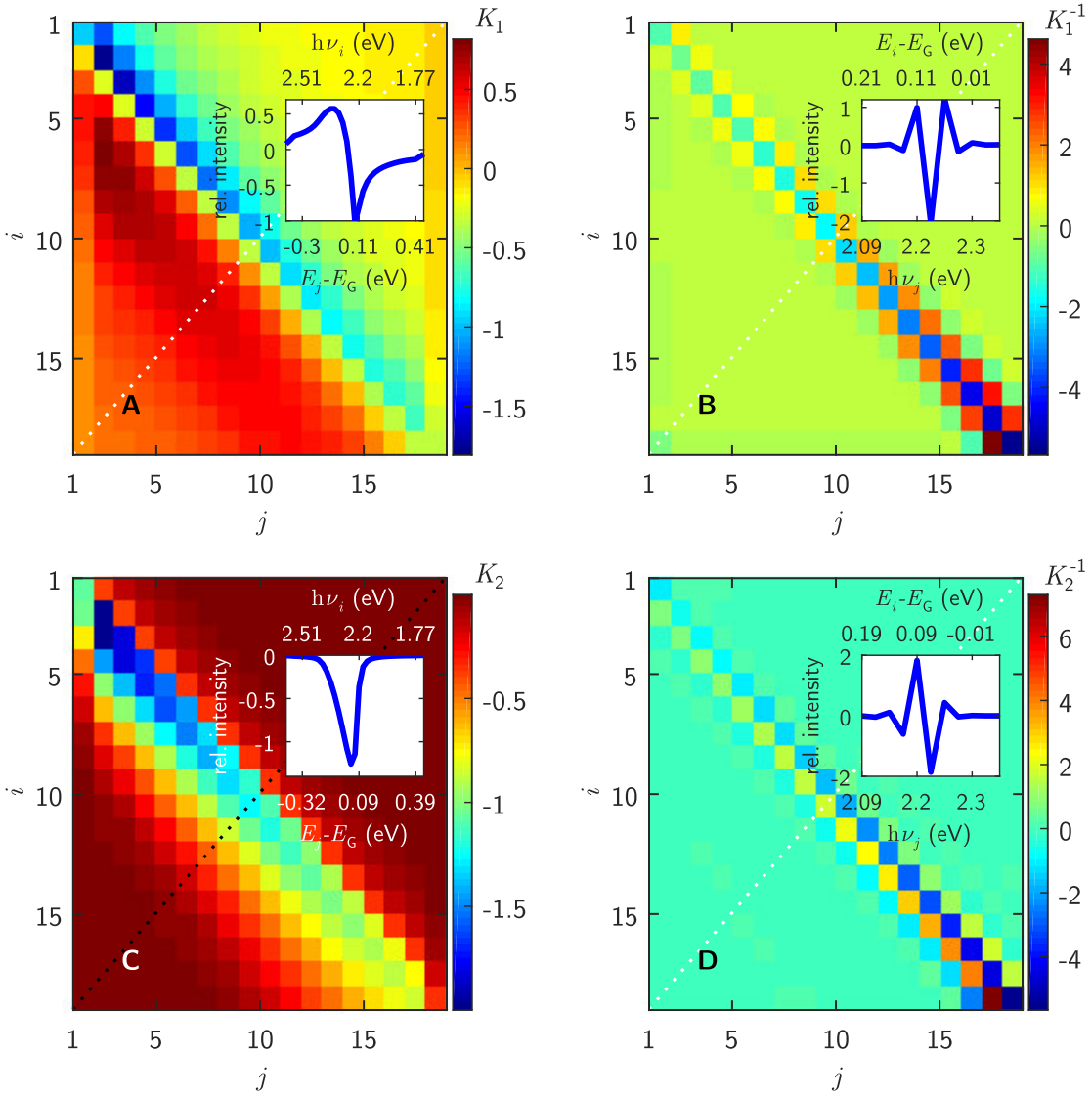

Figure 47: **Linear transformations between the F & ΔF and ϵ & $\Delta\epsilon$.** The matrices **A** and **C** give the linear transformation of F & ΔF at selected values E_j to ϵ & $\Delta\epsilon$ of the upmost d-band to Fermi level transitions taken at specific $h\nu_i$. The matrices **B** and **D** give the inverse transformations. The insets show the diagonal cut from the lower left corner to the upper right corner. The matrix elements (i, j) are connected to the energies $(h\nu_i, E_j - E_G)$ (the x-axes are not linear in energy but in i and j). The insets on **A** and **C** show, that F & ΔF well above the Fermi level (specifically at $E_j - E_G$ = -0.3 eV) contribute to ϵ_1 & $\Delta\epsilon_1$ far above the onset of the d-band to Fermi level transition (at $h\nu$ = 2.5 eV), but not to ϵ_2 & $\Delta\epsilon_2$ at the same energy. The characteristic widths of the cuts which are shown in the insets, are given in Table 8.

thermal fit. In comparison, on the electronic side, the high energy tail is clearly seen after 0.3 ps but vanishes by about 0.6 ps. However, the difference between the negative change in the electronic distribution function below the Fermi level and the change above the Fermi level is likely within the

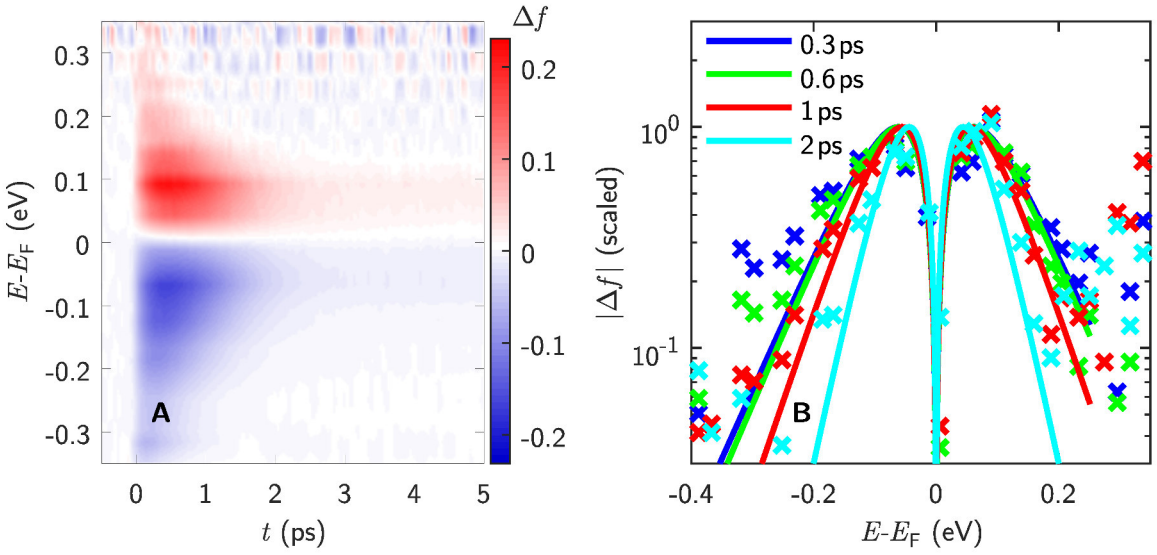

Figure 48: **Change in electronic distribution function Δf around the Fermi level. A** This 2D plot presents Δf as a function of time. **B** The absolute values of the measured spectra at different time delays are presented in a semilogarithmic plot. The lines give the best fit to the data with Fermi-Dirac distribution functions (the fits are described and presented in Section 5.7 and Figure 51).

expected error made within the procedure used for Δf determination. The slight differences are too weak to consider them to be due to different thermalization times of electrons and holes. Therefore all the further data analysis is made by assuming fully antisymmetric $\Delta f(E - E_F)$, although this is not generally the case.

5.6.2 The time evolution of the energy difference, E_G, between the d-bands and the Fermi level

In this section the time dependence of the energy difference between the upmost d-band states and the Fermi level, E_G, is analyzed. This is done based on the experimental ΔF. E_G can change because of (at least) two different effects (see also Section 4.2, equation (50) and Table 2).

One effect is the thermally induced change of the band structure. This effect arises from the lattice expansion driven by the increase of the temperature and results in a change of the width and the position of each band. These changes can be triggered electronically (for example the change in the pressure of the electron gas can cause a lattice expansion) or they are related to the anharmonicity of the lattice (T_{la}-dependent effect).

The second effect is related to a non-constant density of states around the Fermi level. If the density

of states is different at different electron energies around the Fermi level, then the Fermi level shifts with temperature or with any athermal generation of electron-hole pairs. The analysis of the optical data do not allow to distinguish between a shift of the upmost d-band and the change of the position of the Fermi level. The application of the free electron model to the conduction band of Cu suggests a shift of the Fermi level of less than 1 meV for heating the electron gas from 300 K to 1000 K. For all metals with Fermi energies of about 7 eV (e.g. Cu) this effect seems negligible.

The time dependence of E_G is determined from the experimental data by two different methods. They are presented in Figure 49**A** & **B** and the results at two different excitation densities are shown in Figure 49**C** and **D**. The first method is to fit the experimental ΔF (see equation (85)) using a difference of two Fermi-Dirac distribution functions

$$\Delta F(E_j) = \frac{1}{1+\exp\left(\left(E_j - \left(E_\mathsf{G}(T_0) + \Delta E_\mathsf{G}\right)\right) / \left(\mathrm{k_B}\, T_\mathsf{el}\right)\right)} - \frac{1}{1+\exp\left(\left(E_j - E_\mathsf{G}(T_0)\right) / \left(\mathrm{k_B}\, T_0\right)\right)} \tag{95}$$

as illustrated in Figure 49**A**. The results are the blue lines in Figure 49**C** and **D**. The problem of this method is that f is athermal below 1 ps and the fit might not adequately reproduce the experimental data. However, important is the antisymmetry of $\Delta f(E - E_\mathsf{F})$. If ΔF is also antisymmetric, then the fit gives $\Delta E_\mathsf{G} = 0$ even if the electrons are athermal, and $\Delta E_\mathsf{G} \neq 0$ if $\Delta F(E_j - E_\mathsf{F})$ has no antisymmetry. A second method to determine ΔE_G is to analyze the electron-hole imbalance. The electronic distribution function is experimentally determined up to $\sim$ 0.25 eV above the Fermi level and $\sim$ 0.4 eV below the Fermi level. The maximum range to check for electron-hole imbalance is from -0.25 eV up to 0.25 eV relative to the Fermi level. The electron-hole imbalance is presented in Figure 49**B**. If the electron and hole scattering characteristics are equal, the number of electrons and holes in the considered interval is essentially the same at every time delay (all these calculations assume a constant density of states in the conduction band). Thus, E_G is varied until the number of electrons and holes are equal. The results at $\bar{U}_\mathsf{abs} = 33\ \mathrm{J/cm^3}$ and $\bar{U}_\mathsf{abs} = 260\ \mathrm{J/cm^3}$ are plotted in Figure 49**C** and **D** (red curves). ΔE_G shows different temporal characteristic according to the different methods and to the different excitation densities. At the lower excitation density, the first method shows changes up to 3 meV with the characteristic T_el-related time dependence. The second method shows no relation between ΔE_G and the deposit of the energy in the electronic subsystem. The expectation from the thermomodulation fits (the values of Table 6) in combination with $T_\mathsf{la}(t)$ assumes changes as weak as the noise level of the second method. However, the results of both methods lack the systematics as a function of the excitation density. For the higher excitation density presented in

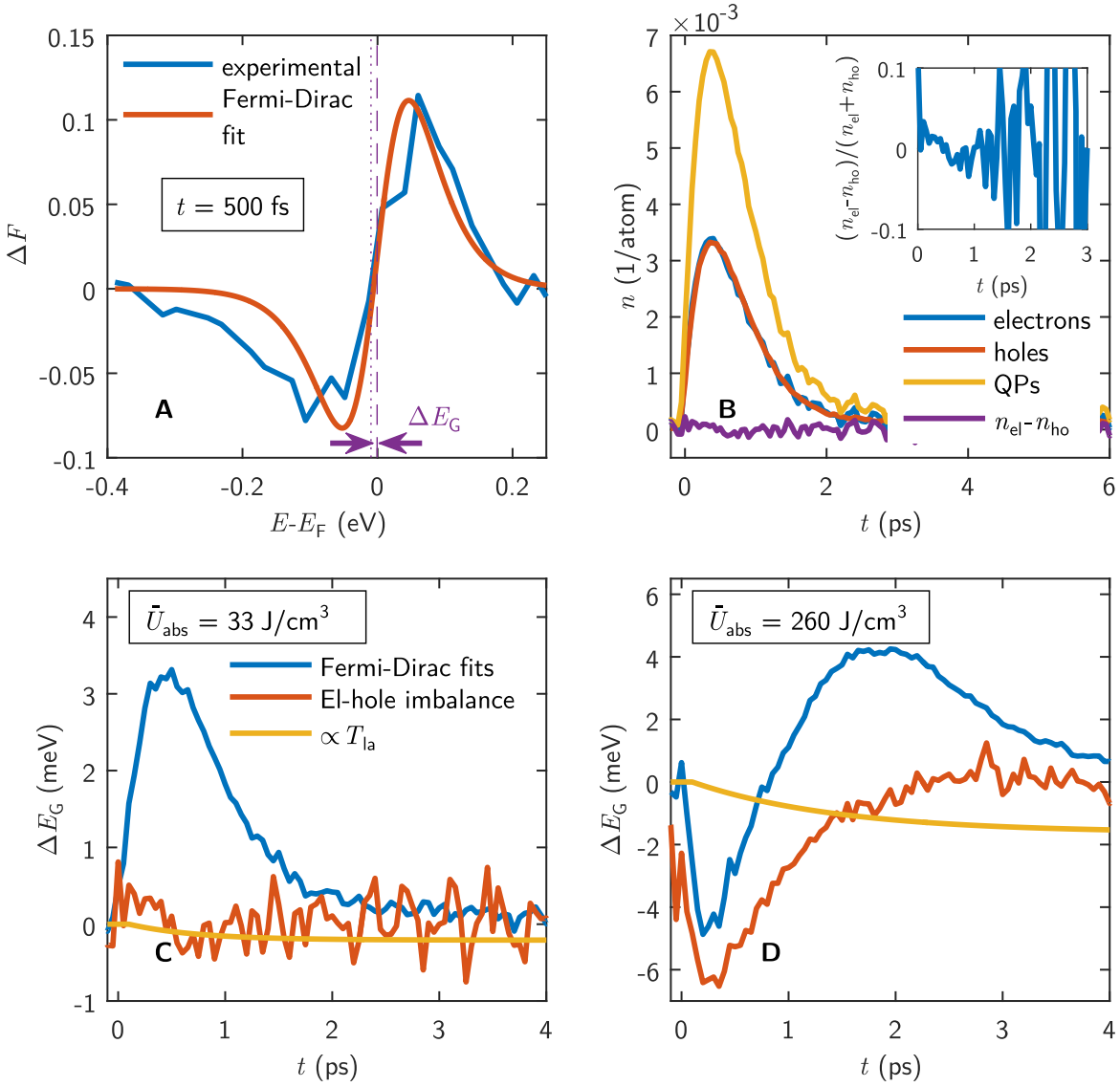

Figure 49: **Time dependent change of the position of the Fermi level relative to the upmost d-band.** **A** presents the technique of fitting the experimental Δf at every time delay with the function (95). The example is taken at $\bar{U}_{abs} = 33\,J/cm^3$ after 500 fs. Note that the curve is asymmetric and does not go through the origin. The time evolution of the number of quasiparticles (electrons and holes) at the same excitation density is presented in **B**. The amplitude of the weak asymmetry is as small as the noise (plotted in the inset). **C** and **D** show the ΔE_G as a function of time at $\bar{U}_{abs} = 33\,J/cm^3$ and $\bar{U}_{abs} = 260\,J/cm^3$. It is determined from the experimental ΔF at two different excitation densities with either the technique presented in **A** (blue line) or the variation of ΔE_G until there is the same amount of electrons and holes in a symmetric interval around the Fermi level (red line, proportional to the violet line in **B**). These results are compared to the result of the thermomodulation fits (see Section 5.3 and Table 6) which is based on the data where both, the electrons and the lattice, are in thermal equilibrium and at the same temperature (yellow line). These parameters are used to extrapolate ΔE_G at short time delays based on $T_{la}(t)$.

Figure 49**D**, ΔE_{G}, which is extracted this way, changes the sign during the relaxation process and at other excitation densities it is positive or negative at all time delays. However, it is always within ± 10 meV, i.e. the effect is weak: $\Delta E_{\mathsf{G}} \ll \mathrm{k_B}\, T_{\mathsf{el}}$.

Up to now, $\Delta E_{\mathsf{G}} = \frac{\partial E_{\mathsf{G}}}{\partial T} \cdot \Delta T$ is taken into account to reduce the deviation between the computed and the experimental $\Delta\epsilon$ in the thermomodulation fits (Section 5.3). The idea behind this section was to extend this relation to the data at shorter time delays (yellow line in Figure 49**A**, the last points are the result of the thermomodulation fit). The ΔE_{G}, which is extracted by the two different methods introduced in this section, are small and not systematic. It is likely, that the extracted ΔE_{G} is due to poor energy resolution (~ 40 meV) or errors in the analysis.

5.6.3 Procedural error analysis

In the previous subsections the procedure to extract Δf from the experimental $\Delta R/R$ and $\Delta T/T$ was described. Beside the statistical error, due to the noise in $\Delta R/R$ and $\Delta T/T$, the result may also contain systematic or methodical errors because of the approximations and simplifications made to model the optical properties of Cu. The analysis of the thermomodulation data provide the possibility to estimate these procedural errors. On the one hand, $\Delta\epsilon$ (for $t > 5$ ps) is extracted from the experimental data (Section 5.4) and on the other hand, the thermomodulation with $\Delta F(\Delta T)$ as an input allows to model $\Delta\epsilon$. The deviation between both $\Delta\epsilon$ is quite large (compare red crosses and green lines in Figure 50**A** and **B**), especially around 2.4 eV. Considering statistical error of about ± 10 %, it cannot account for this deviation. The deviation is systematic and substantial and is basically related to the deviation between the experimental and the simulated $\Delta R/R$ and $\Delta T/T$ of the thermomodulation fits (see Section 5.3, Figure 34**B**). However, the deviation in Δf between the one which is known from the change in temperature and the one which is extracted from the experimental data (see Figure 50**C**) is less pronounced. This is seen from the error bars (dotted lines). Here, the statistical deviations are added to $\Delta\epsilon$ based on random numbers to check for the error propagation between Δf and $\Delta\epsilon$. It turns out (see Figure 50**C**) that these small statistical deviations are sufficient to reduce the deviation between the simulated (green line) and the experimental Δf (solid and dotted red lines). However, the oscillations of Δf above 0.2 eV (see Figure 50**C**) are not affected by noise. These oscillations above 0.2 eV are linked to the substantial deviation in $\Delta\epsilon_2$ between the thermomodulation fits and the experimental data around 2.4 eV (see Figure 50**B**). This pronounced deviation might be linked to the smooth onset of interband optical

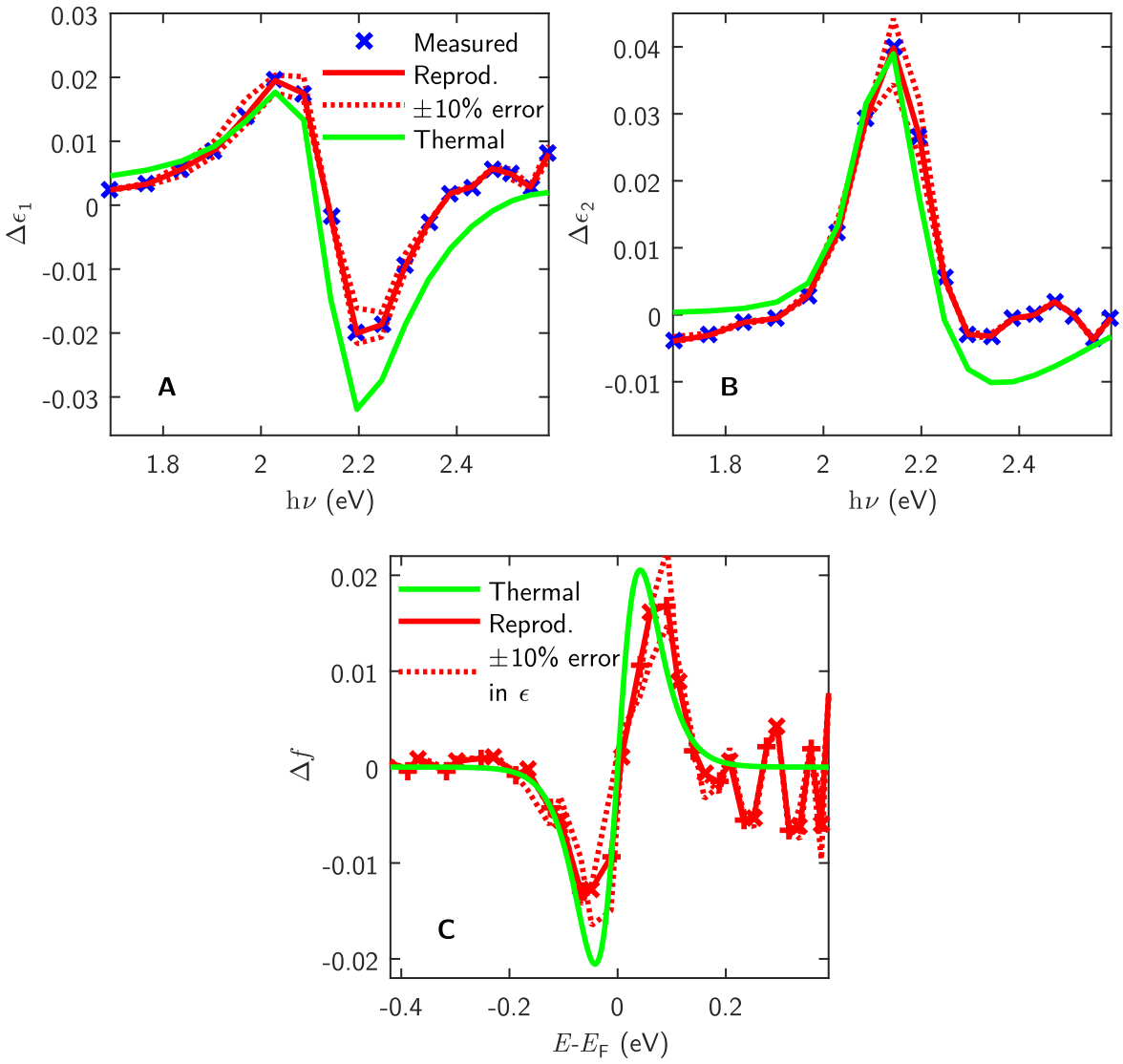

Figure 50: **The procedural error of the matrix inversion method analyzed in comparison to the thermomodulation result at** $t > 5\,\mathrm{ps}$**. C** The matrix inversion method is used to determine Δf (red solid lines) from the experimental $\Delta\epsilon$ and the result is compared to the expectation (green solid lines). **A** and **B** The upmost d-band to Fermi level parts of the experimental $\Delta\epsilon$ (blue crosses and red solid lines) are compared to $\Delta\epsilon$ based on the simulated Δf (green line) (with the corresponding Δf plotted in **C** with a green solid line). Stochastic errors of $\pm 10\,\%$ are added to the experimental dielectric function (red dotted lines) and this error data is used to calculate error-Δfs which are presented in **C**. The red markers "x" in **C** correspond to the points extracted from $\Delta\epsilon_1$ and the red markers "+" originate from $\Delta\epsilon_2$. **A** and **B** share the same legend.

transitions from the lower lying d-bands to the Fermi level. So, the deviations in Δf show different characteristics compared to the deviations in $\Delta\epsilon$: The slowly varying deviation in $\Delta\epsilon$ with respect to the expected curve results in an erroneous oscillation in the reconstructed Δf. This means,

that the linear transformation to Δf shows characteristics similar to a fourier transformation. The conclusions are, that the error in Δf is mainly based on the experimental noise, a simplified model of the optical properties (to keep the number of adjustable parameters low), the (low) experimental energy resolution and bandwidth. Although the deviations between the experimental $\Delta\epsilon$ and the simulated $\Delta\epsilon$ are quite large, the related oscillations in the experimental Δf do not prevent the further analysis, which is carefully performed on Δf.

5.7 The analysis of Δf with Fermi-Dirac fits

The Δf extracted from the experimental data allows one to test whether the electrons are thermally distributed or not. The thermal fit is based on the Fermi-Dirac distribution function and reads

$$\Delta f_{\mathrm{th}}(T_{\mathrm{el}}, E) = \frac{1}{1+\exp\left((E-E_{\mathrm{F}})/(\mathrm{k_B}\,T_{\mathrm{el}})\right)} - \frac{1}{1+\exp\left((E-E_{\mathrm{F}})/(\mathrm{k_B}\,T_0)\right)}\,. \tag{96}$$

The only fit parameter here is the electronic temperature T_{el}, T_0 is the base temperature of 300 K. The comparison between the fit and the experimental Δf is presented in Figure 51**A**. The resulting

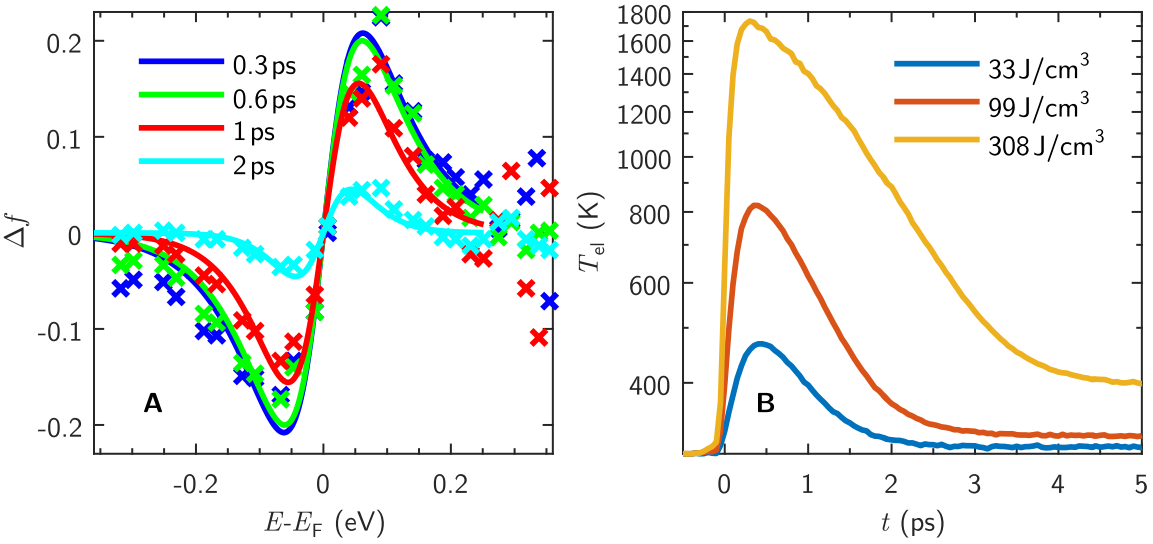

Figure 51: **Experimental Δf fitted with thermal distribution functions.** **A** presents Δf at different time delays (crosses) after excitation with $\bar{U}_{\mathrm{abs}} = 99\,\mathrm{J/cm^3}$. The lines give the best fits to the data based on thermal (Fermi-Dirac) distribution functions (compare also Figure 48). The change in Δf above or below the Fermi level corresponds to excess electrons or holes with respect to the equilibrium distribution function at $T_0 = 300\,\mathrm{K}$. The only fit parameter is the electronic temperature T_{el}, which is plotted in **B** at three different excitation densities.

values of the fit parameter $T_{\mathrm{el}}(t)$ are plotted in Figure 51**B** for different excitation densities. It

turns out, that the fits are good for large time delays, but at short time delays there are major deviations between the data and the fits. The large difference there implies, that the electrons are not in thermal equilibrium yet. In this case, T_{el} represents the "quasi-temperature" of the low energetic quasiparticles. The quality of the fits is elaborated in Figure 53. The temporal evolution of "T_{el}" is close to the time evolution of the spectrally integrated $\Delta\epsilon$. A rise time of about 0.35 ps and similar, excitation density dependent, relaxation times are found. The T_{el} after more than 5 ps corresponds well to the final sample temperature. $\Delta T_{\mathrm{el}}^{\mathrm{max}}$ seems to scale with $\bar{U}_{\mathrm{abs}}$, and not with $\sqrt{\bar{U}_{\mathrm{abs}}}$ as expected maximum temperatures if one would assume the ultrafast or instaneous electron thermalization (e.g. TTM):

$$T_{\mathrm{el}}^{\mathrm{max}} = \sqrt{2\,\bar{U}_{\mathrm{abs}}/\gamma + T_0^2}\,. \tag{97}$$

Surprisingly, the experimental $T_{\mathrm{el}}^{\mathrm{max}}$ are always below these expected maximum temperatures. The experimental and the expected maximum temperatures are compared in Figure 52. Note that the

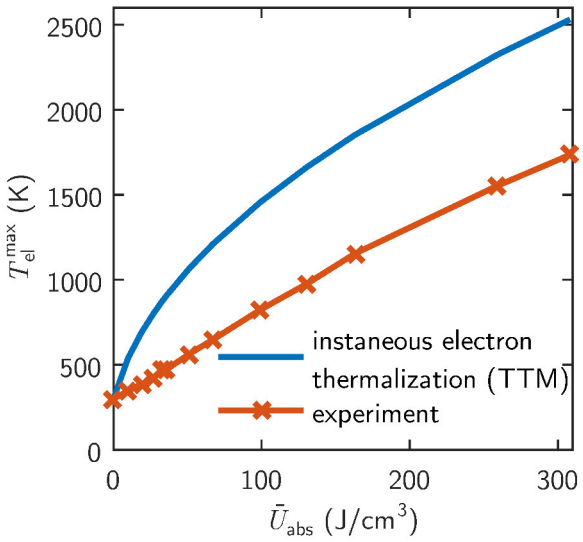

Figure 52: **The maximum electronic temperatures.** The experimental quasi-$T_{\mathrm{el}}^{\mathrm{max}}$ scales with $\bar{U}_{\mathrm{abs}}$ (red crosses). The application of the ultrafast or instaneous electron thermalization assumption, applied with equation (97), results in higher temperatures (blue curve) with a squareroot dependency on $\bar{U}_{\mathrm{abs}}$.

experimental $T_{\mathrm{el}}^{\mathrm{max}}$ is an "quasi-temperature" of the low energy quasiparticles because the electronic subsystem is not in thermal equilibrium at the time when $T_{\mathrm{el}}^{\mathrm{max}}$ is obtained. This topic will be discussed in more detail in the following.

If electrons are non-thermally distributed, the fit-function for thermal electronic distributions, equa-

tion (96), cannot reproduce the experimental data properly. To describe the quality of the fits, the deviation between the experimental datapoints and the fit curve is evaluated by means of the sum of residuals

$$SR = \sum_i |\Delta f_{\mathsf{th}}(T_{\mathsf{el}}, E_i) - \Delta f_i| \ . \tag{98}$$

The deviations between the experimental points and the fit curve depends naturally also on the signal to noise ratio. The noise-, systematic- or procedural-error-related deviation is assumed to consist of a part which naturally scales with the signal amplitude and an additional constant offset (which will dominate at low excitation densities or long time delays)

$$\varsigma_i \approx \varsigma_{0,i} + \varsigma_{\mathsf{sig}} \cdot |\Delta f_i| \ . \tag{99}$$

The noise component, which is proportional to the signal strength, is also proportional to excitation density fluctuations, which have their origin inside the laser system.[30]

The sum of residuals, SR, contains the deviations between the thermal electronic distribution function used in the fit, Δf_{th}, and the noise- and errorless experimental electronic distribution function Δf^{exp} and, in addition, the noise and errors, ς_i ($\Delta f_i = \Delta f_i^{\mathsf{exp}} + \varsigma_i$). The upper limit to SR can be estimated with the triangle inequality applied to the definition (98):

$$SR \leq \sum_i |\Delta f_{\mathsf{th}}(T_{\mathsf{el}}, E_i) - \Delta f_i^{\mathsf{exp}}| + \varsigma_i \, . \tag{100}$$

If Δf^{exp} is thermal or if there are no noise and no errors ($\varsigma_i \equiv 0$), then the inequality (100) is in fact an equation. If Δf^{exp} is thermal and the values of the offset of the noise and errors $\varsigma_{0,i}$ (see equation (99)) are insignificant, i.e. $\varsigma_{0,i} \ll \varsigma_{\mathsf{sig}} \cdot |\Delta f_i|$, then the relative deviation

$$rR = \frac{SR}{SA} \tag{101}$$

is constant. Here

$$SA = \sum_i |\Delta f_i|$$

is the sum of all absolute changes of Δf. The relative deviation reduces in this case to

$$rR = \varsigma_{\mathsf{sig}} \, .$$

If $\sum_i \Delta f_i$ is small compared to $\sum_i \varsigma_{0,i}$, then rR is close to 1. If Δf^{exp} is thermal at temperatures which are not too low ($\Delta f_i \gg \varsigma_{0,i}$ at every i), then the relative deviation stays constant. If Δf_i

[30] Although the experimental data is processed with Fresnel equations and the equation for multiple reflections in thin films, the linearized equations are a good approximation for all the data at hand (see Section 5.4.1, equations (73) and (74)). Therefore the whole data processing is based on linear equations.

(especially at the tails) reaches the offset noise level, then rR increases with decreasing Δf. This increase in rR arises mainly at longer time delays.

The sum of residuals and the relative deviation are evaluated at each time delay and presented in Figure 53 for different excitation densities. rR drops during the first few hundred femtoseconds for all

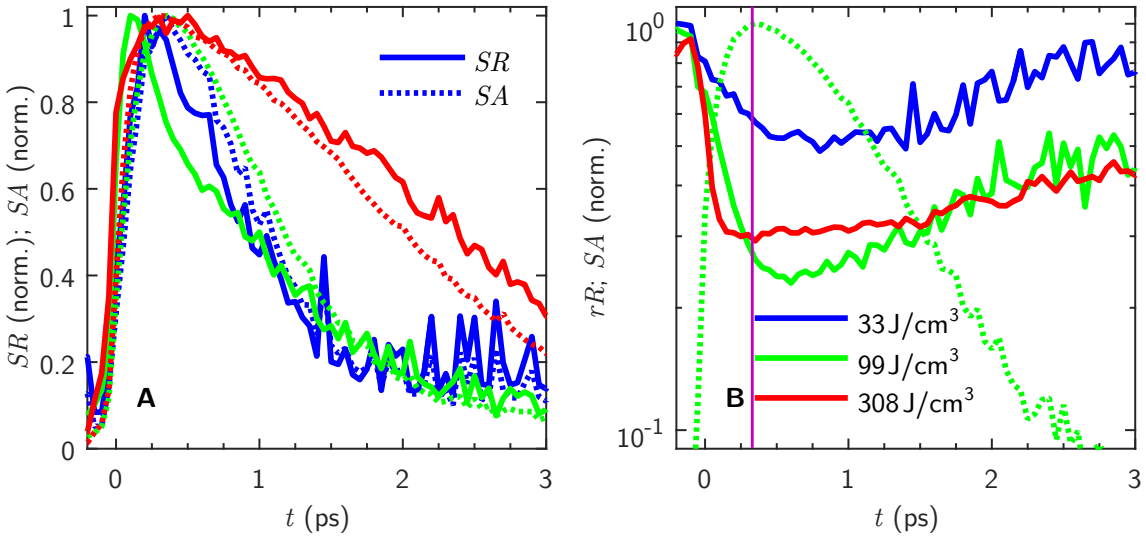

Figure 53: **Quality of the thermal fits (estimation of the electron thermalization time, τ_{th}).** **A** Sum of the residuals of the thermal fits, SR (solid lines), compared to the sum of the absolute changes of Δf (SA, dashed lines). **B** Time dependence of the relative deviation rR. The global minimum corresponds to the electron thermalization time. Around the minimum of rR, the deviation between Δf^{exp} and the Δf_{th} follows the slope of SA (compare with **A**). After the minimum, rR increases slowly over time. The increase is related to the decrease of the signal strength SA as discussed in the text. The violet line marks the time of the peak in $\Delta\epsilon$. For both graphs both legends are used.

excitation densities. This decrease in SR corresponds to Δf^{exp} approaching Δf_{th}. After this initial decrease, SR and SA are parallel for some time. This gives constant rR and it indicates that the electrons are nearly in thermal equilibrium (see equation (101)). The electron thermalization time estimates are obtained from these graphs and they are found to be in the range between 0.4 ps (at high excitation densities) and 0.8 ps (at low excitation densities). After the flat period, the relative deviation increases again. This is because the tails of the spectra reach the offset noise and error level ($\Delta f_i \lesssim \varsigma_{0,i}$ at the tails). This is also demonstrated by the increasing noise in SR and rR over time.

5.8 The electron-phonon thermalization and the determination of the electron-phonon coupling constant

The relaxation process after the electrons are thermalized ($t \geq \tau_{\mathsf{th}}$) could be described by the TTM (introduced in Section 3.1). This model contains the parameter of the electron-phonon coupling strength λ (see Section 2.2). A standard optimization routine is used to optimize the agreement between the numerical solutions of the system of coupled differential equations of the TTM (equations (21) and (22)) and the experimentally determined T_{el}. Here, the electron-phonon coupling strength $\lambda \langle \omega^2 \rangle$, which essentially describes the energy exchange between the electronic and the lattice subsystems via electron-phonon scattering events, is a fit parameter. Figure 54**A** presents this result. The errorbars give the uncertainty of T_{el}, obtained from the quality of the Fermi-Dirac fits to the experimental $\Delta f(t)$. The temperature of the lattice (at $t \geq \tau_{\mathsf{th}}$) is known from the energy conservation law. The electron-phonon coupling strength $\lambda \langle \omega^2 \rangle$ is varied within a fit procedure to reduce the deviation between the experimental and the computed T_{el}.

Figure 54**B** presents the parameter of the TTM fits at different excitation densities, $\lambda \langle \omega^2 \rangle$. The errorbars are based on the uncertainty of T_{el} and the uncertainty of $\lambda \langle \omega^2 \rangle$ in the application of the TTM fit. The electron phonon coupling strength is found to be

$$\lambda \left\langle \omega^2 \right\rangle = 45\,\mathsf{meV}^2\,. \tag{102}$$

This result agrees with the theoretically determined value of Beaulac et al. [BAP82] which is $\lambda \langle \omega^2 \rangle = 46\,\mathsf{meV}^2$. Moreover, the determined $\lambda \langle \omega^2 \rangle$ is independent of the excitation density as it should be. This is a very important result. As it is mentioned in Section 2.2 (see Table 1), applications of different models on different datasets result in different $\lambda \langle \omega^2 \rangle$. This important experimental result allows on the one hand to test and optimize all these models, on the other hand, this improved understanding of the electron-phonon interaction allows to improve the characterization of metals and, in particular, superconductors.

5.8.1 Reading out ΔT_{el} from the experimental $\Delta R/R$ and $\Delta T/T$

The non-thermal electron models such as the model of Sun et al. (see Section 3.4) split the electronic subsystem into two parts. The thermal part mostly covers the quasiparticles at the Fermi level and the non-thermal part covers the high energy quasiparticles. The number of quasiparticles at the Fermi level has a large impact on the optical properties near the upmost d-band to Fermi

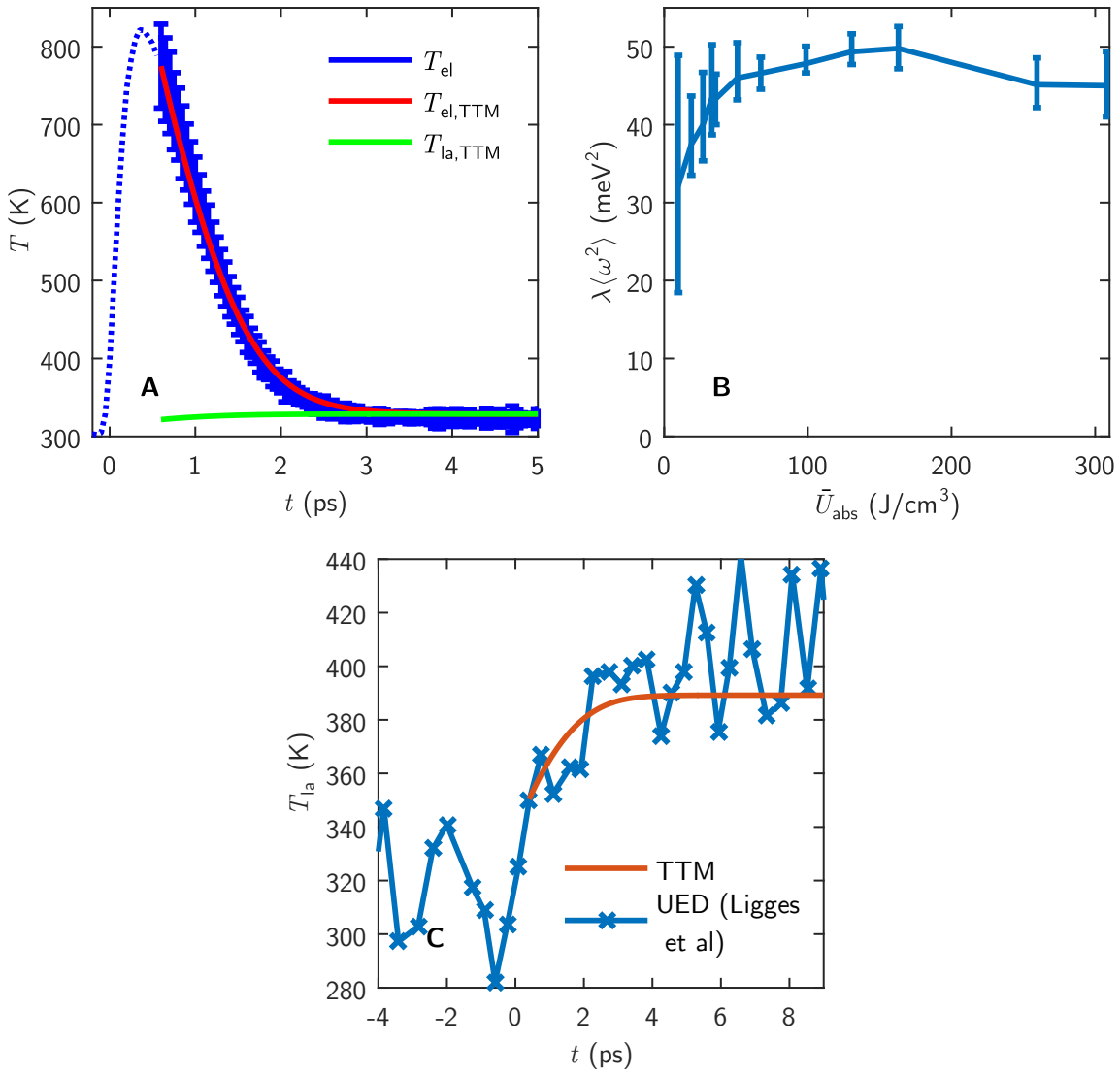

Figure 54: **Thermal relaxation process described by the TTM; Determination of the electron-phonon coupling constant $\lambda\langle\omega^2\rangle$. A** The TTM describes the relaxation of the electrons after they are in thermal equilibrium ($t > \tau_{th}$). The model is fitted to the experimental T_{el} with $\lambda\langle\omega^2\rangle$ being the only fit parameter. The resultant $\lambda\langle\omega^2\rangle$ is plotted in **B**. The electron-phonon coupling constant is found to have a value close to the theoretical prediction of 46 meV^2 [BAP82]. The experiment shows that $\lambda\langle\omega^2\rangle$ depends neither on $\bar{U}_{abs}$ nor on T_{el} in agreement to the theoretical predictions. **C** The time constant of the lattice heat up corresponds to the result of the ultrafast electron diffraction experiment performed by Ligges et al. [Lig+09; Lig09]. The final lattice temperatures are nearly the same in both experiments ($T_{la}^{max} = 390$ K for $\bar{U}_{abs} = 308$ J/cm^3 and $T_{la}^{max} = (405 \pm 20)$ K for the UED-experiment).

level resonance around 2.15 eV, whereas the contribution of non-thermal quasiparticles which are at higher energies is negligible at the resonance. The proportionalities at the resonance are

$$\Delta R/R(2.2\,\mathrm{eV}) \;\propto\; \int_{-\sigma}^{\sigma} |\Delta f|\; \mathrm{d}E\,, \tag{103}$$

$$\Delta T/T(2.14\,\mathrm{eV}) \;\propto\; \int_{-\sigma}^{\sigma} |\Delta f|\; \mathrm{d}E\,. \tag{104}$$

Here, σ is determined by the energy resolution of the probe beam at selected photon energies in addition to the damping constant of the upmost d-band to Fermi level transitions (see Section 4.3.1). In a small interval around the Fermi level, Δf is a linear function of ΔT_{el}

$$\Delta f\big|_{E\approx E_{\mathrm{F}}} \approx \frac{\Delta T_{\mathrm{el}} \cdot (E - E_{\mathrm{F}})}{\mathrm{k_B}\, T_0^2} \frac{\exp\left((E - E_{\mathrm{F}}) \,/\, (\mathrm{k_B}\, T_0)\right)}{\left(1 + \exp\left((E - E_{\mathrm{F}}) \,/\, (\mathrm{k_B}\, T_0)\right)\right)^2} \tag{105}$$

as long as $\Delta T_{\mathrm{el}} = T_{\mathrm{el}} - T_0$ and $|E - E_{\mathrm{F}}|$ are small, which is the case at low excitation densities. In this approximation, equations (103), (104) and (105) result in

$$\Delta R/R(2.2\,\mathrm{eV}) \;\propto\; \Delta T_{\mathrm{el}} \tag{106}$$

$$\Delta T/T(2.14\,\mathrm{eV}) \;\propto\; \Delta T_{\mathrm{el}} \tag{107}$$

at low excitation densities. At high excitation densities with large ΔT_{el} the first order Taylor expansion, given by approximation (105), may fail.

ΔT_{el} as a function of time is known from the Fermi-Dirac fits to the experimental Δf (see Figure 51**B** in Section 5.7). However, the discussed procedure to determine ΔT_{el} is quite elaborate. The proportionalities (106) and (107) allow us to simplify the data analysis. The validity of the proportionality (106) is tested in Figure 55 (the blue solid lines are $\Delta R/R(2.2\,\mathrm{eV})$, scaled to match ΔT_{el} at $t > 5\,\mathrm{ps}$, and they are compared to the experimental ΔT_{el}, the black solid lines). Figure 55 shows ΔT_{el} as a function of time at two different excitation densities. At low excitation densities the proportionalities (106) and (107) are confirmed, whereas at high excitation densities ($> 150\,\mathrm{J/cm^3}$) the deviation between the black and the blue line in Figure 55**B** is most likely the result of the approximation (105). The turning point is at about $150\,\mathrm{J/cm^3}$, which is clearly visible in Figure 55**C**. The TTM is applied to $\Delta T_{\mathrm{el}}(t)$ of the scaled $\Delta R/R(2.2\,\mathrm{eV})$ transients (blue lines). The only fit parameter is the electron-phonon coupling constant with the resulting value of $\lambda \langle \omega^2 \rangle = 44\,\mathrm{meV^2}$. This value is close to the earlier result (102) but is determined with much less experimental and mathematical effort. The points of intersections with the blue solid lines mark the electron thermalization times, which are presented in Figure 55**C**. These points of intersection occur because at short time delays, the electrons are not thermally distributed in the metal and the TTM does not consider the

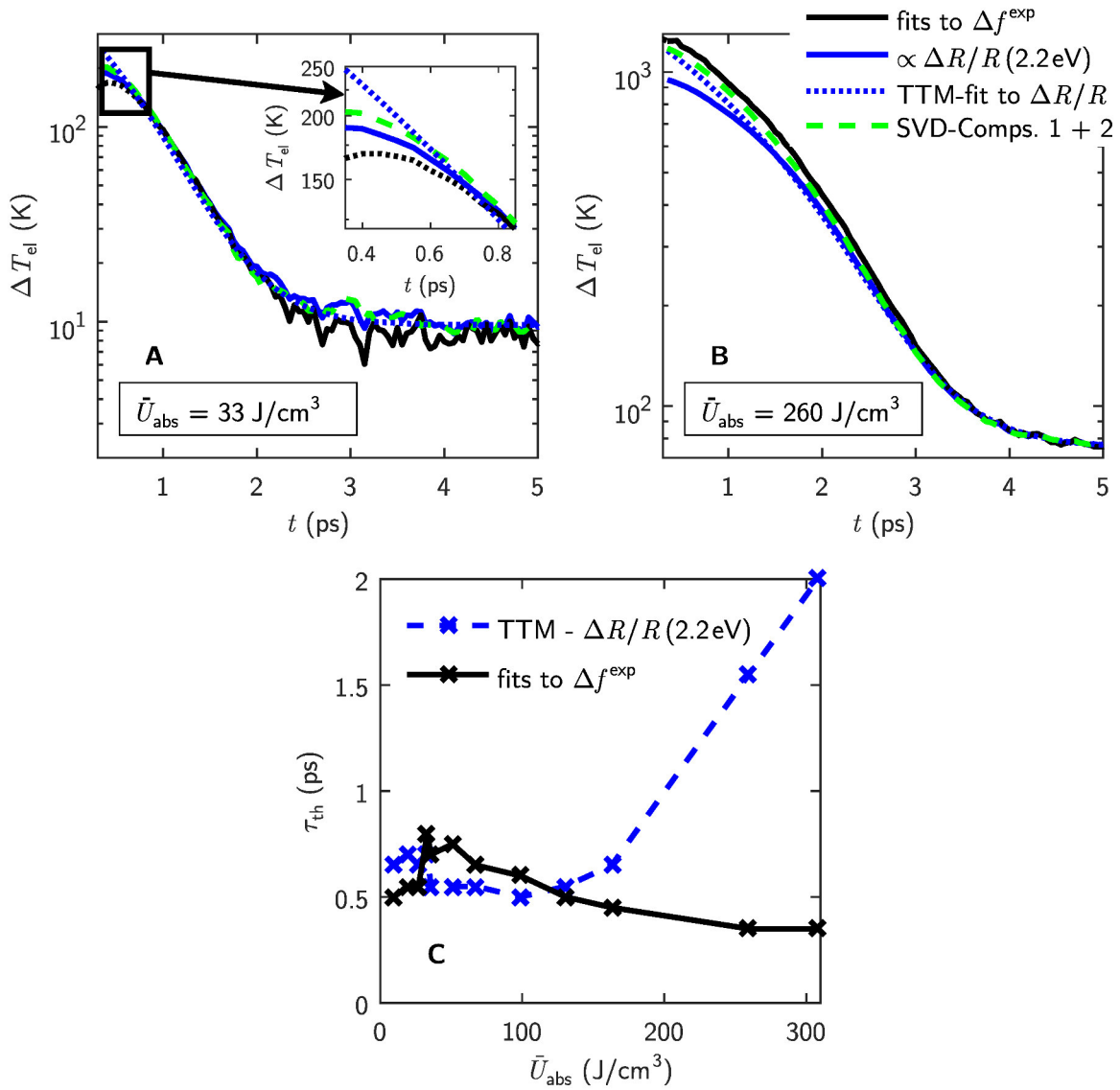

Figure 55: **Application of the TTM analysis to $\Delta R/R$.** **A** and **B** show ΔT_{el} as a function of time at different excitation densities. The results of the Fermi-Dirac fits from Section 5.7 are presented with black solid lines. The resonance transient (at $\mathrm{h}\nu = 2.2\,\mathrm{eV}$) is scaled to reproduce the lattice temperatures after 5 ps (blue solid lines). The TTM is applied to ΔT_{el} of the blue solid lines and the results are presented with the blue dotted lines ($\lambda \langle \omega^2 \rangle$ is the only fit parameter). The intersections between both blue lines represent the electron thermalization times plotted in **C** as a function of the excitation density. The green dashed lines are the scale of the spectral integrated components 1 and 2 of the SVD on $\Delta R/R$ (see the main text and Figure 42).

non-thermal part of the electrons in the energy conservation law. As it is already pointed out, the proportionality (106) is not valid above 150 J/cm^3 and that seems to be the reason for the deviation between the two results for τ_{th} above 150 J/cm^3.

The green dashed line in Figure 55**A** and **B** demonstrate another way to get the proportionality

between an experimental transient and ΔT_{el}. Here, the whole spectra and not just a single transient are taken into account. The SVD is used as a filter (described in Section 5.5.4) to filter out the upmost d-band to Fermi level resonance and to neglect the other parts of the response like the response due to intraband transitions. The optimized $\Delta R/R$ is integrated over the energy at every time delay separately. If the electrons are described by a Fermi-Dirac distribution function, then the integrated response is proportional to ΔT_{el} at every excitation density, i.e.

$$\begin{aligned}\Delta T_{\mathsf{el}} &= \frac{1}{2\,\ln(2)\,D(E_{\mathsf{F}})\,\mathrm{k_B}}\,N_{\mathsf{qp}} = \frac{1}{2\,\ln(2)\,D(E_{\mathsf{F}})\,\mathrm{k_B}}\int\limits_0^\infty |\Delta f(E-E_{\mathsf{F}})|\,\mathrm{d}E \\ &\propto \int\limits_0^\infty \frac{\Delta R}{R}\Big|_{\mathsf{d}\rightarrow\mathsf{Fermi}}\,\mathrm{d}\nu\,,\end{aligned}$$

referring to equation (129). The idea of the proportionality in the last step is that every excited quasiparticle contributes to the measured response with the same spectral weight but shifted in energy (holes contribute with different sign compared to excited electrons). This is a good assumption if the response is purely related to the upmost d-band to Fermi level transitions.

5.8.2 Criticism of the two component method to analyse $\Delta T/T$ with the TTM

In the early beginnings of the ultrafast spectroscopy on metals (see [EA+87; All87; BFI87; Bro+90]), the data were limited to a single transient taken at the photon energy of the used laser system. To interpret the measured transient, some assumptions had to be made. One of those assumptions is to expect the electrons to thermalize on a very short timescale (i.e. instantaneously). This assumption allows to calculate the maximum electronic temperature, $\Delta T_{\mathsf{el}}^{\mathsf{pred}}$, based on equation (1). This temperature is in the next step assigned to either the peak of the response or to the zero time delay. Further, the response is assumed to consist of two different components, one is proportional to ΔT_{el} and the other is proportional to ΔT_{la}, i.e.

$$\Delta T/T = A_{\mathsf{el}}\cdot\Delta T_{\mathsf{el}} + A_{\mathsf{la}}\cdot\Delta T_{\mathsf{la}}\,.$$

In Figure 56 this method is applied to the experimental $\Delta T/T$ in two different ways.
First, the TTM coupled differential equations are solved with variable parameters A_{el}, A_{la} and $\lambda\langle\omega^2\rangle$. It turns out (Figure 56**A** and **B**) that according to this analysis, the lattice has a large impact on the response ($A_{\mathsf{la}}/(A_{\mathsf{el}}+A_{\mathsf{la}}) > 50\,\%$, compare with Figure 56**D**) in contrast to the findings of Section 5.5.1 (compare Figure 40**B** ($\propto \Delta T_{\mathsf{el}}$) and **D** ($\propto \Delta T_{\mathsf{la}}$)), where the ΔT_{la} contribution to the response,

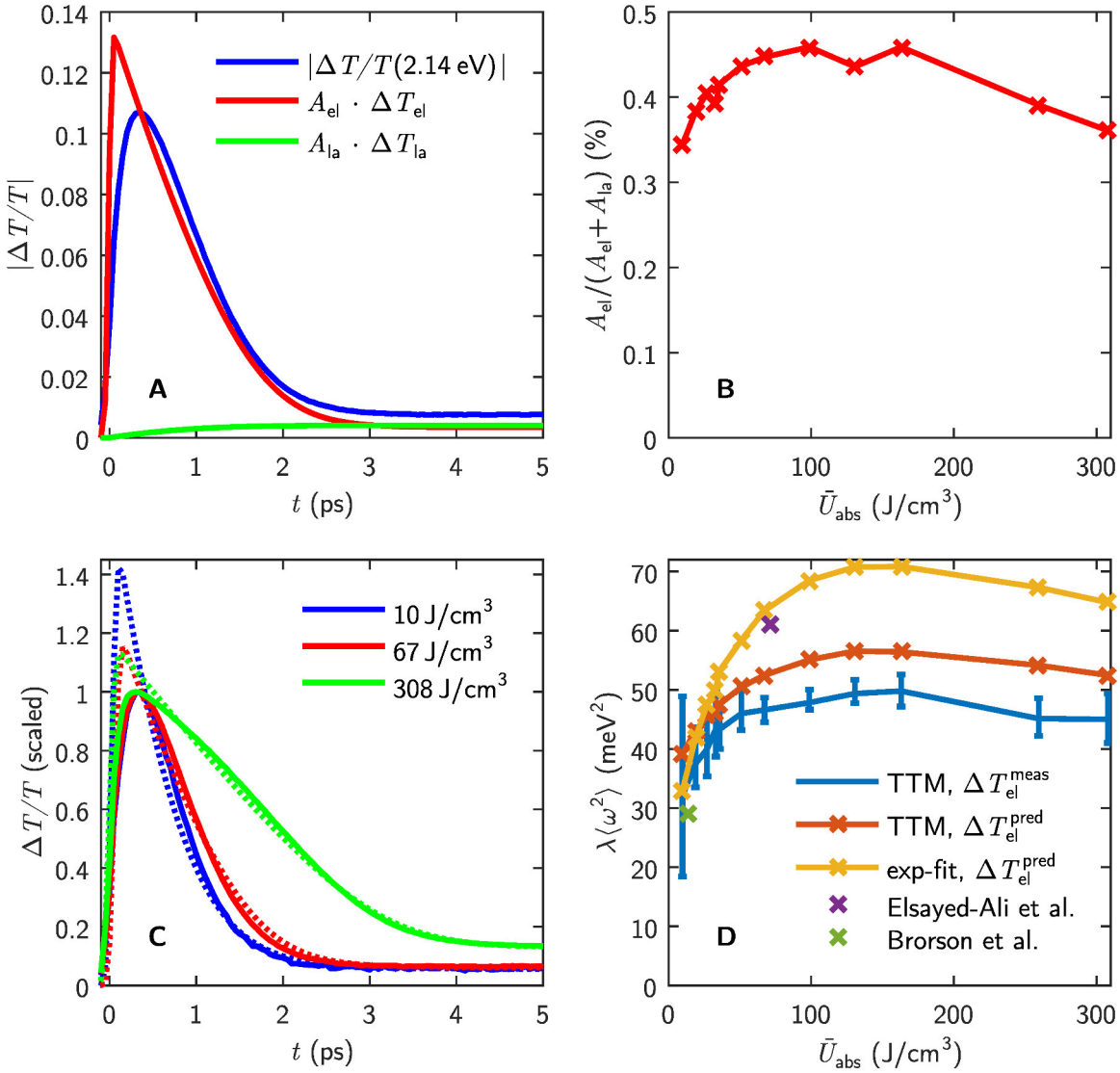

Figure 56: **TTM application to the experimental $\Delta T/T$.** **A** $\Delta T/T$ (blue line) is split into two components, the first one is the lattice component with strength A_{la} (green line) and the second one is the electronic component (red line). **B** Relative strength of the electronic component as a function of the excitation density. **C** $\Delta T/T(2.14\,\text{eV})$ at different excitation densities (the solid lines represent the experimental data) fitted with the TTM (dotted lines); **A** describes the same at 99 J/cm^3. The corresponding electron-phonon coupling constant $\lambda\langle\omega^2\rangle$ is presented in **D** (red line) together with the method of exponential fits described in the main text (yellow line) and the experimental values of Brorson et al. [Bro+90], Elsayed-Ali et al. [EA+87] and the result of this work (blue line; taken from Figure 54**B**).

$A_{\text{la}}/(A_{\text{el}} + A_{\text{la}})$, is less than 25 %. Further, the experimental $\Delta T/T$ is not reproduced at short time delays (see Figure 56**A** and **C**).

Another method to apply the TTM uses an approximate expression for the coupled differential

equations of the TTM which is valid for small ΔT_{el}, i.e.

$$\frac{\partial T_{\mathsf{el}}}{\partial t} = g \cdot \left(T_{\mathsf{la}} - T_{\mathsf{el}}\right) / \left(\gamma\, T_{\mathsf{el}}\right) \approx -g \cdot \left(\Delta T_{\mathsf{el}}\right) / \left(\gamma\, T_0\right).$$

The solution of this differential equation are exponential functions. The exponential fits to the experimental $\Delta T/T$ result in $\lambda \left\langle \omega^2 \right\rangle$ as presented in Figure 56**D** (yellow line). Note, that the quality of the fits gets worse with increasing excitation density.

Using the methods presented in this subsection results in an excitation density dependent electron-phonon coupling constant $\lambda \left\langle \omega^2 \right\rangle$, which is unphysical (at least in the narrow range of excitation densities used). Also, both methods do not reproduce the experimental data well at short time delays (see the deviations between the experimental transient and the TTM fits in Figure 56**C**). The conclusion of this subsection is that the presented methods to apply the TTM to the experimental data recorded at a single wavelength are insufficient to properly determine $\lambda \left\langle \omega^2 \right\rangle$.

However, the spectrally resolved study provides direct access to the time evolution of the electronic distribution function and as a result, $\lambda \left\langle \omega^2 \right\rangle$ is excitation density independent as expected.

6 Non-thermal electron dynamics

In Chapter 5 the introduced data analysis allows to estimate the electron thermalization time and the electron-phonon coupling constant $\lambda\langle\omega^2\rangle$. After the electrons are in thermal equilibrium, the TTM is able to describe the electron-lattice thermalization process. However, the experiment is also sensitive to the process of electron thermalization which takes place at shorter timescales. As there is a lack of reliable theory to describe this process, the published models are tested in this chapter. In particular the question concerning the very quick transfer of energy to the lattice in the first few hundred femtoseconds is addressed.

The chapter starts with the application of the phenomenological TTM-extensions of Sun et al., Carpene et al. and Lisowski et al. (see Section 3.4) to the experimental data ($\Delta f(t)$) in Section 6.1. All these models include a non-thermal electronic subsystem to describe the non-thermal part of Δf. The second section (Section 6.2) extrapolates the experimental data ($\Delta f(t)$) to the energy range outside of the accessible window of our experiment ($|E - E_\mathsf{F}| > 0.2\,\mathrm{eV}$). The approach to describe the energy relaxation of the electronic subsystem is to use the low-excitation-density approximations, for example the spontaneous phonon emission (see Section 2.3) to describe the electron-phonon energy exchange and an low-density approach to quantify the quasiparticle multiplication rate (see Section 2.7) to determine the average quasiparticle energy as a function of time. After hundreds of femtoseconds, these approximations fail and an extended version of the model of Lisowski et al (Section 6.3) and the model of Baranov & Kabanov (Section 6.4) are tested to see, whether they can describe the subsequent electron dynamics or not.

6.1 The extensions of the TTM

6.1.1 Analysis of the experimental data with the model of Sun et al.

Sun et al. [Sun+94] first extended the TTM considering an additional subsystem of non-thermal electrons (the model is introduced in Section 3.4). This non-thermal electronic subsystem overcomes the limitation of the TTM considering thermal electrons only. The TTM system of differential equations is extended by one equation with two additional coupling parameters α and β. These parameters represent the coupling of non-thermal quasiparticles to either the thermal quasiparticles (α) or the lattice (β). α and β are assumed to be independent of the excitation density. In the

beginning, the absorbed electromagnetic energy is fully transferred to the non-thermal quasiparticle subsystem resulting in a step-like Δf (see Figure 4). However, the time evolution of Δf is unknown and the model of Sun et al. does not provide any information about the spectral shape of Δf at time delays before the electrons are thermalized (at $t < \tau_{\mathsf{th}}$, where τ_{th} is the electron thermalization time).

The model of Sun et al. is applied to the experimental $\Delta f(t)$ using the method of least squares. α and β are varied in a way to reproduce the measured changes in the electronic temperatures, ΔT_{el}, at each excitation density, focussing on the time delays with a defined ΔT_{el} (at $t \geq \tau_{\mathsf{th}}$).[31] The resultant (numerical) solution of the coupled differential equations (equations (26), (27) and (28)) provide the information about the energy distribution across the different subsystems at short time delays and it depends on the fit parameters and the boundary conditions (e.g. $\bar{U}_{\mathsf{abs}}$). The result at $\bar{U}_{\mathsf{abs}} = 99\,\mathrm{J/cm^3}$ is illustrated in Figure 57**A**. At other excitation densities, different values for α and β are found as shown in Figure 57**B**. The extracted β is almost independent of the excitation density as expected by the model. The large error bars of α and β include the uncertainty of the experimental ΔT_{el} and the uncertainty of the fit. The inverse of α, which is τ_{th}, varies from 500 fs at intermediate excitation densities, up to 800 fs at low excitation densities. It turns out, that the model of Sun et al. cannot describe the whole experimental dataset with an excitation density independent parameter α. The electron-phonon time constant $\tau_{\mathsf{p}} = 1/\beta$, which is almost independent of the excitation densities, is at about 400 ± 100 fs. The experimental Δf in the accessible window (-0.39 eV $< E - E_{\mathsf{F}} <$ 0.25 eV) is not sufficient to test the energy distribution across the different subsystems at short time delays according to the solution of the model's differential equations. This is because many excited quasiparticles are out of the experimental window and the amount of energy stored in these high energy quasiparticles is unknown. So, the energy density of the high energy quasiparticles is not detected and is missing in the integrated energy density (the cyan curve in Figure 57**A**). Interestingly, although the model assumes the energy of the pump pulse to be transferred to the non-thermal electronic subsystem directly, the simulation suggests, that the maximum energy in this subsystem is only around 65 %. This would imply, that the rest of the energy is already transferred to the lattice and to the thermal electronic subsystem during the time when the light interacts with the electrons (see also Section 6.2). At high excitation densities α and β have almost the same value implying that both subsystems gain the same amount of energy per time (in the

[31] As the energy in the non-thermal electronic subsystem is decreasing exponentially over time (does not go to 0), τ_{th} indicates the time at which the energy in the non-thermal electronic subsystem is negligible.

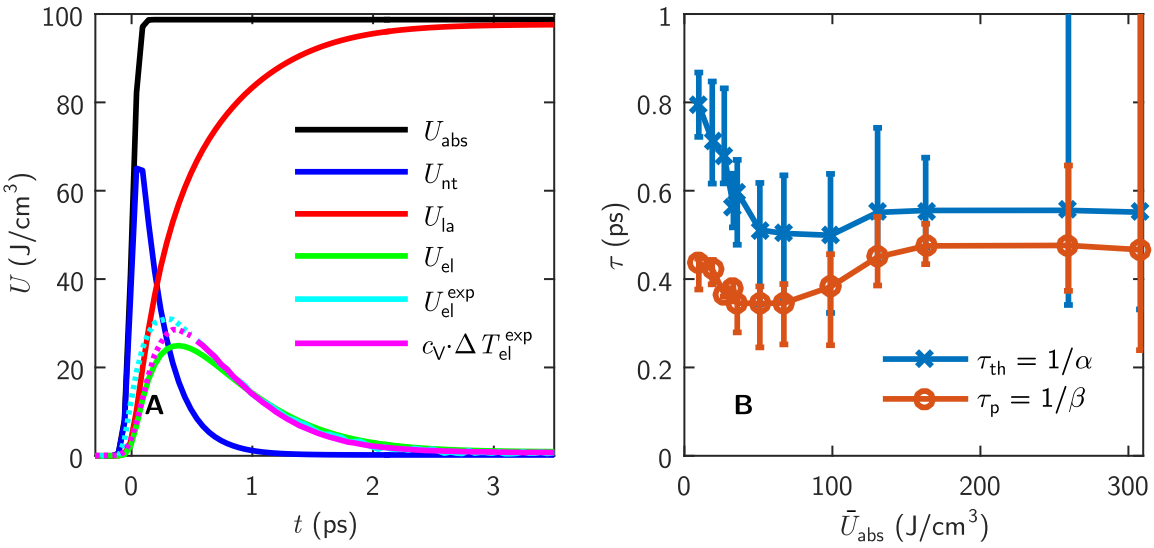

Figure 57: **Application of the extended TTM by Sun et al. [Sun+94]. A** Energy densities of all subsystems (thermal subsystem: green line, non-thermal subsystem: blue line) compared to the result of the Fermi-Dirac fits (magenta line with dotted line for the quasi-temperatures prior to the electron thermalization time). The integrated energy of the experimental spectra (cyan) underestimates the real energy of all excited quasiparticles at short time delays because of the limited experimental window (-0.39 eV $< E - E_F <$ 0.25 eV). The excitation density dependence of the fit parameters α and β are plotted in **B**. The energy relaxation constant β between the non-thermal electronic subsystem and the lattice is almost independent of the excitation density. α connects thermal and non-thermal electronic subsystems and corresponds to the electron thermalization time, τ_{th}. This time constant increases linearly with decreasing excitation density below 70 J/cm^3.

stage of relaxation at short time delays). It would follow, that more than 15 % of the absorbed energy is transferred to the lattice within the first hundred femtoseconds. So, the model implies a very fast heating of the lattice in the beginning of the relaxation process in order to account for the experimental ΔT_{el} at $t > \tau_{th}$.

According to equation (30) one can estimate the average quasiparticle energy of the non-thermal quasiparticles[32]

$$\langle |E_{nt} - E_F| \rangle \lessapprox \frac{\pi \hbar \lambda \langle \omega^2 \rangle}{\beta} \approx 0.1\,\text{eV}\,. \tag{108}$$

This finding does not correspond to the experimental value of $\langle |E_{nt} - E_F| \rangle$ which lies above 150 meV in the first hundreds of femtoseconds even in the (unrealistic) case that there are no quasiparticles at energies outside the experimental window (the experimental values are presented below in Figure 62**C**). In Section 6.2, we introduce a more elaborate model. This model suggests lower lattice heating

[32]The average energy is averaged over all non-thermal quasiparticles and over all times. The averaging over time is weighted by the particle density of the non-thermal quasiparticles N_{nt}.

rates compared the model of Sun et al. (see Figure 62**B**) and uses time dependent energy transfer rates ($\beta \equiv \beta(t)$).

6.1.2 Analysis of the experimental data with the model of Carpene

The TTM extension of Carpene [Car06] (see Section 3.4.1) provides more information about the non-thermal electronic subsystem compared to the model of Sun et al., because it suggests the shape of the non-thermal Δf. This allows us to test the model directly on the experimental Δf for higher accuracy. The energy relaxation rates α and β are replaced by the Δf-relaxation-time-constant τ_0 for the interaction of non-thermal quasiparticles with thermal quasiparticles and τ_p for the interaction of non-thermal quasiparticles with phonons (see equation (31)).[33] Figure 58 presents fits to the experimental Δf. The experimental data was fitted over the entire spectral range and

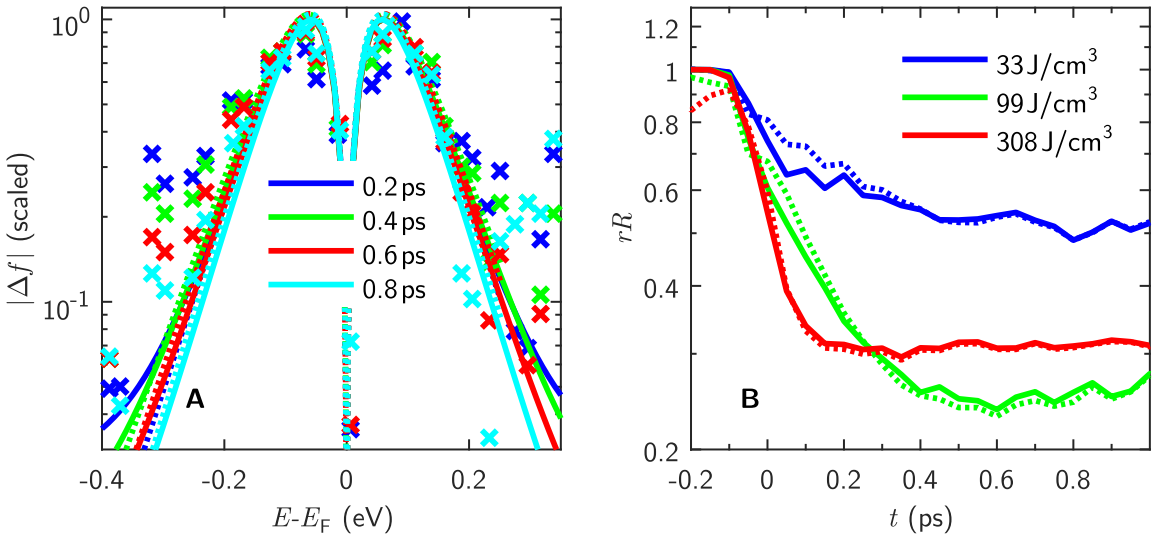

Figure 58: **Data analysis with the model of Carpene [Car06].** The solid lines are the result of the model of Carpene. The dotted lines are best fits to the experimental data based on Fermi-Dirac distribution functions (i.e. considering the electrons to be always in thermal equilibrium). **A** The model of Carpene predicts the change in shape of the non-thermal Δf over time [DV+12]. The model parameters τ_0 and τ_p are adjusted to reproduce the experimental Δf (excited with $\bar{U}_\mathrm{abs} = 99\,\mathrm{J/cm^3}$). **B** Relative deviations between the experimental Δf and the result of the model. At low excitation densities and short time delays the assumed Δf of the model describes the experimental Δf more precisely than Fermi-Dirac distribution functions could do.

over all experimental time delays within a single fit procedure, adjusting the parameters τ_0 and τ_p

[33] Note, the definitions of τ_p are similar in the model of Sun et al. (see Section 6.1.1) compared to the model of Carpene but not exactly the same.

(the fit procedure allows these parameters to be excitation density dependent).

The result of the fit procedure is plotted in Figure 58**A** (the related fit parameters are presented in Figure 59**B**). Δf is non-thermal at low excitation densities and short time delays (see Section 5.8). In this range and at the tails of Δf, the deviation between the Fermi-Dirac fits and the experimental data is pronounced. Compared to the description with Fermi-Dirac distribution functions, the model of Carpene gives an improved agreement between the experimental and computed Δf at the tails and at short time delays. The relative deviations between the experimental data and result of the model integrated over the whole spectral range (rR; see equation (101) in Section 5.7) are presented in Figure 58**B** as a function of time and at three different excitation densities. Although the Fermi-Dirac functions are fitted to the experimental Δf at each time delay separately (one free parameter at each time delay), rR (dotted lines) are larger compared to the result of the application of the model of Carpene, where the model assumes just two time independent free parameters (τ_0 and $\tau_{\text{e-p}}$) to reproduce Δf at every experimental time delay.

The resulting energy relaxation is plotted in Figure 59. The result is similar to the findings based on the model of Sun et al. (compare to Figure 57**A**). The major difference is the larger deviation between the simulated energy of the thermalized quasiparticles (green line) and the experimentally estimated energy of the thermalized quasiparticles (magenta solid line). One can read out the electron thermalization time, τ_{th}, by comparing the experimental electron energy (magenta line in Figure 59) to the simulated energy of the thermal electrons (green line) considering the energy in the non-thermal electron system (blue line). At the time, when the green and the magenta lines start to overlap and the energy in the non-thermal part (blue line) is much smaller, the electrons can be considered to be in thermal equilibrium. Based on this analysis the electron thermalization time is larger compared to the result of the Fermi-Dirac fits (Section 5.8).

Importantly, the values of τ_0 are found to be a factor of 10 to 60 larger than the theoretically predicted value of 0.46 fs. The predicted value is far too small to properly describe the electron dynamics within the model of Carpene. This result is comparable to the findings of Della Valle et al. [DV+12] in Au (they used $\tau_0 = 7$ fs). The high values of τ_0 correspond to a slow reshaping of the non-thermal Δf_{nt}, where the corresponding variance remains large compared to the variance of the thermalized quasiparticles (see Figure 59**C**). It can be easily verified (using (31)), that the equation

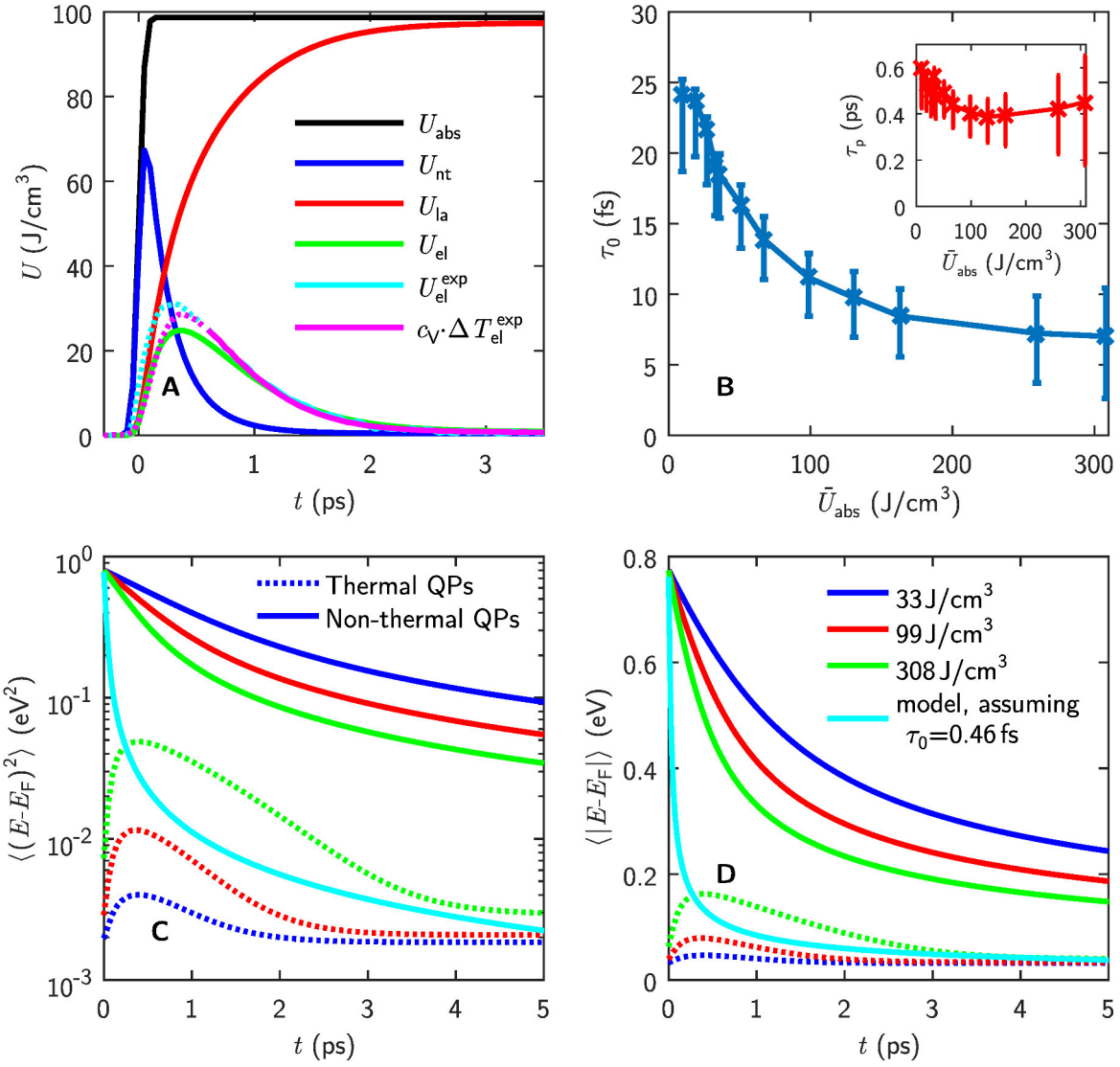

Figure 59: **Model of Carpene [Car06]. The electron energy relaxation and the excitation density dependence of the fit parameters.** **A** Energy distribution as a function of time delay. The maximum energy in the thermal subsystem (green line) is smaller compared to the result of the Fermi-Dirac fits (magenta solid line). The electron thermalization time is below 1 ps. **B** Excitation density dependence of the fit parameter τ_0. τ_0 decreases with increasing excitation density down to the value of 10 fs (the theoretically predicted value of 0.46 fs is more than one order of magnitude smaller). The inset shows the electron-phonon energy relaxation time which is almost independent of the excitation density. **C** The time evolution of variance of Δf. The cyan line presents the resulting variance of the non-thermal quasiparticles for the case that the equations of the model of Carpene are solved with $\tau_0 = 0.46$ fs (the same line at every excitation density). **D** The time evolution of the average energy of a quasiparticle in the non-thermal subsystem. **C** and **D** have the same color coding.

which characterizes the variance is

$$\begin{aligned}\left\langle \left(E_{\mathsf{nt}} - E_{\mathsf{F}}\right)^2 \right\rangle (t) &= \frac{\int\limits_{-\mathrm{h}\nu}^{\mathrm{h}\nu} E^2 \exp\left(-t/\tau_0 \cdot \left(\left(E - E_{\mathsf{F}}\right)/E_{\mathsf{F}}\right)^2\right) \mathrm{d}E}{\int\limits_{-\mathrm{h}\nu}^{\mathrm{h}\nu} \exp\left(-t/\tau_0 \cdot \left(\left(E - E_{\mathsf{F}}\right)/E_{\mathsf{F}}\right)^2\right) \mathrm{d}E} \\ &= \frac{E_{\mathsf{F}}\sqrt{\tau_0}}{\sqrt{t}} \cdot \left(\frac{E_{\mathsf{F}}\sqrt{\tau_0}}{2\sqrt{t}} - \frac{\mathrm{h}\nu \exp\left(-t/\tau_0 \cdot \left(\mathrm{h}\nu/E_{\mathsf{F}}\right)^2\right)}{\sqrt{\pi}\,\mathrm{erf}\left(\sqrt{t/\tau_0} \cdot \mathrm{h}\nu/E_{\mathsf{F}}\right)} \right), \end{aligned} \tag{109}$$

where $\mathrm{h}\nu = 1.55\,\mathrm{eV}$ is the pump photon energy.

The second parameter of the model of Carpene is the electron-phonon relaxtion time τ_{p}, which is the same as previously discussed in the the model of Sun et al. (compare the inset on Figure 59**B** with Figure 57**B**). This τ_{p} corresponds to (see inequality (108))

$$\langle |E_{\mathsf{nt}} - E_{\mathsf{F}}| \rangle \lessapprox 0.1\,\mathrm{eV}\,. \tag{110}$$

In contrast to the analysis based on the model of Sun et al., we have the opportunity to test this inequality. The time evolution of $\langle |E_{\mathsf{nt}} - E_{\mathsf{F}}| \rangle$ in the non-thermal subsystem is plotted in Figure 59**D**. The calculation is based on the equation

$$\begin{aligned}\langle |E_{\mathsf{nt}} - E_{\mathsf{F}}| \rangle (t) &= \frac{\int\limits_{-\mathrm{h}\nu}^{\mathrm{h}\nu} E \exp\left(-t/\tau_0 \cdot \left(E/E_{\mathsf{F}}\right)^2\right) \mathrm{d}E}{\int\limits_{-\mathrm{h}\nu}^{\mathrm{h}\nu} \exp\left(-t/\tau_0 \cdot \left(E/E_{\mathsf{F}}\right)^2\right) \mathrm{d}E} \\ &= \frac{E_{\mathsf{F}}\sqrt{\tau_0}}{\sqrt{\pi\, t}} \cdot \frac{1 - \exp\left(-t/\tau_0 \cdot \left(\mathrm{h}\nu/E_{\mathsf{F}}\right)^2\right)}{\mathrm{erf}\left(\sqrt{t/\tau_0} \cdot \mathrm{h}\nu/E_{\mathsf{F}}\right)}\,. \end{aligned}$$

Averaged up to 4 picoseconds, the average energy of each excited non-thermal quasiparticle is

$$\langle |E_{\mathsf{nt}} - E_{\mathsf{F}}| \rangle \approx 0.3\,\mathrm{eV}$$

(based on the slightly excitation density dependent τ_{p}, see Figure 59**D**). This result is inconsistent with the inequality (110) assuming τ_{p} describes the spontaneous phonon emission. The limitation of the model of Carpene is, that it does not allow the non-thermal quasiparticles to remain in the non-thermal subsystem after a single scattering event (discussed in Section 3.4.1). Furthermore, it does not describe a quasiparticle multiplication process within the non-thermal subsystem (the process is introduced in Section 2.7). This limitation of Carpene's model may be the reason for the presented inconsistency in $\langle |E_{\mathsf{nt}} - E_{\mathsf{F}}| \rangle$. To substantiate these statements, the number of excited quasiparticle as a function of the time delay is compared to the results of other models (which include the quasiparticle multiplication of non-thermal quasiparticles) below (see Figure 62**A** in Section 6.2).

6.1.3 Analysis of the experimental data with the model of Lisowski et al.

The model of Lisowski et al. [Lis+04; Lis05] suggests deviding the conduction band electrons into two parts (thermal and non-thermal) with the deviding parameter r ($0 \leq r < 1$; see Section 3.4.2 for more details). In practice, this is done at the level of the density of states. The density of states of the non-thermal quasiparticles is proportional to r (equation (32)) and the thermal quasiparticles partly occupy the remaining states (their quantity is proportional to $1 - r$; see equation (33)). Both, the thermal and the non-thermal subsystems are used, as if both of them are separately in thermal equilibrium. Here, the non-thermal subsystem is at the higher temperature T_{nt} compared to the thermal subsystem at the temperature T_{el}.

Simulations for different temporal dependencies of r are performed to verify whether the model can describe the experimental dynamics or not. All simulations show, that the energy transfer from the electronic subsystem to the lattice, governed by $\lambda \langle \omega^2 \rangle = 46\,\mathsf{meV}^2$, is too slow to describe the experimental data. Although the model is unable to describe the energy relaxation dynamics correctly, in the following, the electron-phonon coupling strength g is taken as a free parameter to check if the model can describe the shape of the non-thermal part of the experimental Δf or not.[34]

The model is applied to the experimental $\Delta f(t)$ with a small number of free parameters. r is assumed to rise with the absorption of light to a maximum value r_{max}. Thus, r_{max} depends on the excitation density and it is used as a fit parameter. After the initial fast rise, r remains at r_{max}. In this description, the electron thermalization is not characterized by the decrease in r but by the decrease in $T_{\mathsf{nt}} - T_{\mathsf{el}}$.

The application of the model requires a modification of the term, which describes the energy exchange between both electronic subsystems, equation (37), to consider the energy conservation law (in case of an t-dependent r). The energy exchange between both electronic subsystems is supposed to be proportional to the difference of the average quasiparticle energies multiplied by the number of scattering events between particles of different subsystems

$$\left.\frac{\partial U}{\partial t}\right|_{\mathsf{nt}\to\mathsf{el}} = \frac{\langle |E - E_{\mathsf{F}}| \rangle_{\mathsf{nt}} - \langle |E - E_{\mathsf{F}}| \rangle_{\mathsf{el}}}{2\,x} \cdot \frac{N_{\mathsf{sc,el}} + N_{\mathsf{sc,nt}}}{2} \,. \tag{111}$$

The factor x present a measure of the average energy exchange between a thermal and a non-thermal quasiparticle during each scattering event between them. This average energy exchange is

[34] The extended model of Lisowski et al. in combination with the description of the initial relaxation dynamics (Section 6.2) is able to describe the experimental Δf with the correct value of $\lambda \langle \omega^2 \rangle$ (determined in Section 5.8) or g, respectively. The result is given in Section 6.3, but additional parameters are required to perform this simulation.

less ($x > 1$) or equal ($x = 1$) to the half of the difference of their averaged energies. The average energy of a quasiparticle in a Fermi-Dirac distribution is

$$\langle |E - E_\mathsf{F}| \rangle = \frac{\pi^2 \, \mathrm{k_B} \, T}{12 \, \ln(2)} \, . \tag{112}$$

The number of scattering events of non-thermal quasiparticles at thermal quasiparticles (see Fermi liquid theory, Section 2.5) is

$$N_\mathsf{sc,nt} = \frac{\sqrt{N_\mathsf{el} \, N_\mathsf{nt}}}{\tau_0 \, E_\mathsf{F}^2} \left(\left\langle (E - E_\mathsf{F})^2 \right\rangle_\mathsf{nt} + (\pi \, \mathrm{k_B} \, T_\mathsf{el})^2 \right) \, . \tag{113}$$

Thermal quasiparticles also scatter at non-thermal ones and the corresponding equation essentially looks the same (because the non-thermal quasiparticles are described by the same distribution function, but different temperature)

$$N_\mathsf{sc,el} = \frac{\sqrt{N_\mathsf{el} \, N_\mathsf{nt}}}{\tau_0 \, E_\mathsf{F}^2} \left(\left\langle (E - E_\mathsf{F})^2 \right\rangle_\mathsf{el} + (\pi \, \mathrm{k_B} \, T_\mathsf{nt})^2 \right) \, . \tag{114}$$

The rates of temperature changes are finally given by (including equations (111), (112), (113) and (114))

$$\left. \frac{\partial T_\mathsf{nt}}{\partial t} \right|_{\mathsf{nt} \to \mathsf{el}} = - \frac{\mathrm{k_B^2}}{r \, 8 \, \tau_0 \, E_\mathsf{F}^2 \, x \, T_\mathsf{nt}} \cdot (T_\mathsf{nt} - T_\mathsf{el}) \, \sqrt{(1-r) \, r \, T_\mathsf{el} \, T_\mathsf{nt}} \left(T_\mathsf{el}^2 + T_\mathsf{nt}^2 \right) \, .$$

Here, x acts as a fit parameter and it is found to be independent of $\bar{U}_\mathsf{abs}$. The value we obtain is

$$x = 12 \, .$$

This is a result of the application of the model of Lisowski et al. to the experimental data, as discussed below. Such a high value of x corresponds to low energy exchange rates. If x takes the lowest possible value of 1, then two excited and interacting quasiparticles will end up at the same energy after scattering. This would result in an unstable non-thermal subsystem because the clear separation of both particles before scattering turns into a situation where the two particles have the same energy. After a few scattering events, it will be difficult to associate a particle with the non-thermal subsystem any more. So, with such a low value of x, the model of Lisowski et al. would not be applicable. Instead, the model requires the situation of two meta-stable electronic subsystems. If the energy transfer between those two subsystems is too high, they cannot be distinguished any more on the hundred femtoseconds timescale. If one electron belongs to the non-thermal and one to the thermal subsystem and after scattering both electrons will have the same energy, then it is impossible to separately count the resultant electrons to the individual subsystems. If the thermal electron gains

only one tenth of the energy of the non-thermal electron (or even less), then this electron clearly remains as part of the thermal subsystem after undergoing a scattering event. In other words, a large electron-electron scattering rate at high quasiparticle energies is required to redistribute the non-thermal part of the electronic subsystem and increase the number of non-thermal quasiparticles in the first stage of the relaxation process. The scattering rates determine the second factor in equation (111). This equation also relates the characteristic time for the energy loss of a quasiparticle in the non-thermal subsystem to the electronic lifetime multiplied by x.

The result of the application of this model to the experimental data is presented in Figure 60. Here, x, r_{max} and $\lambda\left\langle\omega^2\right\rangle$ are used as fit parameters. The experimental Δf is considered as the composite of the thermal and the non-thermal electronic subsystems. At short time delays, Δf contains a non-negligible number of non-thermal quasiparticles. The model reproduces this contribution, as non-thermal quasiparticles, which are present as the wings of Δf at energies $|E - E_{\mathsf{F}}| > 0.2\,\mathsf{eV}$ (see Figure 60**A**). The deviation between the experimental Δf and the model calculation is - as expected - reduced compared to the fits with the Fermi-Dirac distribution (Figure 60**B**). At later times, the model reproduces the experimental Δf with two distinct temperatures (T_{el} and T_{nt}), as accurately as the single temperature fits (but with three parameters instead of one!). However, the result of fitting the experimental data with this model is a slower electron thermalization compared to the earlier findings (see Figure 55**C** black line). Here, the electron thermalization time is close to the electron-phonon thermalization time (see a large deviation between the magenta and the green line in Figure 60**C**). Finally, the resulting electron-phonon coupling constant is a factor of two larger compared to the theoretical prediction ($\lambda\left\langle\omega^2\right\rangle_{\mathsf{theo}} = 46\,\mathsf{meV}^2$, [BAP82]), and it depends on the excitation density (Figure 60**D**). Again, $\lambda\left\langle\omega^2\right\rangle$ is not expected to depend on excitation density [All87] around or above Θ_{D}. The parameter r is, however, in a good approximation linearly dependent on the excitation density at these excitation densities. This is indeed expected because of an increasing number of excited quasiparticles with increasing excitation density.

At 0.7 ps and $\bar{U}_{\mathsf{abs}} = 99\,\mathsf{J/cm}^3$, the simulation gives temperatures of

$$T_{\mathsf{nt}} = 1950\,\mathsf{K}\,,$$

$$T_{\mathsf{el}} = 570\,\mathsf{K}\,.$$

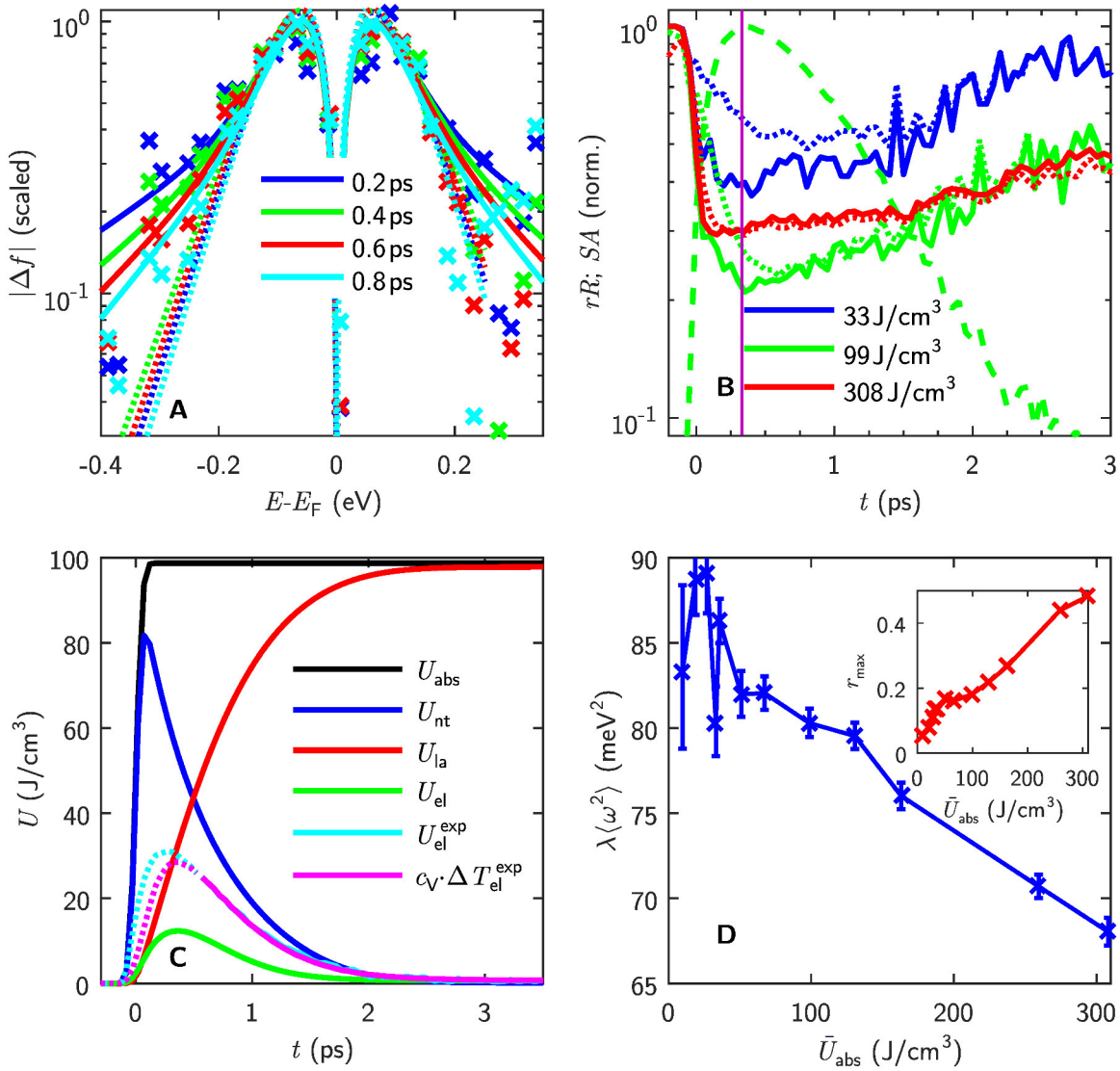

Figure 60: **Application of the heat bath model of Lisowski et al. [Lis+04; Lis05].** The model is applied to the experimental data by fitting Δf. The data at each excitation density is fitted separately. **A** Comparison between the model's Δf and the experimental Δf at different time delays excited with $\bar{U}_{\text{abs}} = 99\,\text{J/cm}^3$ (solid lines). **B** Time dependence of the relative deviations between experimental Δf and the model's Δf (solid lines) or the Fermi-Dirac fits (dotted lines). The dashed line refers to SA (the sum of all absolute changes of the experimental Δf) with its maximum value reached after 350 fs (violett line). **C** Energy density of the different subsystems as function of time delay after excitation. **D** Excitation density dependence of the fit parameters $\lambda\langle\omega^2\rangle$ and r_{max} (inset) used as fit parameters.

The Fermi-Dirac (thermal) fits reproduce the experimental Δf at 0.7 ps with the same accuracy but with a single temperature:

$$T_{\text{el,FD}} = 741\,\text{K}\,.$$

Thus, the model cannot describe the fast lattice heating (with the correct $\lambda \langle \omega^2 \rangle = 46\,\mathrm{meV}^2$), but is able to describe the experimental Δf in the non-thermal regime at short time delays, however with three distinct (time dependent) parameters (T_{nt}, T_{el} and r).

As we can see, none of the introduced extensions to the TTM, which were developed to describe the electron thermalization process at short time delays, allows to adequately describe the experimental data on Cu. Constants appear to be excitation density dependent (e.g. $\lambda \langle \omega^2 \rangle$) or their link to other properties of the sample remains unclear (e.g. τ_0). However, the application of the model of Lisowski et al. did show that main problem that the models are facing is the fast energy transfer from the electronic subsystem into the lattice subsystem on a hundred femtosecond timescale. This energy transfer most be considered because the experiment shows a large discrepancy between the absorbed energy density and the maximum electronic temperature. A rapid energy transfer to the lattice requires a large number of excited quasiparticles which are generated during the first few hundred femtoseconds (we are referring to the theory, which describes the spontaneous phonon emission - see Section 2.3). This important part of the relaxation process is not considered in the model of Carpene, while the model of Lisowski et al. ignores the stage of relaxation at short time delays between the steplike electronic distribution function directly after the optical excitation and the assumed Fermi-Dirac distributed non-thermal electronic subsystem. Indeed, the Fermi-Dirac distributed quasiparticles have a reduced phonon rate because of a reduced number of accessible final electronic states compared to the initial steplike change in the electronic distribution function (see Figure 4). This issue is further discussed in Section 6.2.

6.2 Simulation of $\Delta f(|E - E_{\mathsf{F}}| > 0.2\,\mathrm{eV})$ to account for the fast initial energy transfer to the lattice

All the analysis within this subsection is aimed at getting an idea on how the distribution of the excited quasiparticles is changing during the first few hundred femtoseconds. The experimental data range within this first stage of relaxation is limited, and the rate equations used in this subsection are just first approximations valid for the low perturbation regime. As such, the results of this section should be considered as a rough approximation of the real dynamics, helping to understand the fast energy transfer from the electronic subsystem to the lattice during the first few hundred femtoseconds. In this subsection a method of extrapolation the experimental data to energies outside the limited experimental window is presented. In the second step, the approximate differential equations to

describe the time evolution of the number of excited quasiparticle, N_{qp}, and their energy density, U_{el}, are introduced. These differential equations are solved and the result is presented and discussed at the end of this subsection.

The electronic relaxation process is fully characterized by Δf as a function of time delay and energy. Δf has been determined experimentally but, in a limited energy interval. Especially at short time delays, knowledge of Δf over the broad energy range would be needed. However, the combination of the known number of the excited quasiparticles and their total energy provides the means to perform sensible extrapolations of Δf outside of the experimentally accesible window (such reconstructions are shown in Figure 61, dotted lines). If we know N_{qp} and U_{el}, we can extrapolate Δf outside the

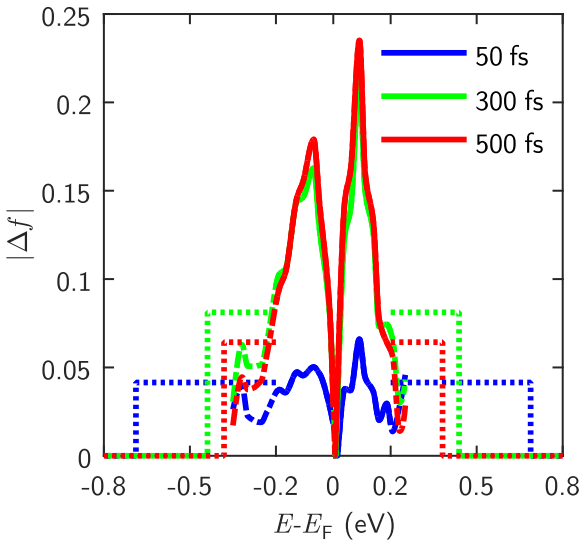

Figure 61: **Extrapolation of Δf to energies outside the experimental window.** The experimental Δf (solid lines) and its extrapolation to higher and lower electron energies beyond the limited experimental window (dotted part of the lines) are plotted at selected time delays. The extrapolations are designed to reproduce the energy and the number of excited quasiparticles according to the green lines in Figure 62**A** and **B**. It can be seen that Δf narrows over time as expected. The number of quasiparticles is proportional to the area below the curve which increases over time up to 150 fs.

experimental window by

$$\Delta f(0.2\,\mathrm{eV} \leq |E - E_{\mathrm{f}}| \leq E_{\mathrm{max}}) = \Delta f^{\mathrm{ep}} = \mathrm{const},$$

where E_{max} and Δf^{ep} are chosen such that U_{el} and N_{qp} are met. I.e., the parameters are determined from the simulated number of excited quasiparticles N_{qp} and their overall energy U_{el} (green lines in

Figure 62**A** and **B**), where the simulation is based on:

$$N_{\mathsf{qp}} = D(E_{\mathsf{F}}) \left(\int_{-0.2}^{0.2} |\Delta f^{\mathsf{exp}}(E)| \, \mathrm{d}E + 2 \cdot \Delta f^{\mathsf{ep}} \cdot (E_{\mathsf{max}} - 0.2\,\mathsf{eV}) \right) ,$$

$$U_{\mathsf{el}} = D(E_{\mathsf{F}}) \left(\int_{-0.2}^{0.2} E \, \Delta f^{\mathsf{exp}}(E) \, \mathrm{d}E + \Delta f^{\mathsf{ep}} \cdot \left(E_{\mathsf{max}}^2 - 0.2\,\mathsf{eV}^2 \right) \right) .$$

This simulation (Δf^{ep}-Simulation) uses two coupled differential equations to describe the time evolution of the electron energy and the number of excited quasiparticles for short time delays

$$\frac{\partial N_{\mathsf{qp}}}{\partial t} = \frac{2}{\mathrm{h}\nu} \cdot \frac{\partial U_{\mathsf{abs}}}{\partial t} \tag{115}$$
$$+4 \cdot D(E_{\mathsf{F}}) \int_{-\infty}^{\infty} \Delta f(E) \cdot (1 - \Delta f(E)) \cdot \gamma_{\mathsf{M}} \left(\frac{E - E_{\mathsf{F}}}{\mathrm{k_B}\, T_{\mathsf{el}}} \right) \cdot \frac{(E - E_{\mathsf{F}})^2 + (\pi\, \mathrm{k_B} T_{\mathsf{el}})^2}{\tau_0 \, E_{\mathsf{F}}^2} \, \mathrm{d}E$$
$$- \left[(1 - w(t)) \cdot \pi \, D(E_{\mathsf{F}}) \, \lambda \, \langle \omega \rangle \, \mathrm{k_B} + w(t) \cdot \frac{2 \, \ln(2) \, D(E_{\mathsf{F}})^2 \, \mathrm{k_B^2} \, \pi \, \hbar \, \lambda \, \langle \omega^2 \rangle}{\gamma \, T_{\mathsf{el}}} \right] \cdot (T_{\mathsf{el}} - T_{\mathsf{la}})$$

$$\frac{\partial U_{\mathsf{el}}}{\partial t} = \frac{\partial U_{\mathsf{abs}}}{\partial t} - \pi \, \hbar \, \lambda \langle \omega^2 \rangle \cdot N_{\mathsf{qp}} - g \cdot (T_{\mathsf{el}} - T_{\mathsf{la}}) \, . \tag{116}$$

In the first equation, equation (115), the number of photo-excited quasiparticles (first term), the quasiparticle multiplication rate (second term, see also Section 2.7 and Figure 63) and the electron-phonon related recombination at the Fermi level (third term, see Figure 64**B**) are considered. Further, equation (116), contains the energy of the absorbed pulse (first term), the spontaneous phonon emission (second term, see also Section 2.3 and Figure 64**A**) and an electron-phonon thermalization term (third term, mainly driving the process sketched in Figure 64**B**). T_{el} is the electronic temperature taken from the Fermi-Dirac fits (see Section 5.7).

The model, based on the equations (115) and (116), includes three processes which are responsible for the changes in the number of excited quasiparticles. Each absorbed photon generates two excited quasiparticles, one electron and one hole. The excited quasiparticles have an average energy of $\mathrm{h}\nu/2 \gg \mathrm{k_B}\, T$. This high energy quasiparticles have short lifetimes (see Fermi-Liquid theory, Section 2.5) and in every scattering event with a non-excited quasiparticle up to two quasiparticles are newly excited (one electron and one hole) as sketched in Figure 63**C**. The idea is, that every high energy quasiparticle which scatters at an electron below the Fermi level excites this electron and empties the previously occupied state (generation of a hole). These scattering events multiply the number of excited quasiparticles in a cascade process, because the generated secondary quasiparticles can further create electron-hole pairs. At low energies, the quasiparticles recombine (by phonon emission), which counteract the increase of the number of excited quasiparticles originating from the quasiparticle multiplication process.

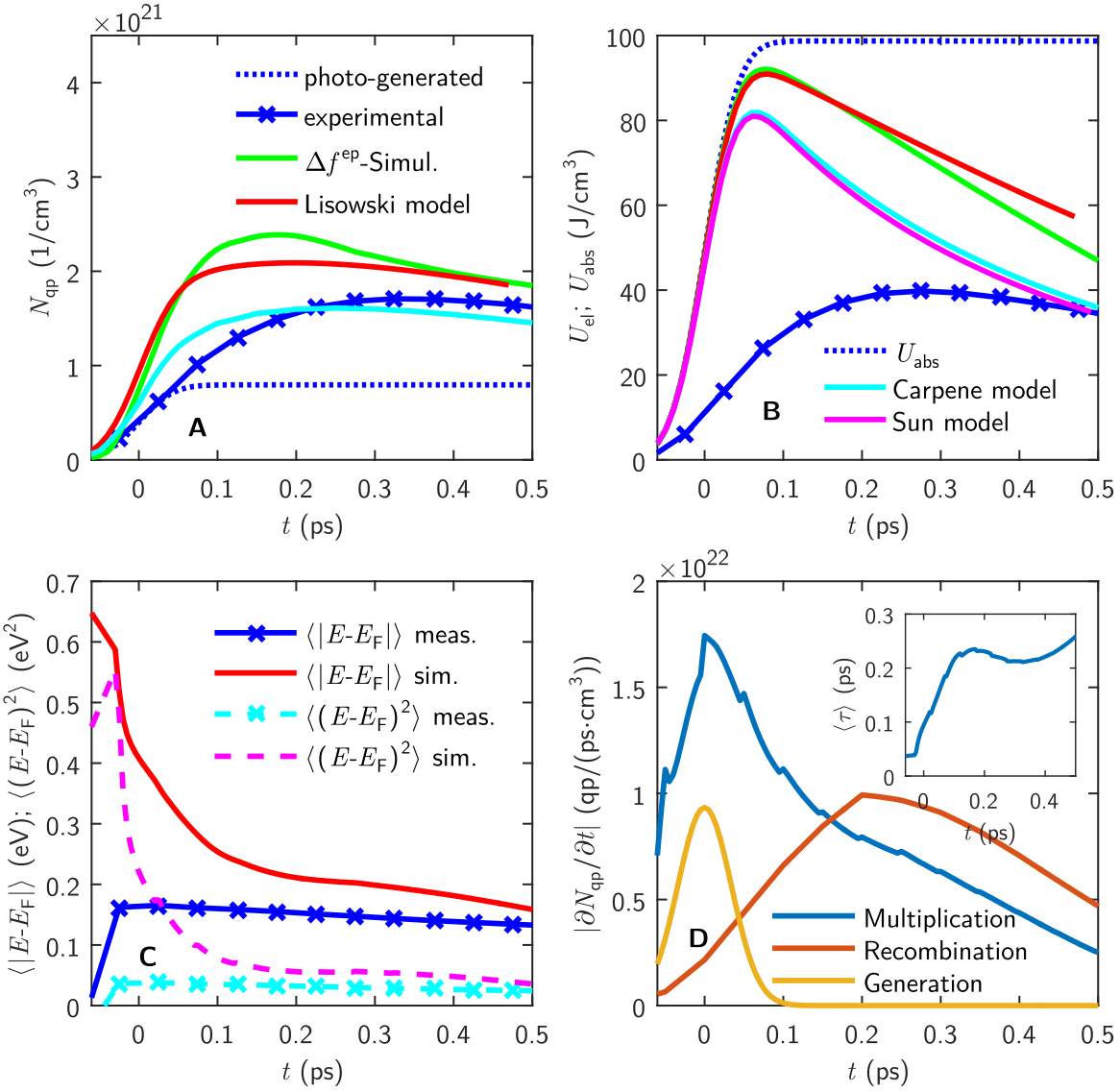

Figure 62: **Simulation of the initial quasiparticle number and energy dynamics.** The model description (equations (115) and (116)) and the extrapolation of the electronic distribution function (Figure 61) allow to simulate the initial energy- and quasiparticle time evolution. The result is shown in **A** and **B** and compared to the results of the different models which are previously described. Both graphs share the same legend. **C** Relaxation of the average energy and the energy variance determined from the extrapolated spectra. **D** Absolute rates for the excitation (generation), multiplication and recombination of the excited quasiparticles. After 150 fs a turnover occurs, at which more excited quasiparticles recombine than quasiparticles are newly generated within the quasiparticle multiplication process. The average quasiparticle lifetime is plotted in the inset on the figure. The curves are not smooth because of the experimental time resolution of about 60 fs.

The cascade electron multiplication processes are described by the second term in equation (115). This term describes the average quasiparticle multiplication rate and takes the probability for the

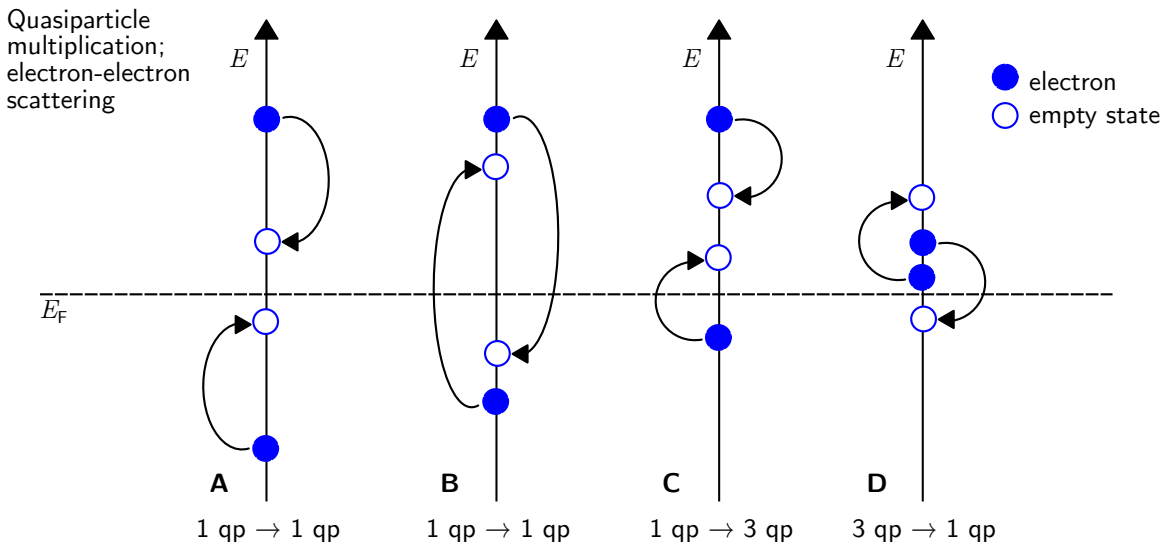

Figure 63: **Characterization of the electron-electron scattering events. A-D** are sketches to characterize the quasiparticle multiplication (or cascade) process which is described in Section 2.7. In **A** and **B** the number of excited quasiparticle remains unchanged. In **C**, a high energetic electron creates an additional electron-hole pair. After scattering, the energy of the scattered electron is partly transferred to a newly created electron-hole pair. **D** Statistically unlikely scattering events could be, that excited electrons gain energy via recombination of electron-hole pairs. Individually, such events could decrease the number of excited quasiparticles.

generation of electron-hole pairs γ_M and their lifetime (see Section 2.7 for the theoretical background) into account. The quasiparticle multiplication rate is plotted in Figure 62**D** (blue line) as a function of time. The quasiparticles at the Fermi level, which recombine in electron-phonon scattering events, are considered in the third term of the equation (115) (see also Figure 64**B**). This term is based on equations (128) and (130) (see Appendix 8.1.2). The factor w is used to dynamically switch between the TTM-expression, which is valid for thermally distributed electrons, and the expression for the recombination of electron-hole pairs in the case of a non-thermal electronic distribution function (it can be separated into thermal and non-thermal parts). In the latter case, the probability to refill the emptied states after each recombination event is enhanced because of the large density of high energy quasiparticles. Thus, the recombination rate of thermally distributed quasiparticles is lower compared to the case of non-thermally distributed quasiparticles. It is reasonable to use

$$w(t) = \begin{cases} 0 & t < 0.2\,\text{ps} \\ \frac{t-0.2\,\text{ps}}{0.45\,\text{ps}} & 0.2\,\text{ps} \leq t < 0.65\,\text{ps} \\ 1 & t \geq 0.65\,\text{ps} \end{cases},$$

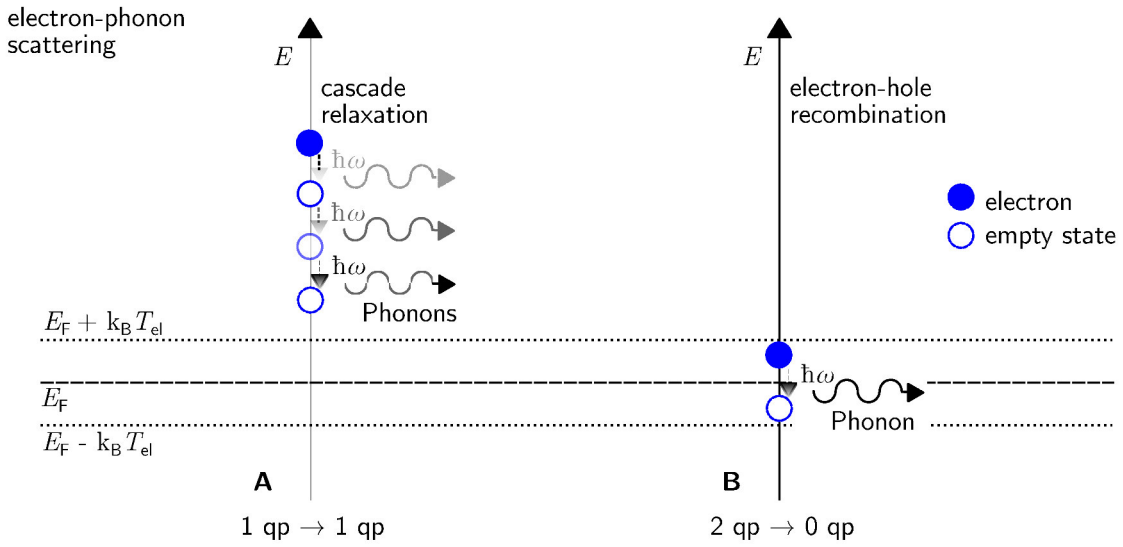

Figure 64: **Characterization of the electron-phonon scattering events.** The electron-phonon scattering events are splitted into two categories, the quasiparticle number conserving cascade scattering events, **A**, and the electron-phonon recombination events at the Fermi level, **B**. The latter events decrease the number of excited quasiparticles by 2 (per event).

where the description of the recombination processes changes from the expression for highly non-thermal electronic distribution functions to the expression for thermal distribution functions.

The numerical solution of the system of differential equations (equations (115) and (116)) together with the extrapolated Δf (see Figure 61) provide the complete information about the electron relaxation dynamics (assuming the approximations used). The results of the simulations are presented in Figure 62**A** and **B**. The result of this simulation (green lines) is close to the result of the model of Lisowski et al. (red lines in Figure 62**A** and **B**; taken from Section 6.1.3) which was applied to the same dataset. In comparison, the models of Carpene (light blue lines; taken from Section 6.1.2) and Sun et al. (magenta line; taken from Section 6.1.1) suggest a much faster lattice heating.

The recombination rate of the Δf^{ep}-Simulation is compared to the multiplication rate in Figure 62**D**. After about 150 fs the recombination rate exceeds the multiplication rate and the number of excited quasiparticles reaches a maximum. The inset of Figure 62**D** presents the underlying average quasiparticle lifetime.

Figure 62**C** presents the average energy and the energy variance as a function of time. Both functions converge to the experimental data (which is determined in a energetically limited window) on the timescale of several hundred femtoseconds. These functions begin at values which are close to the

maxima of $\left\langle (E - E_\mathsf{F})^2 \right\rangle_{\text{initial}} = (\mathrm{h}\nu)^2/3$ and $\langle E - E_\mathsf{F} \rangle_{\text{initial}} = \mathrm{h}\nu/2$.

The result of the Δf^{ep}-Simulation, which is based on the coupled differential equations (115) and (116), show a fast energy transfer from the electronic subsystem to the lattice. In fact, it is fast enough to explain the electronic temperatures which are found after about 700 fs (see Section 5.8), which are far below the temperatures estimated for the case of negligible electron-phonon energy transfer during the electron thermalization process. Thus, the simulation has the power to show, that the whole relaxation process can be described consistently with Boltzmann equations based on lowest order scattering terms (e.g. electron-hole recombination, electron-electron scattering). If the contribution of higher order scattering terms (e.g. electron-electron scattering with an additional created phonon) are not negligible, these processes could further accelerate the energy transfer between the electrons and the lattice. However, this section shows, that the experimental data presented in this work gives no evidence to consider higher order scattering terms in the Boltzmann equations to account for the relaxation of a non-thermal electronic distribution function in a metal.

6.3 Extensions of the model by Lisowski et al.

The model of Lisowski et al. [Lis+04; Lis05] assumes non-thermal quasiparticles to rearrange to a Fermi-Dirac distribution function on a very short timescale.[35] The idea of this section is to describe the short time delay dynamics (up to 150 fs) with the previously described model for the short time delay dynamics (Section 6.2) and the second stage ($t > 150$ fs) by the model of Lisowski et al. Here, Δf is the sum of a broad high temperature Fermi-Dirac distribution function with a decreasing amplitude ($r(t)$) and a Fermi-Dirac distribution function at much lower temperatures (narrow distribution) with increasing amplitude ($1 - r(t)$) (the quantity r represents the weight of the thermal electrons). The simulated Δf is fitted to the experimental data on $\Delta f(t)$ with (slightly) modified differential equations as compared to Lisowski et al. (see equations (34)-(36) and (38) for

[35] In the beginning of the relaxation process the non-thermal electrons are steplike distributed (see Figure 4) and it is expected that the electrons rearrange into a Fermi-Dirac distribution function as described in Section 3.4.2.

comparison). The system of differential equations then reads:

$$\begin{aligned}
\frac{\partial T_{\mathsf{nt}}}{\partial t} &= \frac{1}{r\,\gamma\,T_{\mathsf{nt}}}\left[-r\cdot g\cdot(T_{\mathsf{nt}}-T_{\mathsf{la}})-\left.\frac{\partial U}{\partial t}\right|_{\mathsf{nt\text{-}el}}\right] \\
\frac{\partial T_{\mathsf{el}}}{\partial t} &= \frac{1}{(1-r)\,\gamma\,T_{\mathsf{el}}}\left[-(1-r)\cdot g\cdot(T_{\mathsf{el}}-T_{\mathsf{la}})+\left.\frac{\partial U}{\partial t}\right|_{\mathsf{nt\text{-}el}}\right] \\
c_{\mathsf{la}}\frac{\partial T_{\mathsf{la}}}{\partial t} &= (1-r)\cdot g\cdot(T_{\mathsf{el}}-T_{\mathsf{la}})+r\cdot g\cdot(T_{\mathsf{nt}}-T_{\mathsf{la}})+\frac{1}{2}\frac{\partial r}{\partial t}\gamma\left(T_{\mathsf{el}}^2-T_{\mathsf{nt}}^2\right) \qquad (117) \\
\frac{\partial r}{\partial t} &= -r/\tau_{\mathsf{r}} \\
\left.\frac{\partial U}{\partial t}\right|_{\mathsf{nt\text{-}el}} &= \frac{\langle|E-E_{\mathsf{F}}|\rangle_{\mathsf{nt}}-\langle|E-E_{\mathsf{F}}|\rangle_{\mathsf{el}}}{2\,x}\cdot\frac{N_{\mathsf{sc,el}}+N_{\mathsf{sc,nt}}}{2}\,.
\end{aligned}$$

The decreasing amplitude r reduces the energy in the non-thermal electronic subsystem and increases the energy in the thermal subsystem. The difference between both energies is added to the lattice subsystem (the last term of equation (117) accounts for that). The reason for this assumption is the energy conservation law, and the fact that the number of excited quasiparticles is conserved, if electron-electron scattering events are considered only. Δf^{el}, N_{el} and the related T_{el} linearly increase with r and Δf^{nt}, T_{nt} linearly decreases with r, but the corresponding energies, U_{el} and U_{nt}, quadratically dependent on T_{el} and T_{nt}. Thus, the energy conservation law requires the number of excited quasiparticles $(N_{\mathsf{nt}}+N_{\mathsf{el}})$ to decrease, if r is decreasing over time. The recombination of the excited quasiparticles is realized by the electron-phonon coupling. The r-related lattice heating is given by the last term in equation (117). The decreasing number of excited quasiparticles $(N_{\mathsf{nt}}+N_{\mathsf{el}})$ with decreasing r also defines the time, at which the extension of the model of Lisowski et al. can be applied to the experimental data. The idea is to model the electron multiplication process with the model introduced in Section 6.2 until the number of excited quasiparticles reaches its maximum. After this (for $t > 150\,\mathrm{fs}$), the non-thermal quasiparticles are assumed to be described by the Fermi-Dirac distribution function and their dynamics are described by the extension of the model of Lisowski et al. Here, the fit parameters are x (defined in Section 6.1.3, equation (111)) and τ_{r} (corresponds to the electron thermalization time).

The initial values of r and T_{nt} (at $t \approx 150\,\mathrm{fs}$) are estimated via

$$\begin{aligned}
T_{\mathsf{nt}} &= \sqrt{\frac{2\,U_{\mathsf{nt}}}{r\,\gamma}+T_0^2}\,, \\
r_{\mathsf{max}} &= \frac{N_{\mathsf{qp}}^2\,\pi^2}{2\,\ln(2)\,D(E_{\mathsf{F}})\cdot(12\cdot U_{\mathsf{nt}}\cdot\ln(2)-\pi^2\,k_{\mathsf{B}}\,T_0\cdot N_{\mathsf{qp}})}\,.
\end{aligned}$$

A good agreement with the experimental Δf (see Figure 65) is found with

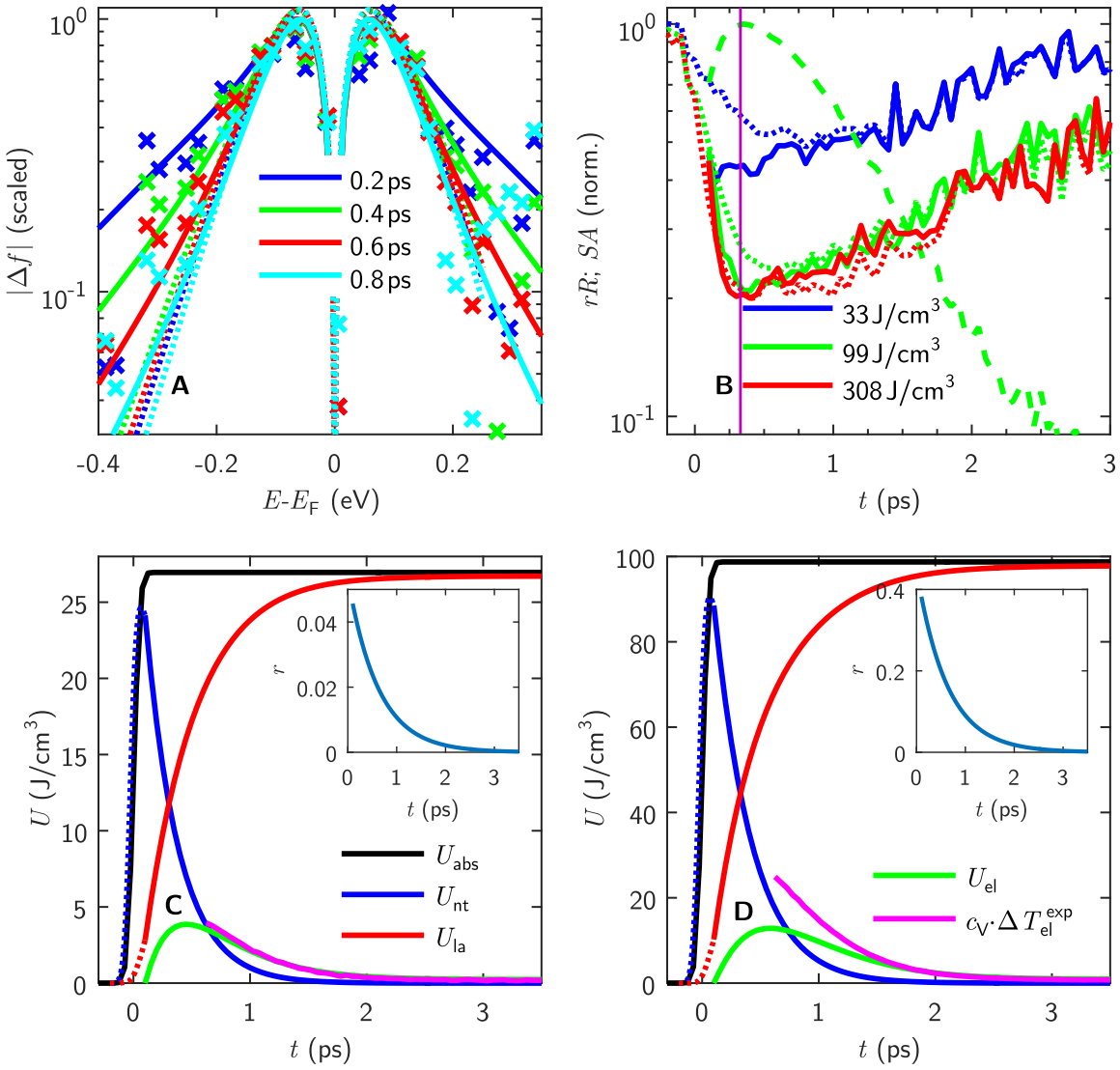

Figure 65: **Extension to the model of Lisowski et al. applied to dynamics for $t > 150$ fs.** The initial dynamics ($t < 150$ fs) are described by the model introduced in Section 6.2. **A** Shape of Δf at different time delays. The dots are the experimental result, the solid lines are the result of this subsection and the dotted lines are the result of the Fermi-Dirac fits in Section 5.7. **B** Deviation between the experimental Δf and the model results. The dashed-dotted line shows the normalized response SA. **C** Energy relaxation dynamics at the low excitation densities. The dotted lines correspond to the reconstructed initial dynamics and the solid line to the extension of the model of Lisowski et al. **D** Energy densities of the different subsystems at high excitation densities. The inset show the relaxation of the parameter r. **C** and **D** belong to the same legends.

$$x = 4.5\,, \tag{118}$$

$$\tau_r = 600\,\text{fs} \tag{119}$$

and the electron-phonon coupling strength $\lambda \langle \omega^2 \rangle = 45\,\mathrm{meV}^2$ (this value is taken from Section 5.8). The non-thermal part of Δf at short time delays is well reproduced by this model (Figure 65**A** and **B**). At lower excitation densities and after more than 600 fs (Figure 65**C**) the modeled energy relaxation dynamics is comparable to the result of the Fermi-Dirac fits, after the electrons are thermalized (for $t > 700$ fs; compare the green line to the magenta line in Figure 65**C**). At higher excitation densities the extracted thermalization time is longer compared to the result of the Fermi-Dirac fits, while the maximum temperatures of the thermal electronic subsystem are much lower compared to the result of the Fermi-Dirac fits (compare the green line to the magenta line in Figure 65**D**). Also, at high excitation densities the deviation between the experimental data and the model Δf is the same for both, the description with the result of the Fermi-Dirac fits and with the extended model by Lisowski et al. (see Figure 65**B**).

This section presents an extension of the model by Lisowski et al. which seems to describe the experimental Δf in a metal before the electrons are thermalized.

In metals with longer electron thermalization times or metals with strong electron-phonon coupling (e.g. superconductors studied in the high temperature (normal) phase) the method of Section 5.8 may not be applicable. To determine the electron-phonon coupling constant $\lambda \langle \omega^2 \rangle$ from the experimental Δf in such a case, one needs to understand and model the electron thermalization process.

6.4 Model of Baranov & Kabanov

The model of Kabanov et al. [BK14; KA08] is based on the linearized Boltzmann equation and it is developed to describe the electronic relaxation process after photo-excitation in the low excitation limit. It relates the linearized Boltzmann equation to a differential equation of the Fokker-Planck type (see Section 3.5). The model allows to determine the time evolution of Δf which can be compared to the experimental $\Delta f(t)$ directly. While the exact solution, which is specific to the investigated metal, can be obtained by solving the Fokker-Planck equation numerically [BK14], the required computations are beyond the scope of this thesis. However, the approximate analytic solution derived in [BK14], can be compared to the experimental data. This approximate solution linearly relates ΔU_{el} to the quantity

$$x(t) = \int_{-\infty}^{t} \int_{-\infty}^{\infty} \tanh\left(|E - E_{\mathrm{F}}| \,/\, (2\,\mathrm{k_B}\,T_0)\right) \Delta f(E, t')\,\mathrm{d}E\,\mathrm{d}t' = \int_{-\infty}^{t} I(t')\,\mathrm{d}t' \qquad (120)$$

(the quantity I represents the number of excited quasiparticles N_{qp} in the limit where the recombination of electron-hole pairs is negligible, see [BK14]). It turns out, that taking both kind of electron-phonon scattering events, the cascade scattering and the recombination at the Fermi level (see Figure 64), need to be considered to improve the agreement between the experimental data and the output of the model.

The experimental U_{el} as a function of x is presented in Figure 66 at low and high excitation density. Here, the time is monotonically increasing with x and the separation between each consecutive data

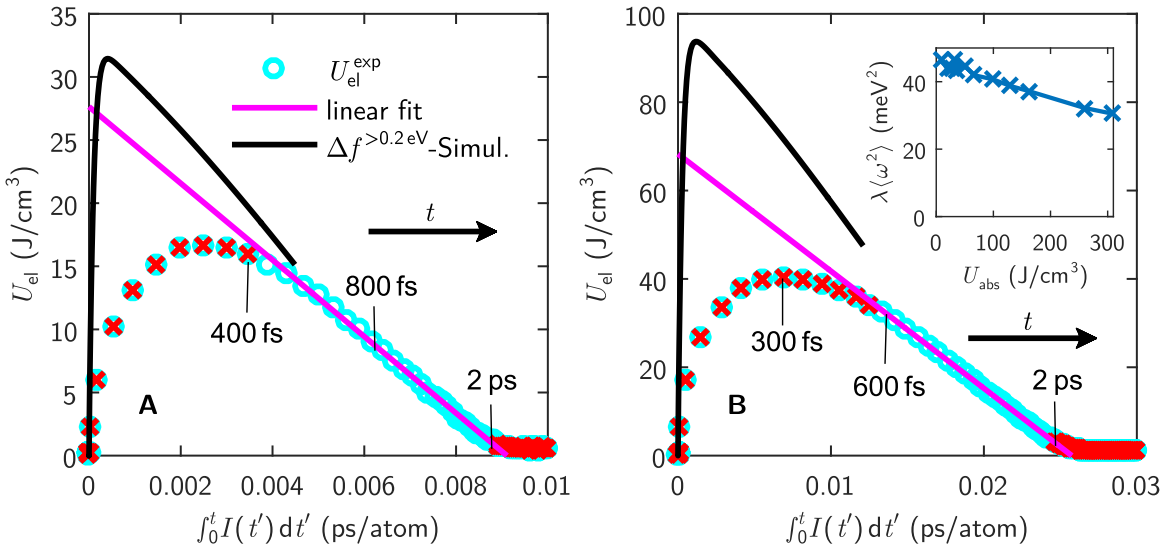

Figure 66: **Model of Baranov, Kabanov & Alexandrov [BK14; KA08] applied to the experimental U_{el}.** U_{el} is plotted as a function of the integrated function I (equation (120)) with cyan dots at different excitation densities in **A** & **B**. According to equation (40) a linear dependence is expected (magenta lines are the results of the linear fit). Because of different reasons, the red crossed dots in the beginning and in the end are not taken into account. The gradient of the curve is proportional to the electron-phonon coupling parameter $\lambda\langle\omega^2\rangle$. The excitation density dependence of the resulting electron-phonon coupling is plotted in the inset on the figure **B**. At low excitation densities the theoretical prediction of $\lambda\langle\omega^2\rangle$ [BAP82] is reproduced. The initial dynamics are described by the model of Section 6.2 (black lines).

point is 50 fs. The points in the beginning are excluded because the experimental data underestimates U_{el} (due to the same reason the x-values are slightly too low as well; the reason for that is that not all of the quasiparticles are counted because the experimental energy window is limited to $|E - E_{\mathrm{F}}| \leq 0.38\,\mathrm{eV}$). The reason for excluding the experimental points at larger time delays is that at those points the relaxation process has already finished.

The linear dependence between U_{el} and $\int_{-\infty}^{t} I(t')\,\mathrm{d}t'$ (see equation (40)) is likely to be valid at

high temperatures and low excitation densities. The slope is related to the electron-phonon coupling constant $\lambda\langle\omega^2\rangle$. The inset on the Figure 66**B** shows the excitation density dependence of this parameter. At low excitation densities the theoretical prediction of $\lambda\langle\omega^2\rangle = 46\,\mathrm{meV}^2$ is reproduced but at high excitation density $\lambda\langle\omega^2\rangle$ is reduced to about $30\,\mathrm{meV}^2$. As discussed above, $\lambda\langle\omega^2\rangle$ is expected to be independent of the excitation density. The result indicate that the model cannot be used to determine $\lambda\langle\omega^2\rangle$ from experimental data at high excitation densities. Another indication that the model does not properly describe the experimental data is seen at $t = 0\,\mathrm{ps}$, where there is a large deviation between the extrapolated $\bar{U}_{\mathrm{abs}}$ and the amount of energy deposited in the electronic subsystem. The excitation density used in Figure 66**A** is $33\,\mathrm{J/cm^3}$ which is about 20 % more than expected from the linear extrapolation (magenta line) to 0 ps (0 ps corresponds to the point 0 on the x-axis).

An alternative description of the initial relaxation dynamics and the non-thermal electronic redistribution is presented in Section 6.2 (black lines in Figure 66). After about 500 fs (see Figure 66**A**) and more than 700 fs (estimated from the slope, see Figure 66**B**) the two curves (black and magenta) overlap. The intersection time is a bit lower in reality because of the experimentally underestimated I-values.

The analysis here shows, that the differential equation of the Fokker-Planck type which was introduced by Kabanov et al. [BK14; KA08] is likely able to describe the electron dynamics in metals at very low excitation densities. Gadermaier et al. [Gad+10] found good agreement of the model with the data on cuprate superconductors, studied in the high temperature (normal) phase. However, here the slope of the electron energy loss is studied in more detail and an upper limit of applicability (excitation density of about $30\,\mathrm{J/cm^3}$) is found. Below this density the model of Kabanov and Baranov shows good agreement with the experimental data, while above the model underestimate the electron-phonon coupling strength.

7 Summary and conclusions

The electron dynamics in the prototype metal Cu were investigated in this thesis. A near-infrared pump and white light probe setup was developed to focus on the electron interband transitions at about 2.1 eV. It could be shown that these transitions are sensitive to the changes in the electronic distribution near the Fermi level. Based on the linear response framework, a model was developed to describe the interband transitions (including the dynamics of intraband and high energy interband transitions). Here, the white light records changes in the interband transition probabilities between the upmost d-band and states near E_F, whose distribution is time dependent. We applied the developed model to our equilibrium data, the published dielectric function and thermomodulation data. This allows to model the temperature dependence of the optical properties and the thermomodulation data of [RL72]. Further, we can address the data at short time delays, where the electronic distribution function is not thermal, to quantitatively determine the dynamics of the electronic distribution function, $\Delta f(t)$. $\Delta f(t)$ is studied after excitation with different excitation densities, spanning more than one order of magnitude.

The electrons are found to thermalize on a timescale of 400-800 fs, dependending on the excitation density. This contradicts the instantaneous electron thermalization assumption which is a basis of the TTM [All87; Bro+90]. This observation is in agreement with other findings [Fan+92; Lis+04; Gad+10]. However, the TTM can be used to describe Δf at time delays after the electrons are in thermal equilibrium (using the experimentally measured electronic temperatures). The electronic temperatures are found to be substantially lower than the electronic temperatures which are expected as a result of the instantaneous electron thermalization. In fact, nearly half of the absorbed energy is found to be transferred to the lattice subsystem before the electrons are thermalized. Importantly, the analysis reproduced the theoretically predicted value for the electron-phonon coupling constant in Cu [BAP82]:

$$\lambda \left\langle \omega^2 \right\rangle = 45\,\mathrm{meV}^2$$

for a broad range of excitation densities. This coupling strength differs substantially from the reported values [EA+87; Bro+90], which were based on single color pump-probe measurements and the instantaneous electron thermalization assumption of the TTM.

The stage of relaxation at short time delays is found to proceed through the combined electron-electron and electron-phonon relaxation. This stage ends with the thermalization of the electronic

subsystem on a 500 fs timescale. We found that none of the extensions of the TTM [Sun+94; Car06; Lis+04] properly describes the experimental $\Delta f(t)$ during this stage. The energy is quickly transferred to the lattice subsystem, which can be explained by the high electron-phonon scattering probability for high energy electrons (where the number of excited electrons is small compared to the accessible empty states). Simulations are performed to extrapolate the experimental $\Delta f(t)$ to regions outside the experimental window to reproduce the number of excited electrons and their average energy. These simulations, combined with the model of Lisowski et al. [Lis+04; Lis05], are consistent with the experimental Δf and these results confirm the electron thermalization times which are found by the Fermi-Dirac fits to the experimental Δf. Further, at low excitation densities another model seems to be applicable, the model of the linearized Boltzmann equations [BK14]. This model allows to determine the electron-phonon coupling constant at low excitation densities. The result is consistent with the other results of this work.

The presented results are based on a very elaborate method to measure and analyze the time-resolved dynamics in metals. Therefore, a way to circumvent the time consuming analysis associated with the determination of $\Delta f(E,t)$ is developed. This simple analysis is directly based on the time- and wavelength-resolved relative change in transmission, $\Delta T/T(\nu,t)$. At first the method of SVD is applied to $\Delta T/T(\nu,t)$ to reduce the influence of the intraband Drude transitions. The filtered data at the upmost d-band to Fermi level transition resonance is shown to be proportional to the electronic temperature at low excitation densities and after the electrons are thermalized. The TTM was applied to the filtered data, giving correct values for the electron-phonon coupling constant and the increasing deviation between the TTM and the experimental data allows to determine the electron thermalization time.

The present study enhances our understanding of the electron thermalization and lattice heating processes. An independent test of available models is presented and additionally a way to address electron-boson coupling strengths in advanced correlated solids like high-T_c superconductors, where the knowledge of coupling strengths is still a matter of discussion.

8 Appendix

8.1 Electron-Phonon scattering and thermalization

The energy density of the electronic subsystem is given by

$$U_{\mathsf{el}} = \sum_{\boldsymbol{k}} D(E_{\boldsymbol{k}})\, E_{\boldsymbol{k}}\, f_{\boldsymbol{k}} = \int_{-\infty}^{\infty} D(E)\, E\, f(E)\, \mathrm{d}E\,.$$

After excitation the electrons are out of equilibrium and because of the electron-phonon interaction, this electron energy density decays over time. The equation (3) (or equivalent the equation (2)) presents the electron-phonon scattering which is a term in Boltzmann equations. The related changes to the electron energy density and the number of excited quasiparticles are

$$\begin{aligned}
\dot{U}_{\mathsf{el}}\big|_{\mathsf{el\text{-}ph}} &= 2\pi \int_{-\infty}^{\infty}\int_{-\infty}^{\infty}\int_{-\infty}^{\infty} \big[\delta(E-E'+\hbar\omega)\cdot\left(\left(f(E')-f(E)\right)N(\omega)+f(E')\left(1-f(E)\right)\right) \\
&\quad +\delta(E-E'-\hbar\omega)\cdot\left(\left(f(E')-f(E)\right)N(\omega)-f(E)\left(1-f(E')\right)\right)\big] \\
&\quad \cdot\alpha^2F(\omega)\, E\, D(E)\, \mathrm{d}E'\, \mathrm{d}\omega\, \mathrm{d}E\,, \qquad (121) \\
\dot{N}_{\mathsf{qp}}\big|_{\mathsf{el\text{-}ph}} &= 4\pi \int_{-\infty}^{E_{\mathsf{F}}}\int_{-\infty}^{\infty}\int_{-\infty}^{E_{\mathsf{F}}} \big[\delta(E-E'+\hbar\omega)\cdot\left(\left(f(E')-f(E)\right)N(\omega)+f(E')\left(1-f(E)\right)\right) \\
&\quad +\delta(E-E'-\hbar\omega)\cdot\left(\left(f(E')-f(E)\right)N(\omega)-f(E)\left(1-f(E')\right)\right)\big] \\
&\quad \cdot\alpha^2F(\omega)\, D(E)\, \mathrm{d}E'\, \mathrm{d}\omega\, \mathrm{d}E\,. \qquad (122)
\end{aligned}$$

For the same reasons the phonon density increases over time [All87]

$$\begin{aligned}
\dot{N}(\omega) &= 2\pi \int_{-\infty}^{\infty}\int_{-\infty}^{\infty} \alpha^2F(\omega)\cdot\big[\delta(E-E'+\hbar\omega)\cdot(N(\omega)+1)f(E')\left(1-f(E)\right) \\
&\quad -\delta(E-E'-\hbar\omega)\cdot N(\omega)\, f(E')\left(1-f(E)\right)\big]\, D(E')/F(\omega)\, \mathrm{d}E'\, \mathrm{d}E\,,
\end{aligned}$$

where N is the distribution function of phonons. The corresponding time derivative of the energy density is

$$\begin{aligned}
\dot{U}_{\mathsf{el}}\big|_{\mathsf{el\text{-}ph}} &= -\dot{U}_{\mathsf{la}}\big|_{\mathsf{el\text{-}ph}} = -2\pi \int_{-\infty}^{\infty}\int_{-\infty}^{\infty}\int_{-\infty}^{\infty} \alpha^2F(\omega)\left[\delta(E-E'+\hbar\omega)\left(N(\omega)+1\right)f(E')\left(1-f(E)\right)\right. \\
&\quad \left.-\delta(E-E'-\hbar\omega)\cdot N(\omega)\, f(E')\left(1-f(E)\right)\right] D(E')\, \mathrm{d}E'\, \mathrm{d}E\, \mathrm{d}\omega\,. \qquad (123)
\end{aligned}$$

8.1.1 The empty final states approximation

The empty final states approximation is applicable in the case of non-thermal electronic distribution where the number of excited quasiparticles is small compared to the accessible empty states, and the

average energy of the non-thermal quasiparticles is quite large (if $\langle |E - E_\mathsf{F}| \rangle_\mathsf{nt} \gg \mathrm{k_B}\, T$). This state is a result of photo-excitation with light in the visible spectral range at low excitation densities. The photons may generate high energy quasiparticles in metals with comparatively low density ($f((E - E_\mathsf{F}) \gg \mathrm{k_B}\, T) \ll 1$). The low density non-thermal part of f is considered in the empty final state approximation. The energy range of accessible final states after scattering at phonons is limited by the energy conservation law to the range $\pm\hbar\omega_\mathsf{D}$ around the initial state. The empty final states approximation assumes the accessible final states to be empty. The non-thermal quasiparticle distribution function is given by

$$\Delta f_\mathsf{nt}(E,t) = f(E,t) - f_\mathsf{thermal}(E,T)\,.$$

Δf_nt is assumed to be small at all energies $|\Delta f_\mathsf{nt}(E,t)| \ll 1$ and time delays, where the empty final states approximation holds. The number of non-thermal quasiparticles is

$$N_\mathsf{nt}(t) = \int_{-\infty}^{\infty} |\Delta f_\mathsf{nt}(E,t)|\; D(E)\,\mathrm{d}E\,.$$

A rate for the energy transfer to the lattice for non-thermal quasiparticles is given by (see equation (123))

$$\begin{aligned}
\dot{U}_\mathsf{nt}\big|_\mathsf{el\text{-}ph} \;\approx\; & -2\,\pi \int_{-\infty}^{\infty}\int_{-\infty}^{\infty}\int_{-\infty}^{\infty} \alpha^2 F(\omega)\,\hbar\omega\,\big[\delta(|E-E'|+\hbar\omega)\cdot(N(\omega)+1)\,\Delta f_\mathsf{nt}(E',t) && (124)\\
& -\delta(|E-E'|-\hbar\omega)\cdot N(\omega)\,\Delta f_\mathsf{nt}(E',t)\big]\,D(E')\,\mathrm{d}E'\,\mathrm{d}E\,\mathrm{d}\omega && (125)\\
=\; & -2\,\pi \int_{-\infty}^{\infty} \alpha^2 F(\omega)\,\hbar\omega\,\mathrm{d}\omega\cdot N_\mathsf{nt}(t) = -\pi\,\hbar\,\lambda\left\langle\omega^2\right\rangle\cdot N_\mathsf{nt}(t)\,. && (126)
\end{aligned}$$

Compared to the result of Tas & Maris [TM94], this result is by a factor of $2\cdot\ln(2)$ larger and corresponds to the spontaneous phonon emission rate derived by Gusev & Wright [GW98] and Baranov & Kabanov [BK14] (see Section 2.3).

8.1.2 The thermal-electron-phonon relaxation process

Section 8.1.1 deals with the non-thermal part of Δf. If the electronic and the phonon distribution functions are thermal, the equations (121) and (122) have analytic solutions [KLT57; All87], which are used in the TTM. If the electronic temperature T_el differs from the lattice temperature T_la, then the energy and number of excited quasiparticles in the electronic subsystem changes over time

according to

$$\dot{U}_{\mathsf{th}}\big|_{\mathsf{el\text{-}ph}} = \pi\, D(E_{\mathsf{F}})\, \hbar\, \lambda \left\langle \omega^2 \right\rangle\, \mathrm{k_B}\, (T_{\mathsf{la}} - T_{\mathsf{el}}) \text{ and} \tag{127}$$

$$\dot{N}_{\mathsf{th}}\big|_{\mathsf{el\text{-}ph}} = \pi\, D(E_{\mathsf{F}})\, \lambda \left\langle \omega \right\rangle\, \mathrm{k_B}\, (T_{\mathsf{la}} - T_{\mathsf{el}})\,. \tag{128}$$

These equations are derived for conduction bands whose bandwidth is large compared to $\mathrm{k_B}\, T$ and for temperatures above the Debye temperature, without any high energy optical phonon branches (i.e. $\hbar\omega \ll \mathrm{k_B}\, T_{\mathsf{el}}$ and $\hbar\omega \ll \mathrm{k_B}\, T_{\mathsf{la}}$ for the majority of the phonon states). If optical phonons are involved in the relaxation process, or if the temperature is very low, higher orders in the Taylor expansion (equation (14) in [All87]) with different powers of $\lambda \left\langle \omega^x \right\rangle$ (equation (14) in [All87]) have to be considered.

A thermal electronic distribution has the temperature dependent number of excited quasiparticles

$$N_{\mathsf{th}}(T_{\mathsf{el}}) = 2\, \ln(2)\, D(E_{\mathsf{F}})\, \mathrm{k_B}\, T_{\mathsf{el}}\,. \tag{129}$$

This equation relates the number of the excited quasiparticles to the excess energy. It is obvious that the equations (127), (128) and (129) are inconsistent and either equation (127), equation (128) or none of them are valid. If equation (127) is valid, there needs to be a mechanism (beside the electron-phonon interaction) to keep the electrons in thermal equilibrium. This mechanism has to conserve the energy of the electronic subsystem (e.g. the electron-electron interaction) and modify the equation (128) by adding an additional term (this will be referred to as the thermal-electron-phonon relaxation process).

Apart from the electron-phonon coupling, the quasiparticles undergo collisions and they redistribute due to electron-electron interaction. If the redistribution is fast enough, the electronic distribution stays in thermal equilibrium after each electron-phonon scattering event and the equation (128) is modified to

$$\dot{N}_{\mathsf{th}}\big|_{\mathsf{el\text{-}ph}} = 2\, \ln(2)\, D(E_{\mathsf{F}})\, \mathrm{k_B}\, \dot{T}_{\mathsf{el}} = \frac{2\, \ln(2)\, D(E_{\mathsf{F}})^2\, \mathrm{k_B^2}\, \pi\, \hbar\, \lambda \left\langle \omega^2 \right\rangle}{\gamma\, T_{\mathsf{el}}}\, (T_{\mathsf{la}} - T_{\mathsf{el}})\,, \tag{130}$$

with the use of the equation (127). The quasiparticle multiplication rate (from the electron-electron scattering events) which is required to support the thermal-electron-phonon relaxation process is given by

$$\dot{M} = \frac{\dot{N}_{\mathsf{qp}}^{\mathsf{th}} - \dot{N}_{\mathsf{qp}}^{\mathsf{e\text{-}p}}}{N_{\mathsf{qp}}^{\mathsf{th}}} = \left(\frac{3\, \hbar\, \lambda \left\langle \omega^2 \right\rangle}{\pi\, \mathrm{k_B}\, T_{\mathsf{el}}} - \frac{\pi\, \lambda \left\langle \omega \right\rangle}{2\, \ln(2)} \right) \frac{T_{\mathsf{la}} - T_{\mathsf{el}}}{T_{\mathsf{el}}}\,.$$

The higher the electronic temperature, the lower is the multiplication rate which is needed to keep the electronic subsystem in thermal equilibrium. A negative $\dot{M}$ points out the necessity that electron-hole pairs recombine with the transfer of the related energy to an excited electron or hole. Usually such events are statistically unlikely (see Figure 63**D** in Section 6.2). A positive $\dot{M}$ refers to the generation of electron-hole pairs. In Cu the parameters are $\lambda \langle \omega^2 \rangle = 46\,\text{meV}^2$ and $\lambda \langle \omega \rangle = 2.16\,\text{meV}$ [BAP82]. The multiplication rate at $T_{\text{el}} = 1000\,\text{K}$ and $T_{\text{la}} = 300\,\text{K}$ is

$$\dot{M} = \frac{1}{200\,\text{fs}}\,. \tag{131}$$

The electron-phonon relaxation annihilates too many electron-hole pairs and new pairs need to be generated in electron-electron scattering events. If the electron-electron scattering rate is too low, Δf would remain too broad with respect to the expected thermal Fermi-Dirac distribution function. The maximum average time to newly excite a quasiparticle and to keep the electronic subsystem in thermal equilibrium during the energy exchange with the lattice is

$$\tau_{\text{M}} = 1/\dot{M} = 200\,\text{fs}\,. \tag{132}$$

This time is short compared to electronic lifetimes at the Fermi level, which are in the range of 300-700 fs (see Section 2.5) and τ_{M} gets even shorter at higher electronic temperatures. Simultaneously, the average quasiparticle lifetime decreases with increasing temperatures. Figure 67 compares the average quasiparticle lifetime based on the Fermi liquid theory (blue line) to the maximum time for the generation of new excited quasiparticles which are required to support the thermal-electron-phonon relaxation process (red dashed line).

This section points out the necessary conditions for the use of two different approximations to describe time-resolved experimental data. The first approximation is the empty final state approximation (see Section 8.1.2) which can be used at short time delays, where the density of non-thermally excited quasiparticles is low. The second approximation is used in the limit, where the electrons are in thermal equilibrium (see Section 8.1.2). Here, the role of the electron-electron interaction during the electron-phonon thermalization process is discussed.

8.2 The linear response framework

The result of this section (in particular the result of the Subsection 8.2.6) has been the starting point for the theory to describe the optical properties of Cu (see Chapter 4).

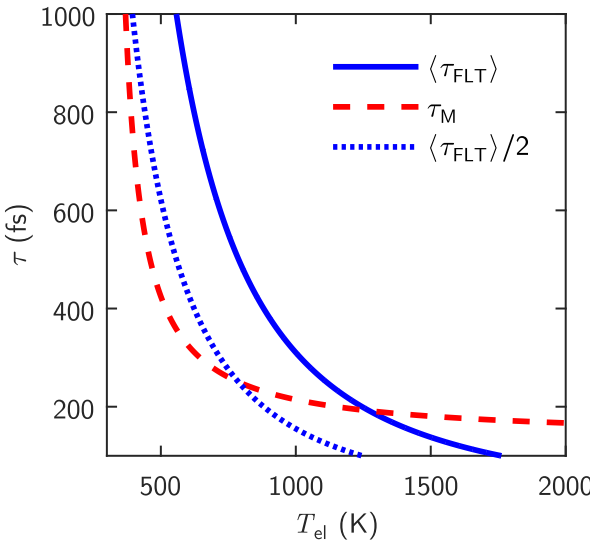

Figure 67: **The maximum time for the generation of new excited quasiparticle to support the thermal-electron-phonon relaxation process in Cu.** The average electronic lifetime (blue solid line) seems to be too large to support the thermal-electron-phonon relaxation process up to about 1300 K. The maximum time for the generation of excited quasiparticles is presented with the red dashed line (see equation (132) at a lattice temperature of $T_{la} = 300\,\mathrm{K}$). However, the Fermi liquid lifetime is close to the requirement and in consideration of the fact that the Fermi liquid theory is developed for high energy quasiparticles with $(E - E_F) \gg k_B T$, it is reasonable to expect the electrons to remain in thermal equilibrium during the exchange of energy between electrons and phonons. To emphasize this, the factor $1/2$ is multiplied to $\langle\tau_{FLT}\rangle$. The factor $1/2$ arises because the lifetime of thermal quasiparticles is the sum of Fermi liquid lifetime of the scatterer and of the scattering partner. This implies that $1/2 \cdot \langle\tau_{FLT}\rangle$ is the lifetime of every excited quasiparticle in thermal equilibrium independent of its energy. Considering the lifetime of thermal quasiparticles, the thermal-electron-phonon relaxation process is supported at electronic temperatures above 700 K.

This section begins with the linear response framework. Although this topic is a part of standard text books (e.g. [DG02]), it is emphasized in this section that the line width of features in the dielectric function is related to the lifetime or dephasing time of the electrons in a solid. Further, the theory is developed to consider both, the photo-induced electric current and the dipole-moment density.

The general theory of the linear response is described in the second quantization in Subsection 8.2.1. The external fields can have an influence on observables (e.g. the current in a metal). The general equation to determine the expectation value of observables is derived in Subsection 8.2.2. The subsequent Subsection 8.2.3 specifies the expectation value to external electric fields. Further, the general wave equation in solids is derived in Subsection 8.2.4 and the dielectric function is defined in Subsection 8.2.5. The application of the theory to crystalline solids is described in Subsection 8.2.6.

In the Subsection 8.2.7 different line shapes are discussed. The Lorentzian line shape is preferentially used in the further analysis because most of the integrations which had to be performed and contained the Lorentzian line shape can be solved analytically.

8.2.1 The time dependent perturbation

The time evolution of non-relativistic systems are described by the Schrödinger equation

$$\mathrm{i}\,\hbar\,\frac{\partial}{\partial t}\left|\tilde{\Psi}(t)\right\rangle = H(t)\left|\tilde{\Psi}(t)\right\rangle\,.$$

$\tilde{\Psi}$ is the wave function of the entire system which describes both, the excited material and the external fields. H is the system Hamiltonian, which also contains the time dependent external fields. In the following, the system is split into three subsystems. These subsystems are: the external fields (e.g. an electromagnetic wave), the excited system (e.g. the electrons in a solid) and the coupled heat bath (e.g. the phonons in a solid). The Hamilton operators of each subsystem contain coupling terms to the other subsystems. The wave function of the entire system is approximately the product of all subsystem wave functions and the time evolutions of these wave functions are the solutions to the Schrödinger equation with the time evolution operator, $\hat{U}$, defined by

$$|\Psi(t)\rangle = \hat{U}(t)\,|\Psi\rangle\,,$$

where $|\Psi\rangle$ is the subsystem's wave function (at $t = 0$, where the external fields are not yet applied to the excited material). The Hamiltonian of the subsystem, which is disturbed (at $t > 0$) by external fields, is the sum of three operators

$$H(t) = H_0 + H_{\mathsf{sc}}(t) + H'(t)\,,$$

where H_0 is the Hamilton operator of this subsystem without both, external fields and the coupling to the heat bath (e.g. a solid at $T = 0$). H' describes the interaction with the external fields, (e.g. absorption of light) and H_{sc} describes the coupling to the heat bath (e.g. via electron-phonon interaction). The time evolution operator has the following properties:

$$\begin{aligned}
\mathrm{i}\,\hbar\,\frac{\partial}{\partial t}\hat{U}(t) &= H(t)\,\hat{U}(t) = (H_0 + H_{\mathsf{sc}}(t) + H'(t))\,\hat{U}(t) \qquad (133)\\
\hat{U}(t) &= \exp\left(-\mathrm{i}\,H(t)/\hbar\cdot t\right)\\
\hat{U}^{\dagger}(t) &= \hat{U}^{-1}(t)\,.
\end{aligned}$$

It is convenient to separate the Hamilton operator which describes the interaction with external fields H' in equation (133) by

$$\hat{U}'(t) = \exp\left(\mathrm{i}\left(H_0 + H_{\mathsf{sc}}(t)\right)/\hbar \cdot t\right) \hat{U}(t)\,, \tag{134}$$

where

$$\begin{aligned}
\hat{U}'^{\dagger}(t) &= \hat{U}'^{-1}(t) = \hat{U}^{\dagger}(t)\, \exp\left(-\mathrm{i}\left(H_0 + H_{\mathsf{sc}}(t)\right)/\hbar \cdot t\right) && (135)\\
\hat{U}'^{\dagger}(t) \cdot \hat{U}'(t) &= 1 \\
\mathrm{i}\,\hbar \frac{\partial}{\partial t}\hat{U}'(t) &= H(t)\,\hat{U}(t) \\
&= \exp\left(\mathrm{i}\left(H_0 + H_{\mathsf{sc}}(t)\right)/\hbar\, t\right) H'(t)\, \exp\left(-\mathrm{i}\left(H_0 + H_{\mathsf{sc}}(t)\right)/\hbar \cdot t\right) \hat{U}'(t)\,. && (136)
\end{aligned}$$

The solution of the differential equation (136) within the first order of perturbation theory, and its complex conjugated counterpart are

$$\begin{aligned}
\hat{U}' &\approx 1 + \frac{1}{\mathrm{i}\,\hbar} \int_{-\infty}^{t} \exp\left(\mathrm{i}\left(H_0 + H_{\mathsf{sc}}(t')\right)/\hbar \cdot t'\right) H'(t')\, \exp\left(-i\left(H_0 + H_{\mathsf{sc}}(t')\right)/\hbar \cdot t'\right) \mathrm{d}t'\,, \\
\hat{U}'^{\dagger} &\approx 1 - \frac{1}{\mathrm{i}\,\hbar} \int_{-\infty}^{t} \exp\left(\mathrm{i}\left(H_0 + H_{\mathsf{sc}}(t')\right)/\hbar \cdot t'\right) H'(t')\, \exp\left(-\mathrm{i}\left(H_0 + H_{\mathsf{sc}}(t')\right)/\hbar \cdot t'\right) \mathrm{d}t'\,.
\end{aligned}$$

8.2.2 The time dependent expectation value

An observable of the system could be affected by the time dependent perturbation. The expectation value is

$$\left\langle \hat{O} \right\rangle (t) = \langle \Psi_0 |\, \hat{U}^{\dagger}(t)\, \hat{O}\, \hat{U}(t)\, |\Psi_0\rangle\ .$$

The expectation value is time independent only if the operators $\hat{O}$ and $\hat{U}$ commute. A full set of states of the fermionic many particle system is required to calculate the expectation value. It is given by

$$\sum_{\ldots, n_{\boldsymbol{k},l}, \ldots} |\ldots, n_{\boldsymbol{k},l}, \ldots\rangle \equiv \sum_{n} |\Psi_0\rangle\ ,$$

where $n_{\boldsymbol{k},l} = \{0, 1\}$ is the number of particles in the state which is characterized by l and $\boldsymbol{k}$ (for electrons in a solid, l counts the bands and $\boldsymbol{k}$ refers to the electron's wave vector). The expectation

value reads

$$\begin{aligned}
\left\langle \hat{O} \right\rangle (t) &= \sum_{n'} \sum_{n''} \langle \Psi_0' | \hat{O} | \Psi_0'' \rangle \\
&\quad \cdot \langle \Psi_0 | \left[1 - \frac{1}{\mathrm{i}\,\hbar} \int_{-\infty}^{t} \exp\left(\mathrm{i}\, \frac{H_0 + H_{\mathsf{sc}}(t')}{\hbar} \cdot t' \right) H'(t') \exp\left(-\mathrm{i}\, \frac{H_0 + H_{\mathsf{sc}}(t')}{\hbar} \cdot t' \right) \mathrm{d}t' \right] \\
&\quad \cdot \exp\left(\mathrm{i}\, (H_0 + H_{\mathsf{sc}}(t))/\hbar \cdot t \right) | \Psi_0' \rangle \cdot \langle \Psi_0'' | \exp\left(-\mathrm{i}\, (H_0 + H_{\mathsf{sc}}(t))/\hbar \cdot t \right) \\
&\quad \cdot \left[1 + \frac{1}{\mathrm{i}\,\hbar} \int_{-\infty}^{t} \exp\left(\mathrm{i}\, \frac{H_0 + H_{\mathsf{sc}}(t')}{\hbar} \cdot t' \right) H'(t') \exp\left(-\mathrm{i}\, \frac{H_0 + H_{\mathsf{sc}}(t')}{\hbar} \cdot t' \right) \mathrm{d}t' \right] | \Psi_0 \rangle
\end{aligned}$$

Because of the uncertainty relation, it takes infinitely long to obtain the exact energy. The interaction with the heat bath induces a localization of the particles in time, thus, the particles are described by wave packets. The line shape of such a wave packet usually depends on the time lag to the localization event:

$$g(t, t') = g(t - t') \,.$$

If this function is not exactly known, one could assume a Gaussian or Lorentzian line shape with a characterizing width, σ_{sc}. The width is antiproportional to the average scattering time τ_{sc} and may depend on the temperature.

The observable changes over time according to

$$\begin{aligned}
\left\langle \hat{O} \right\rangle (t) &\approx \left\langle \hat{O} \right\rangle + \sum_{n'} \\
&\quad \langle \Psi_0' | \frac{1}{\mathrm{i}\,\hbar} \int_{-\infty}^{t} \exp\left(\mathrm{i}\, (\omega_0' (t' - t) + (H_{\mathsf{sc}}(t')\, t' - H_{\mathsf{sc}}(t)\, t)/\hbar) \right) H'(t') \\
&\quad \cdot \exp\left(-\mathrm{i}\, (\omega_0 (t' - t) + (H_{\mathsf{sc}}(t')\, t' - H_{\mathsf{sc}}(t)\, t)/\hbar) \right) \mathrm{d}t' \; | \Psi_0 \rangle \; \langle \Psi_0 | \hat{O} | \Psi_0' \rangle \\
&\quad - \langle \Psi_0 | \frac{1}{\mathrm{i}\,\hbar} \int_{-\infty}^{t} \exp\left(\mathrm{i}\, (\omega_0 (t' - t) + (H_{\mathsf{sc}}(t')\, t' - H_{\mathsf{sc}}(t)\, t)/\hbar) \right) H'(t') \\
&\quad \cdot \exp\left(-\mathrm{i}\, (\omega_0' (t' - t) + (H_{\mathsf{sc}}(t')\, t' - H_{\mathsf{sc}}(t)\, t)/\hbar) \right) \mathrm{d}t' \; | \Psi_0' \rangle \; \langle \Psi_0' | \hat{O} | \Psi_0 \rangle \\
&= \left\langle \hat{O} \right\rangle + \frac{1}{\mathrm{i}\,\hbar} \sum_{n'} \int_{-\infty}^{t} \mathrm{d}t' \\
&\quad \langle \Psi_0' | H'(t') | \Psi_0 \rangle \langle \Psi_0 | \hat{O} | \Psi_0' \rangle \exp\left(\mathrm{i}\, (\omega_0 - \omega_0')\, (t - t') \right) g(t - t', \sigma_{\mathsf{sc}})\, g(t - t', \sigma_{\mathsf{sc}}') \\
&\quad - \langle \Psi_0 | H'(t') | \Psi_0' \rangle \langle \Psi_0' | \hat{O} | \Psi_0 \rangle \exp\left(\mathrm{i}\, (\omega_0' - \omega_0)\, (t - t') \right) g(t - t', \sigma_{\mathsf{sc}})\, g(t - t', \sigma_{\mathsf{sc}}') \,.
\end{aligned}$$

The first term is the expection value without perturbation, the second term describes the energy absorption and the third term the energy emission. Higher order terms with multiples of H' are beyond the scope of the linear response framework.

8.2.3 The response of matter to external electric fields

The energy is the time derivative of the action of electric fields to solids:

$$\begin{aligned} E_{\text{em-el}}(t) &= \frac{1}{\mathrm{c}}\frac{\partial}{\partial t}\sum_{i=1}^{N} q_i\ [\boldsymbol{x}_i(t)\cdot\boldsymbol{A}(\boldsymbol{x}_i,t)] = \sum_{i=1}^{N} q_i\ \left[\dot{\boldsymbol{x}}_i(t)\cdot\boldsymbol{A}(\boldsymbol{x}_i,t)/\mathrm{c} + \boldsymbol{x}_i(t)\cdot\dot{\boldsymbol{A}}(\boldsymbol{x}_i,t)/\mathrm{c}\right] \\ &= \sum_{i=1}^{N} q_i\ [\dot{\boldsymbol{x}}_i(t)\cdot\boldsymbol{A}(\boldsymbol{x}_i,t)/\mathrm{c} - \boldsymbol{x}_i(t)\cdot\boldsymbol{E}(\boldsymbol{x}_i,t)] \\ &= \int_{-\infty}^{\infty} [\boldsymbol{J}(\boldsymbol{x},t)\cdot\boldsymbol{A}(\boldsymbol{x},t)/\mathrm{c} - \boldsymbol{P}(\boldsymbol{x},t)\cdot\boldsymbol{E}(\boldsymbol{x},t)]\ \mathrm{d}\boldsymbol{x}\,. \end{aligned}$$

The first term describes the interaction of light with electric currents and the second term describes the interaction between light and dipoles. The energy of the current in the sample under the influence of the external electric field is

$$E_{\mathsf{c}} = \int_{-\infty}^{\infty} \boldsymbol{J}(\boldsymbol{x},t)\cdot\boldsymbol{A}(\boldsymbol{x},t)/\mathrm{c}\,\mathrm{d}\boldsymbol{x}\,.$$

The spatial distribution of charges provides an additional energy term

$$E_{\mathsf{p}} = \int_{-\infty}^{\infty} -\boldsymbol{P}(\boldsymbol{x},t)\cdot\boldsymbol{E}(\boldsymbol{x},t)\,\mathrm{d}\boldsymbol{x}\,.$$

In many-particle systems the current density

$$\boldsymbol{J}(\boldsymbol{x},t) = \sum_{i=1}^{N} q_i\,\dot{\boldsymbol{x}}_i(t)\,\delta(\boldsymbol{x}-\boldsymbol{x}_i)$$

and the dipole-moment density

$$\boldsymbol{P}(\boldsymbol{x},t) = \sum_{i=1}^{N} q_i\,\boldsymbol{x}_i(t)\,\delta(\boldsymbol{x}-\boldsymbol{x}_i)$$

are used to describe the interaction with external fields. Here, N denotes the number of particles. Transferred to quantum mechanics and into the Schrödinger picture, the corresponding current and dipole-momentum operators are time independent. If Ψ_n with $n \in \{1,\infty\}$ is a full set of orthogonal eigenstates of the many-particle system, then

$$\hat{\mathbf{J}} = q/V\cdot\sum_n\sum_m \langle n|\,\hat{\mathbf{r}}\,|m\rangle\ \mathrm{c}_n^\dagger\,\mathrm{c}_m \text{ and} \tag{137}$$

$$\hat{\mathbf{P}} = q/V\cdot\sum_n\sum_m \langle n|\,\hat{\mathbf{r}}\,|m\rangle\ \mathrm{c}_n^\dagger\,\mathrm{c}_m \tag{138}$$

are operators for the current and polarization densities. The expectation value of every single-particle operator is

$$\hat{O} = \sum_n\sum_m \langle n|\,\hat{o}\,|m\rangle\ \mathrm{c}_n^\dagger\,\mathrm{c}_m\,.$$

The expectation values change under the influence of external electric fields. The expectation value in the first order of perturbation theory reads

$$
\begin{aligned}
\left\langle \hat{O} \right\rangle (\boldsymbol{x}, t) &= \left\langle \hat{O} \right\rangle_0 - \sum_{n'} \frac{1}{\mathrm{i}\,\hbar} \\
&\quad \cdot \int_{-\infty}^{t} \left\langle \Psi_0' \right| \left[\hat{\mathbf{J}} \cdot \boldsymbol{A}(\boldsymbol{x}, t')/\mathrm{c} + \hat{\mathbf{P}} \cdot \boldsymbol{E}(\boldsymbol{x}, t') \right] \left| \Psi_0 \right\rangle \left\langle \Psi_0 \right| \hat{O} \left| \Psi_0' \right\rangle \\
&\quad \cdot \exp\left(\mathrm{i} \left(\omega_0 - \omega_0' \right) (t - t') \right) g(t - t', \sigma_{\mathsf{sc}})\, g(t - t', \sigma_{\mathsf{sc}}') \qquad (139) \\
&\quad - \left\langle \Psi_0 \right| \left[\hat{\mathbf{J}} \cdot \boldsymbol{A}(\boldsymbol{x}, t')/\mathrm{c} + \hat{\mathbf{P}} \cdot \boldsymbol{E}(\boldsymbol{x}, t') \right] \left| \Psi_0' \right\rangle \left\langle \Psi_0' \right| \hat{O} \left| \Psi_0 \right\rangle \\
&\quad \cdot \exp\left(\mathrm{i} \left(\omega_0' - \omega_0 \right) (t - t') \right) g(t - t', \sigma_{\mathsf{sc}})\, g(t - t', \sigma_{\mathsf{sc}}')\, \mathrm{d}t' \qquad (140) \\
&= \sum_{n=1}^{\infty} \sum_{m=1}^{\infty} \left\langle \Psi_0 \right| \left\langle n \right| \hat{o} \left| m \right\rangle \, \mathrm{c}_n^{\dagger}\, \mathrm{c}_m \left| \Psi_0 \right\rangle - \frac{q}{\mathrm{i}\,\hbar} \sum_{n'} \int_{-\infty}^{t} \\
&\quad \cdot \left\langle \Psi_0 \right| \left\langle m \right| \hat{o} \left| n \right\rangle \, \mathrm{c}_m^{\dagger}\, \mathrm{c}_n \left| \Psi_0' \right\rangle \left\langle \Psi_0' \right| \left\langle n \right| \left[\hat{\mathbf{r}} \cdot \boldsymbol{A}(\boldsymbol{x}, t')/\mathrm{c} + \hat{\mathbf{r}} \cdot \boldsymbol{E}(\boldsymbol{x}, t') \right] \left| m \right\rangle \, \mathrm{c}_n^{\dagger}\, \mathrm{c}_m \, \left| \Psi_0 \right\rangle \\
&\quad \cdot \exp\left(\mathrm{i} \left(\omega_0 - \omega_0' \right) (t - t') \right) g(t - t', \sigma_{\mathsf{sc}})\, g(t - t', \sigma_{\mathsf{sc}}') \\
&\quad - \left\langle \Psi_0 \right| \left\langle n \right| \left[\hat{\mathbf{r}} \cdot \boldsymbol{A}(\boldsymbol{x}, t')/\mathrm{c} + \hat{\mathbf{r}} \cdot \boldsymbol{E}(\boldsymbol{x}, t') \right] \left| m \right\rangle \, \mathrm{c}_n^{\dagger}\, \mathrm{c}_m \, \left| \Psi_0' \right\rangle \left\langle \Psi_0' \right| \left\langle m \right| \hat{o} \left| n \right\rangle \, \mathrm{c}_m^{\dagger}\, \mathrm{c}_n \left| \Psi_0 \right\rangle \\
&\quad \cdot \exp\left(\mathrm{i} \left(\omega_0' - \omega_0 \right) (t - t') \right) g(t - t', \sigma_{\mathsf{sc}})\, g(t - t', \sigma_{\mathsf{sc}}')\, \mathrm{d}t' \,.
\end{aligned}
$$

The wave function changes by removing one electron from the state i and subsequently adding one electron to the state j

$$
\left\langle \Psi_0' \right| \mathrm{c}_j^{\dagger}\, \mathrm{c}_i \left| \Psi_0 \right\rangle \,.
$$

The multiplications of the time steps of the initial state wave function and the final state wave function are expected to be approximately given by the multiplications of the time steps of the emptied initial state i and the newly filled state j:

$$
\begin{aligned}
&\exp\left(\mathrm{i} \left(\omega_0' - \omega_0 \right) (t - t') \right) g(t - t', \sigma_{\mathsf{sc}})\, g(t - t', \sigma_{\mathsf{sc}}') \\
&\approx \exp\left(\mathrm{i} \left(\omega_j - \omega_i \right) (t - t') \right) g(t - t', \sigma_i)\, g(t - t', \sigma_j) \,.
\end{aligned}
$$

The corresponding expectation value is

$$\begin{aligned}
\left\langle \hat{O} \right\rangle (\boldsymbol{x}, t) &= \sum_{n=1}^{\infty} \sum_{m=1}^{\infty} \langle \Psi_0 | \langle n | \hat{o} | m \rangle \ \mathrm{c}_n^\dagger \, \mathrm{c}_m \, | \Psi_0 \rangle - \frac{q}{\mathrm{i}\,\hbar} \\
&\quad \cdot \int_{-\infty}^{t} \langle \Psi_0 | \langle m | \hat{o} | n \rangle \ \mathrm{c}_m^\dagger \, \mathrm{c}_n \, \langle n | \left[\hat{\mathbf{r}} \cdot \boldsymbol{A}(\boldsymbol{x}, t')/\mathrm{c} + \hat{\mathbf{r}} \cdot \boldsymbol{E}(\boldsymbol{x}, t') \right] | m \rangle \ \mathrm{c}_n^\dagger \, \mathrm{c}_m \ | \Psi_0 \rangle \\
&\quad \cdot \exp\left(\mathrm{i} \left(\omega_m - \omega_n \right) (t - t') \right) g(t - t', \sigma_m) \, g(t - t', \sigma_n) \\
&\quad - \langle \Psi_0 | \langle n | \left[\hat{\mathbf{r}} \cdot \boldsymbol{A}(\boldsymbol{x}, t')/\mathrm{c} + \hat{\mathbf{r}} \cdot \boldsymbol{E}(\boldsymbol{x}, t') \right] | m \rangle \ \mathrm{c}_n^\dagger \, \mathrm{c}_m \, \langle m | \hat{o} | n \rangle \ \mathrm{c}_m^\dagger \, \mathrm{c}_n \, | \Psi_0 \rangle \\
&\quad \cdot \exp\left(\mathrm{i} \left(\omega_m - \omega_n \right) (t - t') \right) g(t - t', \sigma_m) \, g(t - t', \sigma_n) \, \mathrm{d}t' \\
&= \sum_{m=1}^{\infty} \langle m | \hat{o} | m \rangle \ f_m - \sum_{n=1}^{\infty} \frac{q}{\mathrm{i}\,\hbar} \\
&\quad \cdot \int_{-\infty}^{t} \langle m | \hat{o} | n \rangle \ \langle n | \left[\hat{\mathbf{r}} \cdot \boldsymbol{A}(\boldsymbol{x}, t')/\mathrm{c} + \hat{\mathbf{r}} \cdot \boldsymbol{E}(\boldsymbol{x}, t') \right] | m \rangle \ (1 - f_n) \, f_m \\
&\quad \cdot \exp\left(\mathrm{i} \left(\omega_m - \omega_n \right) (t - t') \right) g(t - t', \sigma_m) \, g(t - t', \sigma_n) \\
&\quad - \langle n | \left[\hat{\mathbf{r}} \cdot \boldsymbol{A}(\boldsymbol{x}, t')/\mathrm{c} + \hat{\mathbf{r}} \cdot \boldsymbol{E}(\boldsymbol{x}, t') \right] | m \rangle \ \langle m | \hat{o} | n \rangle \ (1 - f_m) \, f_n \\
&\quad \cdot \exp\left(\mathrm{i} \left(\omega_m - \omega_n \right) (t - t') \right) g(t - t', \sigma_m) \, g(t - t', \sigma_n) \, \mathrm{d}t' \\
&= \sum_{m=1}^{\infty} \langle m | \hat{o} | m \rangle \ f_m - \sum_{n=1}^{\infty} \frac{q}{\mathrm{i}\,\hbar} \\
&\quad \cdot \int_{-\infty}^{t} \langle m | \hat{o} | n \rangle \ \langle n | \left[\hat{\mathbf{r}} \cdot \boldsymbol{A}(\boldsymbol{x}, t')/\mathrm{c} + \hat{\mathbf{r}} \cdot \boldsymbol{E}(\boldsymbol{x}, t') \right] | m \rangle \ (f_m - f_n) \\
&\quad \cdot \exp\left(\mathrm{i} \left(\omega_m - \omega_n \right) (t - t') \right) g(t - t', \sigma_m) \, g(t - t', \sigma_n) \, \mathrm{d}t' \, .
\end{aligned}$$

The terms in the first order of perturbation theory, where $n = m$, add up to zero.

In many applications, the electromagnetic waves form a wave packet with a finite coherence time, τ_ν, and the spectral width, $\sigma_\nu = \tau_\nu^{-1}$. The associated vector potential reads

$$\begin{aligned}
\boldsymbol{A}(\boldsymbol{x}, t) &= 1/2 \left(\boldsymbol{A}_1(\boldsymbol{x}, t) + \boldsymbol{A}_2(\boldsymbol{x}, t) \right) \\
&= \frac{\mathrm{c}}{2} \left[\boldsymbol{E}_0 \exp\left(\mathrm{i}\, \boldsymbol{q}\, \boldsymbol{x} - \mathrm{i}\, 2\pi\nu\, t \right) + \boldsymbol{E}_0^* \exp\left(-\mathrm{i}\, \boldsymbol{q}^*\, \boldsymbol{x} + \mathrm{i}\, 2\pi\nu\, t \right) \right] g(|t|, \sigma_\nu) \, .
\end{aligned}$$

This definition takes the wave packet to be symmetric in time with respect to $t = 0$. The central frequency of the wave packet is denoted with ν.[36]

The electric field is defined by

$$\boldsymbol{E}(\boldsymbol{x}, t) = -\frac{\partial}{\mathrm{c}\, \partial t} \, \boldsymbol{A}(\boldsymbol{x}, t) \, . \tag{141}$$

[36] The vector potential does not need to have the same line shape as the band electrons. Here the same line shape, g, is assumed.

It follows that the electric field splits up into two parts, which propagate in opposite directions:

$$\boldsymbol{E}(\boldsymbol{x},t) = \boldsymbol{E}_1(\boldsymbol{x},t) + \boldsymbol{E}_2(\boldsymbol{x},t) = \boldsymbol{E}_1(\boldsymbol{x},t) + \boldsymbol{E}_1^*(\boldsymbol{x},t)\,.$$

8.2.4 The electromagnetic wave equation

The wave vector of electromagnetic wave packets inside the many-particle systems is determined by the wave equation [DG02]

$$\nabla \cdot (\nabla \boldsymbol{E}_1) = \mu_0\,\mu_1\,\frac{\partial^2}{\partial t^2}\,\boldsymbol{D}_1 + \mu_0\,\mu_1\,\frac{\partial}{\partial t}\,\boldsymbol{J}_1$$

which is based on Maxwell's equations. A similar equation holds for the second component $\boldsymbol{E}_2$. Wave packets with large spatial extent (or plane waves) have well defined wave numbers, q, and the coupling to the medium is given by

$$|\boldsymbol{q}|^2\;\boldsymbol{E}_1 = -\mu_0\,\mu_1\,\frac{\partial^2}{\partial t^2}\,\boldsymbol{D}_1 - \mu_0\,\mu_1\,\frac{\partial}{\partial t}\,\boldsymbol{J}_1\,. \tag{142}$$

Note that most of the parameters are complex (e.g. q, $\boldsymbol{E}_1$, etc.). If the electromagnetic wave packet is long

$$(\tau_\nu \gg \tau_m)\;\&\;(\tau_\nu \gg \tau_n)\,,$$

then the photo-induced current and polarization follow the electric field of the wave packet and the shape of the electromagnetic wave remains unchanged. The current and polarization responses are, in the first order of perturbation theory, given by

$$\begin{aligned}
\boldsymbol{J} &= 1/2\,(\boldsymbol{J}_1 + \boldsymbol{J}_2) = 1/2\,(\sigma\,\boldsymbol{E}_1 + \sigma^*\,\boldsymbol{E}_2)\,, && (143)\\
\boldsymbol{P} &= 1/2\,(\boldsymbol{P}_1 + \boldsymbol{P}_2) = 1/2\,\epsilon_0\,(\chi\,\boldsymbol{E}_1 + \chi^*\,\boldsymbol{E}_2) && (144)\\
\boldsymbol{D}_1 &= \boldsymbol{P}_1 + \epsilon_0\,\boldsymbol{E}_1 = \epsilon\,\epsilon_0\,\boldsymbol{E}_1
\end{aligned}$$

.

In addition to the standard text book case [DG02], both, the complex conductivity and the complex polarization responses are considered. This gives a more general solution to the problem of the interaction between light and matter, which is applicable even in the case that the material is neither a simple metal nor a pure insulator. Phase-delays are considered for both responses. Thus the conductivity σ and the polarizability χ are complex quantities, both being independent of each other and depend on the frequency of the electromagnetic wave.

The current and the polarization are measurable quantities. Because of the causality the response of the solid follows the perturbation and not vice versa. The causality requires that the conductivity and the polarizability are (independently) Kramers-Kronig invariant.

The electromagnetic wave equation (142) in solids, with the above definitions (equations (141), (143) and (144)) reads

$$|\boldsymbol{q}|^2 \; \frac{\partial}{\mathrm{c}\,\partial t}\,\boldsymbol{A}_1 = -\mu_1\,\epsilon\,\frac{\partial^3}{\mathrm{c}^3\,\partial t^3}\,\boldsymbol{A}_1 - \mu_0\,\mu_1\,\sigma\,\frac{\partial^2}{\mathrm{c}\,\partial t^2}\,\boldsymbol{A}_1\,. \tag{145}$$

8.2.5 The response of matter to electromagnetic plane waves

If the electromagnetic wave packet is spatially extended and thus described by plane waves, then the wave equation (145) reduces to

$$|\boldsymbol{q}|^2 = \frac{\mu_1}{\mathrm{c}^2}\,\left(\epsilon\,(2\pi\nu)^2 + \mathrm{i}\,\sigma\,\frac{2\pi\nu}{\epsilon_0}\right)\,. \tag{146}$$

The linear response is then

$$\begin{aligned}
\left\langle \hat{O} \right\rangle_1 (\boldsymbol{x},t) \;&=\; \sum_{m=1}^{\infty} \langle m|\,\hat{o}\,|m\rangle\; f_m + \sum_{n=1}^{\infty} \frac{q}{\hbar}\;\langle m|\,\hat{o}\,|n\rangle\;(f_m - f_n)\;\langle n|\left[\mathrm{i}\,\hat{\mathbf{r}} - \hat{\mathbf{r}}\,2\pi\nu\right]|m\rangle \\
&\quad \cdot \int_{-\infty}^{t} \frac{\boldsymbol{E}_1(\boldsymbol{x},t')}{\mathrm{i}\,2\pi\nu}\;\exp\left(\mathrm{i}\,(\omega_m - \omega_n)\,(t-t')\right)\,g(t-t',\sigma_m)\,g(t-t',\sigma_n)\,\mathrm{d}t' \\
&=\; \sum_{m=1}^{\infty} \langle m|\,\hat{o}\,|m\rangle\; f_m + \sum_{n=1}^{\infty} \frac{q}{\hbar}\;\langle m|\,\hat{o}\,|n\rangle\;(f_m - f_n)\;\langle n|\left[\frac{\hat{\mathbf{r}}}{2\pi\nu} + \mathrm{i}\,\hat{\mathbf{r}}\right]|m\rangle\;\boldsymbol{E}_1(\boldsymbol{x},t) \\
&\quad \cdot \int_{-\infty}^{t} \exp\left(\mathrm{i}\,(\omega_m - \omega_n + 2\pi\nu)\,(t-t')\right)\,g(t-t',\sigma_m)\,g(t-t',\sigma_n)\,\mathrm{d}t'
\end{aligned} \tag{147}$$

with

$$\boldsymbol{E}_1(\boldsymbol{x},t) = \boldsymbol{E}_1(\boldsymbol{x})\;\exp\left(-\mathrm{i}\,2\pi\nu\,t\right) = \frac{\boldsymbol{A}_1(\boldsymbol{x},t)\,\mathrm{c}}{\mathrm{i}\,2\pi\nu} = \frac{\boldsymbol{A}_0\,\mathrm{c}}{\mathrm{i}\,2\pi\nu}\;\exp\left(\mathrm{i}\,\boldsymbol{q}\,\boldsymbol{x} - \mathrm{i}\,2\pi\nu\,t\right)\,. \tag{148}$$

The result of the integration is a complex quantity with real and imaginary parts

$$\begin{aligned}
I_2^{m,n}(\nu) - \mathrm{i}\,I_1^{m,n}(\nu) \;&\equiv\; I^{m,n}(\nu,t) \\
&=\; \int_{-\infty}^{t} \exp\left(\mathrm{i}\,(\omega_m - \omega_n + 2\pi\nu)\,(t-t')\right)\,g(t-t',\sigma_m)\,g(t-t',\sigma_n)\,\mathrm{d}t' \\
&=\; \int_{0}^{\infty} \exp\left(\mathrm{i}\,(\omega_m - \omega_n + 2\pi\nu)\,s\right)\,g(s,\sigma_m)\,g(s,\sigma_n)\,\mathrm{d}s\,.
\end{aligned} \tag{149}$$

The substitution of t clarifies that the response is time independent. The dielectric function and the conductivity are (see the operator definitions (137) and (138) and the equation (147))

$$\begin{aligned}
\chi(\nu) &= \frac{\mathrm{e}^2}{\epsilon_0 V \hbar} \sum_{m=1}^{\infty} \sum_{n=1}^{\infty} (f_m - f_n) \Big(\langle m| \hat{\mathbf{r}} |n\rangle \langle n| \hat{\mathbf{r}} |m\rangle \, (I_1^{m,n}(\nu) + \mathrm{i}\, I_2^{m,n}(\nu)) \\
&\quad + \langle m| \hat{\mathbf{r}} |n\rangle \langle n| \hat{\hat{\mathbf{r}}} |m\rangle \, \frac{1}{2\pi\nu} \, (I_2^{m,n}(\nu) - \mathrm{i}\, I_1^{m,n}(\nu)) \Big) \\
\sigma(\nu) &= \frac{\mathrm{e}^2}{V \hbar} \sum_{m=1}^{\infty} \sum_{n=1}^{\infty} (f_m - f_n) \Big(\langle m| \hat{\mathbf{r}} |n\rangle \langle n| \hat{\hat{\mathbf{r}}} |m\rangle \, \frac{1}{2\pi\nu} \, (I_2^{m,n}(\nu) - \mathrm{i}\, I_1^{m,n}(\nu)) \\
&\quad + \langle m| \hat{\hat{\mathbf{r}}} |n\rangle \langle n| \hat{\mathbf{r}} |m\rangle \, (I_1^{m,n}(\nu) + \mathrm{i}\, I_2^{m,n}(\nu)) \Big) \\
\widehat{\epsilon}(\nu) &= 1 + \chi(\nu) \, .
\end{aligned}$$

The wavevector of the electromagnetic wave inside the material is given by equation (146) and reads

$$\begin{aligned}
|\boldsymbol{q}|^2 &= \frac{\mathrm{e}^2 \mu_1}{\epsilon_0 \, \mathrm{c}^2 \, V \hbar} \sum_{m=1}^{\infty} \sum_{n=1}^{\infty} (f_m - f_n) \, \Big(\langle m| \hat{\hat{\mathbf{r}}} |n\rangle \langle n| \hat{\hat{\mathbf{r}}} |m\rangle + \langle m| \hat{\mathbf{r}} |n\rangle \langle n| \hat{\mathbf{r}} |m\rangle \, (2\pi\nu)^2 \Big) \\
&\quad \cdot (I_1^{m,n}(\nu) + \mathrm{i}\, I_2^{m,n}(\nu))
\end{aligned} \tag{150}$$

In optical experiments with monochromatic light, it is not possible to distinguish between the phase delay of the photo-induced current and the amplitude of the dielectric response. Further, for the same reasons, the phase delay of the dielectric response is equal to the amplitude of the photo-induced currents. The response can be decoupled into the current and dielectric responses by their different wavelength-dependencies.

Because of the difficulties to decouple the response into current and dielectric components, it is convenient to define the dielectric function ϵ with

$$|\boldsymbol{q}|^2 = \frac{\mu_1}{\mathrm{c}^2} (2\pi\nu)^2 (\epsilon_1 + \mathrm{i}\, \epsilon_2) \, .$$

This equation is used in publications on optical properties in solids. ϵ can be determined from reflectivity and transmission experiments taking the Fresnel equations into account [DAP94a; DAP94b].

8.2.6 The response of electrons described by Bloch waves

In crystalline solids, the electrons can be described by Bloch waves (see any book about solid state physics). For Bloch waves the sum over all states can be transformed into an integration over the

$\boldsymbol{k}$-space of the first Brillouin zone

$$\begin{aligned} |m\rangle &\rightarrow |\boldsymbol{k}, l\rangle \\ \sum_{m=1}^{\infty} &\rightarrow \frac{V}{(2\,\pi)^3} \sum_l \int_{V_{\boldsymbol{k}}} \mathrm{d}\boldsymbol{k} = V \sum_l \int_0^{\infty} D(E)\,\mathrm{d}E\,. \end{aligned}$$

Here, l counts the electronic bands and D is the density of states. The integration over $\boldsymbol{k}$-space is transformed to an integration over energy. Here, the dispersion relation $E(\boldsymbol{k})$ is considered. A convenient approximation to simplify the integration is to assume spherical symmetry for small $\boldsymbol{k}$ within the first Brillouin zone. Here the density of states transforms to

$$D(E) = \frac{2\,V}{(2\,\pi)^3} \frac{1}{|\nabla_{\boldsymbol{k}} E|} = \frac{2\,V}{2\,\pi^2} \frac{(k(E))^2}{|\nabla_k E|}\,.$$

Considering plane waves, the dielectric function is

$$\epsilon = 1 + \chi_1 + \mathrm{i}\,\chi_2 \tag{151}$$

with ($x = 1$,2)

$$\begin{aligned} \chi_x \;=\; & \frac{\mathrm{e}^2}{\epsilon_0\,V\,(2\pi\nu)^2} \sum_l \int_0^{\infty} \sum_{l'} \int_0^{\infty} D(E)\,D(E')\,(f(E) - f(E'))\,I_x(E, E', \nu, \gamma, \gamma') \\ & \Big(\langle k, l|\,\hat{\mathrm{r}}\,|k', l'\rangle\,\langle k', l'|\,\hat{\mathrm{r}}\,|k, l\rangle\,(2\pi\nu)^2 + \langle k, l|\,\hat{\mathrm{r}}\,|k', l'\rangle\,\langle k', l'|\,\hat{\mathrm{r}}\,|k, l\rangle\Big)\,\mathrm{d}E'\,\mathrm{d}E \end{aligned}$$

and

$$I_x^{m,n}(\nu)/\hbar \rightarrow I_x(E, E', \gamma, \gamma', \nu)\,.$$

8.2.7 Common damping terms of wave packets

Gaussian pulse shape

The Gaussian pulse shape is

$$g_{\mathrm{G}}(s, \sigma) = \exp\left(-s^2\,\sigma^2/2\right).$$

The prefactor is taken to be 1 to set the amplitude to 1 at $s = 0$ (the fourier transformation gives a normalized line shape as a function of energy). The integration of equation (149) is performed to obtain an expression for the dielectric function (151) in the case of a Gaussian line shape of the

responding particles. It is

$$\begin{aligned} I_2^{m,n}(\nu) - \mathrm{i}\, I_1^{m,n}(\nu) &= -\int_0^\infty \exp\left(\mathrm{i}\left(\omega_m - \omega_n + 2\pi\nu\right) s\right) g_{\mathsf{G}}(s,\sigma_m)\, g_{\mathsf{G}}(s,\sigma_n)\, \mathrm{d}s \\ &= \sqrt{\frac{\pi}{2\,(\sigma_m^2+\sigma_n^2)}}\, \exp\left(-\frac{(\omega_m-\omega_n+2\pi\nu)^2}{2\,(\sigma_m^2+\sigma_n^2)}\right) \\ &\quad \cdot \left(1 - \mathrm{i}\,\mathrm{erfi}\left(\frac{\omega_m-\omega_n+2\pi\nu}{\sqrt{2\,(\sigma_m^2+\sigma_n^2)}}\right)\right). \end{aligned}$$

Rewriting the parameters in units of energy results in

$$\begin{aligned} I_2(\nu, E-E') - \mathrm{i}\, I_1(\nu, E-E') &= \hbar\sqrt{\frac{\pi}{2\,(\gamma^2+\gamma'^2)}}\, \exp\left(-\frac{(E-E'+\mathrm{h}\nu)^2}{2\,(\gamma^2+\gamma'^2)}\right) \\ &\quad \cdot \left(1 - \mathrm{i}\,\mathrm{erfi}\left(\frac{E-E'+\mathrm{h}\nu}{\sqrt{2\,(\gamma^2+\gamma'^2)}}\right)\right). \end{aligned}$$

Lorentzian pulse shape

An exponential decay

$$g_{\mathsf{L}}(s,\sigma) = \exp\left(-\left|s\right|\,\sigma\right)$$

corresponds to a Lorentzian line shape in energy space. The damping factor I is defined in equation (149) and the dielectric function with Lorentzian damping uses

$$I_2^{m,n}(\nu) - \mathrm{i}\, I_1^{m,n}(\nu) = \frac{(\sigma_m+\sigma_n) + \mathrm{i}\,(\omega_m-\omega_n+2\pi\nu)}{(\omega_m-\omega_n+2\pi\nu)^2 + (\sigma_m+\sigma_n)^2}.$$

In the main text the parameters are defined in units of energy, this gives

$$I_2(\nu, E-E') - \mathrm{i}\, I_1(\nu, E-E') = \hbar\,\frac{(\gamma+\gamma') + \mathrm{i}\,(E-E'+\mathrm{h}\nu)}{(E-E'+\mathrm{h}\nu)^2 + (\gamma+\gamma')^2}. \tag{152}$$

References

[AD75] P. B. Allen and R. C. Dynes. "Transition temperature of strong-coupled superconductors reanalyzed". In: *Phys. Rev. B* 12 (Aug. 1975), pp. 905–922. URL: https://link.aps.org/doi/10.1103/PhysRevB.12.905.

[AKP74] S.I. Anisimov, B.L. Kapeliovich, and T.L. Perel'Man. "Electron emission from metal surfaces exposed to ultrashort laser pulses". In: *Soviet Journal of Experimental and Theoretical Physics* 39 (1974), pp. 375–377.

[AM11] N.W. Ashcroft and N.D. Mermin. *Solid State Physics*. 2011.

[AM83] Philip B. Allen and Božidar Mitrović. "Theory of Superconducting Tc". In: *Solid State Physics* 37 (1983), pp. 1–92. URL: http://www.sciencedirect.com/science/article/pii/S0081194708606657.

[AT02] R.D. Averitt and A.J. Taylor. "Ultrafast optical and far-infrared quasiparticle dynamics in correlated electron materials". In: *Journal of Physics: Condensed Matter* 14 (2002), R1357. URL: http://stacks.iop.org/0953-8984/14/i=50/a=203.

[Ack+07] W. Ackermann et al. "Operation of a free-electron laser from the extreme ultraviolet to the water window". In: *Nature photonics* 1 (2007), pp. 336–342.

[All+86] P. B. Allen, T. P. Beaulac, F. S. Khan, W. H. Butler, F. J. Pinski, and J. C. Swihart. "dc transport in metals". In: *Phys. Rev. B* 34 (Sept. 1986), pp. 4331–4333. URL: http://link.aps.org/doi/10.1103/PhysRevB.34.4331.

[All87] Philip B. Allen. "Theory of thermal relaxation of electrons in metals". In: *Phys. Rev. Lett.* 59 (Sept. 1987), pp. 1460–1463. URL: http://link.aps.org/doi/10.1103/PhysRevLett.59.1460.

[Ant+74] F. Antonangeli, E. Colavita, R. Rosei, and S. E. Salusti. "Optical gaps and interband matrix elements of silver as a function of temperature". In: *Il Nuovo Cimento B (1971-1996)* 24 (1974), pp. 121–129. URL: http://dx.doi.org/10.1007/BF02724037.

[BAP82] T. P. Beaulac, P. B. Allen, and F. J. Pinski. "Electron-phonon effects in copper. II. Electrical and thermal resistivities and Hall coefficient". In: *Phys. Rev. B* 26 (Aug. 1982), pp. 1549–1558. URL: http://link.aps.org/doi/10.1103/PhysRevB.26.1549.

[BB92] R Brendel and D Bormann. "An infrared dielectric function model for amorphous solids". In: *Journal of applied physics* 71 (1992), pp. 1–6.

[BC55] J.R. Beattie and G.K.T. Conn. "XXV. Optical constants of metals in the infrared - Principles of measurement". In: *The London, Edinburgh, and Dublin Philosophical Magazine and Journal of Science* 46 (1955), pp. 222–234. URL: http://dx.doi.org/10.1080/14786440208520565.

[BFI87] S. D. Brorson, J. G. Fujimoto, and E. P. Ippen. "Femtosecond electronic heat-transport dynamics in thin gold films". In: *Phys. Rev. Lett.* 59 (Oct. 1987), pp. 1962–1965. URL: http://link.aps.org/doi/10.1103/PhysRevLett.59.1962.

[BK14] V. V. Baranov and V. V. Kabanov. "Theory of electronic relaxation in a metal excited by an ultrashort optical pump". In: *Phys. Rev. B* 89 (Mar. 2014), p. 125102. URL: http://link.aps.org/doi/10.1103/PhysRevB.89.125102.

[BKB98] B. I. Belevtsev, Yu. F. Komnik, and E. Yu. Beliayev. "Electron relaxation in disordered gold films". In: *Phys. Rev. B* 58 (Sept. 1998), pp. 8079–8086. URL: http://link.aps.org/doi/10.1103/PhysRevB.58.8079.

[BMA15] M. Bauer, A. Marienfeld, and M. Aeschlimann. "Hot electron lifetimes in metals probed by time-resolved two-photon photoemission". In: *Progress in Surface Science* 90 (2015), pp. 319 –376. URL: http://www.sciencedirect.com/science/article/pii/S0079681615000192.

[BP91] Gordon A. Baym and Christopher Pethick. *Landau Fermi liquid theory : concepts and applications*. A Wiley-Interscience publication. New York, 1991, VIII, 203 S. ISBN: 0-471-82418-6. URL: http://scans.hebis.de/HEBCGI/show.pl?02174405_toc.pdf.

[BR73] G. Bergmann and D. Rainer. "The sensitivity of the transition temperature to changes in α^2F(ω)". In: *Zeitschrift für Physik* 263 (1973), pp. 59–68. URL: http://dx.doi.org/10.1007/BF02351862.

[BW95] D. Belitz and M. N. Wybourne. "Eliashberg function of amorphous metals". In: *Phys. Rev. B* 51 (Jan. 1995), pp. 689–692. URL: http://link.aps.org/doi/10.1103/PhysRevB.51.689.

[Bag+80] D. Bagayoko, D.G. Laurent, S.P. Singhal, and J. Callaway. "Band structure, optical properties, and compton profile of copper". In: *Physics Letters A* 76 (1980), pp. 187–190. URL: http://www.sciencedirect.com/science/article/pii/037596018090609X.

[Bea55] J.R. Beattie. "XXVI. Optical constants of metals in the infrared - experimental methods". In: *The London, Edinburgh, and Dublin Philosophical Magazine and Journal of Science* 46 (1955), pp. 235–245. URL: http://www.tandfonline.com/doi/abs/10.1080/14786440208520566.

[Bel87] D. Belitz. "Electron-phonon interaction, ultrasonic attenuation, and Eliashberg function α^2F(ω) in impure metals". In: *Phys. Rev. B* 36 (Aug. 1987), pp. 2513–2518. URL: https://link.aps.org/doi/10.1103/PhysRevB.36.2513.

[Ber76] G. Bergmann. "Amorphous metals and their superconductivity". In: *Physics Reports* 27 (1976), pp. 159–185. URL: http://www.sciencedirect.com/science/article/pii/0370157376900405.

[Bey12] Markus Beyer. "Photo-doping phenomena in the high-temperature superconductor $La_{2-x}Sr_xCuO_4$". In: *Phd thesis, University of Konstanz* (2012).

[Bov07] Uwe Bovensiepen. "Coherent and incoherent excitations of the Gd(0001) surface on ultrafast timescales". In: *Journal of Physics: Condensed Matter* 19 (2007), p. 083201. URL: http://stacks.iop.org/0953-8984/19/i=8/a=083201.

[Bro+90] S. D. Brorson, A. Kazeroonian, J. S. Moodera, D. W. Face, T. K. Cheng, E. P. Ippen, M. S. Dresselhaus, and G. Dresselhaus. "Femtosecond room-temperature measurement of the electron-phonon coupling constant γ in metallic superconductors". In: *Phys. Rev. Lett.* 64 (Apr. 1990), pp. 2172–2175. URL: http://link.aps.org/doi/10.1103/PhysRevLett.64.2172.

[Bur63] Glenn A. Burdick. "Energy Band Structure of Copper". In: *Phys. Rev.* 129 (Jan. 1963), pp. 138–150. URL: http://link.aps.org/doi/10.1103/PhysRev.129.138.

[Bév+14] E. Bévillon, J. P. Colombier, V. Recoules, and R. Stoian. "Free-electron properties of metals under ultrafast laser-induced electron-phonon nonequilibrium: A first-principles study". In: *Phys. Rev. B* 89 (Mar. 2014), p. 115117. URL: http://link.aps.org/doi/10.1103/PhysRevB.89.115117.

[CH66] Y. A. Chang and L. Himmel. "Temperature Dependence of the Elastic Constants of Cu, Ag, and Au above Room Temperature". In: *Journal of Applied Physics* 37 (1966), pp. 3567–3572. URL: http://scitation.aip.org/content/aip/journal/jap/37/9/10.1063/1.1708903.

[CMR75] E. Colavita, S. Modesti, and R. Rosei. "Temperature dependence of the interband absorption edge of copper". In: *Solid State Communications* 17 (1975), pp. 931–934. URL: http://www.sciencedirect.com/science/article/pii/0038109875902227.

[Cam+00] I. Campillo, A. Rubio, J. M. Pitarke, A. Goldmann, and P. M. Echenique. "Hole Dynamics in Noble Metals". In: *Phys. Rev. Lett.* 85 (Oct. 2000), pp. 3241–3244. URL: http://link.aps.org/doi/10.1103/PhysRevLett.85.3241.

[Cao+97] J. Cao, Y. Gao, R. J. D. Miller, H. E. Elsayed-Ali, and D. A. Mantell. "Femtosecond photoemission study of ultrafast electron dynamics on Cu(100)". In: *Phys. Rev. B* 56 (July 1997), pp. 1099–1102. URL: http://link.aps.org/doi/10.1103/PhysRevB.56.1099.

[Cao+98] J. Cao, Y. Gao, H. E. Elsayed-Ali, R. J. D. Miller, and D. A. Mantell. "Femtosecond photoemission study of ultrafast electron dynamics in single-crystal Au(111) films". In: *Phys. Rev. B* 58 (Oct. 1998), pp. 10948–10952. URL: http://link.aps.org/doi/10.1103/PhysRevB.58.10948.

[Car06] E. Carpene. "Ultrafast laser irradiation of metals: Beyond the two-temperature model". In: *Phys. Rev. B* 74 (July 2006), p. 024301. URL: http://link.aps.org/doi/10.1103/PhysRevB.74.024301.

[Che+91] S. V. Chekalin, V. M. Farztdinov, V. V. Golovlyov, V. S. Letokhov, Yu. E. Lozovik, Yu. A. Matveets, and A. G. Stepanov. "Femtosecond spectroscopy of $\mathrm{YBa_2Cu_3O_{7-\delta}}$: Electron-phonon-interaction measurement and energy-gap observation". In: *Phys. Rev. Lett.* 67 (Dec. 1991), pp. 3860–3863. URL: https://link.aps.org/doi/10.1103/PhysRevLett.67.3860.

[Cil+13] F Cilento, S Dal Conte, G Coslovich, F Banfi, G Ferrini, H Eisaki, M Greven, A Damascelli, D van der Marel, F Parmigiani, and C Giannetti. "In search for the pairing glue in cuprates by non-equilibrium optical spectroscopy". In: *Journal of Physics: Conference*

Series 449 (2013), p. 012003. URL: http://stacks.iop.org/1742-6596/449/i=1/a=012003.

[Coh07] Coherent. *Operator's Manual Micra Modelocked Ti:Sapphire Laser*. 2007.

[Coh10] Coherent. *Operator's Manual Verdi Dual FAP Diode-Pumped Laser*. 2010.

[Coh97] Coherent. *Operator's Manual RegA Model 9000 Laser*. 1997.

[DAP94a] M. A. Dupertuis, B. Acklin, and M. Proctor. "Generalization of complex Snell–Descartes and Fresnel laws". In: *J. Opt. Soc. Am. A* 11 (Mar. 1994), pp. 1159–1166. URL: http://josaa.osa.org/abstract.cfm?URI=josaa-11-3-1159.

[DAP94b] M. A. Dupertuis, B. Acklin, and M. Proctor. "Generalized energy balance and reciprocity relations for thin-film optics". In: *J. Opt. Soc. Am. A* 11 (Mar. 1994), pp. 1167–1174. URL: http://josaa.osa.org/abstract.cfm?URI=josaa-11-3-1167.

[DC+12] S. Dal Conte, C. Giannetti, G. Coslovich, F. Cilento, D. Bossini, T. Abebaw, F. Banfi, G. Ferrini, H. Eisaki, M. Greven, A. Damascelli, D. van der Marel, and F. Parmigiani. "Disentangling the Electronic and Phononic Glue in a High-Tc Superconductor". In: *Science* 335 (2012), pp. 1600–1603. URL: http://www.sciencemag.org/content/335/6076/1600.abstract.

[DD11] Jure Demsar and Thomas Dekorsy. *Optical Techniques for Solid-State Materials Characterization*. Ed. by R.P. Prasankumar and A.J. Taylor. CRC Press Boca Raton, FL, 2011. Chap. Carrier dynamics in bulk semiconductors and metals after ultrashort pulse excitation. ISBN: 978-1-4398-1437-6.

[DFJ68] Harold L. Davis, J. S. Faulkner, and H. W. Joy. "Calculation of the Band Structure for Copper as a Function of Lattice Spacing". In: *Phys. Rev.* 167 (Mar. 1968), pp. 601–607. URL: http://link.aps.org/doi/10.1103/PhysRev.167.601.

[DG02] Martin Dressel and George Grüner. *Electrodynamics of Solids*. Cambridge University Press, Jan. 2002. ISBN: 0521597269. URL: http://www.worldcat.org/isbn/0521597269.

[DR06] "Ultrashort Laser Pulse Phenomena". In: *Ultrashort Laser Pulse Phenomena (Second Edition)*. Ed. by Jean-Claude Diels and Wolfgang Rudolph. Burlington: Academic Press, 2006. ISBN: 978-0-12-215493-5.

[DT71] Marie-Martine Dujardin and Marie-Luce Theye. “Investigation of the optical properties of Ag by means of thin semi-transparent films”. In: *Journal of Physics and Chemistry of Solids* 32 (1971), pp. 2033–2044. URL: http://www.sciencedirect.com/science/article/pii/S0022369771803803.

[DV+12] G. Della Valle, M. Conforti, S. Longhi, G. Cerullo, and D. Brida. “Real-time optical mapping of the dynamics of nonthermal electrons in thin gold films”. In: *Phys. Rev. B* 86 (Oct. 2012), p. 155139. URL: http://link.aps.org/doi/10.1103/PhysRevB.86.155139.

[Dre+02] Markus Drescher, Michael Hentschel, R Kienberger, Matthias Uiberacker, Vladislav Yakovlev, Armin Scrinzi, Th Westerwalbesloh, U Kleineberg, Ulrich Heinzmann, and Ferenc Krausz. “Time-resolved atomic inner-shell spectroscopy”. In: *Nature* 419 (2002), pp. 803–807.

[Dru00] P. Drude. “Zur Elektronentheorie der Metalle”. German. In: *Annalen der Physik* 306 (1900), pp. 566–613. URL: http://dx.doi.org/10.1002/andp.19003060312.

[EA+87] H. E. Elsayed-Ali, T. B. Norris, M. A. Pessot, and G. A. Mourou. “Time-resolved observation of electron-phonon relaxation in copper”. In: *Phys. Rev. Lett.* 58 (Mar. 1987), pp. 1212–1215. URL: https://link.aps.org/doi/10.1103/PhysRevLett.58.1212.

[EB78] H. Eschrig and I. Bergert. “An optimized LCAO version for band structure calculations application to copper”. In: *physica status solidi (b)* 90 (1978), pp. 621–628. URL: http://dx.doi.org/10.1002/pssb.2220900221.

[EFN84] H Eckardt, L Fritsche, and J Noffke. “Self-consistent relativistic band structure of the noble metals”. In: *Journal of Physics F: Metal Physics* 14 (1984), p. 97. URL: http://stacks.iop.org/0305-4608/14/i=1/a=013.

[ELRM06] P. G. Etchegoin, E. C. Le Ru, and M. Meyer. “An analytic model for the optical properties of gold”. In: *The Journal of Chemical Physics* 125, 164705 (2006). URL: http://scitation.aip.org/content/aip/journal/jcp/125/16/10.1063/1.2360270.

[ELRM07] P. G. Etchegoin, E. C. Le Ru, and M. Meyer. “Erratum: "An analytic model for the optical properties of gold" [J. Chem. Phys.125, 164705 (2006)]”. In: *The Journal of*

Chemical Physics 127, 189901 (2007). URL: http://scitation.aip.org/content/aip/journal/jcp/127/18/10.1063/1.2802403.

[Eic+15] M. Eichberger, S. Liebermann, C. Klose, M. Obergfell, R. Birmuske, J. Sutter, and J. Demsar. "Cooperative atomic motion probed by ultrafast transmission electron diffraction". In: *Proc. SPIE* 9361 (2015), 93610U–93610U–7. URL: http://dx.doi.org/10.1117/12.2080796.

[Ern+09] Ralph Ernstorfer, Maher Harb, Christoph T. Hebeisen, Germán Sciaini, Thibault Dartigalongue, and R. J. Dwayne Miller. "The Formation of Warm Dense Matter: Experimental Evidence for Electronic Bond Hardening in Gold". In: *Science* 323 (2009), pp. 1033–1037. URL: http://science.sciencemag.org/content/323/5917/1033.

[FC70] C. Y. Fong and Marvin L. Cohen. "Energy Band Structure of Copper by the Empirical Pseudopotential Method". In: *Phys. Rev. Lett.* 24 (Feb. 1970), pp. 306–309. URL: http://link.aps.org/doi/10.1103/PhysRevLett.24.306.

[FWC75] C. Y. Fong, J. P. Walter, and Marvin L. Cohen. "Comparison of band structures and charge distributions of copper and silver". In: *Phys. Rev. B* 11 (Apr. 1975), pp. 2759–2767. URL: http://link.aps.org/doi/10.1103/PhysRevB.11.2759.

[Fan+92] W. S. Fann, R. Storz, H. W. K. Tom, and J. Bokor. "Electron thermalization in gold". In: *Phys. Rev. B* 46 (Nov. 1992), pp. 13592–13595. URL: http://link.aps.org/doi/10.1103/PhysRevB.46.13592.

[Fri+07] D. M. Fritz et al. "Ultrafast Bond Softening in Bismuth: Mapping a Solid's Interatomic Potential with X-rays". In: *Science* 315 (2007), pp. 633–636. URL: http://science.sciencemag.org/content/315/5812/633.

[GSL95] Rogier H. M. Groeneveld, Rudolf Sprik, and Ad Lagendijk. "Femtosecond spectroscopy of electron-electron and electron-phonon energy relaxation in Ag and Au". In: *Phys. Rev. B* 51 (May 1995), pp. 11433–11445. URL: https://link.aps.org/doi/10.1103/PhysRevB.51.11433.

[GV05] Gabriele Giuliani and Giovanni Vignale. *Quantum theory of the electron liquid*. Cambridge: Cambridge Univ. Press, 2005, XIX, 777 S.

[GW98] Vitalyi E. Gusev and Oliver B. Wright. "Ultrafast nonequilibrium dynamics of electrons in metals". In: *Phys. Rev. B* 57 (Feb. 1998), pp. 2878–2888. URL: http://link.aps.org/doi/10.1103/PhysRevB.57.2878.

[Gad+10] C. Gadermaier, A. S. Alexandrov, V. V. Kabanov, P. Kusar, T. Mertelj, X. Yao, C. Manzoni, D. Brida, G. Cerullo, and D. Mihailovic. "Electron-Phonon Coupling in High-Temperature Cuprate Superconductors Determined from Electron Relaxation Rates". In: *Phys. Rev. Lett.* 105 (Dec. 2010), p. 257001. URL: http://link.aps.org/doi/10.1103/PhysRevLett.105.257001.

[Gad+14] C. Gadermaier, V. V. Kabanov, A. S. Alexandrov, L. Stojchevska, T. Mertelj, C. Manzoni, G. Cerullo, N. D. Zhigadlo, J. Karpinski, Y. Q. Cai, X. Yao, Y. Toda, M. Oda, S. Sugai, and D. Mihailovic. "Strain-Induced Enhancement of the Electron Energy Relaxation in Strongly Correlated Superconductors". In: *Phys. Rev. X* 4 (Mar. 2014), p. 011056. URL: https://link.aps.org/doi/10.1103/PhysRevX.4.011056.

[Gen07] James E Gentle. *Matrix algebra: theory, computations, and applications in statistics*. Springer Science & Business Media, 2007.

[Ger+01] A. Gerlach, K. Berge, A. Goldmann, I. Campillo, A. Rubio, J. M. Pitarke, and P. M. Echenique. "Lifetime of *d* holes at Cu surfaces: Theory and experiment". In: *Phys. Rev. B* 64 (Aug. 2001), p. 085423. URL: http://link.aps.org/doi/10.1103/PhysRevB.64.085423.

[Ger68] Ulrich Gerhardt. "Effect of Uniaxial and Hydrostatic Strain on the Optical Constants and the Electronic Structure of Copper". In: *Phys. Rev.* 172 (Aug. 1968), pp. 651–664. URL: http://link.aps.org/doi/10.1103/PhysRev.172.651.

[Gon+09] X. Gonze et al. "ABINIT: First-principles approach to material and nanosystem properties". In: *Computer Physics Communications* 180 (2009), pp. 2582–2615. URL: http://www.sciencedirect.com/science/article/pii/S0010465509002276.

[Gra+77] John E. Graebner, Brage Golding, R. J. Schutz, F. S. L. Hsu, and H. S. Chen. "Low-Temperature Properties of a Superconducting Disordered Metal". In: *Phys. Rev. Lett.* 39 (Dec. 1977), pp. 1480–1483. URL: https://link.aps.org/doi/10.1103/PhysRevLett.39.1480.

[Gri76] G. Grimvall. "The Electron-Phonon Interaction in Normal Metals". In: *Physica Scripta* 14 (1976), p. 63. URL: http://iopscience.iop.org/1402-4896/14/1-2/013.

[Gri81] Göran Grimvall. *The electron-phonon interaction in metals*. Vol. 8. North-Holland Amsterdam, 1981.

[HLB82] L.J. Hanekamp, W. Lisowski, and G.A. Bootsma. "Spectroscopic ellipsometric investigation of clean and oxygen covered copper single crystal surfaces". In: *Surface Science* 118 (1982), pp. 1 –18. URL: http://www.sciencedirect.com/science/article/pii/0039602882900097.

[Hah70] Thomas A. Hahn. "Thermal Expansion of Copper from 20 to 800 K - Standard Reference Material 736". In: *Journal of Applied Physics* 41 (1970), pp. 5096–5101. URL: http://scitation.aip.org/content/aip/journal/jap/41/13/10.1063/1.1658614.

[Hil+87] R W Hill, S J Collocott, K A Gschneidner Jr, and F A Schmidt. "The heat capacity of high-purity gadolinium from 0.5 to 4 K and the effects of interstitial impurities". In: *Journal of Physics F: Metal Physics* 17 (1987), p. 1867. URL: http://stacks.iop.org/0305-4608/17/i=9/a=013.

[Hil11] David J. Hill. *Optical Techniques for Solid-State Materials Characterization*. Ed. by R.P. Prasankumar and A.J. Taylor. CRC Press Boca Raton, FL, 2011. Chap. Ultrafast Pump-Probe Spectroscopy. ISBN: 978-1-4398-1437-6.

[JC72] P. B. Johnson and R. W. Christy. "Optical Constants of the Noble Metals". In: *Phys. Rev. B* 6 (Dec. 1972), pp. 4370–4379. URL: http://link.aps.org/doi/10.1103/PhysRevB.6.4370.

[JC75] P. B. Johnson and R. W. Christy. "Optical constants of copper and nickel as a function of temperature". In: *Phys. Rev. B* 11 (Feb. 1975), pp. 1315–1323. URL: http://link.aps.org/doi/10.1103/PhysRevB.11.1315.

[JGM81] O. Jepsen, D. Glötzel, and A. R. Mackintosh. "Potentials, band structures, and Fermi surfaces in the noble metals". In: *Phys. Rev. B* 23 (Mar. 1981), pp. 2684–2696. URL: http://link.aps.org/doi/10.1103/PhysRevB.23.2684.

[JK54] G. Joos and A. Klopfer. "Die Temperaturabhängigkeit der optischen Konstanten von Cu, Ag und Au bis herab zu 20° K". German. In: *Zeitschrift für Physik* 138 (1954), pp. 251–265. URL: http://dx.doi.org/10.1007/BF01340669.

[JMW77] A. G. M. Jansen, F. M. Mueller, and P. Wyder. "Direct measurement of electron-phonon coupling $\alpha^2F(\omega)$ using point contacts: Noble metals". In: *Phys. Rev. B* 16 (Aug. 1977), pp. 1325–1328. URL: http://link.aps.org/doi/10.1103/PhysRevB.16.1325.

[JMW78] A. G. M. Jansen, F. M. Mueller, and P. Wyder. "Normal Metallic Point Contacts". In: *Science* 199 (1978), pp. 1037–1040. URL: http://science.sciencemag.org/content/199/4333/1037.

[JWM75] J. F. Janak, A. R. Williams, and V. L. Moruzzi. "Self-consistent band theory of the Fermi-surface, optical, and photoemission properties of copper". In: *Phys. Rev. B* 11 (Feb. 1975), pp. 1522–1536. URL: http://link.aps.org/doi/10.1103/PhysRevB.11.1522.

[JZ16] Pengfei Ji and Yuwen Zhang. "Ab initio determination of effective electron-phonon coupling factor in copper". In: *Physics Letters A* 380 (2016), pp. 1551–1555. URL: http://www.sciencedirect.com/science/article/pii/S0375960116001973.

[Joy+13] Hannah J. Joyce, Callum J. Docherty, Qiang Gao, H Hoe Tan, Chennupati Jagadish, James Lloyd-Hughes, Laura M. Herz, and Michael B. Johnston. "Electronic properties of GaAs, InAs and InP nanowires studied by terahertz spectroscopy". In: *Nanotechnology* 24 (2013), p. 214006. URL: http://stacks.iop.org/0957-4484/24/i=21/a=214006.

[KA08] V. V. Kabanov and A. S. Alexandrov. "Electron relaxation in metals: Theory and exact analytical solutions". In: *Phys. Rev. B* 78 (Nov. 2008), p. 174514. URL: http://link.aps.org/doi/10.1103/PhysRevB.78.174514.

[KBB01] R. Knorren, G. Bouzerar, and K. H. Bennemann. "Dynamics of excited electrons in copper: The role of Auger electrons". In: *Phys. Rev. B* 63 (Feb. 2001), p. 094306. URL: http://link.aps.org/doi/10.1103/PhysRevB.63.094306.

[KHE79] J. A. Knapp, F. J. Himpsel, and D. E. Eastman. "Experimental energy band dispersions and lifetimes for valence and conduction bands of copper using angle-resolved photoemission". In: *Phys. Rev. B* 19 (May 1979), pp. 4952–4964. URL: http://link.aps.org/doi/10.1103/PhysRevB.19.4952.

[KHW98] E. Knoesel, A. Hotzel, and M. Wolf. "Ultrafast dynamics of hot electrons and holes in copper: Excitation, energy relaxation, and transport effects". In: *Phys. Rev. B* 57 (May 1998), pp. 12812–12824. URL: http://link.aps.org/doi/10.1103/PhysRevB.57.12812.

[KLT57] M.I. Kaganov, I.M. Lifshitz, and L.V. Tanatarov. "Relaxation between electrons and the crystalline lattice". In: *Soviet Physics Jetp-Ussr* 4 (1957), pp. 173–178.

[Kel10] U. Keller. "Ultrafast solid-state laser oscillators: a success story for the last 20 years with no end in sight". In: *Applied Physics B* 100 (2010), pp. 15–28. URL: http://dx.doi.org/10.1007/s00340-010-4045-3.

[Klo13] Carolin Klose. "Ultrafast electron diffraction on metals". In: *Master thesis, University of Konstanz* (2013), p. 75.

[Kno+00] R. Knorren, K. H. Bennemann, R. Burgermeister, and M. Aeschlimann. "Dynamics of excited electrons in copper and ferromagnetic transition metals: Theory and experiment". In: *Phys. Rev. B* 61 (Apr. 2000), pp. 9427–9440. URL: http://link.aps.org/doi/10.1103/PhysRevB.61.9427.

[LB76] A. Larose and B. N. Brockhouse. "Lattice vibrations in copper at elevated temperatures studied by neutron scattering". In: *Canadian Journal of Physics* 54 (1976), pp. 1990–2009. URL: http://dx.doi.org/10.1139/p76-237.

[LL04] Z. P. Lu and C. T. Liu. "Role of minor alloying additions in formation of bulk metallic glasses: A Review". In: *Journal of Materials Science* 39 (2004), pp. 3965–3974. URL: http://dx.doi.org/10.1023/B:JMSC.0000031478.73621.64.

[LSB81] R. Lässer, N. V. Smith, and R. L. Benbow. "Empirical band calculations of the optical properties of d-band metals. I. Cu, Ag, and Au". In: *Phys. Rev. B* 24 (Aug. 1981), pp. 1895–1909. URL: http://link.aps.org/doi/10.1103/PhysRevB.24.1895.

[Lar75] André Larose. "Phonons in copper at elevated temperatures". In: *Phd thesis, McMaster University - Hamilton* (1975). URL: https://macsphere.mcmaster.ca/handle/11375/14290.

[Len+98] J. Leng, J. Opsal, H. Chu, M. Senko, and D.E. Aspnes. "Analytic representations of the dielectric functions of materials for device and structural modeling". In: *Thin Solid Films*

313-314 (1998), pp. 132–136. URL: http://www.sciencedirect.com/science/article/pii/S0040609097007992.

[Lig+09] M. Ligges, I. Rajkovic, P. Zhou, O. Posth, C. Hassel, G. Dumpich, and D. von der Linde. "Observation of ultrafast lattice heating using time resolved electron diffraction". In: *Applied Physics Letters* 94, 101910 (2009). URL: http://scitation.aip.org/content/aip/journal/apl/94/10/10.1063/1.3095497.

[Lig09] Manuel Ligges. "Untersuchung der schnellen Gitteraufheizung in dünnen (Halb-)Metallfilmen mit Hilfe zeitaufgelöster Elektronenbeugung". German. In: *Phd thesis, University of Duisburg-Essen* (2009). URL: http://duepublico.uni-duisburg-essen.de/servlets/DerivateServlet/Derivate-22548/Ligges_Diss.pdf.

[Lis+04] M. Lisowski, P.A. Loukakos, U. Bovensiepen, J. Stähler, C. Gahl, and M. Wolf. "Ultrafast dynamics of electron thermalization, cooling and transport effects in Ru(001)". In: *Applied Physics A* 78 (2004), pp. 165–176. URL: http://dx.doi.org/10.1007/s00339-003-2301-7.

[Lis05] Martin Julius Lisowski. "Elektronen- und Magnetisierungsdynamik in Metallen untersucht mit zeitaufgelöster Photoemission". German. In: *Phd thesis, Freie Universität Berlin* (2005).

[Loi77] A Loidl. "Zero to first sound transition in copper". In: *Journal of Physics F: Metal Physics* 7 (1977), p. L57. URL: http://stacks.iop.org/0305-4608/7/i=3/a=001.

[MB15] F. Manghi and V. Boni. "Quasiparticle band structure". In: *Journal of Electron Spectroscopy and Related Phenomena* 200 (2015), pp. 181–192. URL: http://www.sciencedirect.com/science/article/pii/S0368204815001127.

[MODS01] Andrea Marini, Giovanni Onida, and Rodolfo Del Sole. "Quasiparticle Electronic Structure of Copper in the GW Approximation". In: *Phys. Rev. Lett.* 88 (Dec. 2001), p. 016403. URL: http://link.aps.org/doi/10.1103/PhysRevLett.88.016403.

[Mal+11] Ermin Malic, Torben Winzer, Evgeny Bobkin, and Andreas Knorr. "Microscopic theory of absorption and ultrafast many-particle kinetics in graphene". In: *Phys. Rev. B* 84 (Nov. 2011), p. 205406. URL: http://link.aps.org/doi/10.1103/PhysRevB.84.205406.

[Mar+02] Andrea Marini, Rodolfo Del Sole, Angel Rubio, and Giovanni Onida. "Quasiparticle band-structure effects on the *d* hole lifetimes of copper within the *GW* approximation". In: *Phys. Rev. B* 66 (Oct. 2002), p. 161104. URL: http://link.aps.org/doi/10.1103/PhysRevB.66.161104.

[Mat+94] R. Matzdorf, R. Paniago, G. Meister, and A. Goldmann. "Upper limits for d-hole inverse lifetimes in copper". In: *Solid State Communications* 92 (1994), pp. 839–842. URL: http://www.sciencedirect.com/science/article/pii/0038109894903255.

[Mat98] René Matzdorf. "Investigation of line shapes and line intensities by high-resolution UV-photoemission spectroscopy - Some case studies on noble-metal surfaces". In: *Surface Science Reports* 30 (1998), pp. 153–206. URL: http://www.sciencedirect.com/science/article/pii/S0167572997000137.

[McM68] W. L. McMillan. "Transition Temperature of Strong-Coupled Superconductors". In: *Phys. Rev.* 167 (Mar. 1968), pp. 331–344. URL: http://link.aps.org/doi/10.1103/PhysRev.167.331.

[Mij73] P.E. Mijnarends. "Positron annihilation in 3d metals". In: *Physica* 63 (1973), pp. 235–247. URL: http://dx.doi.org/10.1016/0031-8914(73)90311-X.

[NKG02] Masaya Nagai and Makoto Kuwata-Gonokami. "Time-Resolved Reflection Spectroscopy of the Spatiotemporal Dynamics of Photo-Excited Carriers in Si and GaAs". In: *Journal of the Physical Society of Japan* 71 (2002), pp. 2276–2279. URL: https://www.jstage.jst.go.jp/article/jpsj/71/9/71_9_2276/_article.

[NR73] G. Nilsson and S. Rolandson. "Lattice Dynamics of Copper at 80 K". In: *Phys. Rev. B* 7 (Mar. 1973), pp. 2393–2400. URL: http://link.aps.org/doi/10.1103/PhysRevB.7.2393.

[Nic+67] R. M. Nicklow, G. Gilat, H. G. Smith, L. J. Raubenheimer, and M. K. Wilkinson. "Phonon Frequencies in Copper at 49 and 298°K". In: *Phys. Rev.* 164 (Dec. 1967), pp. 922–928. URL: http://link.aps.org/doi/10.1103/PhysRev.164.922.

[PN66] David Pines and Philippe Nozières. *The theory of quantum liquids*. Vol. 1. Normal Fermi liquids. New York: Benjamin, 1966, XI, 355 S.

[PNO99] H. Petek, H. Nagano, and S. Ogawa. "Hole Decoherence of d Bands in Copper". In: *Phys. Rev. Lett.* 83 (July 1999), pp. 832–835. URL: http://link.aps.org/doi/10.1103/PhysRevLett.83.832.

[PO97] H. Petek and S. Ogawa. "Femtosecond time-resolved two-photon photoemission studies of electron dynamics in metals". In: *Progress in Surface Science* 56 (1997), pp. 239–310. URL: http://dx.doi.org/10.1016/S0079-6816(98)00002-1.

[PS69] G P Pells and M Shiga. "The optical properties of copper and gold as a function of temperature". In: *Journal of Physics C: Solid State Physics* 2 (1969), p. 1835. URL: http://stacks.iop.org/0022-3719/2/i=10/a=318.

[Pel67] G P Pells. "Measurement of the optical properties of alloys in ultra-high vacuum". In: *Journal of Scientific Instruments* 44 (1967), p. 997. URL: http://stacks.iop.org/0950-7671/44/i=12/a=307.

[Per+07] L. Perfetti, P. A. Loukakos, M. Lisowski, U. Bovensiepen, H. Eisaki, and M. Wolf. "Ultrafast Electron Relaxation in Superconducting $Bi_2Sr_2CaCu_2O_{8+\delta}$ by Time-Resolved Photoelectron Spectroscopy". In: *Phys. Rev. Lett.* 99 (Nov. 2007), p. 197001. URL: https://link.aps.org/doi/10.1103/PhysRevLett.99.197001.

[Pet+00] H Petek, H Nagano, M.J Weida, and S Ogawa. "The role of Auger decay in hot electron excitation in copper". In: *Chemical Physics* 251 (2000), pp. 71–86. URL: http://www.sciencedirect.com/science/article/pii/S0301010499003031.

[Phi71] Norman E. Phillips. "Low-temperature heat capacity of metals". In: *C R C Critical Reviews in Solid State Sciences* 2 (1971), pp. 467–553. URL: http://dx.doi.org/10.1080/10408437108243546.

[QF58] John J. Quinn and Richard A. Ferrell. "Electron Self-Energy Approach to Correlation in a Degenerate Electron Gas". In: *Phys. Rev.* 112 (Nov. 1958), pp. 812–827. URL: http://link.aps.org/doi/10.1103/PhysRev.112.812.

[RCZ11] Yunpeng Ren, J. K. Chen, and Yuwen Zhang. "Optical properties and thermal response of copper films induced by ultrashort-pulsed lasers". In: *Journal of Applied Physics* 110, 113102 (2011). URL: http://scitation.aip.org/content/aip/journal/jap/110/11/10.1063/1.3662897.

[RL72] R. Rosei and D. W. Lynch. "Thermomodulation Spectra of Al, Au, and Cu". In: *Phys. Rev. B* 5 (May 1972), pp. 3883–3894. URL: http://link.aps.org/doi/10.1103/PhysRevB.5.3883.

[Rak+98] Aleksandar D. Rakić, Aleksandra B. Djurišić, Jovan M. Elazar, and Marian L. Majewski. "Optical properties of metallic films for vertical-cavity optoelectronic devices". In: *Appl. Opt.* 37 (Aug. 1998), pp. 5271–5283. URL: http://ao.osa.org/abstract.cfm?URI=ao-37-22-5271.

[Rob60] S. Roberts. "Optical Properties of Copper". In: *Phys. Rev.* 118 (June 1960), pp. 1509–1518. URL: http://link.aps.org/doi/10.1103/PhysRev.118.1509.

[Ros74] R. Rosei. "Temperature modulation of the optical transitions involving the Fermi surface in Ag: Theory". In: *Phys. Rev. B* 10 (July 1974), pp. 474–483. URL: http://link.aps.org/doi/10.1103/PhysRevB.10.474.

[SCT13] S. Tripura Sundari, Sharat Chandra, and A. K. Tyagi. "Temperature dependent optical properties of silver from spectroscopic ellipsometry and density functional theory calculations". In: *Journal of Applied Physics* 114, 033515 (2013). URL: http://scitation.aip.org/content/aip/journal/jap/114/3/10.1063/1.4813874.

[SE85] G. Seifert and H. Eschrig. "LCAO-Xα Calculations of Transition Metal Clusters". In: *physica status solidi (b)* 127 (1985), pp. 573–585. URL: http://dx.doi.org/10.1002/pssb.2221270218.

[SHC94] N. S. Sariciftci, A. J. Heeger, and Y. Cao. "Paramagnetic susceptibility of highly conducting polyaniline: Disordered metal with weak electron-electron interactions (Fermi glass)". In: *Phys. Rev. B* 49 (Mar. 1994), pp. 5988–5992. URL: https://link.aps.org/doi/10.1103/PhysRevB.49.5988.

[SI11] C Suryanarayana and Akihisa Inoue. *Bulk metallic glasses*. Vol. 361. CRC press Boca Raton, FL, 2011.

[SK05] H. Savaloni and Ahmad Reza Khakpour. "Substrate temperature dependence on the optical properties of Cu and Ag thin films". In: *The European Physical Journal - Applied Physics* 31 (Aug. 2005), pp. 101–112. URL: http://www.epjap.org/action/article_S1286004205000534.

[SS96] S. Y. Savrasov and D. Y. Savrasov. "Electron-phonon interactions and related physical properties of metals from linear-response theory". In: *Phys. Rev. B* 54 (Dec. 1996), pp. 16487–16501. URL: http://link.aps.org/doi/10.1103/PhysRevB.54.16487.

[Sai+82] G. Saito, T. Enoki, K. Toriumi, and H. Inokuchi. "Two-dimensionality and suppression of metal-semiconductor transition in a new organic metal with alkylthio substituted TTF and perchlorate". In: *Solid State Communications* 42 (1982), pp. 557–560. URL: http://www.sciencedirect.com/science/article/pii/003810988290607X.

[Sch+00] R. W. Schoenlein, S. Chattopadhyay, H. H. W. Chong, T. E. Glover, P. A. Heimann, C. V. Shank, A. A. Zholents, and M. S. Zolotorev. "Generation of Femtosecond Pulses of Synchrotron Radiation". In: *Science* 287 (2000), pp. 2237–2240. URL: http://science.sciencemag.org/content/287/5461/2237.

[Sch+87] R. W. Schoenlein, W. Z. Lin, J. G. Fujimoto, and G. L. Eesley. "Femtosecond studies of nonequilibrium electronic processes in metals". In: *Phys. Rev. Lett.* 58 (Apr. 1987), pp. 1680–1683. URL: http://link.aps.org/doi/10.1103/PhysRevLett.58.1680.

[Sch+94] C. A. Schmuttenmaer, M. Aeschlimann, H. E. Elsayed-Ali, R. J. D. Miller, D. A. Mantell, J. Cao, and Y. Gao. "Time-resolved two-photon photoemission from Cu(100): Energy dependence of electron relaxation". In: *Phys. Rev. B* 50 (Sept. 1994), pp. 8957–8960. URL: https://link.aps.org/doi/10.1103/PhysRevB.50.8957.

[Seg62] Benjamin Segall. "Fermi Surface and Energy Bands of Copper". In: *Phys. Rev.* 125 (Jan. 1962), pp. 109–122. URL: http://link.aps.org/doi/10.1103/PhysRev.125.109.

[Sla72] John C. Slater. "Statistical Exchange-Correlation in the Self-Consistent Field". In: Advances in Quantum Chemistry 6 (1972), pp. 1–92. URL: http://www.sciencedirect.com/science/article/pii/S0065327608605419.

[Sno68] E. C. Snow. "Self-Consistent Energy Bands of Metallic Copper by the Augmented-Plane-Wave Method. II". In: *Phys. Rev.* 171 (July 1968), pp. 785–789. URL: http://link.aps.org/doi/10.1103/PhysRev.171.785.

[Sun+94] C.-K. Sun, F. Vallée, L. H. Acioli, E. P. Ippen, and J. G. Fujimoto. "Femtosecond-tunable measurement of electron thermalization in gold". In: *Phys. Rev. B* 50 (Nov. 1994), pp. 15337–15348. URL: http://link.aps.org/doi/10.1103/PhysRevB.50.15337.

[TF11] Xiaoli Tang and B. Fultz. "First-principles study of phonon linewidths in noble metals". In: *Phys. Rev. B* 84 (Aug. 2011), p. 054303. URL: http://link.aps.org/doi/10.1103/PhysRevB.84.054303.

[TM94] Guray Tas and Humphrey J. Maris. "Electron diffusion in metals studied by picosecond ultrasonics". In: *Phys. Rev. B* 49 (June 1994), pp. 15046–15054. URL: http://link.aps.org/doi/10.1103/PhysRevB.49.15046.

[TS90] W M Temmerman and P A Sterne. "The band model for the ground state properties of gadolinium metal". In: *Journal of Physics: Condensed Matter* 2 (1990), p. 5529. URL: http://stacks.iop.org/0953-8984/2/i=25/a=005.

[Thi+79] P. Thiry, D. Chandesris, J. Lecante, C. Guillot, R. Pinchaux, and Y. Pétroff. "E vs $\vec{\mathrm{k}}$ and Inverse Lifetime of Cu(110)". In: *Phys. Rev. Lett.* 43 (July 1979), pp. 82–85. URL: http://link.aps.org/doi/10.1103/PhysRevLett.43.82.

[Thè70] Marie-Luce Thèye. "Investigation of the Optical Properties of Au by Means of Thin Semitransparent Films". In: *Phys. Rev. B* 2 (Oct. 1970), pp. 3060–3078. URL: http://link.aps.org/doi/10.1103/PhysRevB.2.3060.

[Tor+08] Marc Torrent, François Jollet, François Bottin, Gilles Zérah, and Xavier Gonze. "Implementation of the projector augmented-wave method in the {ABINIT} code: Application to the study of iron under pressure". In: *Computational Materials Science* 42 (2008), pp. 337–351. URL: http://www.sciencedirect.com/science/article/pii/S0927025607002108.

[VL08] A. Vial and T. Laroche. "Comparison of gold and silver dispersion laws suitable for FDTD simulations". In: *Applied Physics B* 93 (2008), pp. 139–143. URL: http://dx.doi.org/10.1007/s00340-008-3202-4.

[WF97] W. Wallauer and Th. Fauster. "Two-photon excitation processes and linewidths of surface and image states on Cu(111)". In: *Surface Science* 374 (1997), pp. 44–50. URL: http://www.sciencedirect.com/science/article/pii/S0039602896012423.

[Wak65] Shinya Wakoh. "Band Structure of Metallic Copper and Nickel by a Self-Consistent Procedure". In: *Journal of the Physical Society of Japan* 20 (1965), pp. 1894–1901. URL: http://dx.doi.org/10.1143/JPSJ.20.1894.

[Wal+16] Lutz Waldecker, Roman Bertoni, Ralph Ernstorfer, and Jan Vorberger. "Electron-Phonon Coupling and Energy Flow in a Simple Metal beyond the Two-Temperature Approximation". In: *Phys. Rev. X* 6 (Apr. 2016), p. 021003. URL: http://link.aps.org/doi/10.1103/PhysRevX.6.021003.

[Wan+16] Zhijie Wang, Dawei Cao, Liaoyong Wen, Rui Xu, Manuel Obergfell, Yan Mi, Zhibing Zhan, Nasori Nasori, Jure Demsar, and Yong Lei. "Manipulation of charge transfer and transport in plasmonic-ferroelectric hybrids for photoelectrochemical applications". In: *Nature communications* 7 (2016).

[Win+76] P Winsemius, F F van Kampen, H P Lengkeek, and C G van Went. "Temperature dependence of the optical properties of Au, Ag and Cu". In: *Journal of Physics F: Metal Physics* 6 (1976), p. 1583. URL: http://stacks.iop.org/0305-4608/6/i=8/a=017.

[ZCE03] V. P. Zhukov, E. V. Chulkov, and P. M. Echenique. "Lifetimes of *d* holes in Cu and Au: Full-potential LMTO approach". In: *Phys. Rev. B* 68 (July 2003), p. 045102. URL: http://link.aps.org/doi/10.1103/PhysRevB.68.045102.

[Zal66] R. Zallen. *Optical properties and electronic structure of metals and alloys*. Ed. by F Abeles. Proc. Int. Conf, 1966. Chap. The effect of pressure on optical properties of the noble metals.

[Zha+04] W. Zhang, S. H. Brongersma, T. Clarysse, V. Terzieva, E. Rosseel, W. Vandervorst, and K. Maex. "Surface and grain boundary scattering studied in beveled polycrystalline thin copper films". In: *Journal of Vacuum Science & Technology B* 22 (2004), pp. 1830–1833. URL: http://scitation.aip.org/content/avs/journal/jvstb/22/4/10.1116/1.1771666.

[Zhu+01] V. P. Zhukov, F. Aryasetiawan, E. V. Chulkov, I. G. de Gurtubay, and P. M. Echenique. "Corrected local-density approximation band structures, linear-response dielectric functions, and quasiparticle lifetimes in noble metals". In: *Phys. Rev. B* 64 (Oct. 2001), p. 195122. URL: http://link.aps.org/doi/10.1103/PhysRevB.64.195122.

[Yag+84] É. B. Yagubskiĭ, I. F. Shchegolev, V. N. Laukhin, P. A. Kononovich, M. V. Karatsovnik, A. V. Zvarykina, and L. I. Buravov. "Normal-pressure superconductivity in an organic metal (BEDT-TTF)$_2$I$_3$ [bis (ethylene dithiolo) tetrathiofulvalene triiodide]". In: *Soviet Journal of Experimental and Theoretical Physics Letters* 39 (Jan. 1984), p. 12.